Constitutive Modelling of Shear Localisation in Saturated Dilative Sand

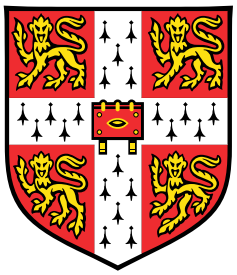

Hansini Erandika Mallikarachchi

Department of Engineering
University of Cambridge

This dissertation is submitted for the degree of
Doctor of Philosophy

Churchill College

April 2019

Declaration

I hereby declare that except where specific reference is made to the work of others, the contents of this dissertation are original and have not been submitted in whole or in part for consideration for any other degree or qualification in this, or any other university. This dissertation is my own work and contains nothing which is the outcome of work done in collaboration with others. This dissertation contains fewer than 65,000 words including appendices, footnotes, tables and equations. It has fewer than 150 figures.

Hansini Erandika Mallikarachchi
April 2019

Abstract

Constitutive Modelling of Shear Localisation in Saturated Dilative Sand

Hansini Erandika Mallikarachchi

Undrained deformation of dilative sand generates negative excess pore pressure. It enhances the strength which is called dilative hardening. This increased suction is not permanent. The heterogeneity at the grain scale triggers localisations causing local volume changes and associated drainage. The negative hydraulic gradient drives fluid into dilating shear zones. It loosens the soil and diminishes the shear strength.

Continuum-based finite element method cannot apprehend pore-fluid movements at grain scale without extreme mesh refinement. This thesis aims to evaluate the capabilities of the finite element method and existing material models to identify the onset and propagation of localisation in dilatant hardening materials. Then constitutive relations are upgraded to provide mesh-independent results for different drainage conditions.

First, the ability of critical state Nor-Sand model to simulate drained and undrained deformation of dense sand is evaluated. Then non-coaxial and non-associative flow theories are integrated. Different flow rules are examined for proportional and non-proportional loading paths. Both theories inhibit the tendency to dilate. Non-coaxial Nor-Sand model reduces the overly stiff response predicted by the original Nor-Sand model during undrained dilative shearing.

Secondly, a bifurcation analysis is conducted to evaluate the potential of constitutive models to detect the onset of localisation. Under strict isochoric constraint, the Rice criterion is never met by the Nor-Sand model. Both non-coaxial and non-associative flow rules do not bring destabilising effects in dilative sand. The local drainage is the triggering mechanism of shear bands in globally undrained dense sand.

Third, the nonlocal regularisation is applied to Nor-Sand model and its capability to produce mesh objective results is elucidated for drained sand. Along with scaling, nonlocal Nor-Sand model can reduce the mesh sensitivity without extreme mesh refinement.

Fourth, a comprehensive parametric study is conducted to examine the rate and mesh dependence of saturated dense sand with closed and open drainage boundaries. In both cases, the hydro-mechanical coupling decides both the onset and propagation of localisation. Depending on the local degree of drainage shear zones can be fully or partially drained. The normalised velocity at the boundary between localised and uniform deformation is mesh dependent.

For saturated sand, the nonlocal method is successful only when either all material points or shear band material points are fully drained depending on global boundary conditions. The regularisation of drained soil skeleton is not effective when the hydro-mechanical coupling is active.

A mesh-independent, rate-dependent constitutive model is developed to capture the pore-fluid diffusion at the grain scale. It describes the macroscopic constitutive behaviour of undrained dense sand in the presence of a locally drained or partially drained shear band.

I would like to dedicate this thesis to my loving parents . . .

Acknowledgements

First and foremost I would like to thank my supervisor Prof.Kenichi Soga for his continuous guidance and encouragement. This journey would not have been possible without his patience and trust in me. I am grateful to him for enduring my impatience and agitation throughout the past four and a half years. I am also deeply indebted to him for giving me the opportunity and funding to work as a visiting research scholar at the University of California, Berkeley.

I also would like to express my sincere gratitude to Dr.Dongfang Liang for his utmost support as my principal supervisor during the last three years. I am also profoundly grateful to Prof. Malcolm Bolton and Dr. Giovanna Biscontin for their valuable feedback and advice on my thesis during my stay in Cambridge.

My heartfelt thanks go to Dr.Loizos Pelecanos, Dr.Krishna Kumar, Dr.Shyamini Kularathna and Dr.James Ferns for mentoring me in their unique way to mould my research carrier. Particularly I appreciate Dr.Loizos Pelecanos's and Dr.Dilan Robert's teachings on ABAQUS software during Tokyo Gas project. I gratefully mention Dr.Krishna Kumar's support to learn high-performance computing and C++. I also would like to acknowledge insights from Mr.Mike Jefferies and Dr.James Ferns about the Nor-Sand constitutive model. I must also thank Dr.Thusyanthan and Dr.Hans Teunissen for sharing their knowledge and expertise.

I would like to give special thanks to Dr.Anthony Haynes and CUED Language Unit for helping me to improve my language skills. I owe a debt of gratitude to Prof.Alex Webb, my tutor in Churchill college for coaching me whenever I was struggling. I wish to thank all staff members in the department of Engineering and Churchill college for their abiding support.

I also would like to mention the immense support I received from my colleagues and friends. Especially, I am grateful for Dr.Nimalika Perera and Dr. Himantha Coorey for assisting me during my hard times.

Finally, I should thank my parents and sister for their understanding and unconditional love. Thank you for standing by me throughout this challenging journey.

Table of Contents

List of Figures

List of Tables

Nomenclature

Superscripts

e	elastic
ep	elastoplastic
num	numerical
out	outside
p	plastic
pc	plastic coaxial
pnc	plastic non-coaxial
sb	shear band

Subscripts

avg	average
c	critical state
i	image state
k	integration point number
max	maximum
min	minimum

P plastic potential

q deviatoric

tc triaxial compression

v volumetric

Other

$[]$ jump or change

Δ incremental

Scalars

$\bar{h}$ softening modulus

$\bar{h}_{pnc}$ non-coaxial modulus

$\bar{k}$ permeability

$\bar{m}$ additional parameter

χ maximum dilatancy coefficient

$\dot{\gamma}$ shear strain rate

ε_q^{sb} bifurcation deviatoric strain

ε_q deviatoric strain

ε_v volumetric strain

η' effective stress ratio

γ_w unit weight of water

κ softening variable

μ area ratio

ν poisson ratio

ϕ	friction angle
Ψ	state parameter
ψ	dilation angle
Θ	lode angle
θ^{sb}	shear band angle
υ	representative volume
$\widehat{h}$	NS hardening coefficient
ξ	local coordinates
c_v	diffucivity coefficient
D	dilatancy
$d\lambda$	Plastic multiplier
D_{50}	mean grain diameter
e	void ratio
F	yeild function
G^e	elastic shear modulus
H	specimen height
h	mesh size
J_2	second invariant of deviatoric stress
J_3	third invariant of deviatoric stress
k	shear factor
K^e	elastic bulk modulus
K^f	fluid bulk modulus

K^p plastic hardening modulus

K_0 lateral earth pressure coefficient

L drainage length

l_c characteristic length

l_k characteristic diffusion length

M critical friction ratio

m over-nonlocal parameter

m_v compressibility coefficient

N volumetric coupling term

n arbitory time step

P plastic potential function

p' effective mean pressure

p_i image pressure

$p_{i,max}$ maximum image pressure

Q particle crushing pressure

q deviatoric stress

R shear coefficient

r pressure exponent

t, n shear band coordinates

t^{sb} shear band thickness

U excess pore pressure

V loading velocity

V_n normalised loading velocity

W hardening parameter

W_2 second order work

x, y, z global coordinates

Tensors and Vectors

δ_{ij} kronecker delta

ε_{ij} total strain

σ'_{ij} effective stress

σ_{ij} total stress

A_{ijkl} non-coaxial flow direction tensor

a_{ij} non-coaxial flow direction vector

D^e_{ijkl} elastic stiffness

D^p_{ijkl} plastic stiffness

D^{ep}_{ijkl} elastoplastic stiffness

e_{ij} deviatoric strain

n_{ij} unit vector normal to shear band

Q^u_{ij} undrained acoustic

Q_{ij} acoustic

s_{ij} deviatoric stress

T_{ijkl} transformation tensor

T_{ij} traction

U_i pore pressure feild

u_i displacement feild

Abbreviations

BC biaxial compression

C-NA Coaxial and Non-associative

C Coaxial

CC Cam-Clay

CSL/CS Critical State Line/Critical State

DEM Discrete Element Method

DP Drucker-Prager

FEM Finite Element Method

MC Mohr-Coloumb

NC-NA Non-coaxial and Non-associative

NC Non-coaxial

NS Nor-Sand

SB shear band

SS simple shear

TC triaxial compression

Chapter 1

Introduction

1.1 Background

During the design of geotechnical structures, the sand is frequently assumed as fully drained material. However, when the sand has a considerable percentage of fine particles, its permeability decreases. Hence, under sufficiently high loading rates, the sand can behave as partially drained or undrained. This notion is substantiated by laboratory and field evidence of soil cutting, ploughing, pile loading, buckling of pipelines, penetrometer and peizocone testing (Bransby and Ireland, 2009; Huy, 2008; Kutter, 2006; Mangal, 1999; Palmer, 1999; Silva and Bolton, 2005)

The mechanical response during undrained deformation of sand is governed by its initial state as shown in Figure 1.1. Out of these, the undrained deformation of loose and medium-dense sand has been widely investigated due to their potential to liquefaction. The behaviour of undrained dense sand is not sufficiently scrutinised. The purpose of this thesis is to address this research gap, focusing on the shear localisation of undrained dense sand.

If dense sand is subjected to shear under constant volume (restricted drainage), its tendency to dilate produces negative excess pore pressure, which is the reason for the observed effective stress increase in Figure 1.1. Theoretically, this can continue until the dilation ceases at the critical state. However, several phenomena can interrupt this strength increase. If suction increases sufficiently to reach the cavitation pressure, the sand may desaturate releasing the isochoric constraint. There are several experimental and numerical studies which state that the localisation in undrained dense sand is delayed until the cavitation takes place. However, in deep-sea condition, the hydrostatic pressure can suppress the cavitation (Kutter, 2006; Palmer, 1999).

Another possible phenomenon is the internal drainage in shear zones. This is confined mostly to theoretical studies. The lack of experimental evidence possibly must have discouraged probing the validity of this hypothesis. However, this is more likely in offshore condition. Hence it is important to understand the mechanism behind this internal drainage and numerically capture it during the design of offshore infrastructure.

In dilative sand, the shear deformation is accompanied by a tendency for particles to move apart. In submerged saturated conditions, the space between particles is filled with incompressible water. Hence pore fluid has to flow into this increased void space which causes a pore pressure gradient. If the deformation is slow, a small gradient is required to drive the flow. Hence pore pressure changes and strength increase are low. If the deformation is rapid, the pore pressure in shear zones drops substantially to produce a large gradient to drive the flow as shown in Figure 1.2. This increased suction tightens soil particles, augmenting effective stress. However, this is not a permanent condition. The hydraulic gradient associated with negative pore pressure drives fluid into dilating zones, which in turn loosens the sand and diminishes the shear strength. Therefore, the duration of this strength enhancement depends on the permeability, compressibility, the rate of loading and width of the shear zone.

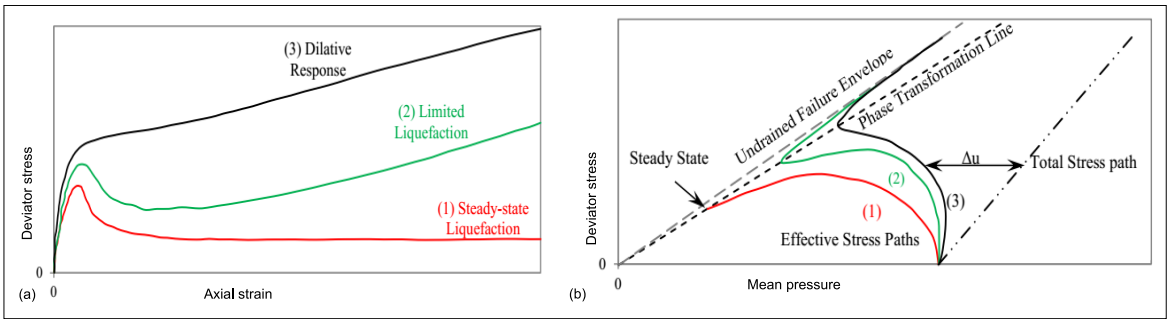

Fig. 1.1 Undrained monotonic loading of triaxial test: (a) stress-strain relationships and (b) stress paths (Soysa, 2015)

1.2 Motivation

In the conventional finite element method, the pore pressure is calculated at nodes. In most geotechnical problems, the element is several magnitudes larger than the grain size. Hence internal water movements which occur at a scale smaller than element size are can not be captured. Therefore, shear resistance of saturated dilative sand is overestimated assuming a uniform deformation. Mallikarachchi et al. (2018), Soga et al. (2015) and Cheong (2006) investigated the loading rate effect‘ on buried offshore pipelines. They reported a continuous

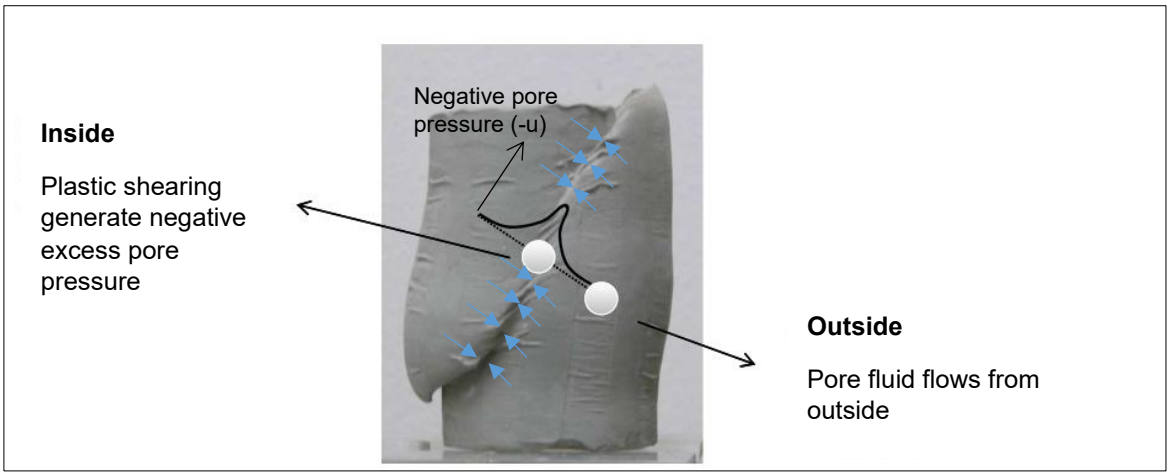

Fig. 1.2 Excess pore pressure gradient across the shear band

increase of reaction force on pipelines under higher loading rates. This progressive dilative strengthening occurred regardless of the material model used.

Figures 1.3 and 1.4 illustrate shear strain and excess pore pressure contours during upheaval buckling of buried offshore pipelines simulated with two mesh sizes. The 0.6m pipe is displaced 0.3m during 0.1s (strain rate 5/s). The minimum iteration time step is 0.001s. The soil is simulated with the Mohr-Coulomb model with constant friction angle 40° and dilation angle 16°. Permeability is 0001m/s and diffusivity coefficient is $5\text{m}^2/\text{s}$. In both figures, it is observed that elements within the proximity of the pipe are subjected to considerable shear deformation due to fast loading which generates high negative excess pore pressure.

In Figure 1.3 and 1.4, the maximum distances between two nodes around the pipe are about 0.24m and 0.06m, receptively. For the considered diffusivity the characteristic times required to dissipate pore pressure across these distances are 0.0125s and 0.0007s for coarse and fine meshes respectively. Since the adopted time step is smaller than the dissipation time for the coarse mesh, the pore pressure is accumulated. Hence Figure 1.3(b) displays a uniform increase of negative pore pressure around the pipe. As a result, the force exerted on the pipe is increased. The numerical model in Figure 1.3(a) shows a diffused type failure rather than localised one. It cannot capture the onset of localisation and pore fluid diffusion at micro-scale. Therefore, irrespective of remote boundary condition, the elements near the pipe act as undrained. Moreover, conventional Mohr-Coulomb type models assume constant dilation leading to a continuous generation of negative excess pore pressure. On the contrary, in the finer mesh, the characteristic diffusion time is shorter than the time step. Hence shear bands caused by local drainage are triggered earlier. Figure 1.4(a) displays

several micro-localisations which facilitate pore pressure diffusion. As a result, suction in Figure 1.4(b) is lower than that of Figure 1.3(b).

In field condition micro-scale localisations take place around the pipe. If the permeability is large enough, the generated negative excess pore pressure can dissipate at shear band scale reducing the strength. The characteristic time for the pore pressure to dissipate across a 0.001m thick shear band of is 2×10^{-6}s for the considered diffusivity. Hence, taking account of increased shear resistance predicted by coarse mesh sizes can lead to unsafe design. In essence, finite element predictions are unreliable unless the mesh is refined near the shear zones. Since it is computationally expensive, an alternative mechanism should be sought to numerically capture the micro-kinematics at grain scale with affordable mesh sizes. For that, capabilities and limitations of the finite element method to simulate localisation in saturated dilative sand should be probed in details. Further, the importance of using a critical state soil model based on stress-volumetric relationship is highlighted.

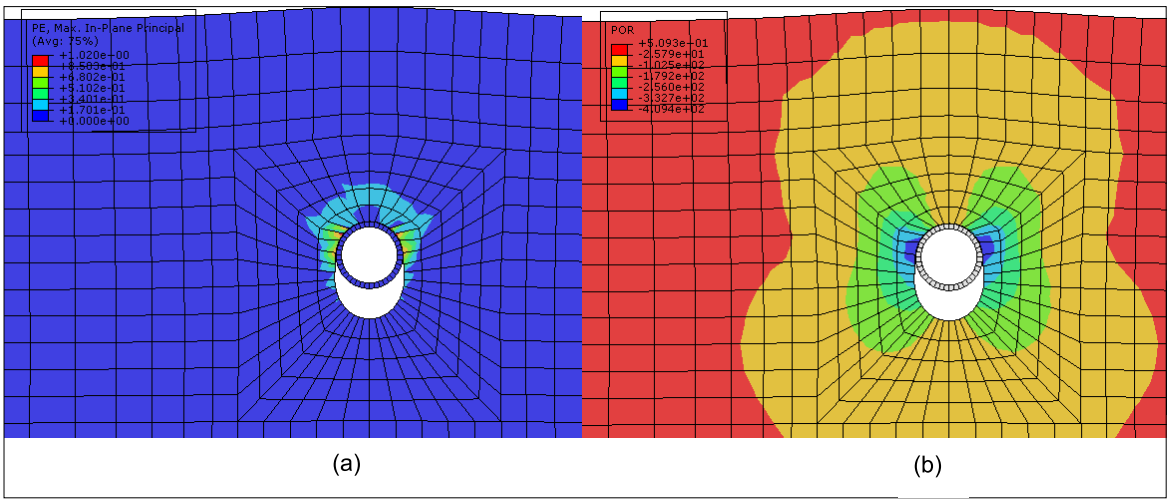

Fig. 1.3 Deformation of a buried pipeline simulated with a coarse mesh: Contours of (a) shear strain and (b) pore pressure

It is worthwhile to clarify the phrase "mesh-dependency" which will be used throughout this thesis. Predictions of FE simulations are sensitive to the adopted mesh size until a converged solution is reached. Hence for a particular boundary value problem, a mesh convergent study should be performed refining the mesh until there is no difference in FE results. Further, the localisation zone becomes vanishingly small with continuous mesh refinement. Practically, it is impossible to refine the mesh size to comply with the real shear band thickness at the granular scale. This thesis focuses on pathological mesh sensitivity within the range of non-converged element sizes.

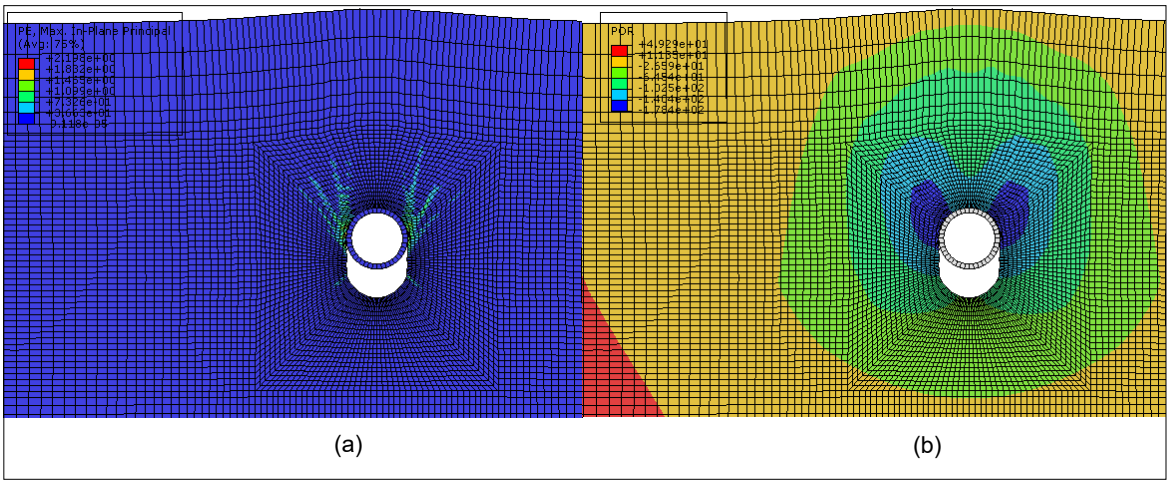

Fig. 1.4 Deformation of a buried pipeline simulated with a fine mesh: Contours of (a) shear strain and (b) pore pressure

1.3 Objectives

Motivated by the aforementioned research prospect, this thesis focuses on upgrading the constitutive relations of saturated dilatant granular materials. The following objectives are achieved in the process. The content of this thesis is limited to results of biaxial compression tests which is a preliminary attempt to solve the problem.

- Assess the ability of constitutive models to capture undrained (uniform) deformation of saturated dense sand for both proportional and non-proportional loading paths

- Evaluate the potency of constitutive models to detect the onset of localisation and explore possible triggering mechanisms of shear bands in undrained dense sand

- Examine the influence of time and space parameters for the localisation and internal fluid movements during the deformations with open and closed remote drainage boundaries

- Implement a regularisation technique to prevent mesh sensitivity of post-localised deformation and appraise its potential for saturated sand under different drainage conditions

- Develop a mesh-independent, two-scale constitutive relationship to capture local drainage at the shear band scale during undrained deformations

1.4 Main Contributions

The key contributions of this thesis are summarised below. These will be elaborated at the end of each chapter.

- Integration of non-coaxial flow theory into critical state Nor-Sand model

  During shear localisation, considerable principal axis rotations take place, and hence the stress paths deviate from those of proportional loading. In those cases, conventional constitutive relations built upon coaxiality are not valid. Therefore, the Nor-Sand model is improved with yield vertex theory, and its performance during plane-strain simple shear and biaxial compression is evaluated with single element modelling. During simple shear deformation, it is observed that the non-coaxial Nor-Sand model softens the mechanical response. It inhibits the tendency to dilate and reduces the volume changes for the drained tests and excess pore pressure generation for the undrained tests. Hence it can reduce the overly stiff undrained dilative hardening response predicted by coaxial models.

- Exploring the initiation of localisation during undrained deformation of dilative sand

  Under strict isochoric constraint, continuum-based constitutive relations do not satisfy drained or undrained localisation criteria. The Nor-Sand model cannot predict the onset of localisation in uniformly undrained dense sand even with non-associative and/or non-coaxial flow rules. Local drainage initiated by inhomogeneity is required to bring destabilising effects in dilative hardening materials.

  In globally undrained dense sand, non-coaxial flow rule delays the local volume changes and hence the localisation. Although the loading path is globally proportional, the non-coaxial effect softens the global stress-strain response due to principal axis rotation inside the shear band.

- Application of nonlocal regularisation to a critical state model

  The Nor-Sand model is enriched with nonlocal regularisation. It can successfully circumvent the mesh sensitivity of post-localised deformation in drained sand. Mesh objective force-displacement curves and band widths are achieved by integrating a characteristic length into constitutive formulations. Scaling can be applied with nonlocal regularisation to produce a physically realistic mechanical response without extreme mesh refinement.

Limitations of nonlocal Nor-Sand model are discussed, enlightening the range of length scales of the element to grain size ratios for which the method is effective.

- Investigation of local drainage in globally undrained saturated dense sand

  Through a comprehensive parametric study, the rate and mesh dependence of saturated dense sand is elucidated. Depending on the interplay between the generation and dissipation of excess pore pressure gradient across the shear band, the behaviour of globally undrained dense sand can be characterised as fully drained, partially drained and locally undrained. The lower boundary of the undrained uniform deformation is both mesh and rate dependent whereas the upper boundary of the fully drained shear band region is sensitive to rate and specimen dimension.

  The mesh dependency of local drainage in an undrained biaxial compression test is displayed in Figures 1.5 (a) and (b). The coarse mesh in Figure 1.5 (a) cannot detect the localisation and related pore-fluid movements which occur at a scale smaller than its mesh size. Hence it predicts a uniform undrained deformation with greater negative excess pore pressure.

- Investigating the suitability of nonlocal regularisation for multi-phase material

  The nonlocal Nor-Sand model is proved to be successful only when either all material points or shear band material points are fully drained. For rate-independent plasticity, the regularisation of underlying drained soil skeleton is not effective for the partially drained condition. This is mainly because the onset of localisation is affected by the hydro-mechanical coupling.

  In Figure 1.5(b) a shear band is already triggered while Figure 1.5(a) is still showing an almost uniform deformation. Hence the nonlocal regularisation is not effective in these circumstances.

- Development of a novel constitutive model for undrained dense sand with an embedded localisation

  A two-scale constitutive model is produced in this study to capture pore fluid diffusion at shear band scale while simulating macroscopic mechanical response of undrained dense sand. The influence of both rate and scale parameters is incorporated. Hence it is inherently mesh-independent.

  The macroscopic response of a bifurcated material point in Figure 1.5(a) is phenomenologically represented by the average response of two constituents: shear band and

outside material, as displayed in Figure 1.5(d). Hence bifurcated gauss points in the coarse mesh can capture the localised response simulated by the fine mesh (Figure 1.5(c)). Pore fluid movement between the shear band and outside is calculated at the constitutive level using the diffusion equation. Depending on the band thickness and the interplay between the rate of generation and dissipation of pore pressure, the embedded shear band can be fully or partially drained.

It is found in this study that undrained dilative hardening predicted by a homogeneous material model is considerably reduced due to the pore fluid movement between the shear band and outside materials. This phenomenon can precede the cavitation under sufficiently high back pressure. The model is applied to large-scale biaxial tests.

1.5 Thesis Outline

This thesis consists of two main parts. Chapters 2 and 3 investigate constitutive modelling and pre-bifurcation deformation. Chapters 4, 5 and 6 explore the modelling of post-localised deformation.

- Chapter 2

  This chapter presents basic theoretical concepts on constitutive modelling of granular material within critical state elasto-plasticity. Formulations of Nor-Sand model are described, and its potency in simulating both drained and undrained dense sand is appraised. Two new flow rules are introduced to the original Nor-Sand model, and their influences in predicting the behaviour of dense sand are evaluated under plane-strain simple shear and biaxial compression. The main purpose of this chapter is to provide a theoretical platform for the succeeding chapters.

- Chapter 3

  The instability analysis of multi-phase granular material is scrutinised in this chapter. A broad literature review on detecting the onset of localisation is presented. Then bifurcation theories are applied to both drained and undrained saturated dilative sand. The capability of different flow rules to capture the onset of localisation is examined. The local drainage is identified as the triggering mechanism of localisation in globally undrained dense sand.

- Chapter 4

  The post-localised mesh sensitivity and regularisation techniques of single-phase material are discussed in this chapter. The nonlocal theory is applied to Nor-Sand

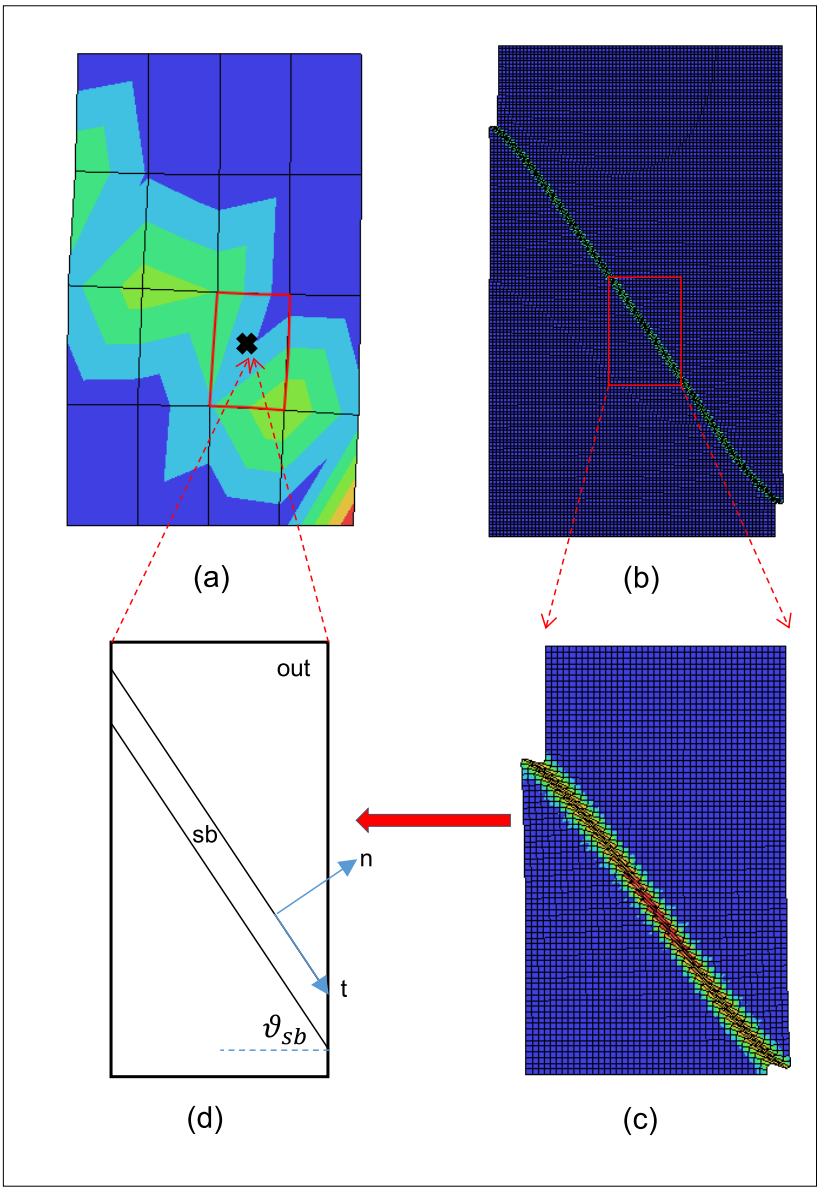

Fig. 1.5 Illustration of the hypothesis behind the proposed two-scale constitutive model: the gauss point in (a) should replicate the mechanical behaviour inside the rectangle in (b)

model, and its capability to produce mesh objective results during post-bifurcation deformation of drained dense sand is evaluated. Strengths and limitations of the method are assessed.

- Chapter 5

  The rate dependence of saturated dense sand and its association with local drainage are investigated. A parametric study is conducted on the loading rate, permeability, mesh and specimen size under closed and open remote drainage boundaries. The

influence of time and space parameters on the generation and dissipation of pore fluid is identified. The competency of nonlocal regularisation to prevent mesh sensitivity of hydro-mechanical coupled problems is evaluated.

- Chapter 6

  A novel constitutive model is introduced for undrained dilative sand to apprehend internal water movements independent of the element size. It takes account of time and space dependence of pore fluid diffusion in saturated dense sand. The model is validated and applied for large-scale boundary value problems. Its strengths and limitations are discussed.

- Chapter 7

  This chapter summarises the main findings of the thesis and proposes possible extensions of work.

Chapter 2

Constitutive Modelling of Dilative Dense Sand

2.1 Preface

The mechanical response of granular media is governed by micro-mechanisms at grain scale. A general application of conventional continuum theories to a discontinuous assembly of particles is a rough approximation. This chapter presents some continuum based constitutive relations which describe fundamental mathematical idealisation of dilative granular material. Their strengths and limitations are scrutinised justifying the selected material model for the purpose of this thesis.

Section 2.2 outlines basic concepts and equations in constitutive modelling, which will be used throughout the thesis. Features of Nor-Sand model are presented in section 2.3. Section 2.4 details the numerical procedure for plane-strain single element simulations. The potency of the original Nor-Sand model to capture biaxial compression in both drained and undrained conditions is evaluated in 2.5. Non-coaxial and non-associative flow rules are introduced to the original Nor-Sand model in section 2.6. The influence of two flow rules for different loading paths is discussed in section 2.7.

2.2 Basic Ingredients of Constitutive Models

2.2.1 Stress and strain invariants

In general space (x, y, z), stress and strain vectors are defined in voigt notation as

$$\sigma_{ij} = \{\sigma_{xx}, \sigma_{yy}, \sigma_{zz}, \sigma_{xy}, \sigma_{xz}, \sigma_{yz}\} \tag{2.1}$$

$$\varepsilon_{ij} = \{\varepsilon_{xx}, \varepsilon_{yy}, \varepsilon_{zz}, 2\varepsilon_{xy}, 2\varepsilon_{xz}, 2\varepsilon_{yz}\} \tag{2.2}$$

Unless otherwise defined, stresses are in effective terms as

$$\sigma'_{ij} = \sigma_{ij} - U\,\delta_{ij} \tag{2.3}$$

where δ_{ij} is Kronecker delta whose value is 1 when $i = j$ and 0 otherwise. U is the pore water pressure. Familiar Cambridge type scalar invariants of stress and strain measures are adopted here.

$$p' = \frac{\sigma'_{ii}}{3} \tag{2.4}$$

$$q = \sqrt{\frac{3}{2}}\sqrt{s_{ij}s_{ij}} \tag{2.5}$$

where deviatoric stress vector is defined as $s_{ij} = \sigma'_{ij} - p'\delta_{ij}$. p' and q are effective mean pressure and deviatoric stress respectively. The effective stress ratio is defined as

$$\eta' = \frac{q}{p'} \tag{2.6}$$

In general stress plane, the stress state is defined by (p', q, Θ). The Lode angle Θ is defined as

$$\Theta = \frac{1}{3}\sin^{-1}\left[\frac{3\sqrt{3}}{2}\frac{J_3}{J_2^3}\right] \tag{2.7}$$

where J_3 and J_2 are defined as

$$J_2 = \sqrt{\frac{s_{ij}s_{ij}}{2}} = \sqrt{\frac{1}{3}}q \tag{2.8}$$

$$J_3 = \frac{1}{3}s_{ij}s_{jk}s_{ki} \tag{2.9}$$

ε_v and ε_q are volumetric and deviatoric strain invariants respectively.

$$\varepsilon_v = \varepsilon_{ii} \tag{2.10}$$

$$\varepsilon_q = \sqrt{\frac{2}{3}}\sqrt{e_{ij}e_{ij}} \tag{2.11}$$

where deviatoric strain vector is defined as $e_{ij} = \varepsilon_{ij} - \frac{\varepsilon_v}{3}\delta_{ij}$. Above stress and strain invariants are work conjugates of each other and also valid for rate or incremental terms.

2.2.2 Elasticity

When the soil is elastic, the stress condition lies within the yield surface. The elastic deformation can be expressed using elastic bulk modulus K^e, elastic shear modulus G^e and Poisson's ratio ν.

$$d\sigma'_{ij} = D^e_{ijkl}\, d\varepsilon_{kl} \tag{2.12}$$

$$D^e_{ijkl} = \begin{bmatrix} K^e + \frac{4G^e}{3} & K^e - \frac{2G^e}{3} & K^e - \frac{2G^e}{3} & 0 & 0 & 0 \\ K^e - \frac{2G^e}{3} & K^e + \frac{4G^e}{3} & K^e - \frac{2G^e}{3} & 0 & 0 & 0 \\ K^e - \frac{2G^e}{3} & K^e - \frac{2G^e}{3} & K^e + \frac{4G^e}{3} & 0 & 0 & 0 \\ 0 & 0 & 0 & G^e & 0 & 0 \\ 0 & 0 & 0 & 0 & G^e & 0 \\ 0 & 0 & 0 & 0 & 0 & G^e \end{bmatrix} \tag{2.13}$$

$$G^e = R\, p'^r \tag{2.14a}$$

$$K^e = \frac{2(1+\nu)}{3(1-2\nu)} G \tag{2.14b}$$

where R is the shear coefficient and r is the pressure exponent. Generally, soil elastic stiffness is non-linear. It reduces with shear strain and increases with confining stress (Cheong, 2006). Ideally, R should be a function of shear strain. Since the focus of this thesis is large deformation, R is assumed as constant.

2.2.3 Plasticity

Yield surface

Plastic (irrecoverable) deformation of soil is caused by rearrangement of soil grains. Yield surface F defines the development of strength. For critical state models it is associated with grains interlocking and inter-granular friction resulted from volume change. When the stress state reach the yield surface plastic deformation begins.

Flow rule

Flow rule defines the direction and magnitude of plastic strain increment which is generally assumed to be normal to the plastic potential function P.

$$d\varepsilon^p_{ij} = d\lambda \frac{\partial P}{\partial \sigma_{ij}} \tag{2.15}$$

where $d\lambda$ is the plastic multiplier. The flow rule is associative if the yield and plastic potential functions are equal ($P = F$) and non-associative otherwise ($P \neq F$).

Consistency condition

According to consistency condition the derivative of the yield function is zero when the stress state is on the yield surface.

$$dF = \frac{\partial F}{\partial \sigma'_{ij}} d\sigma'_{ij} + \frac{\partial F}{\partial \varepsilon^p_{ij}} d\varepsilon^p_{ij} = 0 \tag{2.16}$$

Hardening rule

The hardening rule determines how the size of yield surface evolves with the plastic strain. The size of the yield surface is governed by the scalar hardening parameter W.

$$\frac{\partial F}{\partial \varepsilon^p_{ij}} = \frac{\partial F}{\partial W} \frac{\partial W}{\partial \varepsilon^p_{ij}} \tag{2.17}$$

2.2.4 Stress-strain relationship

In soil, the stress-strain relationship is non-linear, hence effective stress rate $d\sigma'_{ij}$ should be expressed in incremental form as

$$d\sigma'_{ij} = D^{ep}_{ijkl}\, d\varepsilon_{kl} \tag{2.18}$$

The total strain increment $d\varepsilon_{ij}$ can be decomposed into plastic and elastic components as

$$d\varepsilon_{ij} = d\varepsilon^e_{ij} + d\varepsilon^p_{ij} \tag{2.19}$$

where superscripts e, p and ep denote elastic, plastic and elasto-plastic components respectively.

$$D^{ep}_{ijkl} = D^e_{ijkl} - D^p_{ijkl} \tag{2.20}$$

where D^e, D^p and D^{ep} are elastic, plastic and elasto-plastic stiffness matrices respectively.

$$d\sigma'_{ij} = D^e_{ijkl}\, d\varepsilon^e_{kl} = D^e_{ijkl}\, (d\varepsilon_{ij} - d\varepsilon^p_{ij}) = D^e_{ijkl}\, (d\varepsilon_{ij} - d\lambda \frac{\partial P}{\partial \sigma_{ij}}) \tag{2.21}$$

Combing Equation 2.16 with 2.21, the elasto-plastic stiffness matrix is derived as

$$D^{ep}_{ijkl} = \left[D^e_{ijkl} - \frac{D^e_{ijkl} \left(\frac{\partial P}{\partial \sigma_{ij}}\right) \left(\frac{\partial F}{\partial \sigma_{ij}}\right)^T D^e_{ijkl}}{-\left(\frac{\partial F}{\partial W}\right) \left(\frac{\partial W}{\partial \varepsilon^p_{ij}}\right)^T \left(\frac{\partial P}{\partial \sigma_{ij}}\right) + \left(\frac{\partial F}{\partial \sigma_{ij}}\right) D^e_{ijkl} \left(\frac{\partial P}{\partial \sigma_{ij}}\right)^T} \right] \tag{2.22}$$

The plastic hardening modulus can be defined as

$$K^p = -\left(\frac{\partial F}{\partial W}\right) \left(\frac{\partial W}{\partial \varepsilon^p_{ij}}\right)^T \left(\frac{\partial P}{\partial \sigma_{ij}}\right) \tag{2.23}$$

Partial derivatives of stress

The partial derivatives of yield and plastic potential functions are given by Equations 2.24 and 2.25 respectively.

$$\frac{\partial F}{\partial \sigma_{ij}} = \frac{\partial F}{\partial p'}\frac{\partial p'}{\partial \sigma_{ij}} + \frac{\partial F}{\partial q}\frac{\partial q}{\partial \sigma_{ij}} + \frac{\partial F}{\partial \Theta}\frac{\partial \Theta}{\partial \sigma_{ij}} \tag{2.24}$$

$$\frac{\partial P}{\partial \sigma_{ij}} = \frac{\partial P}{\partial p'}\frac{\partial p'}{\partial \sigma_{ij}} + \frac{\partial P}{\partial q}\frac{\partial q}{\partial \sigma_{ij}} + \frac{\partial P}{\partial \Theta}\frac{\partial \Theta}{\partial \sigma_{ij}} \tag{2.25}$$

The partial derivative of mean effective stress is

$$\frac{\partial p'}{\partial \sigma_{ij}} = [1/3, 1/3, 1/3, 0, 0, 0]^T \tag{2.26}$$

The partial derivative of deviatoric stress is

$$\frac{\partial q}{\partial \sigma_{ij}} = \frac{3}{2q}\left[s_{xx}, s_{yy}, s_{zz}, 2s_{xy}, 2s_{xz}, 2s_{yz}\right]^T \tag{2.27}$$

The partial derivative of Lode angle is

$$\frac{\partial \Theta}{\partial \sigma_{ij}} = \frac{\sqrt{3}}{2}\frac{1}{cos(3\Theta)}\frac{1}{J_2^3}\left[\frac{\partial J_3}{\partial \sigma_{ij}} - \frac{3J_3}{J_2}\frac{\partial J_2}{\partial \sigma_{ij}}\right]^T \tag{2.28}$$

$$\frac{\partial J_3}{\partial \sigma_{ij}} = \begin{bmatrix} \frac{2}{3}s_{yy}s_{zz} - \frac{1}{3}s_{xx}s_{zz} - \frac{1}{3}s_{xx}s_{yy} - \frac{2}{3}s_{yz}^2 + \frac{1}{3}s_{xy}^2 + \frac{2}{3}s_{xz}^2 \\ \frac{2}{3}s_{xx}s_{zz} - \frac{1}{3}s_{yy}s_{zz} - \frac{1}{3}s_{xx}s_{yy} - \frac{2}{3}s_{xz}^2 + \frac{1}{3}s_{xy}^2 + \frac{2}{3}s_{yz}^2 \\ \frac{2}{3}s_{xx}s_{yy} - \frac{1}{3}s_{xx}s_{zz} - \frac{1}{3}s_{yy}s_{zz} - \frac{2}{3}s_{xy}^2 + \frac{1}{3}s_{xz}^2 + \frac{2}{3}s_{yz}^2 \\ -2s_{zz}s_{xy} + 2s_{xz}s_{yz} \\ -2s_{yy}s_{xz} + 2s_{xy}s_{yz} \\ -2s_{xx}s_{yz} + 2s_{xy}s_{xz} \end{bmatrix} \tag{2.29}$$

$$\frac{\partial J_2}{\partial \sigma_{ij}} = \frac{1}{2J_2}\left[s_{xx},\ s_{yy},\ s_{zz},\ 2s_{xy},\ 2s_{xz},\ 2s_{yz}\right]^T \tag{2.30}$$

The aforementioned relations can be used for any constitutive model.

2.2.5 Elasto-plastic models for granular material

The focus of this section is not to elaborate about soil constitutive models, but to discuss the strengths and limitations of the prevailing models and to justify reasons for selecting the Nor-Sand model for this thesis.

Within the context of elasto-plasticity, constitutive models are abundant in the research literature to simulate the pressure dependent granular materials. Mohr-Coulomb (MC) and

Drucker-Prager (DP) type models are still widely utilised in the field of geotechnics. In these models, the yield surface is approximated as the Coulomb failure criterion which is based on experimental evidence. However, yielding and failure are not synonymous. Even after adopting a non-associative flow rule and hardening/softening functions to vary friction and dilation, the aforementioned models are still incapable of capturing many facets of real soil. Especially for frictional materials, plastic stress state is associated with volume change. Hence a yield surface derived upon a proper stress dilatancy relationship is necessary.

The ability to change volume by shearing distinguishes particulate materials such as soil from other materials. The behaviour of granular materials is dictated by their initial states. On shearing, initially dense sand exhibits slight contraction followed by dilation, whereas initially loose sand always contracts upon shearing. This propensity of soil to change in volume during shearing is called the dilatancy, and it is the kernel of the critical state soil mechanics.

$$D = -\frac{\mathrm{d}\varepsilon_v^p}{\mathrm{d}\varepsilon_q^p} \tag{2.31}$$

“Dilation towards critical states is central to understanding of soil behaviour" (Bolton, 1986)

Based on energy conservation the first stress-dilatancy relationship was proposed by Taylor (1948) which laid the foundation for the critical state Cam-Clay model by Roscoe et al. (1963).

$$\eta' = M - D \tag{2.32}$$

$$q_c = M p_c' \tag{2.33}$$

where the critical friction ratio M is a soil property which varies with the stress path or the proportion of intermediate principal stresses. p_c' and q_c are effective mean pressure and deviatoric stress at the critical state.

The critical state theory identifies the density of soil as a state variable rather than a soil property, which satisfactorily explains volume changes during shear deformation. It is the main advantage of Cambridge type critical state models over conventional ones. They form a surface in p’-q-e space as shown in Figure 2.1 (b) and (c). This is called the state boundary surface. If stress-volumetric state lies on the yield surface, the behaviour is elasto-plastic, and if it is inside, the behaviour is elastic (Potts and Zdravkovic, 1999). If stress state lies on the yield surface right to the point ‘C’ in Figure 2.1 (a), the volumetric strains are positive (compressive), such that yield surface is hardening. This side is called wet or subcritical side of yield. If the stress state is on the left of the point ‘C’, the soil is dilating (expanding)

which ensues the softening of yield surface. This is called dry or supercritical side (Potts and Zdravkovic, 1999).

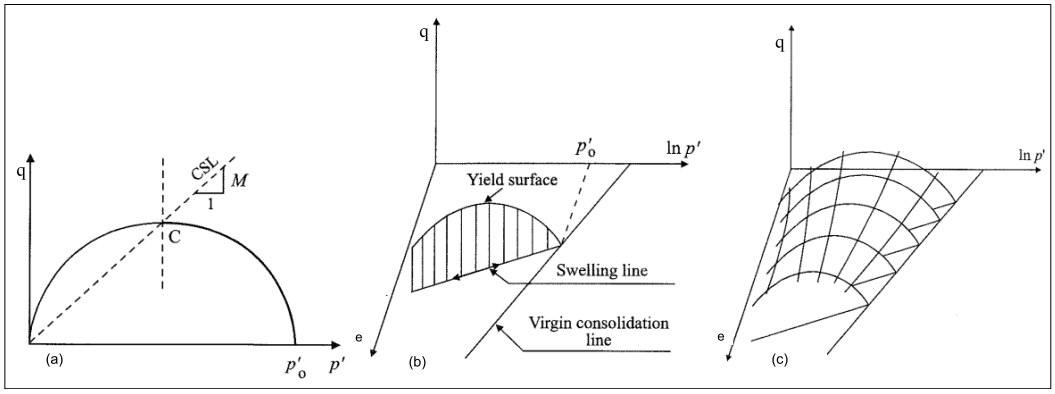

Fig. 2.1 (a) Yield surface and (b),(c) state boundary surface of critical state models (Potts and Zdravkovic, 1999)

Irrespective of some limitations such as ignorance of fabric anisotropy and rate dependence, Cam-Clay models can capture the real behaviour of soil in the wet side of the critical state. However, these models overestimate the failure stress of dense sand or overconsolidated clay which are in the dry side of the critical state. Although Hvorslev surface is proposed to overcome this drawback, the discontinuity between two yield surfaces introduces significant numerical difficulties (Potts and Zdravkovic, 1999; Yu, 2006). Therefore, original critical state models are less successful in modelling granular materials. They fail to predict experimentally observed peak and softening of drained dense sand or undrained loose sand.

2.2.6 Critical state in sand

Applicability of critical state theory for the granular materials is not straightforward as for clay. There is also controversy in the existence of an unique critical state line (CSL) and a normal compression line for sand. The experimental data on sand is not conclusive as for clay (Yu, 2006). Nevertheless, Been et al. (1991) confirmed the uniqueness of the critical state line of sand irrespective of the stress path and the initial fabric.

The curvature of the CSL of sand is also subjected to controversy. Generally, the CSL has been approximated as linear in a semi-logarithmic plot. This can be a reasonable approximation for the stress range between 10 kPa to 500 kPa of quartz sand, but for a wider stress range, a second order curvature is apparent. Based on the test results of Erksak sand and Leighton Buzzard sand, the critical state line is observed to be bilinear with a breakpoint at 1 MPa which is depicted in Figure 2.2 (Been et al., 1991; Pestana and Whittle, 1995). This is attributed to the breakage of grains at high stress levels, which depends on the sand mineralogy (Been et al., 1991). Within low stress levels, the shearing mechanism is due to

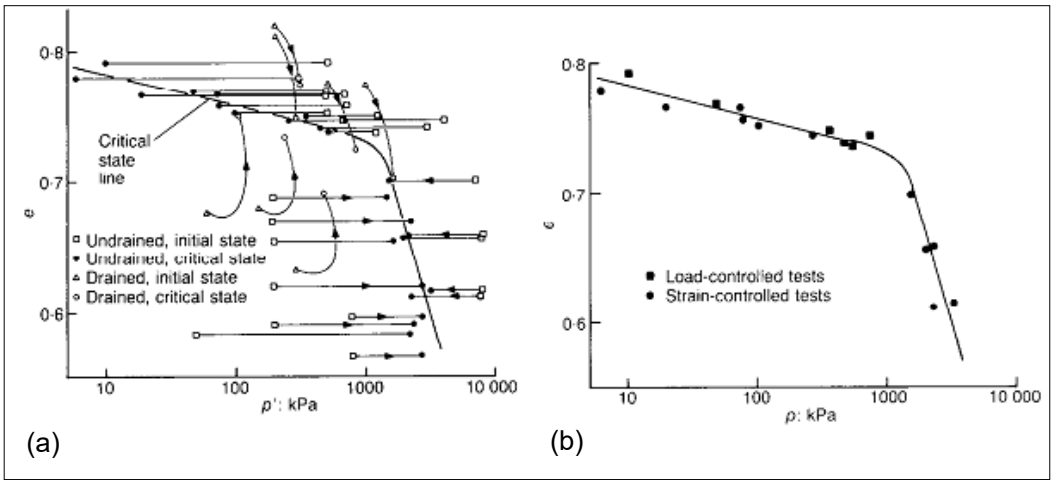

Fig. 2.2 Uniqueness of CSL: The effect of (a) the initial state and (b) the controlling variable on the CSL (Been et al., 1991)

particle rearrangement by sliding and rotation. Under higher pressures soil particles may crush before they override, hence reducing the dilation and increasing the slope of CSL Bolton (1986).

Using the works of Bolton (1986),Cheong (2006) utilised a simple relationship for the critical void ratio in which e_{max} and e_{min} are maximum and minimum void ratios respectively. Q is related to the particle crushing pressure. It is assumed as 20 MPa throughout the thesis such that $lnQ = 10$ (assuming quartz and feldspar). This equation is only defined in the region when $p' < Q$. The influence of Q on simulation results will be discussed in section 2.5.

$$e_c = e_{max} - \frac{e_{max} - e_{min}}{\ln Q - \ln p'} \tag{2.34}$$

2.2.7 State parameter concept

Granular materials display a powerful relationship between distortional and volumetric strains which are significantly affected by states of the material such as density, stress condition as well as the fabric of packing. Especially the initial state of the soil governs its overall behaviour. The relative dilatancy index (I_R) by Bolton (1986) and the state parameter (Ψ) by Been and Jefferies (1985) integrate the influence of density and normal stress into a single parameter. They measure the influence of the void ratio and the stress level simultaneously

with reference to an ultimate state. It should be emphasised that the state parameter is a description of physical condition as opposed to material property.

$$I_R = \frac{(e_{max} - e)}{(e_{max} - e_{min})}(\ln Q - \ln p') - 1 \quad \text{(Bolton, 1986)} \tag{2.35a}$$

$$\Psi = e - e_c \quad \text{(Been and Jefferies, 1985)} \tag{2.35b}$$

In the conventional MC type models, sand with different densities are considered as different materials, and the effects of normal stress and density are considered independently. The state concept enables to measure the combined influence of the void ratio and the normal stress on the sand behaviour. Therefore, soil models with state parameters are privileged of using a single set of material parameters for a wide range of initial void ratios and confining pressures.

2.3 Nor-Sand Model

Nor-Sand (NS) is a critical state model based on the state parameter concept. The critical state (CS) is defined by two axioms given by Equation 2.36 (Jefferies, 1993). The first states that the void ratio is not changing and the second states that this unchanging nature should be continuous, not instantaneous. It can be redefined in terms of dilation and the rate of dilation as in Equation 2.37 (Fern, 2016). Cam-clay type models couple these two criteria. Hence, they can not differentiate the phase transformation point from the critical state which are two distinct conditions for the supercritical soil (Fern, 2016).

$$\forall\, \varepsilon_q, \quad \exists \quad \text{CS}|_{dp'=0} \quad \ni \quad d\varepsilon_v = 0 \quad \wedge \quad \frac{d\varepsilon_v}{dt} = 0 \tag{2.36}$$

$$\forall\, \varepsilon_q, \quad \exists \quad \text{CS}|_{dp'=0} \quad \ni \quad D = 0 \quad \wedge \quad \frac{\partial D}{\partial \varepsilon_q} = 0 \tag{2.37}$$

The NS model decouples these two conditions by introducing an image of the critical state. It represents a situation when one of the two conditions of the critical state is met ($D = 0, \frac{\partial D}{\partial \varepsilon_q} \neq 0$). At the image condition, the void ratio of soil is unchanging, but the rate of dilation continues until the image state coincides with the critical state ($D = 0, \frac{\partial D}{\partial \varepsilon_q} = 0$). The image pressure p_i dominates the size of the yield surface as displayed in Figure 2.3 (a). The position of the current stress state with respect to p_i dictates whether the current volumetric trend is contracting (A to B: $p' > p_i$) or dilating (B-C-B':$p' < p_i$). Hence p' approaches p_i at the phase transition point (lowest point in Figure 2.3 (b)).

2.3.1 Yield function

NS is originated from Nova's stress dilatancy flow rule.

$$D = \frac{M - \eta'}{1 - N} \tag{2.38}$$

where N is a volumetric coupling term which decides the shape of the yield surface hence the direction of the stress increment. This equation resembles the Cam-Clay flow rule when $N = 0$. Based on laboratory experiments, N is a material constant for sand independent of density(Nova, 1982; Stroud, 1971). Jefferies (1993) ascertained that the dilatation computed from the above equation and those measured from experimental data are in close agreement. The NS yield function is derived by coupling the above relationship with the normality. It is written as

$$F = \eta' - \frac{M}{N}\left[1 + (N-1)\left(\frac{p'}{p_i}\right)^{\frac{N}{1-N}}\right] \qquad \text{if} \quad N \neq 0 \tag{2.39a}$$

$$F = \eta' - M\left[1 + \ln\left(\frac{p'}{p_i}\right)\right] \qquad \text{if} \quad N = 0 \tag{2.39b}$$

NS yield surface also has a bullet like shape similar to the original Cam-Clay. Jefferies (1993) reported that $0 \leq N \leq 0.4$ for real sand. As shown in Figure 2.3 (a) the plastic flow is normal to the yield surface in the original NS model.

2.3.2 Plastic potential function

The original NS model follows the associative flow rule such that in Equation 2.15, $P = F$. Several attempts have been made to incorporate non-associative flow rule to the NS model (Andrade and Borja, 2007; Fern, 2016). They introduced a plastic potential function by just changing the shape of the yield surface. Thus, new volumetric coupling term N_P is introduced for the potential function. Andrade and Borja (2007) reported that N_P should be smaller than N. As the current stress state should satisfy both functions, the image pressure of potential function ($p_{i,P}$) is different from p_i. NS plastic potential function is written as

$$P = \eta' - \frac{M}{N_P}\left[1 + (N_P - 1)\left(\frac{p'}{p_{i,P}}\right)^{\frac{N_P}{1-N_P}}\right] \qquad \text{if} \quad N > N_P \neq 0 \tag{2.40a}$$

$$P = \eta' - M\left[1 + \ln\left(\frac{p'}{p_{i,P}}\right)\right] \qquad \text{if} \quad N > N_P = 0 \tag{2.40b}$$

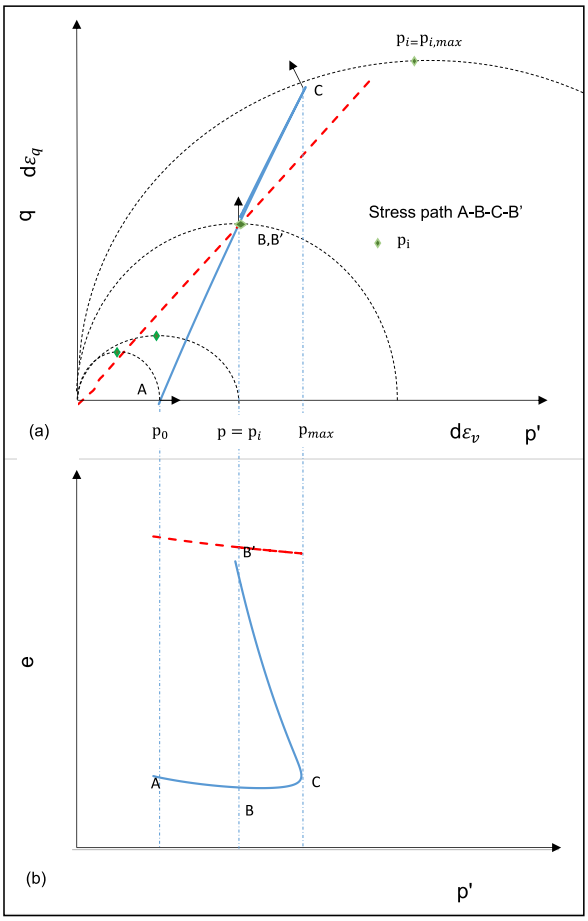

Fig. 2.3 Deformation of initially dense sand: (a) stress path and (b) volumetric path

2.3.3 Hardening law

Jefferies (1993) introduced the limiting hardness concept by adopting a maximum yield surface. The proximity to the maximum yield surface from the current yield surface is governed by the state parameter and dilatancy characteristics of the real soil. According to experimental data, a linear relationship can be obtained between the maximum dilatancy D_{max} and the state parameter at the image state Ψ_i (Jefferies, 1993).

$$D_{max} = \chi_{tc} \Psi_i \tag{2.41}$$

where χ_{tc} is the maximum dilatancy coefficient which depends on the sand fabric.

$$\Psi_i = e - (e_c)_i \tag{2.42}$$

where $(e_c)_i$ is the critical void ratio at the image mean pressure and can be calculated from Equation 2.34 by replacing p' with p_i. The rate of hardening or softening is dictated by the distance between the current image pressure p_i and peak image pressure $p_{i,max}$ which is displayed in Figure 2.4. A simple hardening rule is proposed by Jefferies (1993).

$$\frac{dp_i}{d\varepsilon_q^p} = \widehat{h}(p_{i,max} - p_i) \tag{2.43}$$

where $\widehat{h}$ is the hardening/softening coefficient. The hardening/softening rate (rate of dilation) is zero at the peak ($\frac{\partial D}{\partial \varepsilon_q} = 0, D \neq 0$). Fern (2016) interprets this hardening concept as similar to bounding surface or subloading surface models. But in NS, yield surface and maximum yield surface superimpose continuously only at the critical state ($\frac{\partial D}{\partial \varepsilon_q} = 0, D = 0$) unlike conventional bounding surface models.

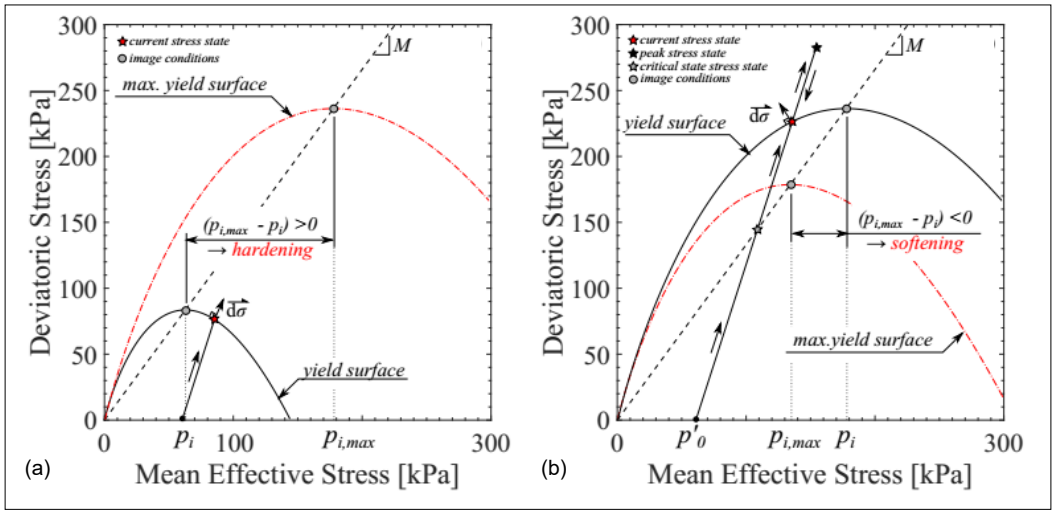

Fig. 2.4 (a) Hardening and (b) softening in Nor-Sand model (Fern, 2016)

In the original NS model, the extent of hardening is constrained by adhering to the normality condition. Using the maximum dilatancy in Equation 2.41, the maximum image pressure $p_{i,max}$ can be calculated from

$$\frac{p_{i,max}}{p'} = \left(1 + D_{max}\frac{N}{M_{tc}}\right)^{\frac{N-1}{N}} \qquad \text{if} \quad N \neq 0 \tag{2.44a}$$

$$\frac{p_{i,max}}{p'} = \exp\left(\frac{D_{max}}{M_{tc}}\right) \qquad \text{if} \quad N = 0 \tag{2.44b}$$

2.3.4 Extension to general stress space

Effect of lode angle

Considering M as a material constant leads to a poor representation of sand behaviour. Triaxial compression, extension and plane-strain experiments conducted on Brasted sand exhibited that the critical friction ratio M is a function of the lode angle (Jefferies and Been, 2006). There are several approaches to evaluate M as a function of lode angle. MC representation assumes a hexagon shape in the deviatoric plane. Matsuoka and Nakai (1974)

introduced a new stress plane called “spatially mobilised plane", and it has the concept of statistically averaging the MC criterion. While the MC criterion is not preferred due to its sharp corners, Matsuoka-Nakai model is continuous and better suited for finite element programmes. Two functions are shown in Figure 2.5. Matsuoka and Nakai (1974) criterion denotes M as an implicit function, and it is used in this thesis.

$$27-3M^2 = A\left[3-M^2+\frac{8}{9}M^3\sin\Theta\left(\frac{3}{4}-\sin^2\Theta\right)\right] \tag{2.45a}$$

$$A = \frac{27-3M_{tc}^2}{3-M_{tc}^2+\frac{2}{9}M_{tc}^3} \tag{2.45b}$$

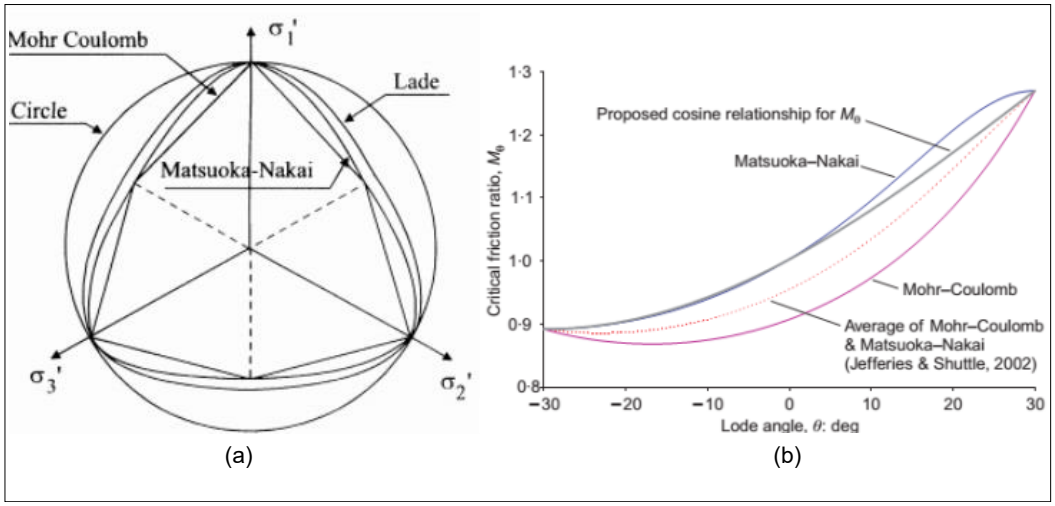

Fig. 2.5 (a) Failure surfaces in deviatoric plane (Potts and Zdravkovic, 1999) and (b) variation of critical friction ratio with lode angle (Jefferies and Shuttle, 2002)

In all aforementioned equations in section 2.3, M should be calculated based on the current lode angle. However, empirical correlations and material parameters in the hardening rule are derived based on triaxial compression data. Therefore, they should be modified for the general stress space. Jefferies and Shuttle (2002) extended the hardening rule to the general stress space as

$$\frac{dp_i}{d\varepsilon_q} = \widehat{h}\frac{M}{M_{tc}}(p_{i,max}-p_i) \tag{2.46}$$

Since the correlation for D_{max} is also derived from triaxial compression data, it is modified for the general stress state.

$$D_{max} = \frac{M}{M_{tc}}\chi_{tc}\Psi_i \tag{2.47}$$

2.3.5 Mobilised friction ratio at image state

Apart from the lode angle, M is experimentally proved to be dependent on the state parameter. Slightly departing from the original definition, M can be redefined as the stress ratio at

$D = 0$. For dilative sand, both image and critical states satisfy $D = 0$ condition. This results in a new definition of image stress ratio M_i which reaches M as the critical state is approached, as expressed by Equations 2.48. Manzari and Dafalias (1997) and Li (2002) clearly distinguished these two states in their bounding surface models. More accurate representation of dense sand can be obtained if M_i is used in the NS equations instead of M. However, this comes with the burden of an additional material parameter $\bar{m}$. Therefore, in this thesis, a distinction is not made between the stress ratios at critical and image states. Jefferies and Been (2006) advocate that the variable N from Nova's flow rule scales the variation of M. Hence, its influence is marginal.

$$M_i = M + \bar{m}\Psi \qquad \text{(Manzari and Dafalias, 1997)} \tag{2.48a}$$

$$M_i = M + \exp(\bar{m}\Psi) \qquad \text{(Li, 2002)} \tag{2.48b}$$

2.3.6 Partial derivatives of yield function

The partial derivatives of NS yield function with respective to stress invariants are given below.

$$\frac{\partial F}{\partial p'} = -\frac{M}{N}\left[1 + \frac{N-1}{1-N}\left(\frac{p'}{p_i}\right)^{\frac{N}{1-N}}\right] \quad N \neq 0 \tag{2.49}$$

$$\frac{\partial F}{\partial q} = 1 \tag{2.50}$$

$$\frac{\partial F}{\partial M} = -\frac{p'}{N}\left[1 + (N-1)\left(\frac{p'}{p_i}\right)^{\frac{N}{1-N}}\right] \quad N \neq 0 \tag{2.51}$$

The partial derivatives of the yield function with respective to the plastic strain is

$$\frac{\partial F}{\partial \varepsilon_{ij}^p} = \frac{\partial F}{\partial p_i}\frac{\partial p_i}{\partial \varepsilon_{ij}^p} \tag{2.52}$$

$$\frac{\partial F}{\partial p_i} = \frac{N-1}{1-N} M \left(\frac{p'}{p_i}\right)^{\frac{1}{1-N}} \tag{2.53}$$

$$\frac{\partial p_i}{\partial \varepsilon_{ij}^p} = \frac{\partial p_i}{\partial \varepsilon_q^p}\frac{\partial \varepsilon_q^p}{\partial \varepsilon_{ij}^p} \tag{2.54}$$

Above derivatives can be substituted in Equation 2.24 to find $\dfrac{\partial F}{\partial \sigma_{ij}}$. Analogous partial derivatives of plastic potential $\dfrac{\partial P}{\partial \sigma_{ij}}$ can be calculated if the non-associative flow rule is used.

2.3.7 Loading criterion

The loading criterion adopted in this thesis is different from the conventional implementation of plasticity which assumes that the stress state inside the yield surface is elastic. From the beginning of the deformation, the image pressure is always calculated assuming that the current stress state is on the yield surface. In other words, the model is assumed to be elasto-plastic from the beginning. The foundation for this criterion lies in the sub-loading surface concept proposed by Hashiguchi (2009). It facilitates both smoothness and continuity of the stress-strain relationship as observed experimentally. Figure 2.6 demonstrates that if the interior of the yield surface is assumed to be purely elastic, the prediction by the model is stiffer and discontinuous. The loading criterion states

$$d\varepsilon_{ij}^{p} \neq 0 \quad if \quad \left(\frac{\partial F}{\partial \sigma'_{ij}}\right) D_{ijkl}^{e} d\varepsilon_{kl} > 0 \tag{2.55a}$$

$$d\varepsilon_{ij}^{p} = 0 \quad if \quad \left(\frac{\partial F}{\partial \sigma'_{ij}}\right) D_{ijkl}^{e} d\varepsilon_{kl} \leq 0 \tag{2.55b}$$

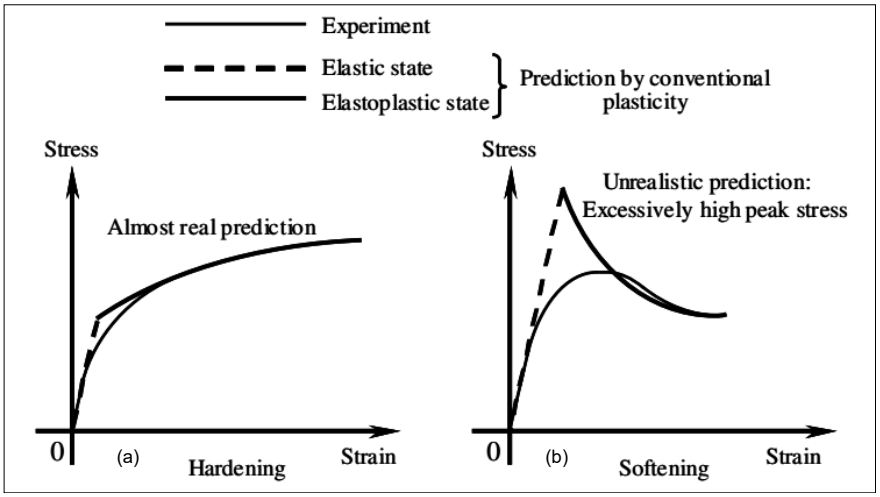

Fig. 2.6 Predictions by conventional plasticity: (a) hardening and (b) softening (Hashiguchi, 2009)

2.4 Numerical Simulations of Plane Strain Single Element Tests

Single element analysis is generally conducted to evaluate the (homogeneous) constitutive response of a material for a given load path. A series of displacement controlled drained and undrained plane-strain tests are conducted with ABAQUS finite element software. NS constitutive model is implemented in a user-defined material model. Two loading paths: biaxial compression and simple shear are explored.

A plane-strain four-node element with reduced integration (CPE4R) which has unit height and width is deployed. For the undrained analysis, the same element with additional pore pressure (CPE4RP) degree of freedom is utilised. All edges are assumed to be impermeable for the undrained simulation. A general static analysis is conducted for the drained case whereas a transient consolidation analysis is done for the undrained case with fluid permeability of 0.001 m/s. Both analysis are conducted by ABAQUS/Standard in which inertia effects are ignored. A confining pressure of 100 kPa is applied to the side and top surfaces. Assumed NS material parameters are given in Table 2.1. For all the analysis, the initial void ratio is specified as 0.55. Hence the initial stress state is in the dry side of the critical state which denotes a negative initial state parameter.

Table 2.1 Material parameters of Nor-Sand model

M_{tc}	e_{max}	e_{min}	N	$\widehat{h}$	R	r	ν	χ_{tc}
1.25	0.76	0.51	0.3	400	1500	0.5	0.3	3.3

2.4.1 Biaxial compression

For the biaxial element, the bottom left node is constrained in two directions whereas the bottom right node is assumed to be roller supported. Top nodes are unconstrained to allow free movement in both directions. During the initial step, all boundary constraints and initial void ratio are specified. A vertical downward displacement of 0.5 m (strain rate 50 % /s) is applied to the top nodes during the last step.

2.4.2 Simple shear

A series of displacement controlled simple shear simulations are conducted to evaluate the potential of different flow rules during principal stress rotations. Simulations are similar to biaxial tests apart from slight changes in boundary conditions. In the simple shear element, all bottom nodes are constrained in two directions. Horizontal displacement of 0.5 m is applied to two top nodes. Further, an equation constraint is applied to two top nodes, such that their displacements are the same in both directions. This makes zero horizontal strain throughout the element. Hence, the volumetric strain is equal to the vertical strain in the drained analysis. In the undrained simulation, the vertical strain is also restricted due to impermeable boundaries.

2.5 Results of Original (Associative) Nor-Sand Model

The aim of this section is to evaluate the potency of the NS model to capture the salient features of drained and undrained dense sand qualitatively. Therefore a quantitative validation with experimental data is not included.

2.5.1 Drained biaxial compression analysis

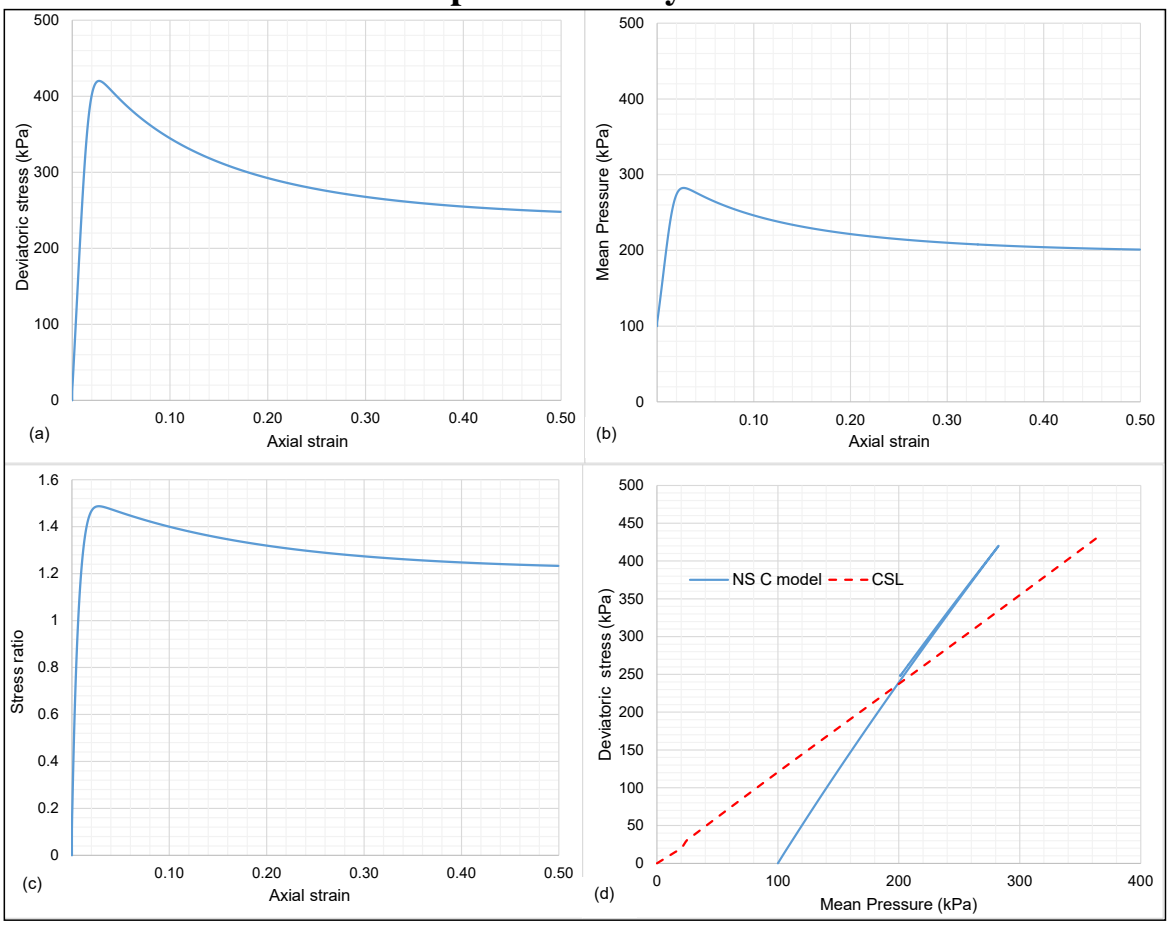

Fig. 2.7 Mechanical response of drained biaxial compression test: (a) deviatoric stress, (b) mean pressure, (c) stress ratio against axial strain and (d) stress path

Figure 2.7 demonstrates the mechanical response of the single element biaxial compression simulations of drained (dry) dense sand. Due to elasto-plastic behaviour from the beginning, the stress-strain response is smooth and continuous throughout. In Figure 2.7 (a) and (b), both deviatoric stress and effective mean pressure reach their peak strengths simultaneously. The peak stress ratio in Figure 2.7 (c) also coincides with this. By 50 % of axial strain, the stress ratio shows signs of reaching the mobilised critical stress ratio. This ratio depends on the lode angle at the critical state. It is different from the reference input value at the triaxial compression mentioned in Table 2.1. The use of mobilised critical stress ratio in Equations 2.46 and 2.47 scales those input values to the general stress space.

Unlike triaxial tests, the stress path in Figure 2.7 (d) is not linear due to the effect of intermediate principal stress in plane-strain tests. Even the critical state line is slightly non-linear due to the changing critical stress ratio. It is observed that the lode angle and the critical stress ratio in plane-strain biaxial tests vary until about 10% of axial strain and then

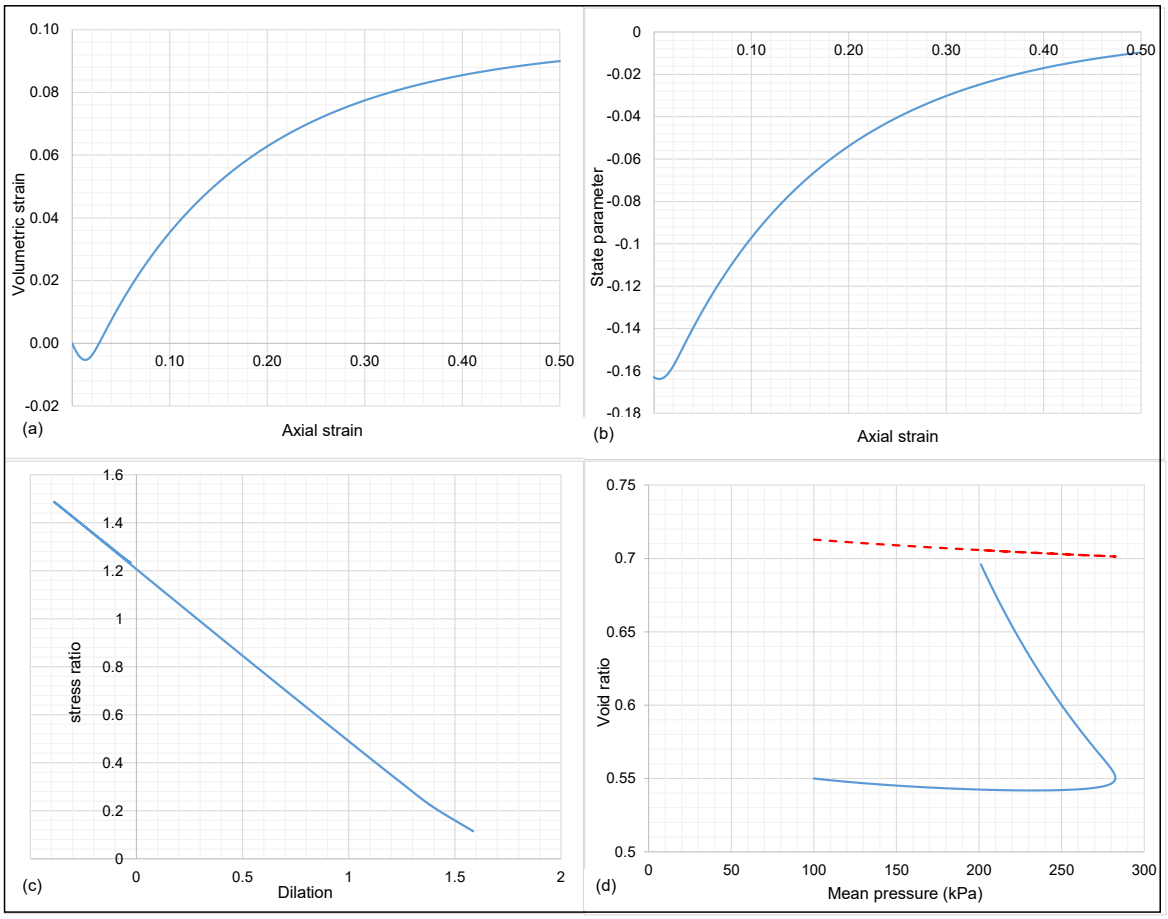

Fig. 2.8 Volumetric relationships of drained biaxial compression test: (a) volumetric strain, (b) state parameter against axial strain, (c) stress dilatancy relationship and (d) void ratio against mean pressure

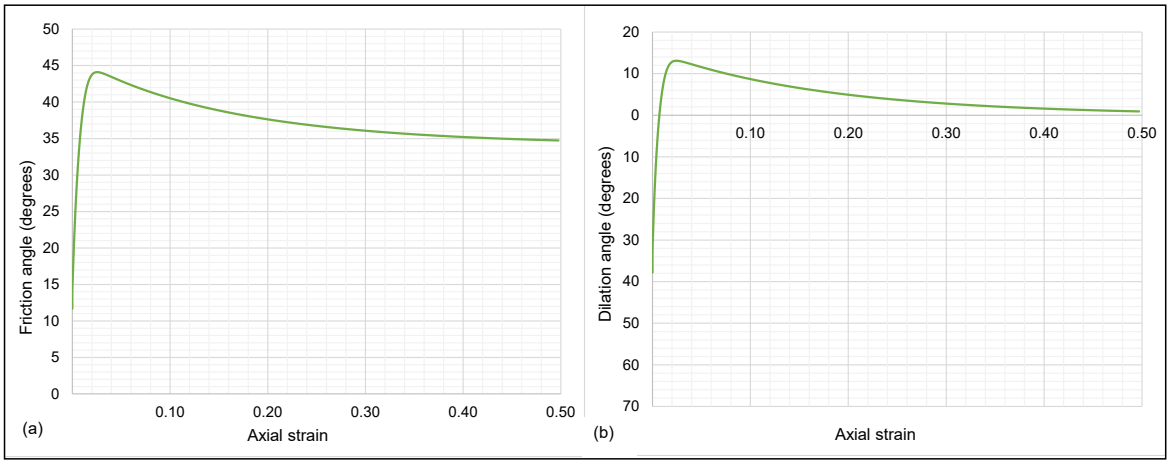

Fig. 2.9 Mobilised (a) friction angle and (b) dilation angle of drained biaxial compression test

become constants. They are always lower than respective triaxial values. The stress path in Figure 2.7 (d) reverses at the peak and terminates at the critical state.

Figure 2.8 (a) illustrates the volumetric relationship during biaxial tests. It shows an initial contraction followed by dilation which ceases at the critical state. The hardening in Figure 2.7 (a) takes place both during both contraction and dilation until the peak at which the dilation is maximum. Afterwards, the softening accompanies with the reducing dilation until the volume becomes constant at the critical state. The state parameter in Figure 2.8 (b) reduces during compaction and increases during dilation. It approaches zero near the critical state. This is affirmed by Figure 2.8 (d) in which the distance between the blue and red dash line represents the state parameter. In Figures 2.8 (a),(b) and (d), the lowest points correspond to image state.

Jefferies and Shuttle (2002),Jefferies and Been (2006) and Robert (2010) numerically simulated plane-strain biaxial compression tests of dense sand using NS model. Their stress and volumetric relationships are qualitatively similar to Figure 2.7 (a) and 2.8 (a) respectively. Jefferies and Shuttle (2002) successfully validated their results with experimental data of Cornforth (1961) until the peak, but post-peak results diverged considerably from experiments due to the shear localisation. Mallikarachchi (2015) reported the same trend while comparing NS biaxial simulations with laboratory experiments of Houston sand from Desrues and Viggiani (2004).

The slope of the stress dilatancy relationship in Figure 2.8 (c) is dictated by the volumetric coupling term N. In this Figure, both image and critical state stress ratios coincide when the dilation is zero. This is due to the assumption that the stress ratio at image state is the same as the critical stress ratio. Manzari and Dafalias (1997), Li (1997), Jefferies and Shuttle (2002) doubted about this and hypothesised that stress ratio at image state M_i is different from M. It explained the experimentally observed "hook" in the stress dilatancy plots of dense sand. However, experimental observations are doubtful during softening as laboratory specimens in plane-strain are no longer homogeneous after the peak.

Figure 2.9 illustrates the plane-strain friction and dilation angles. The mobilised peak and critical friction angles in drained tests are 44° and 35° respectively in Figure 2.9 (a). The mobilised peak dilation angle is around 13° in Figure 2.9 (b).

2.5.2 Undrained biaxial compression analysis

Figure 2.10 illustrates the undrained behaviour of the dilative dense sand. In this case, the constant volume constraint is applied to the plane-strain biaxial compression test due to impermeable boundaries. The inhibited dilation generates excess pore pressure. Both

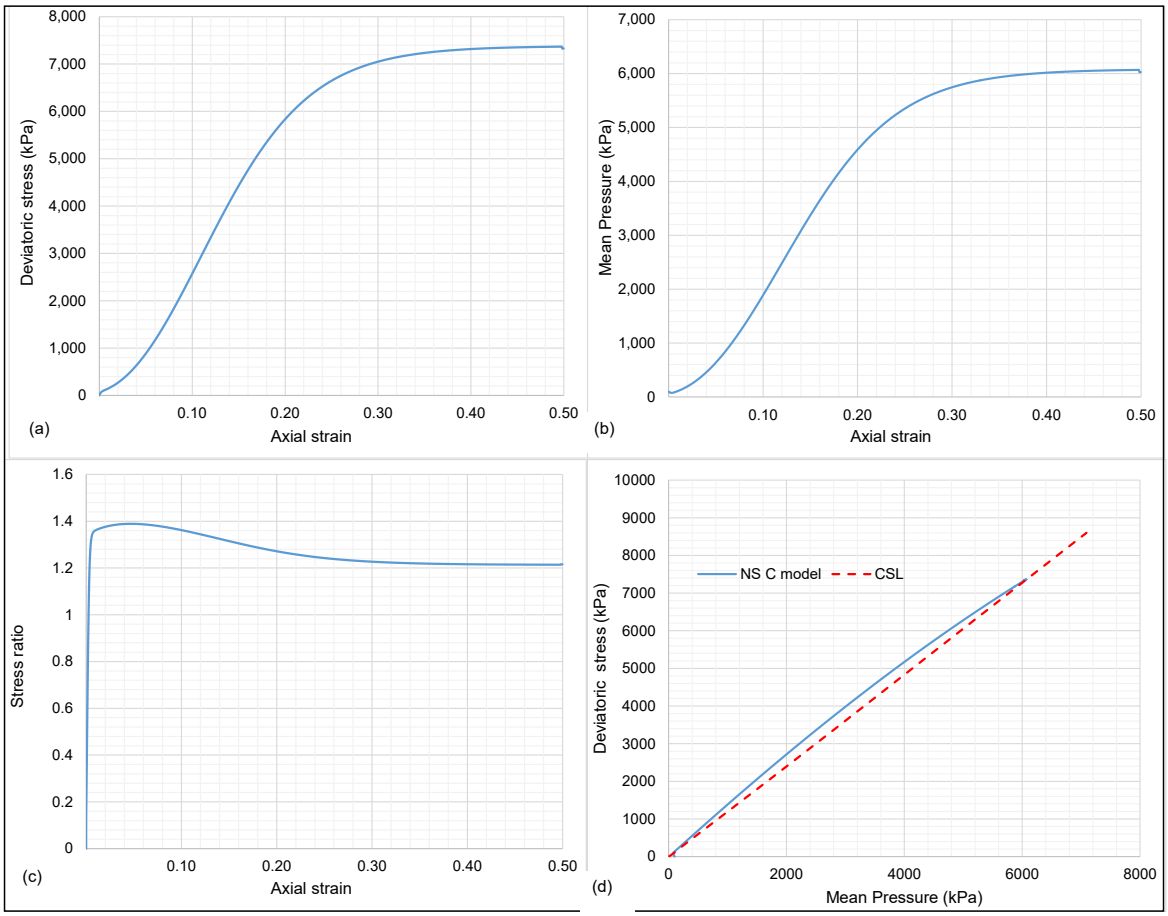

Fig. 2.10 Mechanical response of undrained biaxial compression test: (a) deviatoric stress, (b) effective mean pressure, (c) effective stress ratio against axial strain and (d) effective stress path

deviatoric stress and mean pressure in Figure 2.10 (a) and (b) continuously rise until plateaus are reached at the critical state. This increase in strength is due to the generation of negative excess pore pressure. Figure 2.11 (a) shows that the suction is generated continuously followed by initial positive pore pressure. It only ceases at the critical state. This phenomenon is known as dilative hardening (Li, 1997; Rice, 1975). Unlike MC/DP type models with constant dilation, NS model predicts a termination of dilative tendency with accumulated deviatoric strain. This is responsible for the observed plateaus in Figures 2.10 (a) and 2.11 (a).

Figure 2.11 (b) shows that the state parameter becomes zero eventually. Figure 2.11 (d) displays that the critical state is reached only by increasing the effective mean pressure, keeping the volume constant. In fact, two critical state axioms in Equation 2.36 are valid only when $dp' = 0$. Therefore, in undrained deformation, the change in hydrostatic pressure dictates the state parameter.

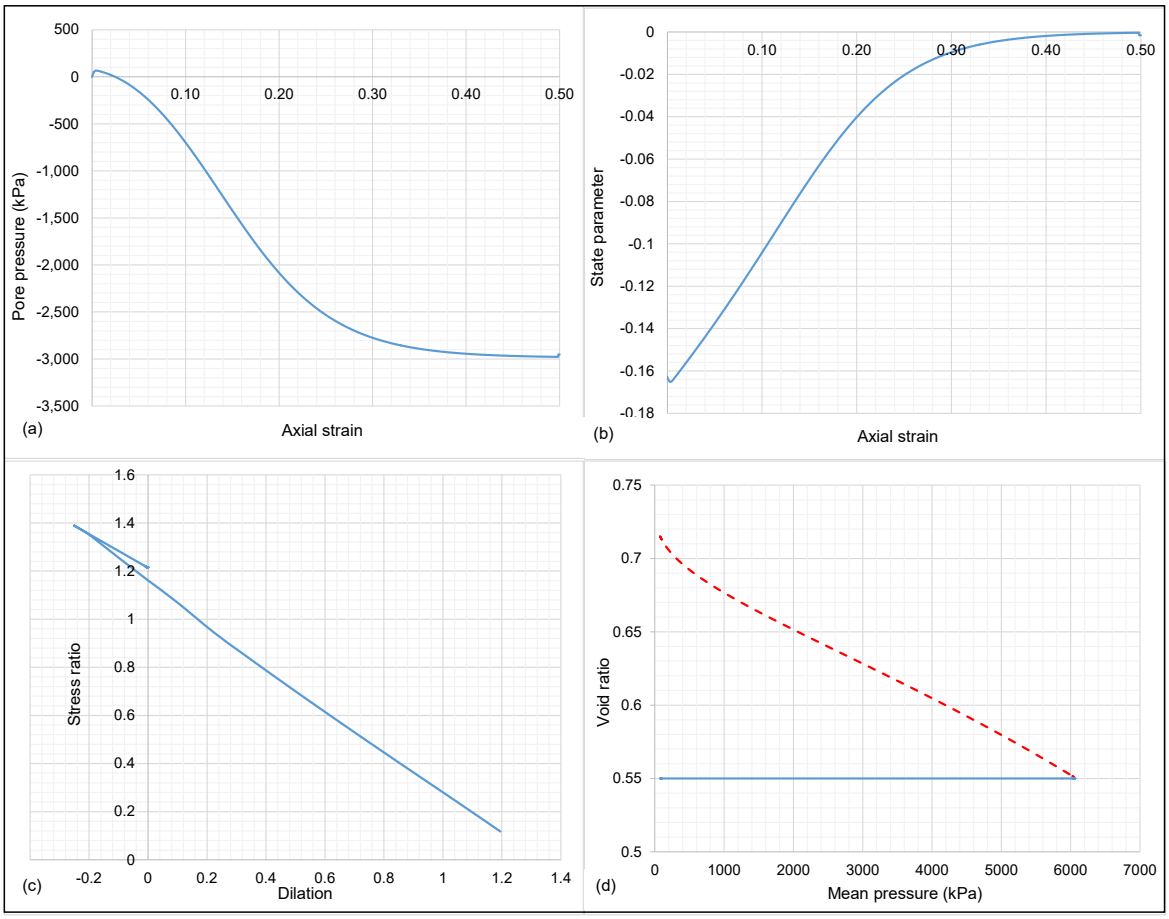

Fig. 2.11 Volumetric relationships of undrained biaxial compression test: (a) volumetric strain, (b) state parameter against axial strain, (c) stress dilatancy relationship and (d) void ratio against effective mean pressure

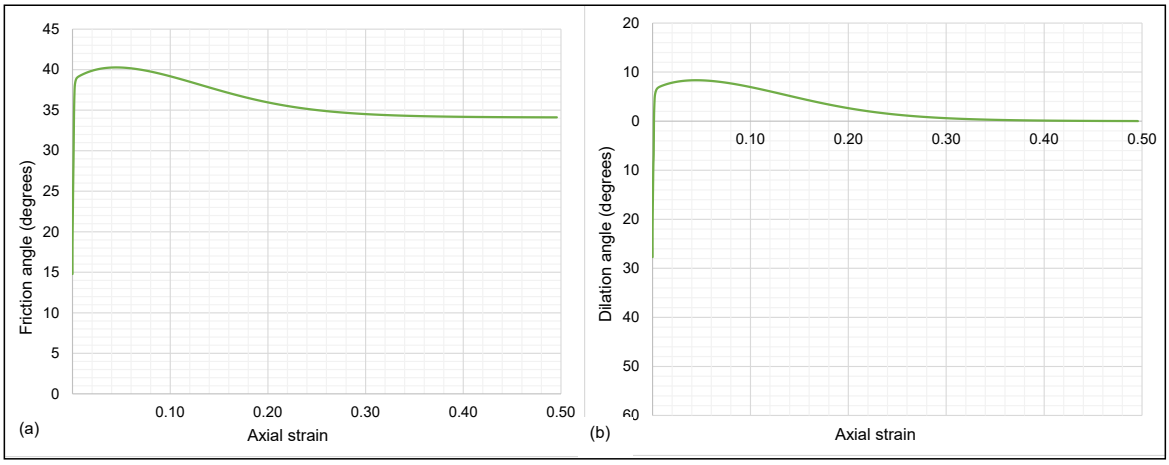

Fig. 2.12 Mobilised (a) effective friction angle and (d) dilation angle (calculated from plastic strains) of undrained biaxial compression test

Although the deviatoric stress in Figure 2.10 (a) does not have a peak, a maximum stress ratio is observed in Figure 2.10 (c). This means the Coulomb limiting state is reached without passing the Tresca state. In the framework of bounding surface critical state plasticity, Manzari and Dafalias (1997), Li (1997, 2002) and Yi (1997) modelled the dilative hardening behaviour of undrained dense sand during triaxial compression and validated with experimental data. Their stress-strain relationships are qualitatively similar to the curve in Figure 2.10 (a). They also emphasised that strength of the undrained dense sand can increase even after the maximum stress ratio. Plane-strain experimental data for dilative hardening behaviour is hard to find since tests are interrupted by instabilities (Han and Vardoulakis, 1991; Mokni and Desrues, 1999).

The stress path in Figure 2.10 (d) shows a slight decrease in mean pressure initially followed by a continuous strength increase. Although the stress path reaches the critical state line almost asymptotically just after the phase transformation stage, it never intersects the critical state line until the actual critical state. Fern (2016) simulated undrained triaxial compression of dense sand with NS model. He claimed that the soil reaches to a "near critical state" shortly after the phase transformation, without ever reaching it. This is probably because maximum strain he used is not sufficient to reach the critical state for the undrained dense sand. However, according to Manzari and Dafalias (1997), Li (1997, 2002) and Yi (1997), triaxial compression stress paths reach the CSL by 15 to 20 % strain.

The stress dilatancy relationship in Figure 2.11 (c) shows a slightly different slope before and after the peak stress ratio. This clearly demonstrates the difference between image and critical stress ratios. The maximum dilation is associated with the peak stress ratio rather than the peak deviatoric stress. It is very significant to recognise this difference by a constitutive model which simulates dilative hardening materials. Kutter (2006) clearly pointed out the misleading nomenclature used in soil mechanics in which "strain softening" is used for negative tangent modulus. He suggested using the word "strain softening" for the case where the tangent modulus decreases as the stress increases and "strain weakening" for the negative tangent modulus.

It is observed in Figure 2.12 that the undrained peak and critical friction angles are 40° and 34° respectively whereas peak dilation angle is 8°. It is noted that the peak mobilised friction and dilation are smaller in the undrained analysis compared to the drained case, even with the same material parameters. This is because they are behavioural properties which depend on test type compared to intrinsic material properties.

Based on the above simulations of dilative sand the potential of NS model can be appraised. It has the ability to distinguish the phase transition ($p' = p_i < p_{i,max}$) from the critical state

($p' = p_i = p_{i,max}$). Even with an associative flow rule, the mobilised dilation is always lower than the mobilised friction. Hence it is an ideal candidate for modelling supercritical soil. One defect is that NS is not capable to macroscopically model the inherent fabric of sand and the fabric evolution during shearing. Nevertheless, even Manzari and Dafalias (1997) mention that the NS model is sufficient for monotonic loading.

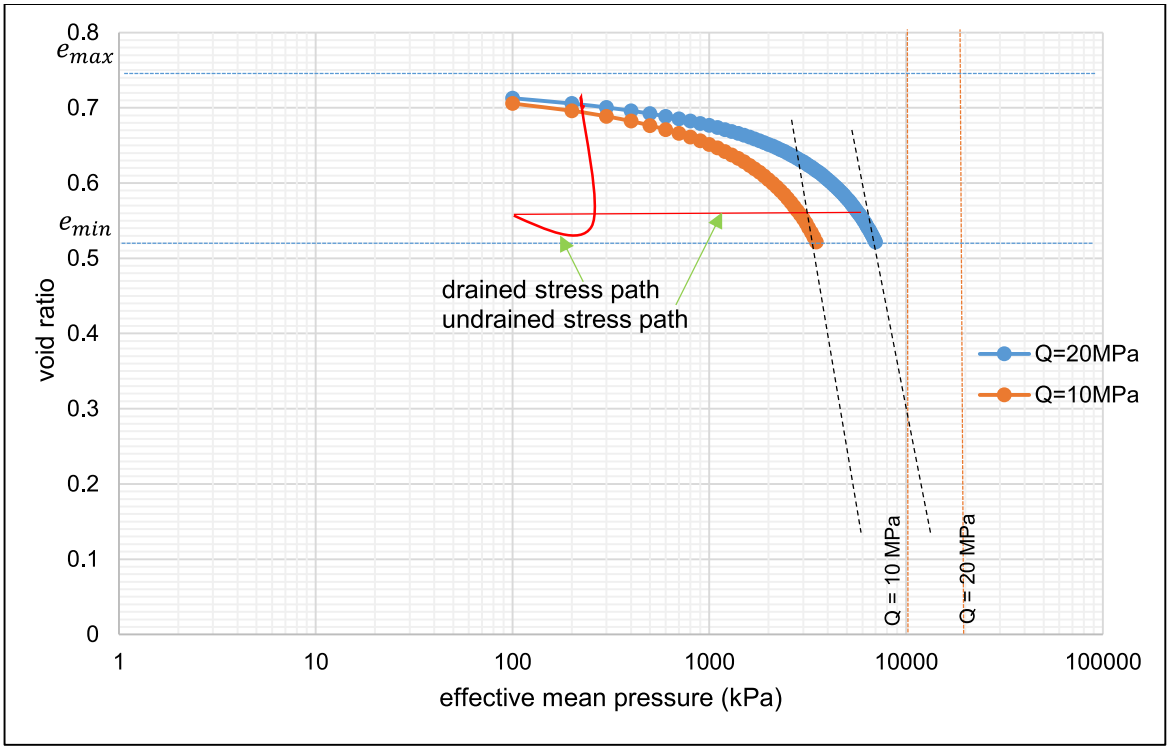

Fig. 2.13 Influence of critical state line

At this point, it is important to discuss the influence of CSL (Equation 2.34) on the aforementioned results. Figure 2.13 plots CSL for two Q values along with drained and undrained stress paths. This equation is not valid in the region where the grain crushing is the predominant mode of shearing (below the minimum void ratio). As the grain crushing pressure is approached, the CSL are proved to be linear as shown in dotted lines (Been et al., 1991; Pestana and Whittle, 1995). Nevertheless, all simulations in this thesis are conducted in the region above the minimum void ratio; hence they will not be affected by the change in CSL. Therefore, Equation 2.34 is used throughout the thesis.

When $Q = 20$ MPa (blue line), the maximum effective mean pressure does not rise more than 6 MPa even for fully undrained deformation. Hence, p' is always lower than Q throughout this thesis. If soil with weaker grains is assumed, Q should be smaller; hence, the dilation might be suppressed at a lower effective mean pressure. Hence the choice of Q profoundly influences the results of undrained deformation.

2.6 Effect of Flow Rules in Modified Nor-Sand Models

For pressure dependent materials, the direction and magnitude of plastic flow can vary with material properties, initial state and loading path. Therefore, the flow rule should be selected based on the intended problem. For dilative sand, it should be able to predict plastic flow during both softening and hardening. Further, it should capture post-localised deformation which involves non-proportional loading paths. Hence, it is worthwhile to investigate the influence of different flow rules on the behaviour of dense sand.

In this section, the original NS model is extended for non-associative and non-coaxial flow rules. The motivation behind this implementation is twofold. The first is to explore the influence of these flow rules on the mechanical and volumetric relationships of drained and undrained dense sand compared to the original NS model. The second objective is to evaluate the potential of different flow rules for the bifurcation analysis: prediction of onset of a shear band. This will be studied in Chapter 3.

2.6.1 Non-associative flow rule

It is widely accepted in geomechanics community that non-associative flow rule is necessary to correctly characterise volumetric changes in frictional geo-materials (Lade and Bopp, 1993). On the other hand, Hashiguchi (1991) questioned the validity of this notion and reported that non-associative flow rule renders physically unacceptable results for stress probe tests.

Original NS model by Jefferies (1993) strictly follows the Drucker et al. (1957)'s stability postulate and assumes normality. However, the extent of hardening is controlled by limiting hardening concept such that normality does not conflict with producing physically reasonable dilation rates. In the family of Cambridge type models, the yield surface is different from the failure surface. Therefore, unlike conventional MC, DP type models, their yield surfaces are sized such that dilation from normality matches with reality. Specifically, in the NS model, the maximum dilatation is governed by $p_{i,max}$ which is related to state parameter and experimentally matched dilation coefficient.

It is observed in Figure 2.14 (a) that on the dry side of the critical state, the plastic strain increments are almost normal to the yield surface (Fern, 2016). Figure 2.14 (b) shows that NS yield surface is very close to the plastic potential surface in the supercritical side whereas there is a huge discrepancy between two in the subcritical side. This notion is further verified by Liu (2013) who claims that the flow rule in the sand is density dependent. In his unified sand model, he integrated both associative and non-associative rules. He reports

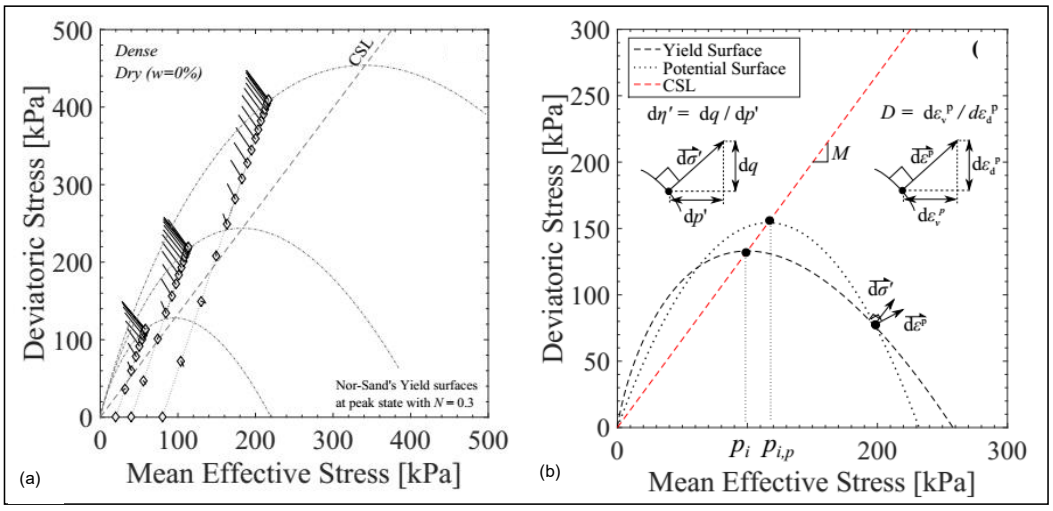

Fig. 2.14 (a) The directions of plastic strain increments during triaxial compression tests of dry Chiba sand and (b) difference in yield and plastic potential functions (Fern, 2016)

that the associative flow rule is satisfactory for dense sand. Considering all aforementioned arguments, associative flow rule in original NS can be justified at least for dense sand.

However, most of these arguments are valid only in the pre-bifurcation regime. Normality based on Drucker et al. (1957)'s stability postulate is valid in the work-hardening regime. Jefferies (1993) reports that post-peak softening of NS does not match well with experimental results (Jefferies, 1993). It is expected since phenomenological constitutive relations are no longer valid after the bifurcation because the material is no longer homogeneous.

In this context of ambiguity, it is interesting to scrutinise the effect of non-associativity for drained and undrained dense sand. The original NS model is modified integrating the non-associative flow rule. A separate plastic potential function with $N_p = 0.1$ is utilised as described in section 2.3.2. Results of drained and undrained single element simulations with non-associative NS model will be presented in section 2.7.

2.6.2 Non-coaxial flow rule

Conventional constitutive models assume that the orientation of principal stresses coincides with that of principal plastic strain rate, which is termed as coaxility. Although this assumption is valid for proportional loading paths such as triaxial, biaxial tests, practical loading conditions often deviate from this idealistic behaviour. Progressive failure of soil often accompanies with diffused or localised modes of instabilities. Under large shear deformations, a considerable amount of principal axis rotation takes place within these shear band. As a result, the orientation of principal stresses does not coincide with that of principal plastic strain rates as shown in Figure 2.15. In essence, conventional flow theories are proved to be not valid under principal stress rotations.

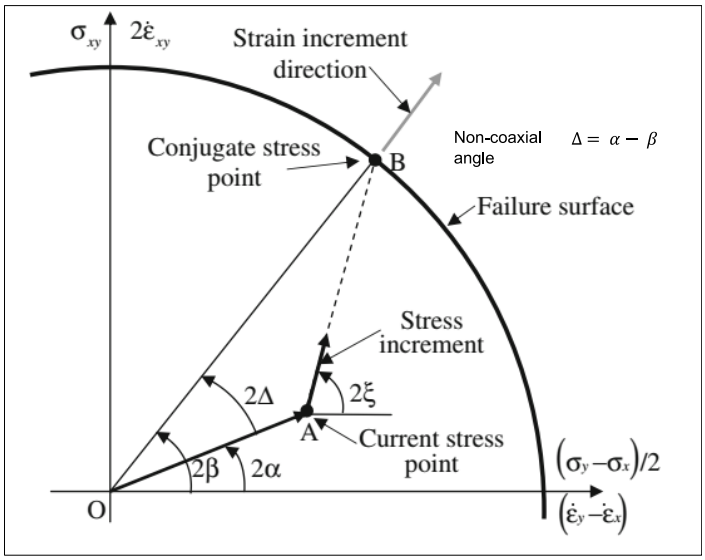

Fig. 2.15 Representation of stress path and plastic strain increment path in 2D stress rotation plane (Gutierrez and Ishihara, 2000)

This phenomenon is verified by various laboratory experiments such as stress probe tests (Gutierrez and Ishihara, 2000; Gutierrez et al., 1991, 1993), simple shear tests (Cole, 1968; Roscoe, 1970), hollow cylinder tests (Cai, 2010; Miura et al., 1986) etc. These laboratory experiments report following common observations.

- Both the magnitude and direction of plastic deformation are dependent on the direction of stress rates (Gutierrez and Ishihara, 2000; Gutierrez et al., 1991).

- The degree of non-coaxility is greater in the beginning, and principal stress and principal plastic strain rate directions coincide near the critical state (Cole, 1968; Roscoe, 1970).

- A plastic deformation can be induced solely by the rotation of principal stress axes even if magnitudes of principal stresses are constant (Arthur et al., 1980; Gutierrez and Ishihara, 2000; Gutierrez et al., 1991; Ishihara and Towhata, 1983).

Theoretical studies on the micro-mechanical point of view on grains also support the concept of non-coaxility (Oda and Konishi, 1974a,b). Discrete element simulations scrutinising fundamental inter-granular contacts also have reported evidence on the non-coaxial plastic flow (Ai et al., 2014; Jiang et al., 2016; Yu, 2008). Within the context of continuum plasticity, various theories have been put forward to describe the principal axis rotation and the non-coaxility of granular material.

Yield vertex theory

Yield vertex theory initially introduced by Rudnicki and Rice (1975) has been applied by many researchers to model the non-coaxial behaviour successfully. In essence, this theory recognises the plastic stretching caused by stress rates tangential to the yield surface in the deviatoric plane as shown in Figure 2.16 (a). Equation 2.19 can be modified replacing $d\varepsilon_{ij}^{p}$ with $d\varepsilon_{ij}^{pc}$ as coaxial plastic strain rate and $d\varepsilon_{ij}^{pnc}$ as non-coaxial plastic strain rate.

$$d\varepsilon_{ij} = d\varepsilon_{ij}^{e} + d\varepsilon_{ij}^{pc} + d\varepsilon_{ij}^{pnc} \tag{2.56}$$

Non-coaxial plastic flow rate is mathematically determined by Equation 2.57 in which $\bar{h}_{pnc}$ is the non-coaxial plastic modulus and a_{ij} represents the direction of flow.

$$d\varepsilon_{ij}^{pnc} = \frac{1}{\bar{h}_{pnc}} a_{ij} \tag{2.57}$$

Original yield vertex theory was proposed for simple constitutive models with circular yield surfaces (in the deviatoric plane) and isotropic hardening as expressed by Equation 2.58 and shown in Figure 2.16 (a). Over the years this theory has been implemented to simulate simple shear behaviour and boundary value problems by Yu (2006), Yang and Yu (2006b, 2010, 2006c).

$$a_{ij} = ds_{ij} - \frac{s_{ij}s_{kl}}{2J_2^2} ds_{kl} \tag{2.58}$$

where ds_{ij} is the direction of deviatoric stress vector. This can be rearranged as

$$d\varepsilon_{ij}^{pnc} = \frac{1}{\bar{h}_{pnc}} A_{ijkl} d\sigma_{ij} = \frac{2G^e}{\bar{h}_{pnc} + 2G^e} A_{ijkl} d\varepsilon_{ij} \tag{2.59}$$

$$A_{ijkl} = \frac{1}{2}\left(\delta_{ik}\delta_{jl} + \delta_{il}\delta_{jk} - \frac{2}{3}\delta_{ij}\delta_{kl} - \frac{s_{ij}s_{kl}}{J_2^2}\right) \tag{2.60}$$

Hashiguchi (1993, 1998) generalised this original theory for non-circular yield surfaces and all types of hardening. The difference lies in the non-coaxial flow direction vector a_{ij} (and A_{ijkl}) as shown in Figure 2.16 (b). $\bar{a}_{ij}^{*}$ in Equations 2.61 and 2.62 represents the unit vector along the direction normal to the yield surface in deviatoric plane, whereas in Equation 2.58 , the $\frac{s_{ij}}{\sqrt{2}J_2}$ indicates the unit vector in the direction along the deviatoric stress. Both criteria coincide for a circular yield surfaces. Non-circular yield surfaces depend on lode angle hence there is a clear distinction between these two directions as illustrated by Figure 2.16(b).

$$a_{ij} = ds_{ij} - \bar{a}_{ij}^{*}\bar{a}_{kl}^{*} ds_{kl} \tag{2.61}$$

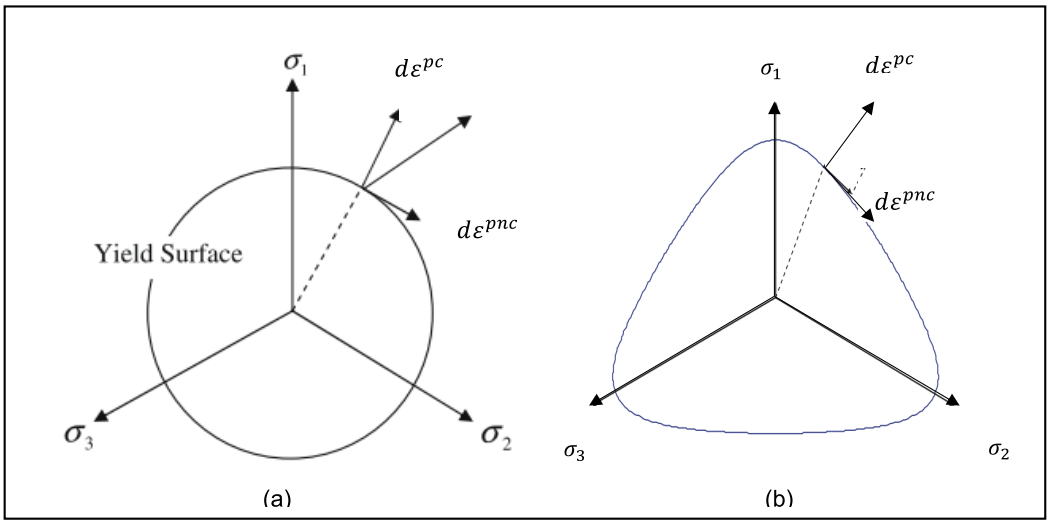

Fig. 2.16 Illustration of coaxial and non-coaxial plastic strain rates on (a) circular yield surface (Yang et al., 2011) and (b) non-circular yield surface (Hashiguchi and Tsutsumi, 2001) in deviatoric plane

$$\bar{a}^*_{ij} = \frac{\left(\frac{\partial F}{\partial \sigma_{ij}}\right)^*}{\| \left(\frac{\partial F}{\partial \sigma_{ij}}\right)^* \|} \tag{2.62}$$

$$\left(\frac{\partial F}{\partial \sigma_{ij}}\right)^* = \left(\frac{\partial F}{\partial \sigma_{ij}}\right) - \frac{1}{3}\left(\frac{\partial F}{\partial \sigma_{ij}}\right)_{ii} \tag{2.63}$$

$$A_{ijkl} = \frac{1}{2}\left(\delta_{ik}\delta_{jl} + \delta_{il}\delta_{jk} - \frac{2}{3}\delta_{ij}\delta_{kl} - \bar{a}^*_{ij}\bar{a}^*_{kl}\right) \tag{2.64}$$

The final constitutive relationship is given by

$$d\sigma_{ij} = D^{ep}_{ijkl} d\varepsilon_{kl} = \left[D^e_{ijkl} - \frac{D^e_{ijkl}\left(\frac{\partial P}{\partial \sigma_{ij}}\right)\left(\frac{\partial F}{\partial \sigma_{ij}}\right) D^e_{ijkl}}{K^p + \left(\frac{\partial F}{\partial \sigma_{ij}}\right) D^e_{ijkl}\left(\frac{\partial P}{\partial \sigma_{ij}}\right)} - \frac{4G^{e2}}{\bar{h}_{pnc} + 2G^e} A_{ijkl} \right] d\varepsilon_{ij} \tag{2.65}$$

Apart from the yield vertex theory, there are other methods which integrate non-coaxial plasticity into constitutive formulations. Gutierrez and Vardoulakis (2007) observed that the energy dissipation during shearing is different before and after the localisation even for proportional loading tests. This is because of the principal stress rotations inside the shear band. Accordingly they derived a novel stress-dilatancy relationship including the non-coaxial angle.

Fabric tensors are also utilised to describe non-coaxial behaviour of sand. Gao and Zhao (2013, 2016) declared that accounting for soil fabric and its evolution is enough to capture the non-coaxial behaviour of soil naturally. Yu (2008) stated that induced fabric anisotropy is a

consequence of loading with principal axis rotations. Jefferies et al. (2015) also incorporated the principal axis rotation into the NS model by changing the original hardening law.

Non-coaxial theories mentioned above have been utilised to simulate experimental observations of simple shear, biaxial compression, true triaxial and hollow cylinder tests. The influence of non-coaxial theory on simple shear simulations varies considerably depending on the characteristics of the constitutive model. The current study adopts the modified yield vertex theory to incorporate non-coaxial behaviour into the NS model.

2.7 Results of Modified Nor-Sand Models

The influence of two flow rules on the mechanical response of dense sand is explored during two loading paths: biaxial compression and simple shear. Abbreviated terms for different models are given below. Additional to the material parameters in Table 2.1, h_{pnc} is $0.5G^e$ for non-coaxial models and N_P is 0.1 for non-associative models.

- Nor-Sand associative coaxial model - NS C
- Nor-Sand associative non-coaxial model - NS NC
- Nor-Sand non-associative coaxial model - NS C NA
- Nor-Sand non-associative non-coaxial model - NS NC NA

2.7.1 Drained and undrained biaxial compression analysis

Figure 2.17 displays the response of drained biaxial compression tests of dense sand predicted by original and three modified NS models. It is observed that the deviatoric stress in Figure 2.17 (a) is not much affected by flow rules during the pre-peak deformation. The peak is slightly enhanced by the non-coaxial flow rule but unaffected by the non-associative flow rule. After the peak, coaxial and non-coaxial stress-strain relationships are superimposed. On the contrary, non-associative flow rule predicts a reduced softening than the associative models. Hence the residual strength is greater for non-associative models. Both associative and non-associative rules predict almost the same stress paths in Figure 2.17 (d). On the other hand, non-coaxial models display an increased mean pressure before the peak. Therefore, the pre-peak stress ratios in Figure 2.17 (c) are also different between coaxial and non-coaxial models.

Generally, in plane-strain biaxial compression tests, the principal axis rotation does not take place in the two-dimensional plane. Therefore, the non-coaxility is hardly activated, and deviatoric stress-strain relationship is not much altered from the coaxial models. This is in line with reports of Lu et al. (2014). However, in the general stress space, the principal stress

rotation takes place in the intermediate direction during the initial variation of lode angle. It leads to an overestimation of the intermediate principal stress and hence the mean pressure by the non-coaxial models. This must be the reason for the observed disparity between coaxial and non-coaxial flow rules in biaxial tests. This non-coaxility ceases as the stress reaches the critical state.

The difference between associative and non-associative flow rules during the post-peak deformation can be explained using the volumetric relationship in Figure 2.17 (b). It is evident that non-associativity reduces the rate of dilation and hence the volumetric expansion during softening. On the contrary, non-coaxility does not show significant influence on the (total) volumetric relationship during biaxial compression. The sensitivity analysis of N_P and h_{pnc} is not included in this thesis due to the space limitation. It is observed that lower these two parameters, the deviation from the original model is higher.

In essence, the non-associative flow rule seems to affect the behaviour of drained dense sand only during softening for the biaxial stress path. If the variation of intermediate stress is ignored, non-coaxial model does not change the mechanical response of dense sand for proportional loading paths. However, it is difficult to comment on the accuracy of flow rules after the peak based on experimental observations since the deformation is no longer homogeneous.

Predictions for the undrained biaxial compression tests of dense sand by four NS models are depicted in Figure 2.18. A clear distinction between simulations by different flow rules can be witnessed in Figure 2.18 (a). Under isochoric constraint, the undrained strength is dependent on the effective mean stress which in turn is governed by the generated excess pore pressure. Both non-coaxial and non-associative rules predict reduced excess pore pressure generation, and hence smaller stiffness in the deviatoric stress-strain relationships. Differences in stress paths are barely noticeable in the scale of Figure 2.18 (d), but the peak stress ratios in Figure 2.18 (c) are slightly affected.

In the implemented NS model the shear stiffness is dependent on the effective mean pressure. Therefore both hardening modulus and non-coaxial modulus are sensitive to the generated negative pore pressure. Thus the influence of flow rules on the stiffness is exacerbated. As the tendency to dilation ceases near the critical state, predictions of all four models are superimposed by then.

Although there are many previous studies which investigated the plane-strain biaxial compression with non-coaxial and non-associative flow rules, their main intention was detecting the onset and inclination of shear bands (Hashiguchi, 2009; Hashiguchi and Tsutsumi, 2003;

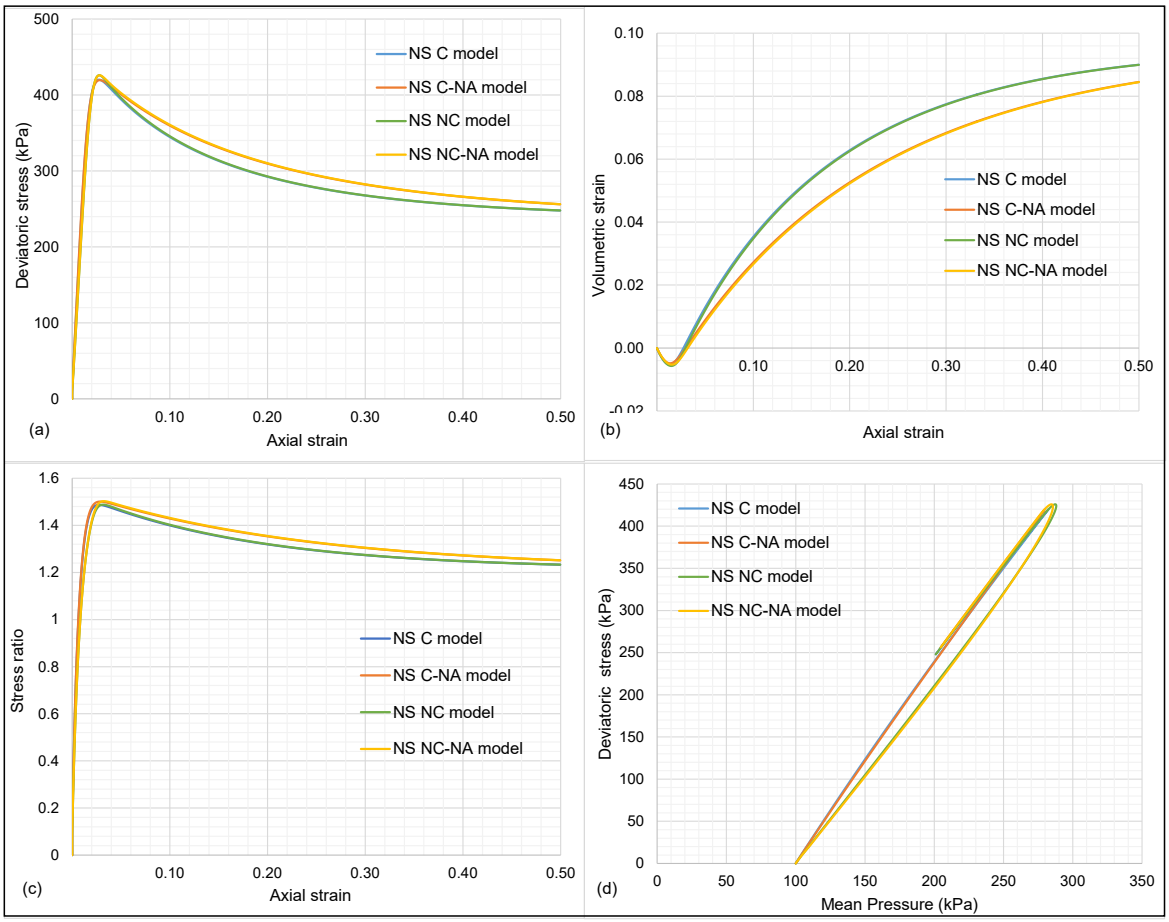

Fig. 2.17 Stress and volumetric relationships of drained biaxial compression test of dense sand predicted by modified Nor-Sand models: (a) deviatoric stress, (b) volumetric strain, (c) stress ratio against axial strain and (d) stress path

Lu et al., 2014; Papamichos and Vardoulakis, 1995; Yatomi et al., 1989b). This chapter only explores the mathematical implications of two flow rules applied to the NS model. In author's point of view, the basic constitutive features of dense sand during a biaxial compression test can be perceived with sufficient accuracy with the original NS model without any modifications.

2.7.2 Drained and undrained simple shear analysis

Figures 2.19 and 2.20 display simple shear simulation results of the drained and undrained dense sand respectively. Shear deformation induces the rotation of principal axis which activates non-coaxial stretching in the deviatoric plane. Therefore, the influence of non-coaxial flow rule is highlighted in both Figures compared to the biaxial simulations. It is observed in Figure 2.19 (a) that the non-coaxial flow rule softens the stress-strain response. It delays the peak and also slightly reduces its magnitude. The non-coaxial effect ceases gradually as the critical state is reached. These findings affirm the observations of Yang and

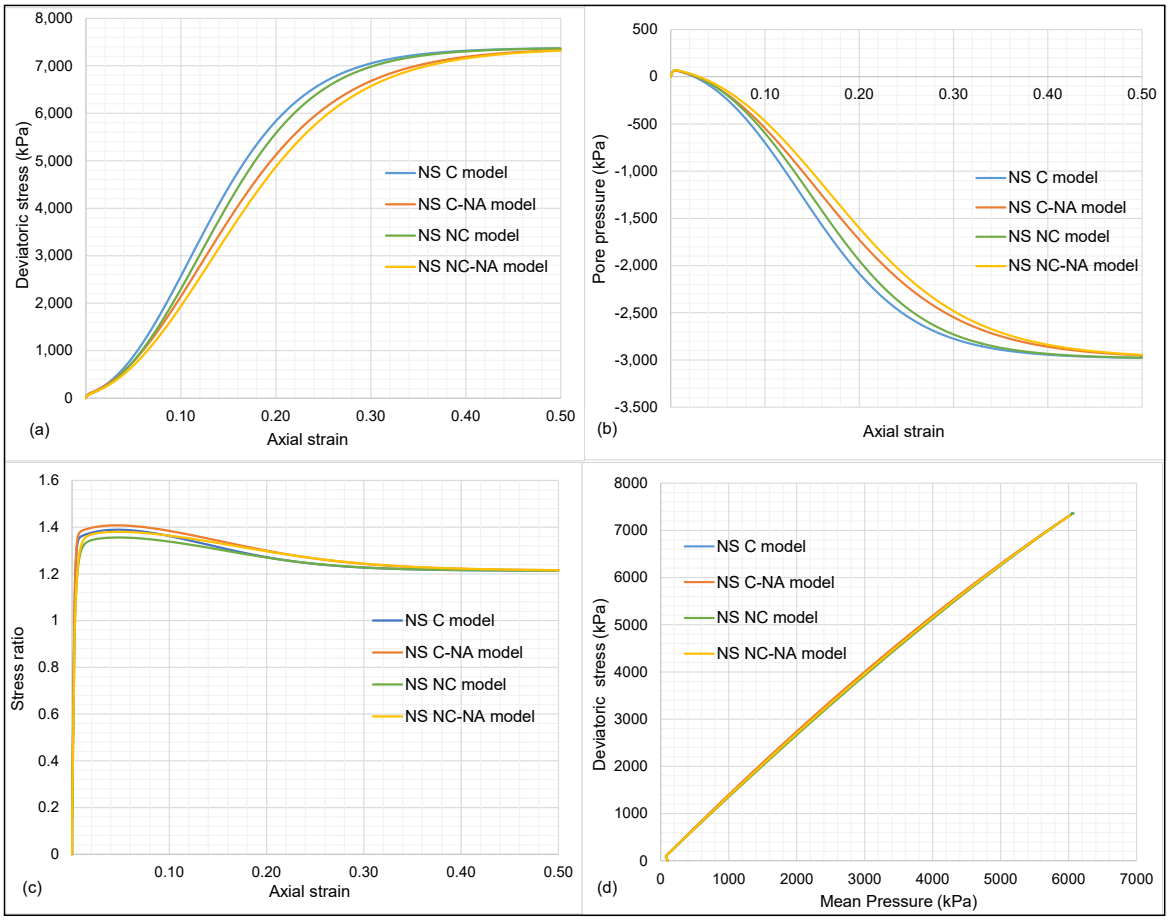

Fig. 2.18 Stress and pore pressure relationships of undrained biaxial compression test of dense sand predicted by modified Nor-Sand models: (a) deviatoric stress, (b) excess pore pressure, (c) stress ratio against axial strain and (d) stress path

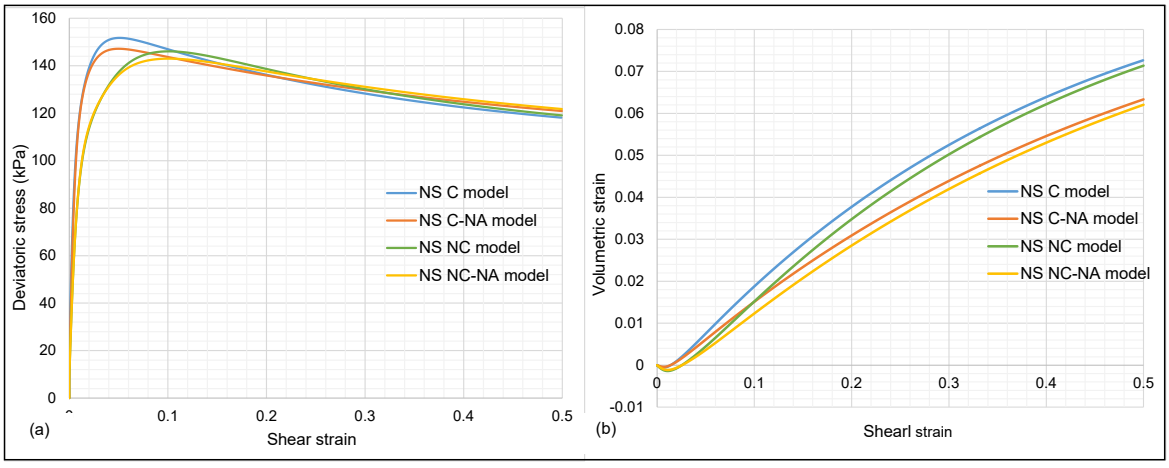

Fig. 2.19 Stress and volumetric relationships of drained simple shear test of dense sand predicted by modified Nor-Sand models: (a) deviatoric stress and (b) volumetric strain against shear strain

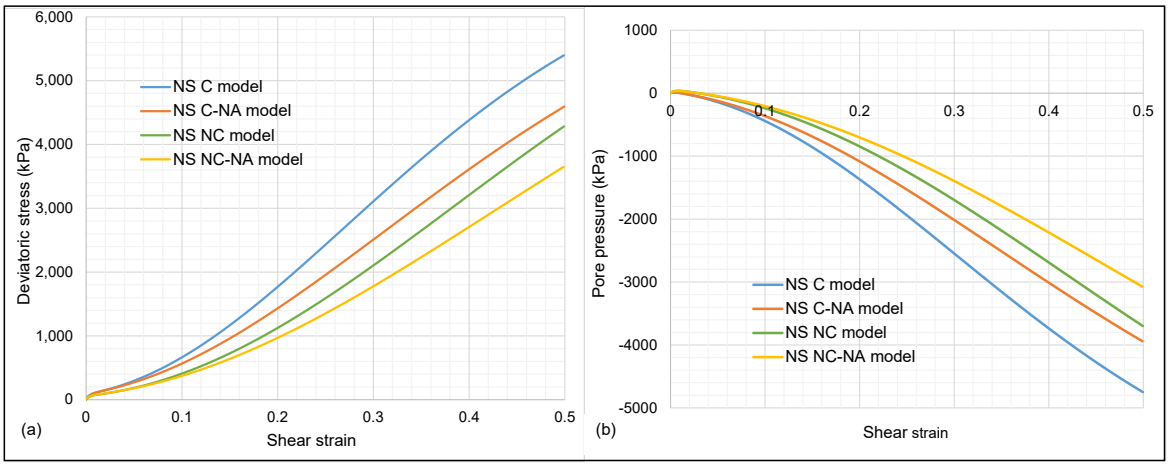

Fig. 2.20 Stress and pore pressure relationships of undrained simple shear test of dense sand predicted by modified Nor-Sand models: (a) deviatoric stress and (b) excess pore pressure against shear strain

Yu (2006a,b). The accumulated volumetric strains predicted by non-coaxial models are lower than their coaxial counterparts in Figure 2.19(b). Even the phase transformation point is delayed.

It should be also mentioned that since the original NS model is developed based on the sub-loading concept, the implementation of non-coaxial plasticity is straightforward. Since the model is elasto-plastic from the beginning, the principal axis rotation commences from the start of the deformation in contrast to Yang and Yu (2006a,b). The instabilities involved with the elasto-plastic transition are eradicated here.

Mallikarachchi and Soga (2018) validated this non-coaxial NS model for simple shear laboratory experimental data of Cole (1968). The model predictions agreed well with dense and medium dense sand but slightly deviated for loose sand. Mallikarachchi and Soga (2018) further pointed out that the plastic strain increment direction is ahead of stress direction for $K_0 = 0.4$.

On the other hand, the non-associative model predictions concur with associative ones until slightly before the peak. They produce somewhat smaller peaks than associative rules. However, the softening rate is reduced by the non-associativity which results in slightly higher residual strength. Associative and non-associative rules render almost the same volumetric strain until the peak. Afterwards, the non-associative rule predicts lower volume expansion.

In undrained simple shear simulations in Figure 2.20, both non-coaxial and non-associative rules lead to a reduction in the hardening stiffness and the generated negative excess pore

pressure. Unlike drained tests, undrained simple shear deformation has not reached the critical state until 50 % strain.

Although the original NS model can grasp the main features of the simple shear deformation, the mechanism of principal axis rotation cannot be captured without a proper non-coaxial theory. Jefferies et al. (2015) attached an additional softening term to the hardening rule of NS to fabricate the effect of principal stress rotation. However, excessive dilation is reported when they compared modified NS predictions with monotonic undrained simple shear tests. They concluded that the softening of the yield surface during principle stress rotation is not sufficient to model the undrained simple shear tests, the rotation of the strain increment direction should be considered as well. The non-coaxial NS model proposed in this study can easily lower the dilation by reducing the non-coaxial modulus and prevent the overly-stiff response at small strains.

2.8 Conclusions

This chapter presents the results of single element modelling which assumes fully homogeneous condition throughout the deformation. The contents in this chapter is a preparation for the bifurcation and post-bifurcation analysis in upcoming chapters.

The plane-strain drained biaxial test results indicate that the NS model has the capacity to distinguish the phase transformation, peak and critical state in the soil in the dry side of the critical state. The plane-strain undrained biaxial test does not show any sign of the peak until the critical state although it passes the maximum stress ratio. Even with an associative flow rule, NS model can accurately predict evolving dilation.

The non-associative flow rule is effective regardless of the loading path, but non-coaxility is active only during the principal axis rotation. Both theories inhibit the tendency to dilate and reduce the volume changes for the drained tests and excess pore pressure generation for the undrained tests. For both boundary conditions and loading paths, non-associativity is more noticeable after the peak effective stress ratio. On the contrary, the non-coaxility is more visible during the initial deformation and ceases near the critical state.

2.8.1 Contributions

The main contribution of this chapter is the integration of the yield vertex theory into the critical state plasticity and exploring its influence on the mechanical response of undrained dilative sand. It is observed that the yield vertex theory reduces the tendency to dilate, and hence the generation of negative excess pore pressure. Therefore, the dilative hardening effect is hindered by the non-coaxial yield vertex theory. Combined with the sub-loading

concept, this can circumvent the overly stiff response predicted by prevailing models during undrained dilative shearing. To the author's knowledge, the yield vertex theory has not been evaluated previously on the coupled simulation of the undrained dilative sand along with pore pressure generation. Furthermore, this is the first time, mathematical implications of different flow rules are explored in a single platform for both drained and undrained boundary conditions, under two loading paths.

Chapter 3

Instability and Localisation in Granular Soil

3.1 Preface

The stability of granular material has been subjected to extensive experimental, numerical and analytical investigations. Instability may appear in different forms such as diffused instability, localisation or liquefaction. The onset and inclination of shear bands in dry/drained soil can be solely predicted based on the constitutive equations. Their theoretical predictions are generally consistent with experimental observations. On the contrary, different observations are made from experimental investigations about the localisation in saturated undrained soil. Further, they are not in consensus with mathematical predictions from constitutive equations. The focus of this chapter is to scrutinise the onset criteria for localisation in the dry and saturated dense sand. The role played by the constitutive model for the detection of material instability is investigated using different flow rules.

Section 3.2 briefly outlines the mathematical foundation for the instability analysis of both single and multi-phase materials. The influence of the hydro-mechanical coupling on shear localisation is delineated. Experimental findings on the localisation in globally undrained sand are recorded in section 3.3. Previous numerical simulations to detect the onset and inclination of shear bands are reported in section 3.4. The results of bifurcation analysis with the original and modified NS models are included in section 3.5. The competency of constitutive models described in Chapter 2 to capture the onset of localisation in the undrained dense sand is evaluated. This chapter concludes by emphasising the importance of local drainage on the initiation of shear bands in globally undrained dilative sand.

3.2 Fundamentals of Instability Analysis

Basic mathematics underlying the instability and/or localisation of both single and multi-phase material are summarised in the succeeding section.

3.2.1 Loss of material stability

A system is said to be unstable if and only if an infinitesimal perturbation generates finite changes in states of the system. Hill (1958) suggested sufficient condition for the material stability as the positiveness of the second order work. The material instability is mathematically associated with the loss of positive definiteness of the symmetric part of the material stiffness matrix.

$$dW_2 = d\varepsilon_{ij}{}^T d\sigma_{ij} > 0 \tag{3.1}$$

3.2.2 Bifurcation analysis of drained/dry soil

Bifurcation occurs whenever a state of the system suddenly branches into multiple states under a continuous variation of state variables. It is associated with the loss of ellipticity of governing partial differential equations. The bifurcation analysis consists of finding the perturbation solutions (the difference between the heterogeneous and homogeneous fields of incremental solution) that satisfy the constitutive law and are compatible with boundary conditions (Guo and Stolle, 2013). The conventional bifurcation analysis of dry/drained soil is solely based on the constitutive behaviour of the materials.

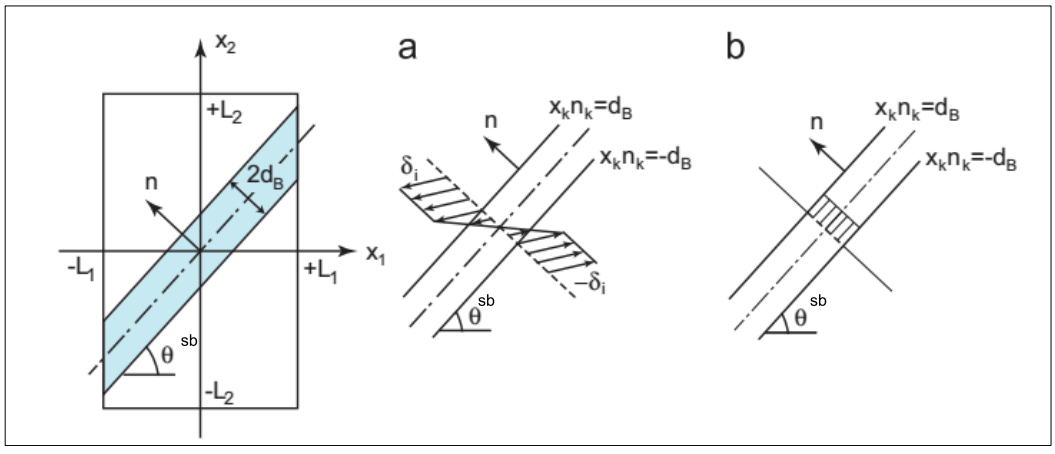

Fig. 3.1 Thomas-Hill-Mandel shear band model with (a) an inhomogeneous displacement field and (b) jump in displacement gradient (strain) and pore pressure (Guo and Stolle, 2013)

The onset of a shear band is derived according to conventional Thomas-Hill Mandel shear band model. It assumes the shear band as a weak discontinuity with a finite thickness across which the displacement (or velocity) is continuous while its gradient at the layer

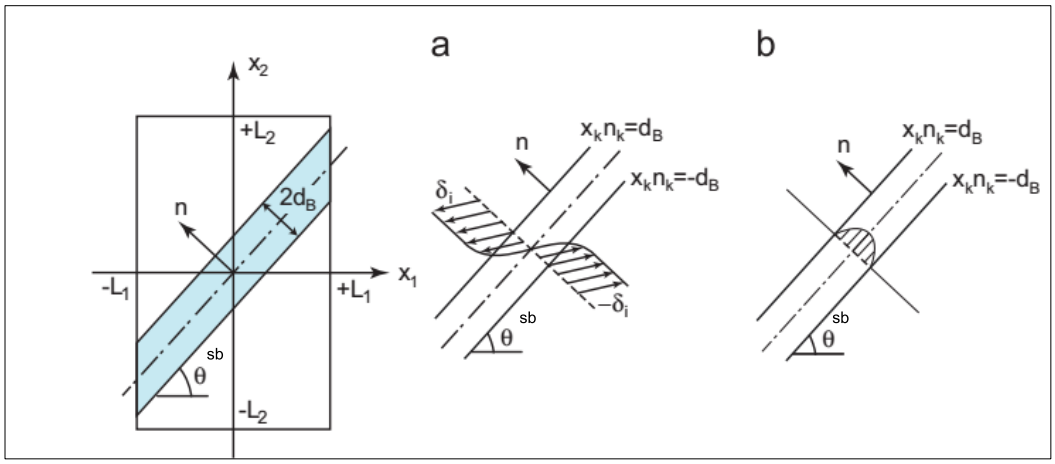

Fig. 3.2 Modified shear band model with (a) an inhomogeneous displacement field and (b) continuous displacement gradient (strain) and pore pressure (Guo and Stolle, 2013)

boundary experiences a jump. This is displayed by a schematic diagram in Figure 3.1. The inhomogeneous incremental displacement field: $\Delta u_i = \Delta u_i^{sb} - \Delta u_i^{out}$ is expressed as

$$\Delta u_i = \begin{cases} \delta_i & \text{for} \quad x_k n_k > d_B \\ \dfrac{\delta_i x_k n_k}{d_B} & \text{for} \quad |x_k n_k| < d_B \\ -\delta_i & \text{for} \quad x_k n_k < -d_B \end{cases} \tag{3.2}$$

where n_i is the unit normal to the shear band and δ_i is a displacement field at shear band boundaries. d_B is the half of shear band thickness ($t^{sb} = 2d_B$) and θ^{sb}. Δ denotes an increment in any field during a time increment Δt. The jump or discontinuity in the displacement gradient (strain) is defined as

$$[\Delta u_{i,j}] = g_i n_j \tag{3.3}$$

$$[\Delta \varepsilon_{ij}] = \frac{g_i n_j + g_j n_i}{2} \tag{3.4}$$

where $g_i = \dfrac{\delta_i}{d_B}$. The notation [] denotes a difference in quantity (jump) inside and outside the band. The static equilibrium requires the traction T of both sides of the band to be equal.

$$\begin{aligned} \Delta\, T_{ij}^{sb} &= \Delta\, T_{ij}^{out} \\ n_j \cdot \Delta \sigma_{ij}^{\prime sb} &= n_j \cdot \Delta \sigma_{ij}^{\prime out} \\ [\Delta \sigma_{ij}^{\prime}]\, n_j &= 0 \end{aligned} \tag{3.5}$$

Using the constitutive relation and neglecting geometric terms, Equation 3.5 can be rewritten as

$$[(D_{ijkl})\, g_k n_l] n_j = 0 \tag{3.6}$$

$$Q_{ik}\, g_k = 0 \tag{3.7}$$

where the acoustic tensor Q_{ik} is defined as

$$Q_{ik} = (D_{ijkl})\, n_j n_l \tag{3.8}$$

It is worthwhile to mention that the acoustic tensor is derived based on plastic loading both inside and outside the shear band. This is because the continuous bifurcation (plastic loading in and out of the band) precedes the discontinuous bifurcation (plastic loading inside and unloading outside) (Rice, 1976; Rice and Rudnicki, 1980). Bifurcation criterion states that the determinant of the acoustic tensor to be zero at the onset of localisation. In other words, the singularity of the acoustic tensor is the necessary condition for the loss of ellipticity of governing partial differential equations. The direction of the shear band is determined during the process of calculating the minima of $det\,[Q]$. In two-dimensional plane-strain condition (x-y plane) it is calculated as

$$det\,[Q] = f(\theta^{sb}) = a_4 \tan^4\,\theta^{sb} + a_3 \tan^3\,\theta^{sb} + a_2 \tan^2\,\theta^{sb} + a_1 \tan\,\theta^{sb} + a_0 \tag{3.9}$$

$$\begin{aligned}
a_0 =& D_{yyyy} D_{yxyx} - D_{xxxy} D_{yxxx} \\
a_1 =& D_{yyyy} D_{yxxx} + D_{yyyy} D_{xxyx} - D_{yyyx} D_{xxyy} - D_{yyxx} D_{yxyy} \\
a_2 =& D_{yyyy} D_{xxxx} + D_{yyyx} D_{yxxx} + D_{yxyy} D_{yyxy} - D_{yyxx} D_{yxyx} - D_{yyxx} D_{xxyy} - D_{yxyx} D_{xxyy} \\
a_3 =& D_{yyyx} D_{xxxx} + D_{yxyy} D_{xxxx} - D_{yyxx} D_{xxyx} - D_{yxxx} D_{xxyy} \\
a_4 =& D_{yxyx} D_{xxxx} - D_{xxyx} D_{yxxx}
\end{aligned}$$

A change in the sign of the minima of the polynomial $f(\theta^{sb})$ signals the onset of localisation. However, Thomas-Hill-Mandel shear band model assumes a linear inhomogeneous displacement field, hence a jump in the strain which is proved to be inaccurate. With digital image correlations, Rechenmacher (2006) and Alshibli et al. (2003) observed a parabolic displacement field across the width of the shear band. Therefore, Guo and Stolle (2013) introduced a modified shear band model as shown in Figure 3.2 preserving the continuity of strain and pore pressure. Analytical expressions derived for the onset of shear banding and its inclination angle based on rate-independent elasto-plastic models are reported to be consistent with the experimental findings of dry soil. However, this is not the case regarding the localisation of saturated soil.

3.2.3 Bifurcation analysis of saturated soil

In fluid saturated geomaterials, the diffusion of pore fluid in response to the deformation introduces a rate dependence to overall behaviour, even though underlying drained solid is rate independent (Benallal and Comi, 1999, 2003; Rudnicki, 2009). Hence the use of the conventional bifurcation approach alone may overlook some instability phenomena inherent to rate-dependent materials. This rate dependency is governed by the interplay between

the rate of deformation and fluid mass exchange rate. Perturbation and acceleration wave analysis are valid for rate-dependent problems regardless of the drainage conditions. They can be conducted either for quasi-static or dynamic conditions.

Rudnicki (2009) mentioned that the fully undrained condition (when pore pressure is constant) can be reasonably considered as rate-independent such that general bifurcation analysis can be applied. Therefore, the process of deriving acoustic tensor for one phase solid can be directly applied to the undrained bifurcation analysis.

Bifurcation of saturated undrained soil

In a saturated medium, apart from incremental displacement/velocity gradient, the pore pressure rate can also be discontinuous across the shear band interface as shown in Figure 3.1(b). The static compatibility condition can be expressed in total traction.

$$\begin{aligned}[\Delta\sigma'_{ij} + \Delta U\,\delta_{ij}]n_j = 0\\ [\Delta\sigma'_{ij}]n_j + [\Delta U]n_i = 0\\ Q_{ik}g_k + [\Delta U]n_i = 0\end{aligned} \tag{3.10}$$

Q_{ik} is the acoustic tensor calculated from the effective stress. For undrained condition, the mass conservation is applied across the discontinuous surface.

$$\begin{aligned}[\Delta\varepsilon_{ii}] = \frac{[\Delta U]}{K_f}\frac{e}{1+e}\\ g_i n_i = \frac{[\Delta U]}{K_f}\frac{e}{1+e}\end{aligned} \tag{3.11}$$

where $[\Delta U]$ is the pore pressure discontinuity and K_f is the bulk modulus of water. Upon the elimination of $[\Delta U]$, the undrained acoustic tensor Q^u_{ik} can be derived from the undrained stiffness D^u_{ijkl}.

$$Q^u_{ik}g_k = 0 \tag{3.12}$$

$$Q^u_{ik} = \left(D^u_{ijkl}\right) n_j n_l \tag{3.13}$$

$$D^u_{ijkl} = D_{ijkl} + \delta_{ij}\frac{K_f}{e}(1+e)\,\delta_{kl} \tag{3.14}$$

Bifurcation of saturated partially drained soil

For a general deformation path which is neither drained or undrained, the strain localisation can occur when either drained or undrained acoustic tensor first becomes singular (Benallal and Comi, 1999, 2003). In other words, under quasi-static conditions, the emergence of stationary discontinuities under drained or undrained conditions set the limit for the unbounded growth of perturbations. The instability under dynamic conditions is not discussed here. Therefore, regardless of the rate dependence of hydro-mechanical coupling, acoustic

tensors derived from static bifurcation analysis in section 3.2.2 can be utilised as the limiting values which signal the localisation.

For associative plasticity, it is proven that the singularity of the drained acoustic tensor is met before that of the undrained acoustic tensor. However, for non-associative behaviour either can be expected depending on the loading path and constitutive equation. For compactive material, the undrained response is prone to be unstable before the corresponding drained response. This is the opposite for dilative materials (Benallal and Comi, 1999, 2003).

3.2.4 Global vs local drainage in soil

The fluid flow in a saturated medium can be inhibited by the poor diffusion of the material or impermeable boundaries of the domain. The former can be considered as locally undrained whereas the latter is said to be globally undrained. The local drainage, which depends on the permeability of the material, the velocity of loading and drainage length, is difficult to control. Most of the laboratory experiments are conducted under globally undrained conditions. In these cases, the specimen does not remain homogeneous, and the local drainage can occur. Hence load path is not unique for all material points in the specimen.

There can be two instability criteria during a globally undrained deformation. One is the locally undrained condition where a strict isochoric constraint is met at each material point. The other is the locally drained condition under globally undrained boundaries. The initial state of the soil decides which criterion is to be satisfied.

Bifurcation of locally undrained loose sand

Theoretically, locally undrained loose and medium dense sand can experience two types of instabilities. First is two-phase bifurcation or solid-fluid coupled instability. This is signalled by the singularity of the undrained acoustic tensor and corresponds to the state of maximum deviatoric stress (Tresca state). The orientation is calculated to be 45° regardless of constitutive behaviour. It is possible only for undrained contractive soil and shown as point T in Figure 3.3. However, Vardoulakis (1996a,b), Guo (2013), Guo and Stolle (2013) dismissed this type of localisation. They are unlikely to happen under laboratory conditions since they lead to pore pressure shocks at shear band boundaries. For pore pressure diffusivity coefficient of $2\,\mathrm{m}^2/\mathrm{s}$ and shear band thickness of 3.5mm, the characteristic time required for the pore pressure to dissipate across the shear band is about 100 ms (Vardoulakis, 1996a). Thus, the pore pressure generated inside the band tends to dissipate very fast at least for highly permeable sand. Therefore, Guo and Stolle (2013) concluded that this is a diffuse type of instability rather than a localised one.

The other criterion is the bifurcation of the soil skeleton. It happens without a pore pressure jump at shear band boundaries. This is only possible if both determinants of drained and undrained acoustic tensors are zero. This is the strong criterion of localisation during an undrained loading path, and it is shown as point US in Figure 3.3. This may happen only in the contractive sand in the deviatoric softening regime with a negative tangent shear modulus.

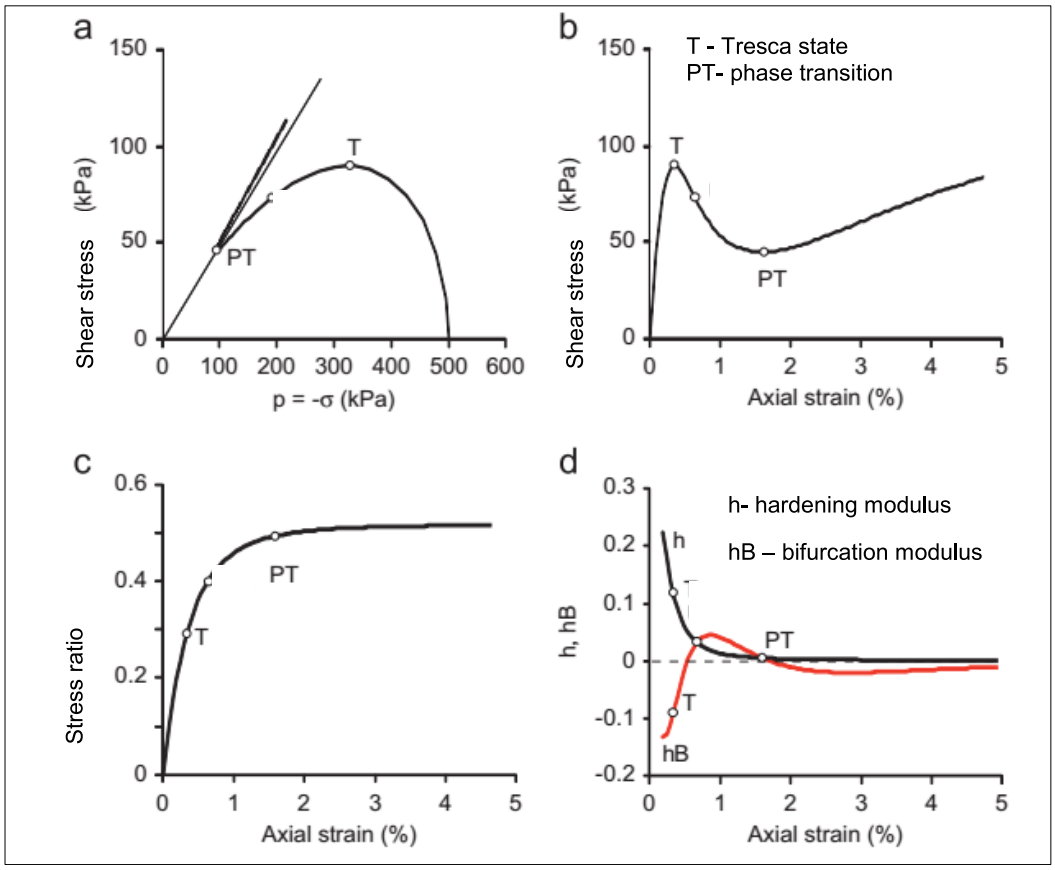

Fig. 3.3 Relationships of medium dense Ottawa sand ($e_0 = 0.68$ and $p_0 = 500$kPa): (a) stress path, (b) shear stress, (c) stress ratio and (d) hardening modulus vs axial strain (Guo and Stolle, 2013)

Bifurcation of locally undrained dense sand

Dilatant materials cause a reduction in pore pressure under undrained plastic shearing which leads to a monotonic increase of deviatoric stress. If the bifurcation criterion is regarded as the singularity of the undrained acoustic tensor, this dilative hardening phenomenon can delay the instability. On the other hand, there is no consensus in the literature whether the undrained dense sand meets the singularity of the drained acoustic tensor.

Rice (1975) showed using the perturbation analysis that homogeneous undrained deformation of dilative materials can be unstable when the condition for localisation is met in terms of the underlying drained response. For a simple shear deformation with constant normal stress

as considered by Rice (1975), this condition is met at the peak of the underlying drained shear stress-strain curve. This is depicted in Figure 3.4 as point C. For a general deformation, this can occur well before or after the peak of the drained shear stress-strain curve (Rudnicki, 1985, 2000). By analysing acceleration waves under dynamic conditions, Loret and Harireche (1991), Loret and Prevost (1991) came to the same conclusion. Stationary discontinuities (acceleration waves with vanishing speed) are first observed when the localisation criterion is met for the drained deformation. Furthermore, Vardoulakis (1985, 1986) mathematically proved for plane strain biaxial and simple shear loading, that dilatant material can become unstable only in the softening regime of underlying drained behaviour.

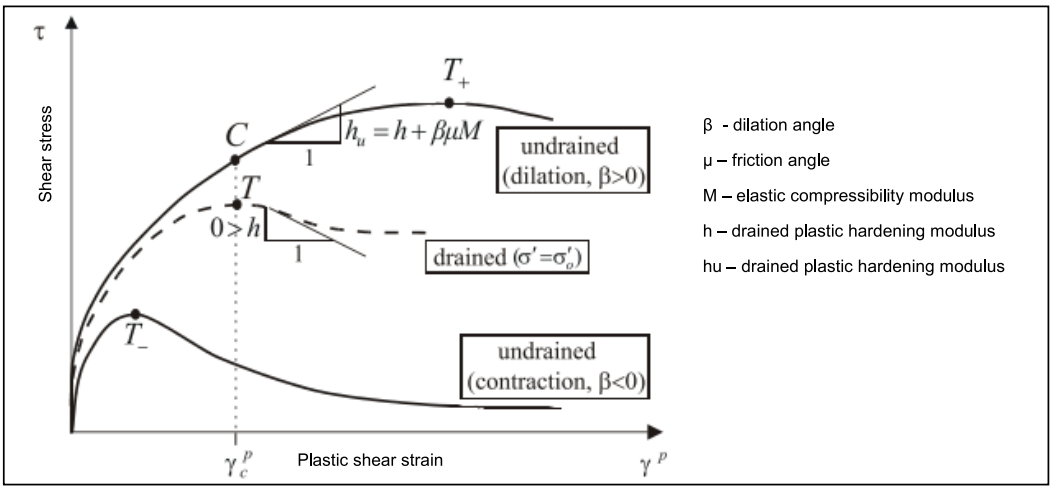

Fig. 3.4 Shear stress vs plastic shear strain (Garagash and Rudnicki, 2002)

On the contrary, Larsson and Larsson (2000a,b) stated that in the absolute absence of inhomogeneities, no shear band can occur even though the drained localisation criterion is met. In other words, for a homogeneous plastic state, unloading outside the band will not appear until the undrained localisation criterion is satisfied. Guo (2013),Guo and Stolle (2013) mathematically proved that the strict isochoric constraint prevents undrained shear bands in the dense dilative sand.

Bifurcation due to local drainage in globally undrained dense sand

Vardoulakis (1996b),Guo (2013),Guo and Stolle (2013) presented the concept of the locally drained shear bands under globally undrained conditions. It is signalled by nullity of the drained acoustic tensor when the undrained acoustic tensor is still positive. Only this type of instability is possible for dilative dense sand. Bifurcation with local volume change is stable since local pore pressure decreases within the band (Guo, 2013; Guo and Stolle, 2013). The local volume changes are always accompanied by water flow associated with a pore pressure gradient. This means there should be a jump in volume change across the shear band when the pore pressure is dissipated. Although the bifurcation criterion is the same, Rice

(1975),Rudnicki (1985, 2000) did not mention about the local drainage. Their predictions were derived under the assumption of uniform material response. In contrast, the material heterogeneity should be considered for the initiation of the local drainage. Hence it cannot be predicted upon constitutive relationship.

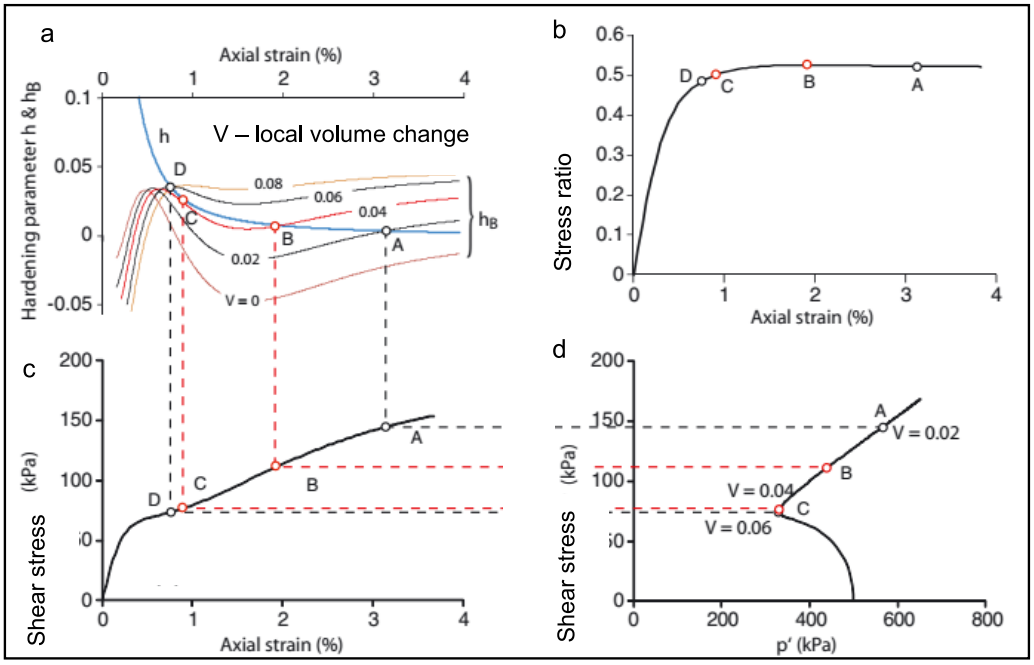

Fig. 3.5 (a) Hardening modulus, (b) stress ratio, (c) shear stress vs axial strain and (d) stress path of dense sand ($e_0 = 0.62$) with local drainage (Guo and Stolle, 2013)

Figure 3.5 shows that the onset of a shear band is dictated by the rate of local volume change (or rate of pore fluid dissipation). Guo (2013) theoretically showed that it can happen both in hardening or softening regime of the mobilised friction angle. However, it is most likely that a shear band initiates with a minimum deviation from the isochoric constraint, after the peak friction angle. Because in this region, the jump in local volume change required to trigger a dilative shear band is smaller. Guo (2013) also pointed out that the orientation of this locally drained shear band also depends on the rate of local volume change.

On the other hand, if the isochoric constraint is lifted due to cavitation, full internal drainage is possible. Hence the localisation can occur very early (Guo, 2013). Therefore, in most experimental conditions, the internal fluid flow is suppressed, and cavitation can precede that.

3.3 Experimental Evidence of Localisation in Globally Undrained Tests

To interrogate the validity of aforementioned mathematical interpretations some experimental findings on localisation in biaxial compression tests of saturated sand with impermeable boundaries are summarised in this section. Strain localisation in undrained granular material is a subject of controversy. This is mainly because the coupled localisation is sensitive to the geometrical parameters (size of the specimen, aspect ratio), loading rate, material properties (friction, dilation, permeability), boundary conditions (triaxial, plane-strain) and initial conditions (back pressure, cell pressure). Table 3.1 encapsulates the details of previous laboratory studies on the localisation of undrained sand.

Table 3.1 Experiments of undrained biaxial compression tests

Reference	Grain size D_{50} (mm)	Void ratio (min - max)	Permeability $\bar{k}$ (m/s)	Specimen size (mm × mm)	Loading rate (mm/min)	Confining pressure (kPa)	Back pressure (kPa)
Han and Vardoulakis (1991)	0.165	0.47 - 0.88	4×10^{-6} - 1.6×10^{-5}	140×40	0.2-0.5	750-800	300-600
Mooney et al. (1997)	0.32	0.6 - 0.875		140×40	0.006	200-600	200
Mokni and Desrues (1999)	0.5 - 1.5	0.6 - 1	1×10^{-4}	340×100	1.2	200-1000	50-900
Roger et al. (1997)	0.35	0.64		174×88	0.05- 5.2	375-675	300-600

3.3.1 Onset of shear band

Han and Vardoulakis (1991) carried out a comprehensive study on displacement controlled undrained plane-strain experiments of fine grained saturated sand. They observed strain localisation in saturated dense and medium dense sand, but not in the loose sand. In medium dense sand, the deviatoric stress curve in Figure 3.6(a) depicts a clear peak (Tresca state) at a very small strain, which is followed by a re-hardening regime. The Coulomb limit state or the maximum effective stress ratio is reached during this re-hardening regime as shown in Figure 3.6(c). In Figure 3.7(a), the deviatoric stress of dense sand continues to rise without a peak, and the Coulomb state is reached during hardening regime in Figure 3.7(c). In both, shear bands occurred past the Coulomb state in the softening regime of effective stress ratio.

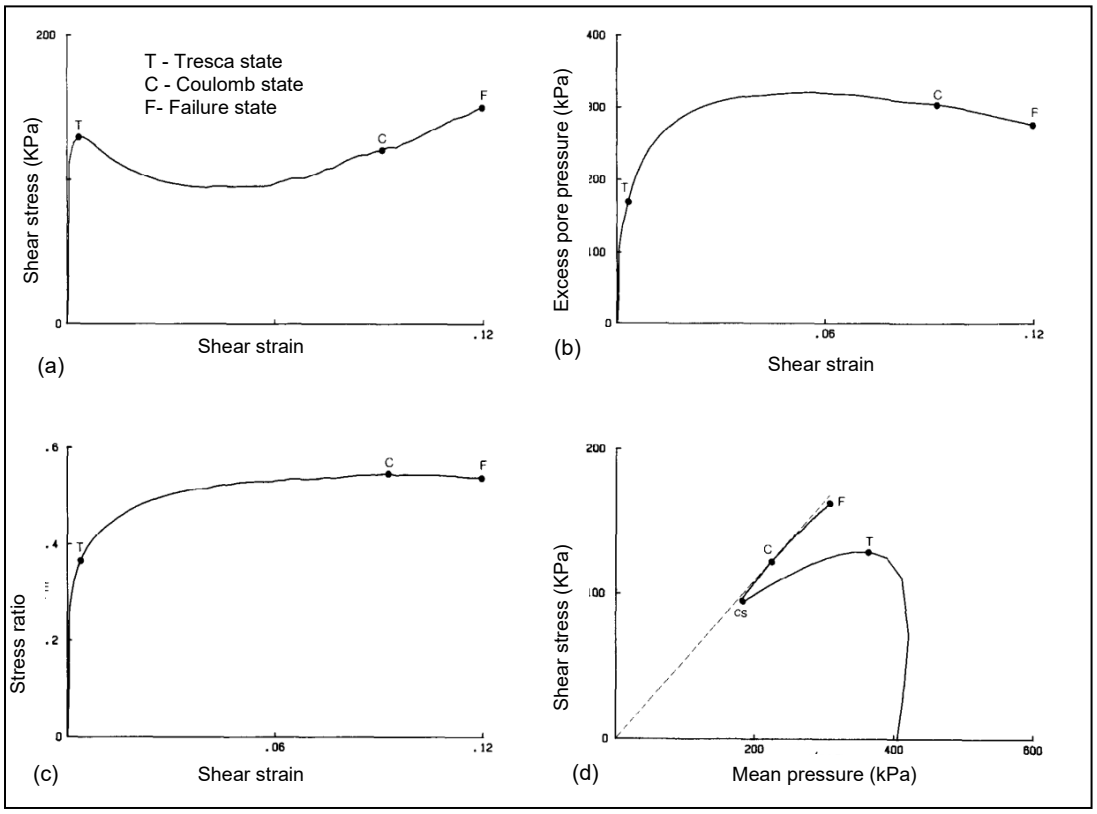

Fig. 3.6 Pre-failure test data for medium dense sand (void ratio-0.647): (a) deviatoric stress, (b) excess pore pressure, (c) effective stress ratio against shear strain and (d) effective stress path (Han and Vardoulakis, 1991)

Based on undrained plane-strain biaxial compression tests of Houston sand, Mokni and Desrues (1999) reported shear localisations in both contractive and dilative sand. However, in the latter, the localisation was delayed until the strict isochoric constraint was lifted by cavitation. In dense sand, the localisation is accompanied by a sudden drop in the stress ratio as shown in Figure 3.8 (a). Also, it is observed that the shear band occurs between increments $9-10$, much later than the peak effective stress ratio. Even in loose sand, the shear band occurs between increments $5-6$, slightly after the Coulomb state. Figure 3.9(a) demonstrates that the onset of localisation in undrained dense sand depends on the initial back pressure. The pore pressure drops until it reaches the same limiting cavitation pressure. Hence, higher initial back pressures delay localisations. Figure 3.9 (b) illustrates the stress paths of undrained dense sand. The locus of the peaks at which the strain localisation occurs in drained tests and the phase transformation line are drawn. The stress paths of undrained tests lie between these two lines. As long as the isochoric constraint holds, the undrained stress paths cannot reach the peak stress line of drained tests.

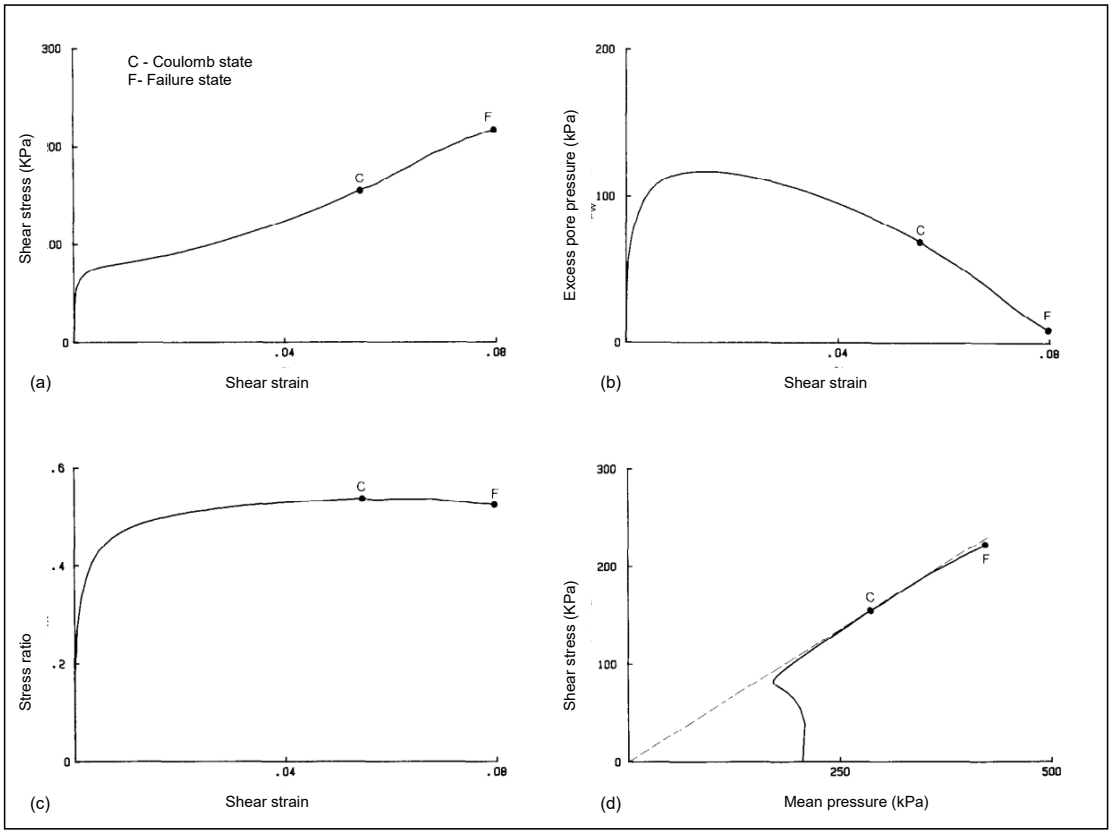

Fig. 3.7 Pre-failure test data for dense sand (void ratio-0.597): (a) deviatoric stress, (b) excess pore pressure, (c) effective stress ratio against shear strain and (d) effective stress path (Han and Vardoulakis, 1991)

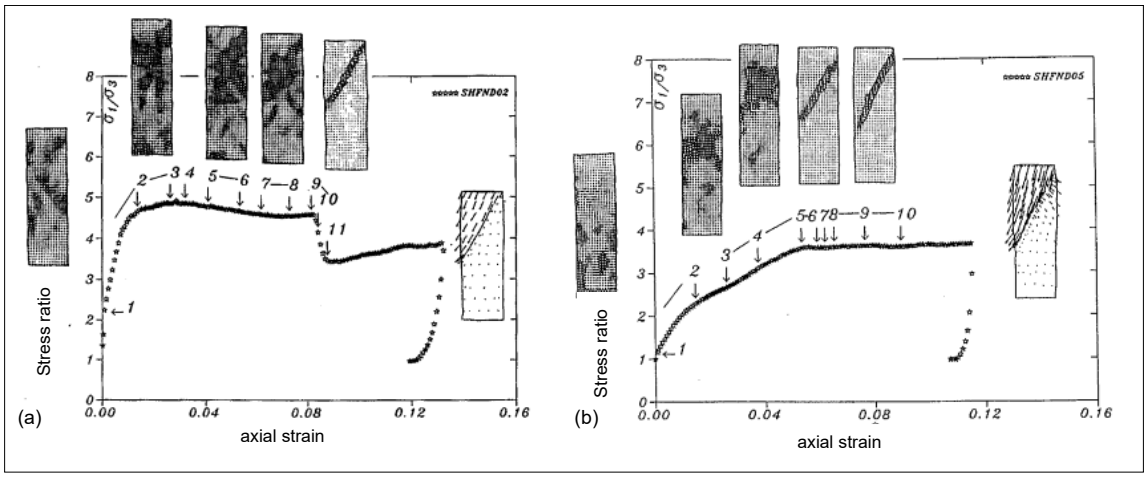

Fig. 3.8 Effective stress ratio against axial strain in undrained biaxial tests of Houston RF sand: (a) dense and (b) loose (Mokni and Desrues, 1999)

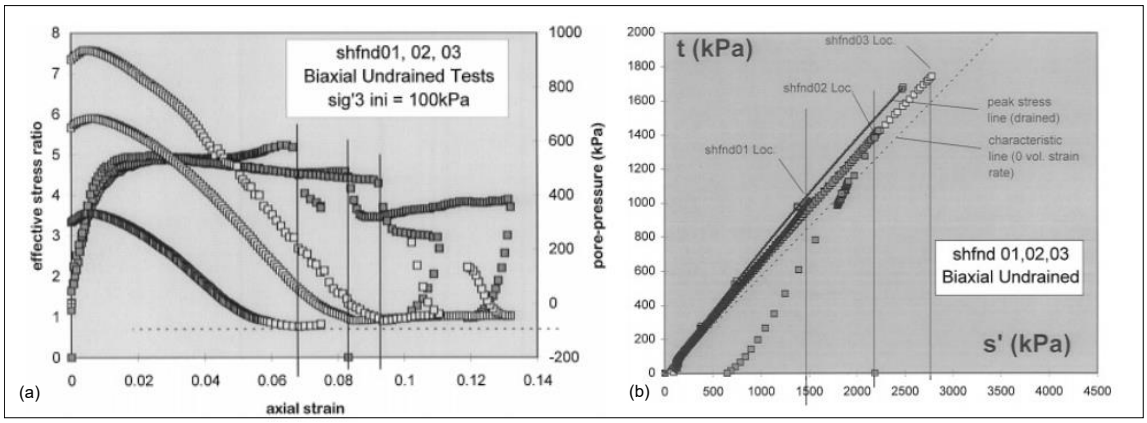

Fig. 3.9 (a) Effective stress ratio and excess pore pressure against axial strain and (b) stress paths in undrained biaxial tests of dense Houston RF sand (Mokni and Desrues, 1999)

Therefore, Mokni and Desrues (1999) concluded that non-drainage can preclude the localisation in the dense sand until cavitation in the pore-fluid relaxes the isochoric constraint. This notion is supported by Roger et al. (1997). In contrast, Vardoulakis (1996b) reported that the cavitation occurs inside the dilative shear band. Figure 3.10 indicates that the shear band is initiated in the vicinity of the Coulomb state, just before the cavitation. Therefore, the experimental findings are inconclusive about the localisation in globally undrained dense sand.

3.3.2 Orientation of shear band

The inclinations of shear bands with respect to the major principal axis in the undrained sand are recorded by several authors. Desrues and Mokni (1998) reported that the shear band orientation is 30° for dense sand which departs significantly from the mobilised Coulomb angle at the onset of localisation. It is about 25° for loose sand which agrees well with the Coulomb orientation. Mooney et al. (1997) recorded an average shear band angle of 31° for loose sand. Han and Vardoulakis (1991) reported that the shear band orientations are 28° and 33° for medium dense and dense sand respectively which agree with the Coulomb orientations at failure. This discrepancy is because Desrues and Mokni (1998) observed lower mobilised friction angle at the emergence of the shear band than Han and Vardoulakis (1991). Desrues and Mokni (1998) observed fully drained shear band due to cavitation whereas Han and Vardoulakis (1991) noticed locally drained bands. The shear band inclination is also sensitive to the initial confining pressure as well.

3.4 Numerical Predictions on Initiation of Localisation

Mathematical modelling of the strain localisation consists of two main phases, both of which are important to get a clear view of the failure of geomaterials.

- Detection of the onset of material instability
- Capturing the post-localised behaviour

The former identifies the emergence and inclination of the localised band, whereas the latter determines a physically meaningful representation of the material during a localised deformation. The following section briefly describes previous studies on mathematical detection of the onset of localisation based on bifurcation analysis.

3.4.1 Importance of constitutive model for bifurcation analysis

According to the literature, the prediction of onset and inclination of the shear band is governed by the pre-localised constitutive relation. It is reported that classical plastic idealisations often poorly predict the onset of shear band (de Borst et al., 1993; Huang et al., 2010; Lu et al., 2014, 2015; Papamichos and Vardoulakis, 1995; Rudnicki and Rice, 1975; Yatomi et al., 1989a). Smooth yield surfaces and normality condition render a symmetric elasto-plastic stiffness matrix. Due to these simplifications, criteria for failure, diffused instability and localisation coincide with the peak stress ratio. This is not consistent with experimental findings which state that the instability and/or localisation in a single phase material tends to appear in the hardening regime. Therefore, both non-normality of plastic strain increments and vertex like yield surfaces have been adopted in the past to induce a destabilising effect (Rudnicki and Rice, 1975). According to de Borst et al. (1993), the lack of symmetry in the elasto-plastic stiffness itself is sufficient for the loss of material stability. Nevertheless, it should be questioned whether this instability is simply a mathematical outcome of the non-symmetric stiffness itself or the real soil behaviour.

Yatomi et al. (1989a) reported that the non-coaxial term facilitates easier access to the elliptic/hyperbolic boundary. Papamichos and Vardoulakis (1995) also discovered that the shear band orientation and its inception are influenced by the degree of non-coaxility. Hashiguchi and Tsutsumi (2003) stated that the tangential stress rate increases the shear band inclination angle. Huang et al. (2010), Lu et al. (2014, 2015) conducted recent bifurcation studies on the drained and undrained sand in plane-strain condition.. They reported that the prediction of localisations is significantly improved from the non-coaxial theory.

Nevertheless, aforementioned bifurcation studies were conducted on strain softening materials (dry dense sand, undrained loose or medium dense sand). None of these studies considered instability of undrained dilative hardening materials except Vardoulakis (1996b). He stated that the non-coaxial bifurcation point is close to the experimentally observed localisation while coaxial models tend to underpredict it as shown in Figure 3.10. However,

it is not clear whether these results are based on uniform material response or heterogeneous response with local drainage.

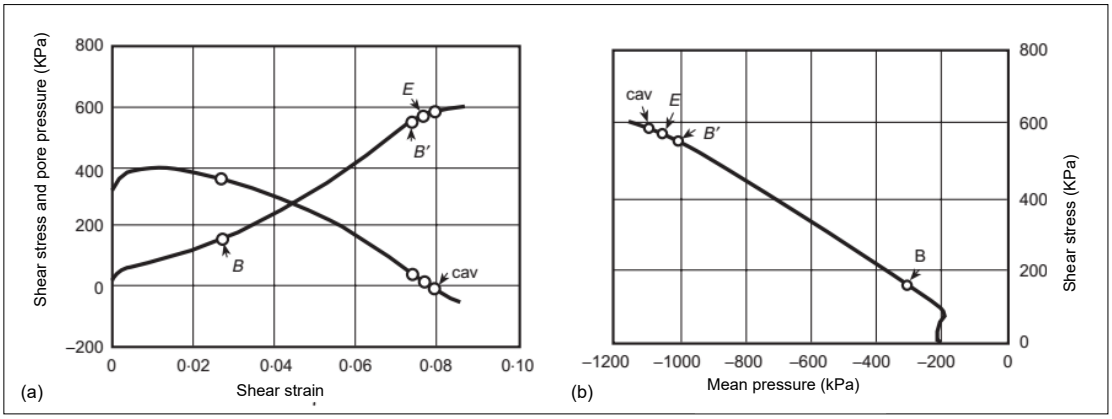

) (Vardoulakis, 1996b)

Fig. 3.10 (a) Deviatoric stress and excess pore pressure against shear strain and (b) stress path of undrained biaxial compression test of dense sand (B- coaxial, B'- non-coaxial bifurcation points, E- experimental onset of shear band, cav- cavitation

3.5 Results of Bifurcation Analysis

In this study, a bifurcation analysis is conducted with different constitutive relationships for the plane-strain biaxial compression tests. Same single element (dimensions 1×1) results shown in Chapter 2 are used for this analysis. Different criteria for diffused instability and localisation are calculated. The purpose of this section is to evaluate the potential of original and modified NS models to capture the shear localisation in dense sand under drained and undrained boundary conditions.

- Maximum deviatoric stress (Tresca state) - Condition 1
- Maximum effective stress ratio (Coulomb state) - Condition 2
- Zero determinant of the drained acoustic tensor (loss of ellipticity of governing equations) - Condition 3
- Zero determinant of the symmetric part of stiffness matrix (zero second-order work) - Condition 4
- Zero determinant of the undrained acoustic tensor - Condition 5

3.5.1 Bifurcation analysis of original Nor-Sand model

The results of the coaxial and associative NS model are shown in Figure 3.11. It is observed in Figures 3.11 (a) and (b) that for the drained sand that all four criteria are clustered at the

peak of the stress-strain relationship. This results from the symmetry of the stiffness matrix which causes instability, localisation and failure criteria to coincide. It contradicts the widely cited observation that the drained frictional material bifurcates in the hardening regime of the stress ratio in biaxial tests.

On the contrary, the undrained dense sand does not satisfy any criteria except the maximum stress ratio as shown in Figures 3.11 (c) and (d). This observation agrees with analytical findings of Guo (2013),Guo and Stolle (2013). They mentioned that under strict isochoric constraint the localisation in very dense sand is prevented since its deviatoric stress is continuously increasing. However, it was initially expected that at least the Rice criterion (zero drained acoustic tensor) to be fulfilled for the undrained dense sand. According to Rudnicki (1985, 2000), Garagash and Rudnicki (2002) this condition signals the instability of the underlying soil skeleton. The reason behind this observation can be the difference in constitutive models used. For MC type models, the plastic hardening modulus is a function of the derivative of mobilised stress ratio. Hence it is zero at the peak stress ratio. In the NS model, the plastic hardening modulus is driven by the limiting hardness which becomes null only at maximum deviatoric stress. In undrained dense sand, the deviatoric stress is always increasing. Hence the limiting hardness is positive even if the stress ratio is decreasing. Collin et al. (2010) mentioned that for highly dilatant material the Rice criterion is never met, supporting the findings of this thesis. It should be noted here, for medium dense sand which exhibits deviatoric softening, the Rice criterion is fulfilled. The results of medium dense sand are not shown in this thesis.

3.5.2 Bifurcation analysis of modified Nor-Sand models

Table 3.2 summarises the different bifurcation criteria for modified NS models. The influence of non-associativity and non-coaxility for the initiation of shear bands or diffuse instability is examined. Especially, destabilising effect from the non-symmetric stiffness matrix is explored for the NS model. This section aims to qualitatively evaluate the potential of different constitutive models regarding their ability to predict instability. Therefore, a quantitative validation with experimental data is not conducted here.

It is observed for dry, dense sand, that non-symmetric stiffness matrix separates criteria for localisation and instability. The Coulomb state occurred after Tresca state for all modified NS models. The condition for shear localisation (zero determinant of drained acoustic tensor) happens in the hardening regime of stress ratio as predicted by both analytical and experimental observations (Desrues and Viggiani, 2004; Wan et al., 2013). The condition for diffused instability coincides with the singularity of the symmetric part of the stiffness matrix. This takes place before the localisation criterion and coincides with the peak deviatoric stress,

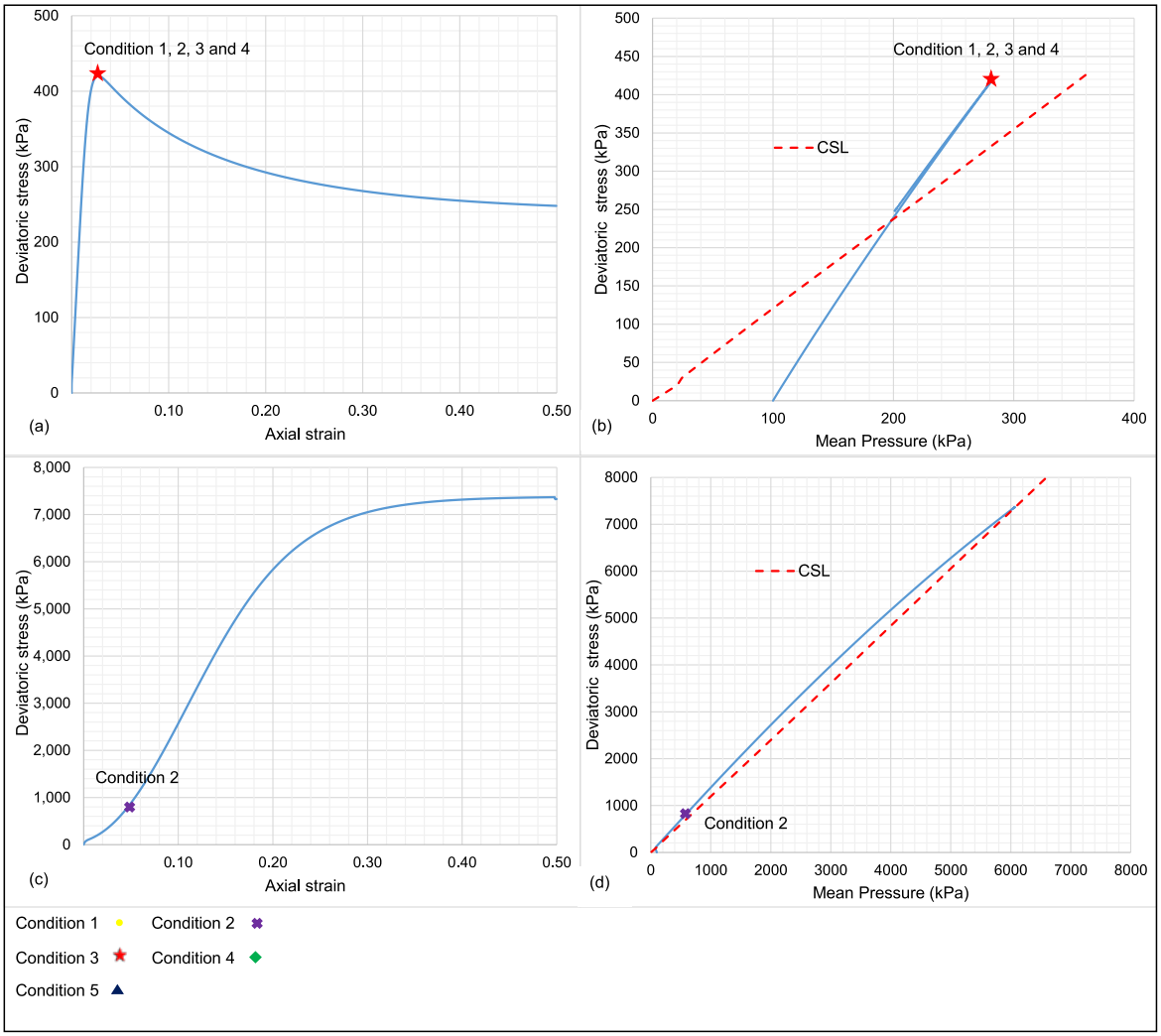

Fig. 3.11 Bifurcation points of (a),(b) dry and (c),(d) saturated undrained sand : (a),(c) stress-strain relationships and (b),(d) stress paths

Table 3.2 Axial strains at which different bifurcation criteria are met in single element models

Drainage condition	material model	Condition 1	Condition 2	Condition 3 (band angle)	Condition 4
drained	C	0.028	0.028	0.028 (51°)	0.028
drained	NC	0.028	0.032	0.03 (54°)	0.028
drained	C-NA	0.028	0.0295	0.029 (53°)	0.028
drained	NC-NA	0.0285	0.033	0.031 (57°)	0.028
undrained	C		0.047		
undrained	NC		0.048		
undrained	C-NA		0.044		
undrained	NC-NA		0.054		

which is followed by softening. The results in Table 3.2 depend on the shape of plastic potential N_P and the magnitude of the non-coaxial modulus h_{pnc}. It is also observed that both non-associative and non-coaxial models delay the localisation and increase the orientation of the shear band. As for non-coaxial models, this observation is in agreement with results of Papamichos and Vardoulakis (1995), Huang et al. (2010), Hashiguchi and Tsutsumi (2003) and Lu et al. (2014, 2015). However, Zervos et al. (2007) reported that non-associativity expedites the localisation and decreases the shear band angle. This can be mainly due to the difference in the constitutive model used. Associative MC model has equal dilation and friction angles while in associative NS model, mobilised dilation is always lower than friction.

As for undrained dense sand, even modification of flow rule does not result in either drained or undrained localisation. The peak stress ratio (Coulomb state) is however delayed by the non-coaxial flow rule. This observation does not agree with Vardoulakis (1996b)'s finding which states that non-associative and non-coaxial flow rules together can induce instability in the undrained dense sand. He mentioned that the drained acoustic tensor from MC type model becomes zero near the Coulomb state (Figure 3.10). On the contrary, based on the results of non-associative NS model, Andrade and Borja (2007) mentioned that their homogeneous undrained dense sand sample did not localise and continued to harden until the end of the simulation. Moreover, Larsson and Larsson (2000a,b) mentioned that, although the Rice criterion is met, a fully homogeneous material is unlikely to localise until the undrained localisation criterion is reached.

There is not enough evidence to evaluate the validity of bifurcation in the undrained dense sand. Most experimental findings exclude the possibility of localisation in the undrained dense sand unless cavitation takes place (Desrues and Mokni, 1998; Roger et al., 1997). Numerical and analytical predictions apparently depend on the type of constitutive model used.

Based on the results of this thesis, it is concluded that the instability in the undrained dilative sand cannot be taken into account by simply changing the flow rule. Localisation in the undrained dense sand is only possible through local drainage agreeing with mathematical findings of Guo (2013),Guo and Stolle (2013). Internal volume changes are likely to occur after the peak stress ratio preserving the globally isochoric constraint. This is not a material response which can be identified from conventional bifurcation analysis. The localisation associated with local drainage stems from the inherent heterogeneity of the soil. Single element simulations can only indicate the macroscopic homogeneous response of the material. Therefore, it is worthwhile to investigate internal volume changes of saturated dense sand

under globally undrained conditions, using a multi-element model. The volume is held constant in an average sense, allowing the release of local kinematic constraint.

3.5.3 Bifurcated points in globally undrained saturated dense sand

A displacement controlled, plane-strain biaxial compression finite element analysis is conducted with fully impermeable global boundaries. The specimen is 0.25 m wide and 0.50 m high. The element size is 0.0125 m. Saturated dense sand has the same material properties prescribed in Chapter 2 for associative NS model. The permeability $\bar{k}$ and bulk modulus K_f of pore fluid are specified as 0.001 m/s and 200 000 kPa respectively. A weak material point is included in the bottom right corner to trigger the localisation. The initial confining pressure is 100 kPa. A displacement of 0.1 m is applied to top nodes during 1 s. A transient consolidation analysis is carried out. A detailed numerical implementation of undrained biaxial compression tests will be described in Chapter 5. At each material point, both drained and undrained acoustic tensors are calculated according to Equations 3.8 and 3.13 respectively. They represent the loss of ellipticity of drained and undrained tangent operators locally. In the latter, the bulk compressibility of fluid plays a role, and it is valid only when there is no diffusion involved in considered material points.

Local response

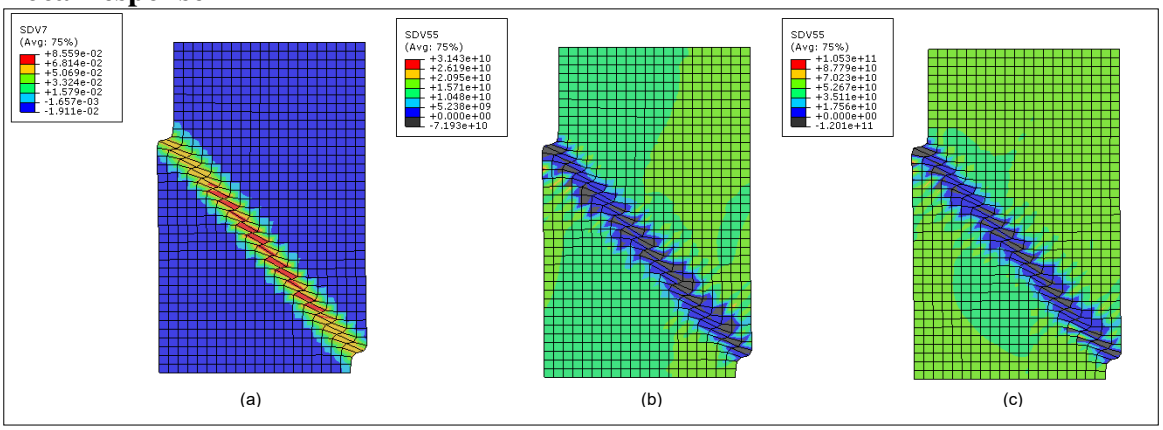

Fig. 3.12 Globally undrained biaxial compression test of saturated dense sand: Contours of (a) volumetric strain , (b) determinant of drained acoustic tensor and (c) determinant of undrained acoustic tensor at vertical displacement of 0.08 m

Figures 3.12, 3.13 and Table 3.3 demonstrate the multi-element biaxial compression results of the original NS model. Figure 3.12 (b) and (c) display the contours of locally drained and undrained acoustic tensors at displacement 0.08 m. The onset of localisation is represented by the loss of positive definiteness of the local acoustic tensor. In both Figures, negative magnitudes of acoustic tensors are indicated in black. It is evident that, by the displacement 0.08 m, most of the material points inside the shear band have passed the criterion for the

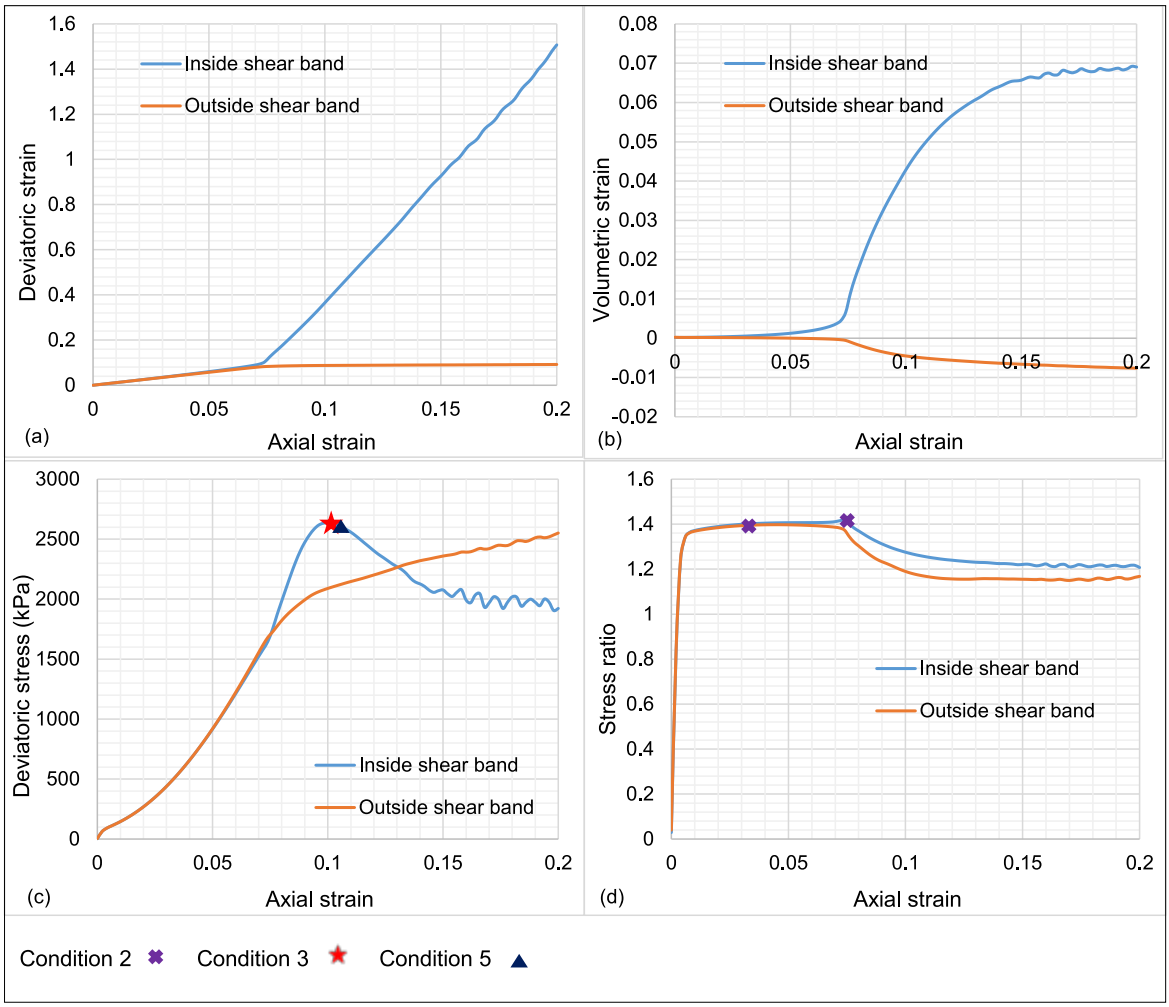

Fig. 3.13 The local response of material points both inside and outside the shear band: (a) deviatoric strain, (b) volumetric strain, (c) deviatoric stress and (d) stress ratio vs axial strain ($p'_0 = 100$kPa)

drained localisation. Out of them, some have even satisfied the criterion for the undrained localisation. It should be reminded that neither conditions were met during the deformation of an undrained single element. Therefore, the local volume changes shown in Figure 3.12 (a) are the triggering mechanism for this observed localisation, irrespective of globally undrained condition.

For further illustration, the local stress-strain responses of selected material points inside and outside the shear band are depicted in Figure 3.13. Table 3.3 encapsulates the axial strains at which two material points meet different bifurcation conditions. It appears that the shear band point meets the Coulomb condition initially. It was shown in the single element simulations that Coulomb and Tresca states occur concurrently if the material is fully drained,

for associative NS mode. Here, these two conditions detach due to the partial drainage at the considered point.

It is also observed in Figure 3.13 (b) that local volume changes in the shear band material point initiate near the Coulomb state of the outside material point. It happens even before the start of the shear strain concentration in Figure 3.13 (a). This is because internal volume change is progressive in nature and influenced by the behaviour of the neighbourhood. The local volume changes begin at an early stage of deformation in weak material points and propagate within the shear band. Nevertheless, the shear band behaviour deviates from the outside after reaching its Coulomb state. The drained localisation condition is satisfied even after that. The undrained localisation which depends on the compressibility of pore fluid follows the drained localisation.

The material outside the band contracts slightly, preserving the global isochoric constraint. Hence both drained or undrained acoustic tensors are always positive. It can be deduced that the satisfaction of instability criteria depends on the local boundary conditions. For dense sand, the localisation criterion is satisfied only if the local isochoric constraint is relaxed.

Table 3.3 Axial strains at which different bifurcation criteria are met by individual points

	Condition 1	Condition 2	Condition 3	Condition 4	Condition 5
shear band material point	0.1	0.074	0.1	0.1	0.106
outside material point		0.044			

Global response

Figure 3.14 illustrates the global axial stress-strain relationships of globally undrained multi-element biaxial compression tests. Along with the original NS model, results of modified NS models are also included for comparison. The drained or undrained localisation is defined as the first time respective acoustic tensors vanish at any gauss point in the sample. Bifurcation criteria for different constitutive models are given in Table 3.4.

The sample dilatively hardens almost homogeneously until any gauss point reaches the Coulomb state locally. This condition initiates the internal volume change which is also fuelled by the material heterogeneity (weak points). The Coulomb state is then followed by the fulfilment of drained localisation criterion locally. The red star indicates the position when the drained acoustic tensor at any gauss point becomes singular for the first time. A clear change in the global stiffness is observed only after the drained localisation is signalled. Although there is no softening effect in the global response, Figure 3.13(c) indicates local

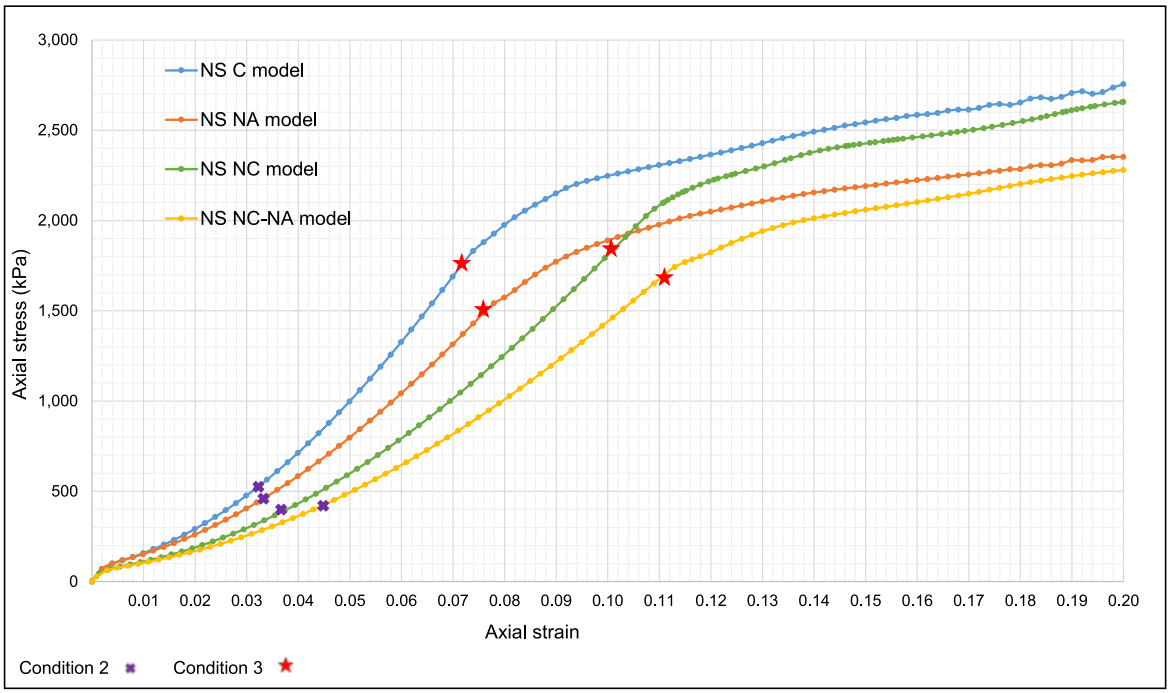

Fig. 3.14 Force-displacement relationships of globally undrained biaxial compression tests of dense sand

Table 3.4 Axial strains at which different bifurcation criteria are first time met in multi-element tests

material model	Condition 1	Condition 2	Condition 3	Condition 4	Condition 5
C	0.072	0.032	0.072	0.072	0.076
NC	0.105	0.0374	0.105	0.105	0.107
C-NA	0.076	0.033	0.076	0.076	0.08
NC-NA	0.111	0.045	0.111	0.111	0.12

softening. It is responsible for the reduction in overall stiffness. For dense sand, always drained localisation precedes undrained one. Both non-associative and non-coaxial flow rules delay the onset of bifurcation for multi-element undrained biaxial tests. This is because they retard the rate of volume change as discussed in Chapter 2. Thus, they delay the local drainage associated with the local volume change.

The global response in Figure 3.14 is totally different from the single element behaviour of the undrained dense sand. Furthermore, Figure 3.13 clearly illustrates two distinct kinematic constraints (hence material behaviours) inside and outside the shear band. Thus, it can be concluded that, unlike fully drained material, even the onset of localisation in undrained dilative sand cannot be captured by the pre-localised constitutive relation. Both onset and

propagation of shear band in globally undrained sample rely on the local volume changes and associated drainage, which occur at micro-scale. As for continuum numerical tests, this micro-scale is represented by the element size. These micro-kinematics are overlooked by macroscopic constitutive relationships regardless of the flow rule adopted. It leads to a prediction of unrealistically high dilative hardening in saturated undrained dense sand.

3.6 Conclusions

This chapter outlines the theoretical foundation for the onset of localisation in fluid saturated soil along with an appraisal of experimental and numerical insights. The existing literature is not conclusive regarding the formation of shear bands in the undrained dilative sand. Although different theories have been presented, they are not firmly validated by enough experimental evidence. The numerical predictions are apparently subjective of the constitutive model utilised.

This study concludes that under strict isochoric constraint, the Rice criterion (singularity of drained acoustic tensor) is never met by the NS model. Neither non-associative nor non-coaxial flow rules brings destabilising effects on the dilative hardening materials until the critical state is reached. This observation is subjective of the type of the constitutive model, and its definition of the hardening rule. The only mechanism which triggers shear bands in the globally undrained sand is the local drainage and associated volume changes. It is a result of heterogeneity within the soil sample and hence cannot be detected by constitutive relationship. Alternatively, if the suction is high enough, the desaturation can lift the isochoric constraint, and shear band may occur after the cavitation.

3.6.1 Contribution

The main contribution of this chapter is the qualitative comparison of different flow rules of their ability to detect instabilities in drained and undrained dilative sand. Limitations of conventional bifurcation analysis to detect instabilities in dilative hardening materials are recognised. The distinction between local vs global drainage and its influence on localisation are identified. The drained bifurcation criterion is met only by material points inside the locally drained shear bands. The non-coaxial flow rule delays the local volume change and hence the onset of localisation. The principal axis rotation commences even before the full mobilisation of the shear band. Therefore, even during a proportional loading path, the non-coaxial effect softens the global stress-strain response.

Chapter 4

Nonlocal Regularisation of Drained Dense Sand

4.1 Preface

In the event of shear localisation, the deformation is no longer uniform, and microstructural length scale comes into play, invalidating the continuum assumption of the finite element method. In this case, an individual material point can experience a larger strain than the neighbourhood resulting in a higher displacement gradient. In strain softening materials this leads to a significant reduction in strength of that point only. Hence, governing partial differential equations change from elliptic to hyperbolic (for static problems) resulting in mathematically ill-posed boundary value problems. The focus of this chapter is to investigate the mesh dependence and related complexities of post-localised deformation of drained dense sand. A regularisation technique to circumvent the problem is scrutinised.

Section 4.2 delineates the post-localised mesh dependence of FEM and popular regularisation techniques. Sections 4.3 to 4.5 describe previous studies on the nonlocal method. The implementation of nonlocal NS model is outlined in section 4.6. The procedure for numerical simulation of biaxial compression tests is described in section 4.7. The results of local and nonlocal NS models are given in section 4.8. Chapter 4 concludes by discussing the limitations of the nonlocal theory in section 4.9.

4.2 Mesh Sensitivity of Post-localised Deformation

Finite element modelling of strain localisation frequently suffers from pathological mesh dependence and numerical errors from lack of convergence. Solutions are sensitive to the

spatial discretisation such as alignment and size of mesh. In typical FE analysis, displacements are calculated at nodes. Thus their relative locations govern the shear band thickness and its direction.

The conventional continuum approach is adequate if the characteristic wavelength of the deformation field remains above the resolution level of the material model which corresponds to the element size. In granular materials, the thickness of localisation is experimentally proved to be the size of several particle diameters. It serves as a measure of the physical thickness or resolution the soil is represented. However, available limited computational resources forbid to refine the mesh to match the physical characteristic length of the shear band. Hence, the characteristic wavelength of the field is below the resolution level of the model. Therefore, the post-bifurcation response of finite element continuum is inherently mesh dependent (Bazant and Jirasek, 2002).

Further, the continuous mesh refinement leads to shrinking of the numerical shear band thickness unlimitedly. It will result in either predicting an ambiguous response or non-convergence after the peak. Therefore, the accuracy of post-failure deformation is doubtful, even when the finite element mesh can resolve to the real shear band thickness (Borja and Regueiro, 2001). Hence, it is necessary to opt for an adequate macroscopic description which captures the underlying microscopic deterioration of soil. Enrichment techniques are used to regularise the mesh dependence of finite element method by introducing a characteristic length which is related to physical shear band thickness. The objectivity is achieved by bridging the gap between microstructure and the continuum. Techniques used for the post-bifurcation analysis in past few decades fall into several categories. Depending on the method, the internal length scale is embedded either in the constitutive model itself (nonlocal, viscous plasticity) or equilibrium equations (Cosserat theories, micro-polar theories). Gradient theory can fall into both categories.

- Visco-plastic or rate-dependent models

  Oka (1985), Oka et al. (1995, 2002) explored rate-dependent behaviour of soil for both static and dynamic analysis. It implicitly introduces a length scale into finite element formulations. Although this method restores the well-posedness in dynamic problems, for pure static problems, viscous regularisation is not effective (Brinkgreve, 1994).

- Nonlocal models

  Nonlocal theories are based on spatial averaging of stress and/or strain within a representative volume of the material (Bazant and Lin, 1988; Eringen and Edelen, 1972; Eringen, 1981, 1983). It is grounded on the hypothesis that the material response

should depend on the deformation field of not only a solitary material point but also of the neighbourhood of that point. Bazant and Jirasek (2002) mentioned that growth of a crack is decided by the release of energy from the surrounding volume.

- Cosserat continuum theories

  An additional degree of freedom (rotational) is utilised to describe the micro-deformation at the particle level in addition to displacement fields which governs the macro-deformation at the structural level (Vardoulakis, 1989; Vardoulakis and Sulem, 1995).

- Strain gradient theories

  These models consist of higher order gradient terms (Laplacian) in governing equations. These terms integrate a length scale and regularise the strain softening. These type of models also belong to the family of nonlocal theory (Aifantis, 1984; Chambon et al., 2001; Collin et al., 2010; Zervos and Papanastasiou, 2010; Zervos et al., 2001).

All the above methods assume a weak discontinuity approach with the hypothesis that the localised zone has a finite thickness. Hence, the shear band contains one or more elements. This is more suitable for softening of dilatant granular materials such as dense sand. On the contrary, strong discontinuity method was used by Borja and Regueiro (2001) to regularise localisation in clay.

From potential regularisation techniques used for post-bifurcation analysis, nonlocal methods can be directly implemented in commercial finite element codes. This is because they can be applied at the constitutive level without altering equilibrium equations. Therefore, in this study, the nonlocal method is implemented in ABAQUS user-defined material model to examine the localisation in dense sand.

4.3 Nonlocal Models of Integral Type

Local continuum theories are grounded on the assumption that the mechanical response of a material point is dictated by the deformation field of a solitary point. These theories are sufficient to predict macroscopic stress-strain fields of numerous engineering applications. However, deformation of a shear band is not characterised by the location of highest strain but by the energy released from the surrounding volume (Bazant and Jirasek, 2002; Summersgill et al., 2017a). With this school of thought, the nonlocal approach assumes that micro-kinematics of a singular point influence surrounding points as well. In essence, a constitutive law of a single point in an integral type nonlocal model involves the weighted average of variables over a certain neighbourhood of that point. Gradient theories also in principle fall

into the family of nonlocal theory. The presence of a characteristic length in the constitutive law is an important feature of this kind of models (Bazant and Jirasek, 2002).

4.3.1 Evolution of nonlocal theory

The concept of the nonlocal continuum was proposed for elasticity by Eringen (1966),Eringen and Edelen (1972). The original philosophy was introducing the nonlocal character to many fields such as stress, mass, body forces and energy which was later termed as the fully nonlocal theory. They were too complicated to be implemented in finite element formulations (Bazant and Jirasek, 2002). Later Eringen and Kim (1974) simplified the theory considering only the constitutive relationship as nonlocal while equilibrium equations remain unaltered. Stress at a point is considered as a function of mean strain averaging over a representative volume centred at that point. Figure 4.1 displays that macro strain at the centre differs from average micro strains over the representative volume. The average stress and strain are defined respectively by Equation 4.1 and 4.2. Bar notation denotes the average. i, j notations are excluded here for simplicity.

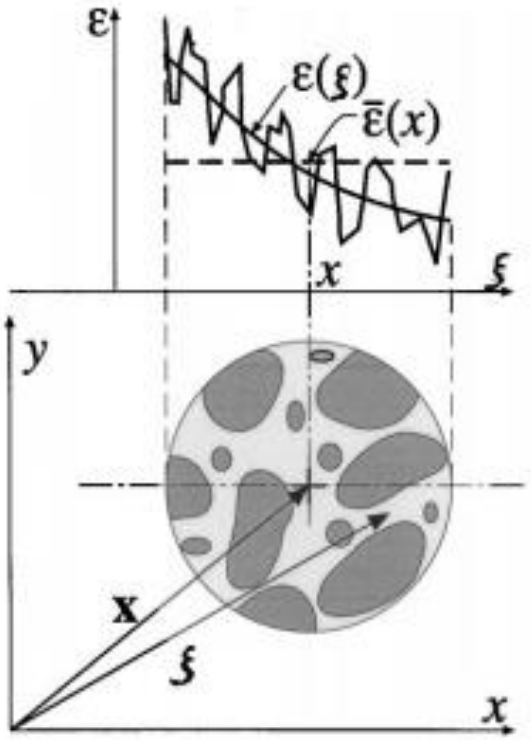

Fig. 4.1 Philosophy behind the nonlocal theory, bottom- representative volume used for strain averaging , top- scatter of micro, macro and average strain profiles (Bazant and Jirasek, 2002)

$$\overline{\sigma}(x) = \frac{1}{\upsilon}\int_{\upsilon} w(x,\xi)\sigma(\xi)d\xi \tag{4.1}$$

$$\overline{\varepsilon}(x) = \frac{1}{\upsilon}\int_{\upsilon} w(x,\xi)\varepsilon(\xi)d\xi \tag{4.2}$$

$$\upsilon = \int_{\upsilon} w(x,\xi)d\xi \quad \text{is the representative volume.} \tag{4.3}$$

x and ξ are the global and local coordinates respectively as shown in Figure 4.1. w is the weight function which is chosen such that nonlocal contribution fades away with the distance. The weight function depends on the distance between the kernel x and neighbouring points ξ. Its integral over the entire volume should be unity. Generally, nonlocal weight function takes the form of Gaussian distribution or polynomial bell-shaped function as shown in Figure 4.2. The standard deviation of this function serves as the internal length l_c.

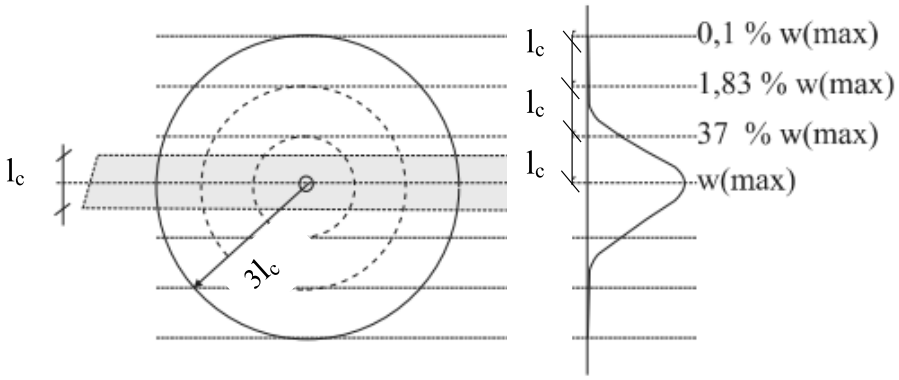

Fig. 4.2 Bell-shaped weight function and zone of averaging (Vermeer and Marcher, 2000)

The ground of nonlocal constitutive relationship can be illustrated with a simple elastic law as follows.

$$\overline{\sigma}(x) = \frac{1}{\upsilon}\int_{\upsilon} w(x,\xi)D^e(x,\xi)\varepsilon(\xi)d\xi \tag{4.4}$$

where $D^e(x,\xi)$ is the generalised form of elastic stiffness. For a constant elastic stiffness D^e, Equation 4.4 can be rewritten establishing a relationship between nonlocal stress and strain.

$$\overline{\sigma}(x) = D^e\frac{1}{\upsilon}\int_{\upsilon} w(x,\xi)\varepsilon(\xi)d\xi = D^e\overline{\varepsilon}(x) \tag{4.5}$$

The nonlocal theory was extended to plasticity by Eringen (1981, 1983) which was limited to perfect plasticity and hardening models. Later Bazant and Chang (1984),Bazant and Lin (1988) applied nonlocal averaging concepts for strain softening damage models to prevent spurious mesh dependence. However, the selected nonlocal plastic variable evolved over the years. The first candidate was nonlocal plastic stress, but it demonstrated spurious mesh distortions. Next, the cumulative plastic strain which controls the strain softening was subjected to the nonlocal treatment (Bazant and Lin, 1988).

$$\overline{\sigma}(x) = D^e(\varepsilon - \overline{\varepsilon^p}) \tag{4.6}$$

$$\overline{\varepsilon}^p(x) = \frac{1}{\upsilon}\int_{\upsilon} w(x,\xi)\varepsilon^p(\xi)d\xi \tag{4.7}$$

To overcome numerical difficulties associated with above approaches, nonlocal damage theories were later developed such that nonlocal averaging was applied only to scalar damage variable (Bazant and Pijaudier, 1988; Chow et al., 2011; Duddu and Waisman, 2013; Planas et al., 1996). The most recent adoption to the nonlocal softening plasticity is to treat only the scalar softening variable - κ as nonlocal. This method exhibits to be computationally efficient (Bazant and Jirasek, 2002). This kind of approach is termed as the partial nonlocal theory.

$$h = h_0 + h(\overline{\kappa}) \tag{4.8}$$

$$\overline{\kappa}(x) = \frac{1}{\upsilon}\int_{\upsilon} w(x,\xi)\kappa(\xi)d\xi \tag{4.9}$$

This was later adopted for soil plasticity to simulate the shear localisation. The softening parameter which drives the yield stress degradation was treated nonlocal. The selected nonlocal variable varied with the adopted constitutive model (Brinkgreve, 1994; Summersgill et al., 2017a, 2014, 2017b; Vermeer and Marcher, 2000). However, as mentioned by Brinkgreve (1994), an accurate determination of the plastic multiplier from this kind of model results in integro-differential equations which demand complex numerical procedure. Hence, this method requires some simplifications for computational efficiency.

4.3.2 Influence of weight functions

The most commonly used weight function in the nonlocal theory is the Gaussian distribution which has a maximum at the centre. In two dimensional cases, Gauss function is written as Equation 4.10 and plotted in Figure 4.3. It gives the greatest contribution of the averaging variable at the centre. This ultimately leads to a central concentration of the softening variable. Hence the mesh dependence is not eliminated albeit reduced (Brinkgreve, 1994; Galavi and Schweiger, 2010; Summersgill et al., 2017a, 2014, 2017b). Several attempts have been made to address this issue by altering the weight function or the averaging procedure itself.

$$w(x,\xi) = \frac{1}{\sqrt{\pi}\, l_c}\, exp\left[-\frac{(x-\xi)^2}{l_c^2}\right] \tag{4.10}$$

Based on the hypothesis that the deformation at a point is more influenced by response in the neighbourhood rather than the concentrated deformation at the point itself, Galavi and Schweiger (2010) introduced the GandS weight function in Equation 4.11. As shown in Figure 4.3, the contribution of the softening variable at the considered point is zero. This

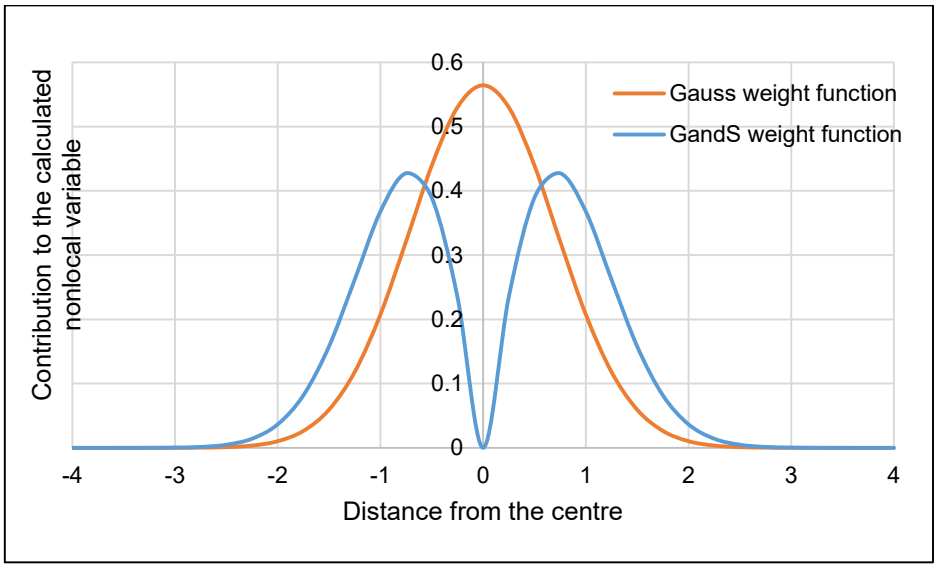

Fig. 4.3 Weight distribution functions for $l_c = 1$

function has two peaks such that the maximum is from either side of the central point. The contribution from both functions diminishes over three times the characteristic length from the centre.

$$w(x,\xi) = \frac{(x-\xi)}{l_c}\, exp\left[-\frac{(x-\xi)^2}{l_c^2}\right] \tag{4.11}$$

Over-nonlocal method introduced by Brinkgreve (1994) alters the nonlocal averaging formulation to circumvent the concentrated peak at the centre. This smears the averaging variable in the neighbourhood without changing the weight function. Equation 4.12 introduces a new parameter m which provides the percentage of contribution from local and nonlocal parts. m should be over unity for the localised zone to have a finite width. Compared to Gaussian distribution, modified functions distribute the averaging variable over the area adjacent to the central zone and reduce the local concentration.

$$\overline{\kappa}(x) = (1-m)\ \kappa(x) + m \int_v w(x,\xi)\kappa(\xi)d\xi \tag{4.12}$$

4.4 Numerical Results of Biaxial Compression Analysis with Nonlocal Theory

This section details the results of biaxial compression tests modelled with nonlocal elasto-plastic constitutive models. Vermeer and Marcher (2000) utilised the DP model with friction softening to simulate dry dense sand. The total volumetric strain was taken as the nonlocal softening parameter. The original nonlocal method was adopted with a Gaussian weight

function. As shown in Figure 4.4 nonlocal DP model rendered mesh-independent results compared to its local counterpart.

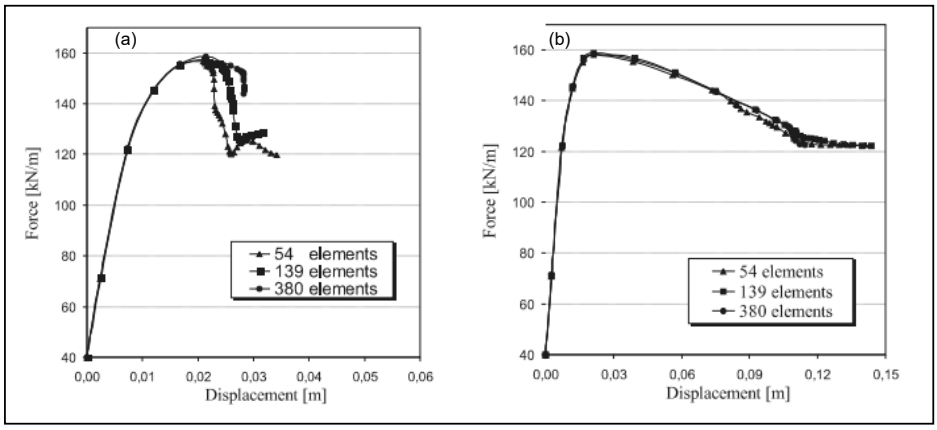

Fig. 4.4 Force-displacement curves of (a) local and (b) nonlocal Drucker-Prager models (Vermeer and Marcher, 2000)

Brinkgreve (1994) used the DP model with cohesion softening to simulate biaxial compression tests of drained clay samples. The total volumetric strain was chosen as the softening variable and was averaged using the over-nonlocal formulation. With an appropriate value of over-nonlocal variable Brinkgreve (1994) obtained mesh objective force-displacement curves and shear band thickness. Brinkgreve (1994) recommended the over-nonlocal parameter to be 2. The use of total strain instead of plastic strain proved to be computationally efficient.

Galavi and Schweiger (2010) adopted nonlocal formulations with GandS weight function in their multilaminate model. The nonlocal softening was applied to damage strain which is a function of both plastic volumetric and deviatoric strains. Figure 4.5 illustrates force-displacement curves and shear strain contours for friction softening. Although the mesh dependence is fairly diminished, there is a slight disagreement in curves near the residual state. Galavi and Schweiger (2010) attributed this to the reduction in dilation near the residual state.

Summersgill et al. (2014) compared the original nonlocal method with two weight functions and over-nonlocal method, for undrained biaxial compression tests with Tresca yield criterion. When the Gauss distribution was incorporated, the full objectivity could not be obtained. The over-nonlocal and GandS methods proved to be more efficient as displayed in Figure 4.6. Summersgill et al. (2017a) extended the biaxial compression simulations for drained analysis with Mohr-Coulomb yield surface. The nonlocal softening variable was chosen as plastic deviatoric strain. It can be observed from Figure 4.7 that the nonlocal method reduces the mesh dependence of drained analysis even though not very satisfactory as undrained analysis. This was attributed to different patterns of slip surfaces formed. Sum-

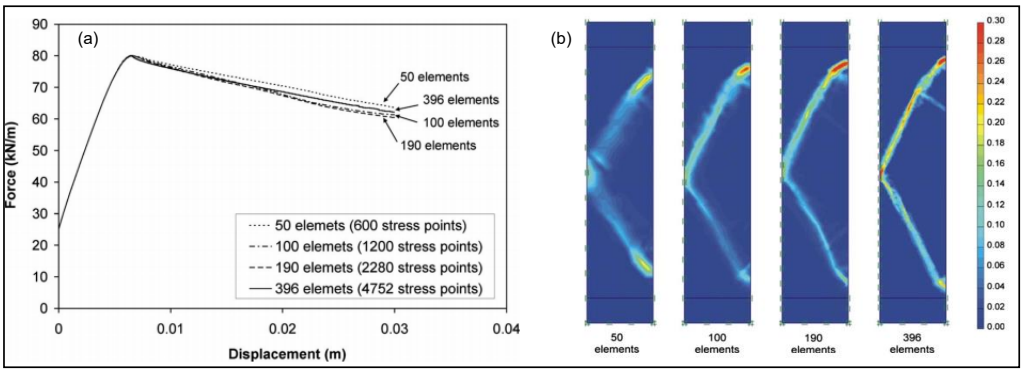

Fig. 4.5 Results of nonlocal multilaminate model with friction softening (a) force-displacement curves and (b) contours of shear strain (Galavi and Schweiger, 2010)

mersgill et al. (2017a) concluded that the GandS method shows the least mesh dependence for both drained and undrained simulations.

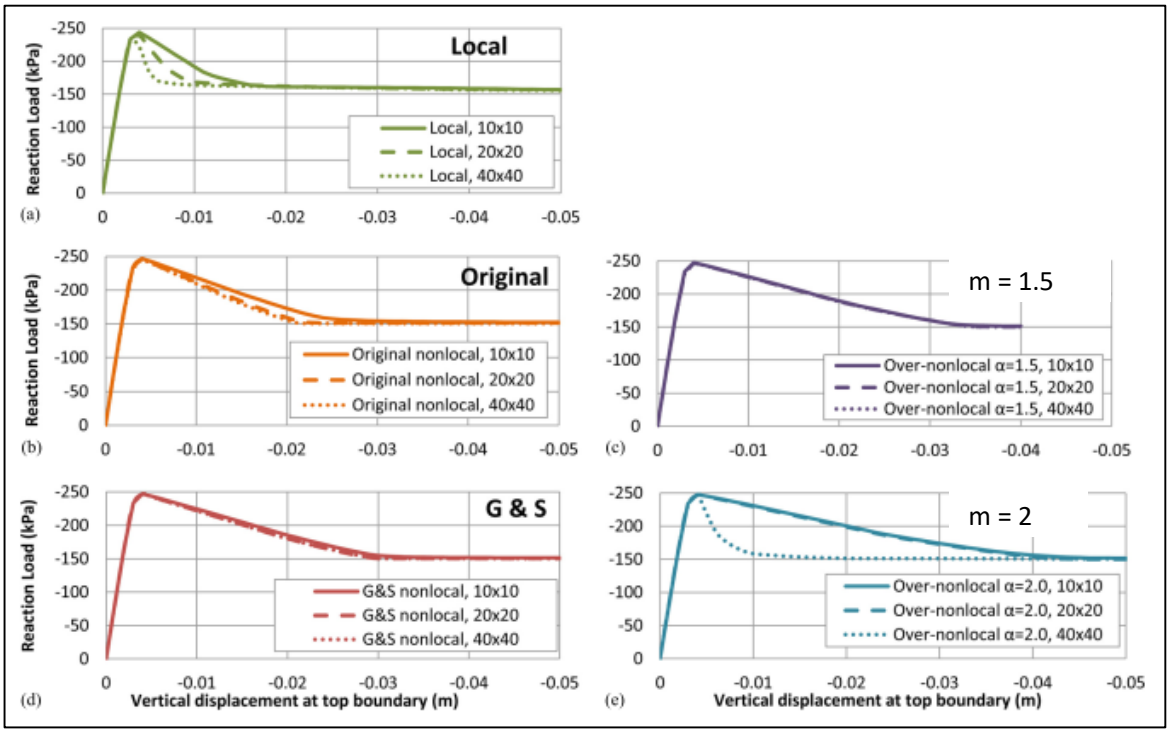

Fig. 4.6 Local and nonlocal load-displacement curves for undrained analysis (Summersgill et al., 2014)

4.5 Softening Scaling

Above biaxial compression results illustrate the validity of the nonlocal method as a regularisation technique. It is capable of producing results objective of the spatial discretisation. Both shear band thickness, as well as the force-displacement curves, are independent of the mesh size. However, for geoengineering applications, the width of a shear band is minimal

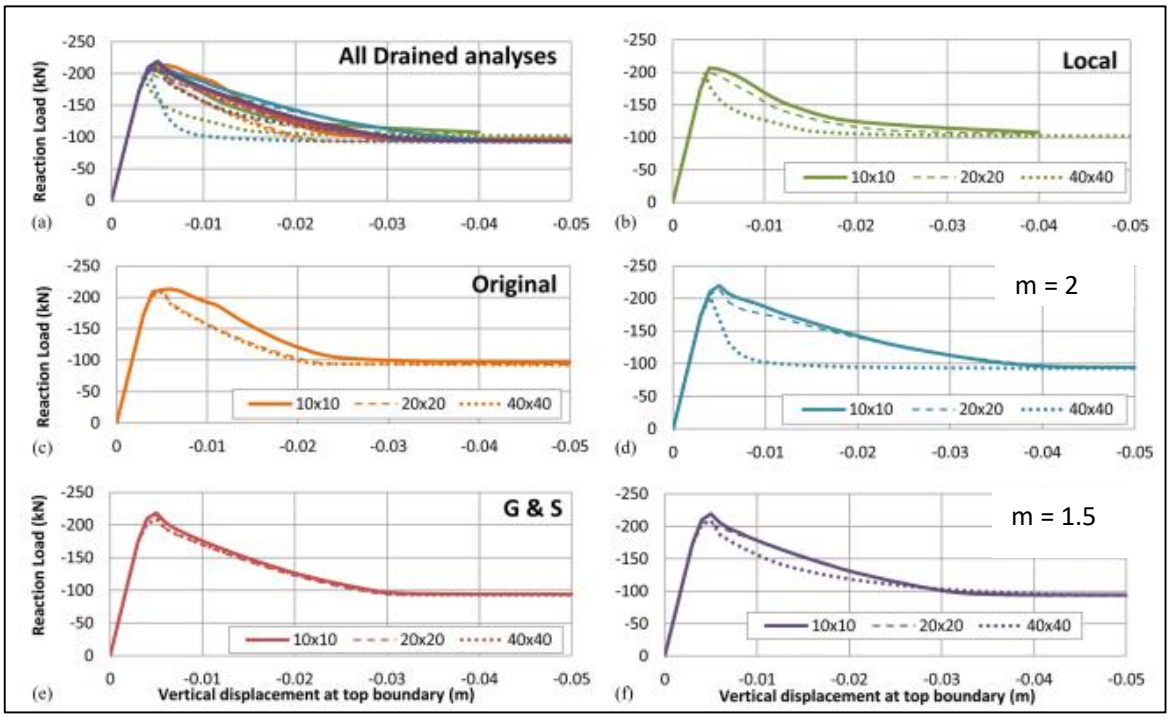

Fig. 4.7 Local and nonlocal load-displacement curves for drained analysis (Summersgill et al., 2017a)

compared to the dimension of geometry. Practical mesh size utilised in simulations are several orders of magnitude larger than the physical shear band thickness.

Pietruszczak and Mroz (1981) used a simple strategy to circumvent the mesh dependence of post-bifurcation analysis without sophisticated regularisation. They embedded a scaling factor (ratio of element size to physical shear band thickness) within the constitutive model itself to produce reasonably objective load-displacement curves. Although this appears to be the most versatile solution, the boundary value problem is still ill-posed, and numerical convergence issues may arise.

Therefore, Brinkgreve (1994) proposed to employ the softening scaling along with the nonlocal regularisation. Here, the intrinsic material length (physical shear band thickness) is correlated to the numerical band thickness resulting from the nonlocal averaging. The scaling factor is defined as the ratio between the numerical shear band thickness $t^{sb,num}$ to physical band thickness $t^{sb,sand}$. The rate of softening is dependent on the softening modulus and shear band thickness. The physical softening stiffness $\bar{h}^{sand}$ multiplied by this scaling factor bestows a realistic post-peak softening in the load-displacement response.

$$\bar{h}^{num} = \bar{h}^{sand} \frac{t^{sb,num}}{t^{sb,sand}} \tag{4.13}$$

The numerical shear band thickness is governed by mesh properties such as size, shape, and number of integration points in local methods and characteristic length (and over-nonlocal parameter) in nonlocal methods. Empirical correlations are found between numerical band thickness and the characteristic length (Brinkgreve, 1994; Galavi and Schweiger, 2010; Vermeer and Marcher, 2000). However, they are not universal and depend on mesh properties. The physical shear band thickness is found to be $10-20D_{50}$ (Muhlhaus and Vardoulakis, 1987). This is ascertained by Figure 4.8 which encapsulates experimental shear band thickness for different sand types. Brinkgreve (1994),Vermeer and Marcher (2000) and Galavi and Schweiger (2010) combined nonlocal regularisation with softening scaling to obtain physically realistic force-displacement curves.

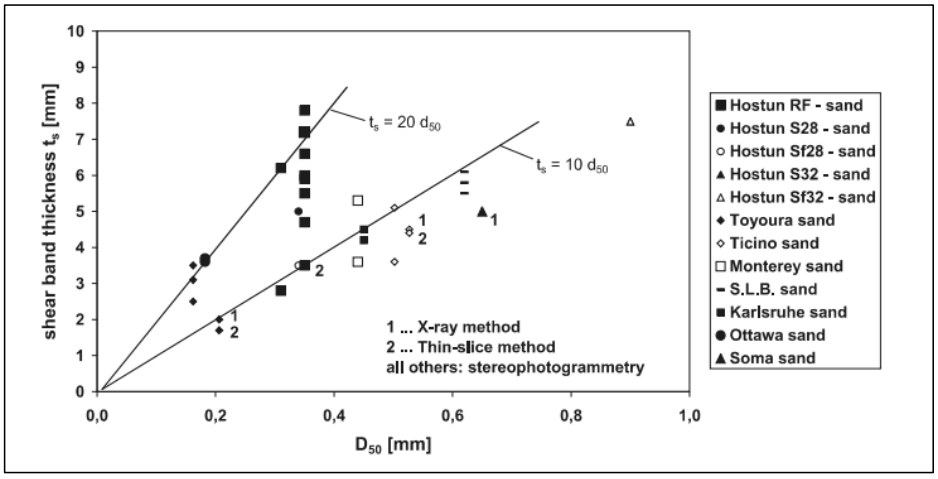

Fig. 4.8 Physical shear band thickness as a function of mean grain size for different sand types (Vermeer and Marcher, 2000)

4.6 Implementation of Nonlocal Nor-Sand model

The nonlocal theory has been so far applied to simple elasto-plastic models such as DP, MC and Von-Mises. They adopt linear softening rules to predict the degradation of strength (friction, cohesion) from the peak to residual assuming a constant dilation. In reality, the softening of dilative shear bands is governed by the coupling between volumetric and shear deformation. Only Galavi and Schweiger (2010) used a function for the decreasing dilation, and they claimed nonlocal regularisation is not effective near the residual state when the dilation is zero. It is noted that the nonlocal theory has not been appraised previously for critical state models with a proper stress-dilatancy relationship.

To address this gap, the nonlocal concept is applied for the NS constitutive model. The most crucial decision in the development of the nonlocal NS model is identifying a suitable nonlocal parameter. Unlike the linear softening models, the parameter which drives the

hardening function in NS model is not lucid. In Equation 2.43, the hardening or softening in NS is driven by the plastic deviatoric strain. On the other hand, maximum dilatancy is dictated by the state parameter which is driven by the volumetric strain. While the spatial averaging of deviatoric plastic strain in the hardening rule did not show expected mesh independence, the use of the average void ratio rendered satisfactory results. Hence, it is deduced that the void ratio and thus the state parameter is the dominating hardening or softening variable in the NS model. This choice is backed by Vermeer and Marcher (2000)'s argument that the void ratio predominantly governs the friction softening in dense sand. Therefore, the update of the void ratio in the NS model is modified as

$$e = e + (1+e)\, d\varepsilon_{v,avg} \tag{4.14}$$

$$d\varepsilon_{v,avg} = \frac{\sum_{k=1}^{n} \upsilon_k w_k \, d\varepsilon_{v,k}}{\sum_{k=1}^{n} \upsilon_k w_k} \tag{4.15}$$

where n is the number of integration points and υ_k , w_k and $d\varepsilon_{v,k}$ are representative volume, weight function and volumetric strain increment of the integration point k.

The numerical implementation of nonlocal models in ABAQUS subroutine is adopted from Chow et al. (2011). Generally, UMAT is called by the main finite element programme at each gauss integration point (IP). It has only access to information at the current IP only. However, to implement the nonlocal theory, it is also necessary to access information from IPs in the neighbourhood of current IP. To overcome this hurdle, a common block which can store information about each IPs is introduced here. It is a three-dimensional array in which the first and second dimensions are element and integration point identifiers respectively. The third identifier can be chosen as IP coordinates and softening parameters. Information on the common block is updated after each time step. IP coordinates are used to calculate the relative distance to surrounding IPs.

It should be noted that this is a computationally expensive process. To increase the efficiency, the spatial averaging is limited to the radius of three times the characteristic length. Summersgill et al. (2017a) pointed out that the influence of IPs beyond this length is marginal. Going along the steps of Brinkgreve (1994), the elastic stiffness matrix is used to ascertain the convergence of equilibrium equations. The exact formulation of a nonlocal tangent matrix is cumbersome, and an approximation of a local tangent matrix might yield a softer structural response (Brinkgreve, 1994). In the vicinity of the boundary the nonlocal averaging is performed only in the domain of influence within the specimen. However, this assumption is not theoretically supported (Bazant and Jirasek, 2002).

4.7 Biaxial Compression Analysis of Drained (Dry) Sand

Numerical biaxial compression simulations are conducted to assess the validity of the nonlocal theory on NS model. The biaxial specimen is 0.25 m wide and 0.50 m high. The plane-strain condition assumed throughout. The bottom boundary conditions are such that the leftmost node is pinned and other nodes are roller supported. The top and side boundaries are not restrained. Some weak material points are included at the bottom right corner. It facilitates a formation of single shear band diagonally across the specimen. The area of weak region is maintained equal in all mesh sizes (0.025 m $\times$ 0.025 m).

During the first step, the specimen is consolidated homogeneously with a confining pressure of 100 kPa. During the second step, 0.1m vertical displacement is applied to the top nodes to allow an axial compression within 1s. This “time" does not relates to mass acceleration. Inertia effects and geometric non-linearity are neglected. Static general analysis is conducted with plane-strain quadratic isoparametric elements with reduced integrations (8 nodes and 4 integration points- CPE8R).

The analysis comprises a comparison of four meshes with different element sizes (h) which are shown in Figure 4.9. They are named as large (0.025m), medium (0.0125m), small (0.01m) and extra-small (0.00625m). The characteristic length for the nonlocal model is selected equal to the largest mesh size. Dense sand with an initial void ratio of 0.55 is used for all the analysis. Only the original NS model is utilised throughout this Chapter. Material parameters are the same as in Table 2.1.

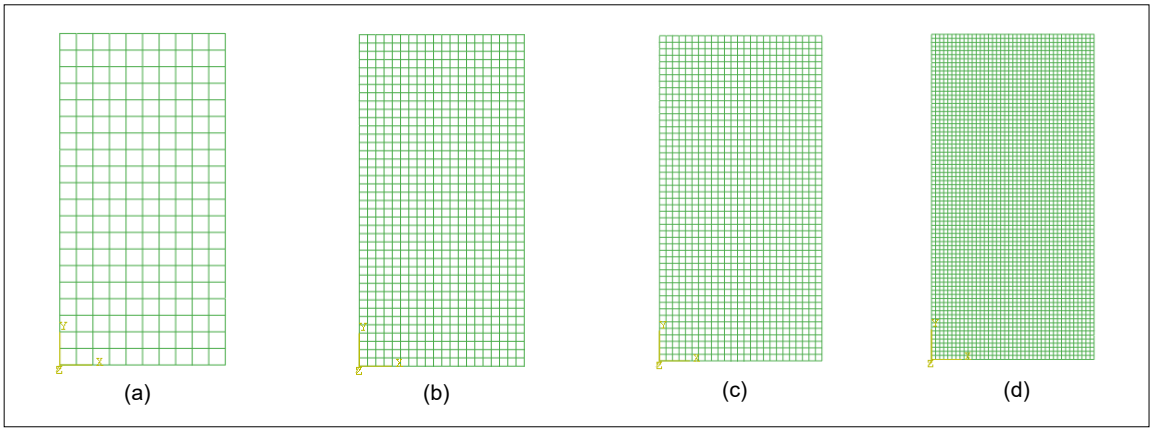

Fig. 4.9 Different mesh sizes used for biaxial compression tests: (a) large- 0.025m, (b) medium- 0.0125m, (c) small- 0.01m and (d) extra-small- 0.00625m

The variation of parameters across the shear band can be studied from cross-sectional profiles. For this purpose, two random cross-sections are chosen, starting from the coordinates $0.05, 0.05$ (Section 1) and $0.0, 0.15$ (Section 2) perpendicular to the shear band.

4.8 Results of Drained Analysis

4.8.1 Force-displacement relationships

The force-displacement relationships predicted by local NS model for drained dense sand are shown in Figure 4.10 (a). They are insensitive to the mesh size until the peak and become mesh dependent afterwards. Unlike MC type models, forces at the critical state are observed to be mesh dependent as well. The larger the mesh, the higher the critical state strength. The softening rate is enhanced when the mesh size is refined to the extent that the extra-small mesh fails to converge beyond the peak.

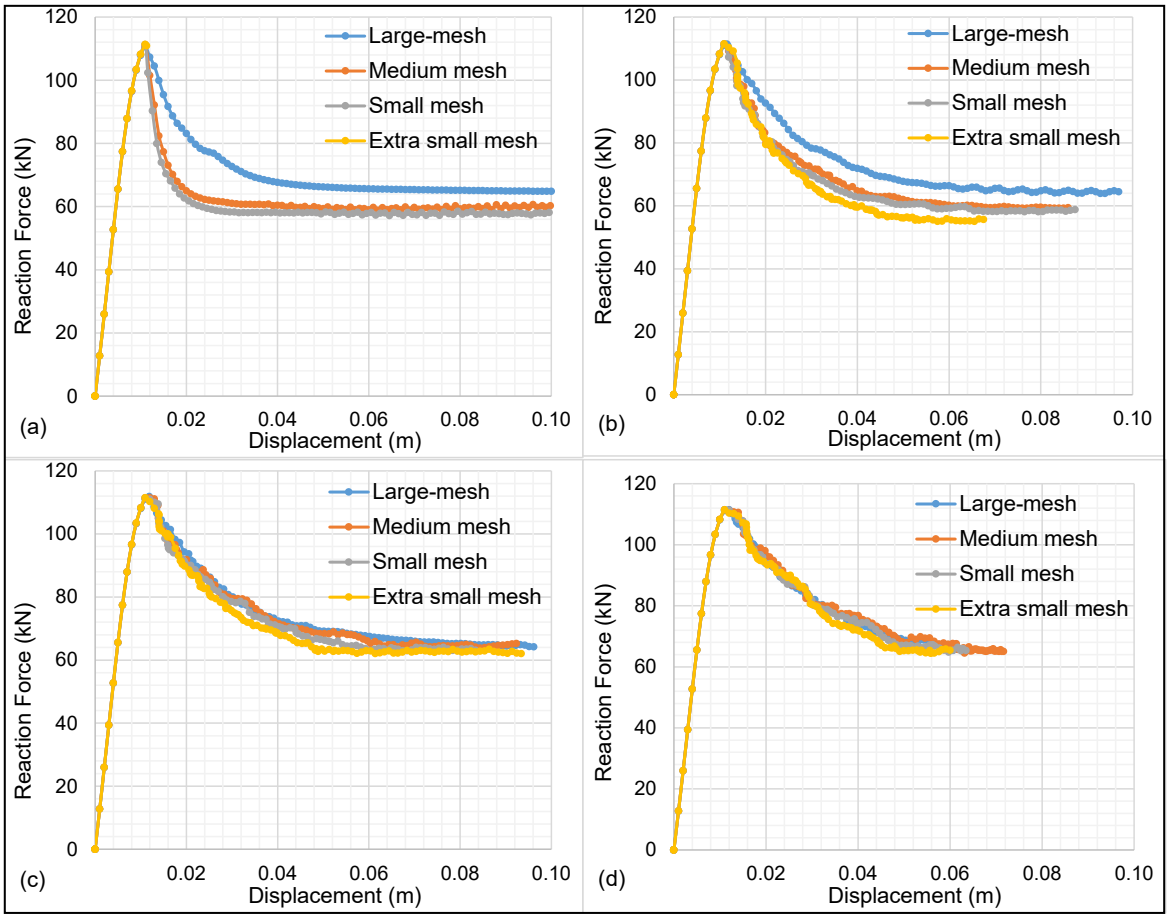

Fig. 4.10 Force-displacement relationships of drained analysis (width of specimen 0.25m): (a) local NS model and nonlocal NS models with (b) Gaussian function (c) GandS function, (d) over-nonlocal method with $m = 2$

The effectiveness of three nonlocal methods to regularise the post-localisation response of NS model is explored with the characteristic length of 0.025 m in Figures 4.10 (b),(c) and (d). It can be observed in Figure 4.10 (b) that, for the given characteristic length, the original nonlocal method with Gauss distribution function is not successful in fully regularising the

mesh dependence. Contrarily, both GandS and over-nonlocal methods sufficiently provide mesh independent force-displacement responses as shown in Figures 4.10 (c) and (d). Even the resulted critical state strengths are almost insensitive to the mesh size. In both methods, the softening rate is reduced, and the critical state is delayed. This facilitates the convergence of the extra-small mesh providing a positive-definite global stiffness matrix.

4.8.2 Comparison of different nonlocal methods

The state parameter governs the softening/hardening behaviour of the NS model. In the nonlocal implementation of NS model, the void ratio is regularised taking the weighted average of volume change. This leads to the homogenisation of the state parameter. The efficacy of smearing the state parameter by each method is explored in Figure 4.11 for large and small meshes. Albeit reduced, the original nonlocal method with Gaussian distribution still has a concentrated state parameter at the centre. So the force-displacement curves in Figure 4.10 (b) are still mesh dependent. Comparatively, GandS weight function sufficiently reduces the central peak. The over-nonlocal method smears the concentration over a larger distance showing the widest band thickness. Hence both methods are capable of eradicating the mesh dependence from the force-displacement curves.

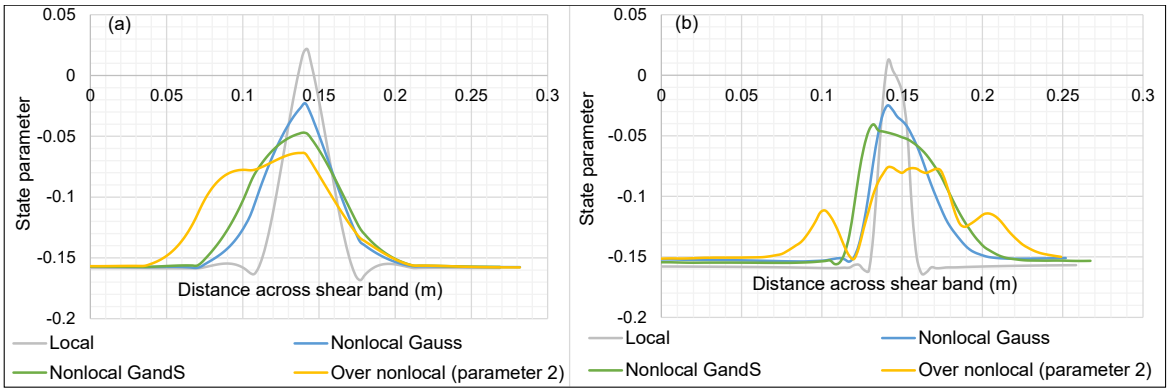

Fig. 4.11 State parameter profiles across cross-section 2 at displacement of 0.03m for (a) large mesh and (b) small mesh

Contour plots of accumulated deviatoric strain (at the displacement of 0.03 m) in large and small meshes obtained with different nonlocal methods are compared in Figure 4.12. It is observed that, for the same characteristic length, the thickness of the shear band is very close for Gauss and GandS weight functions. Contrarily, the shear band is much wider for the over-nonlocal method with parameter 2. The orientation of the shear bands are not altered considerably by GandS and Gauss nonlocal methods, but it is greater for the over-nonlocal method.

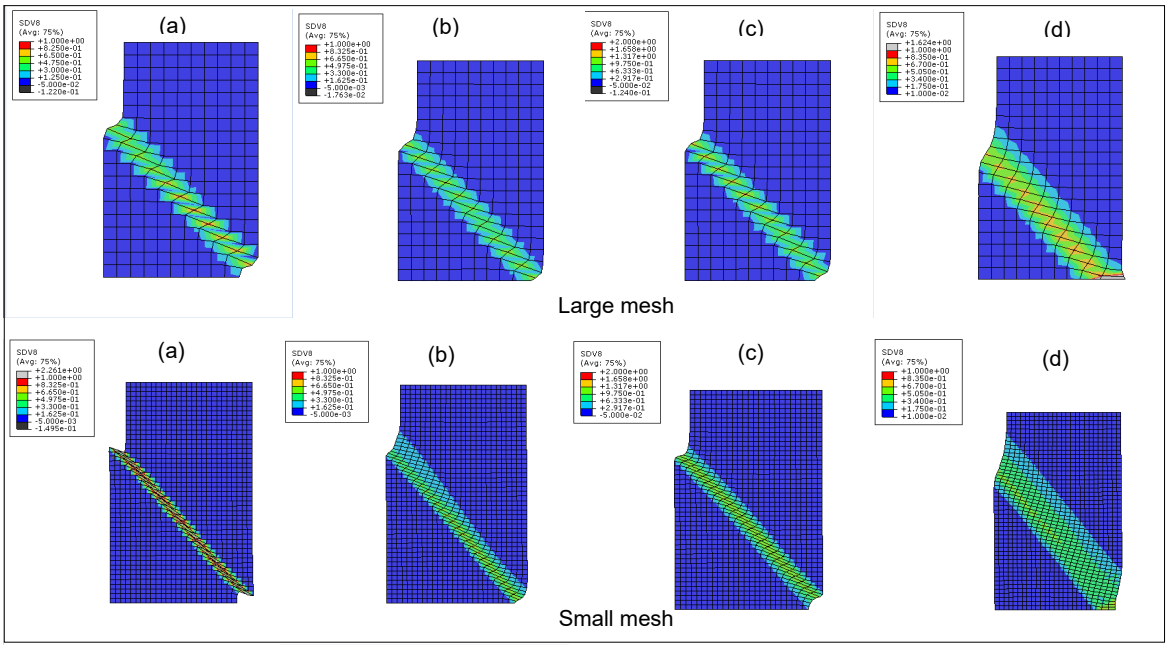

Fig. 4.12 Comparison of contour plots of deviatoric strain at displacement 0.03m for large mesh (upper row) and small mesh (lower row) from different methods: (a) local , (b) GandS function, (c) Gaussian function (d) over-nonlocal method

The performance of different nonlocal methods varies with mesh size, characteristic length, nonlocal parameter. These factors govern the concentration of the softening parameter, hence the numerical shear band thickness. For an effective regularisation, the characteristic length should be equal to or larger than the maximum mesh size such that sufficient gauss points lie within it.

The influence of the mesh size on the characteristic length ratio is mathematically represented in Figures 4.13 and 4.14. A unit step function is assumed as the initial local distribution of strain across the band. When the mesh size reduces, the width of the step function decreases displaying a higher gradient. If the same characteristic length is employed, the ratio of mesh size to characteristic length decreases in Figures 4.13 and 4.14 (a) to (d).

As observed in Figure 4.13 the regularisation by Gaussian distribution is not effective when the mesh size to characteristic length ratio is larger. GandS weight function bestows a wider distribution and a lower maximum. This is preferred over Gaussian weight function particularly for large mesh size to characteristic length ratios. However, it shows two peaks when the mesh size to characteristic length ratio is reduced than 0.5. This phenomenon can be misleading for very fine meshes. Because, after regularisation of a single shear band, two conjugate shear bands may result. Jostad and Grimstad (2011) discredited GandS weight distribution due to its irregular homogenisation. To obtain a smooth homogenised solution

with the GandS weight function, the characteristic length should not be larger than twice the mesh size.

Similarly, for the over-nonlocal method, three or two peaks are possible after the regularisation, depending on the mesh size to characteristic length ratio and over-nonlocal parameter. Larger the over-nonlocal parameter and smaller the mesh size to characteristic length ratio, irregularities are dominant as displayed in Figure 4.14. This is the reason behind the three peaks observed in the state parameter profile in Figure 4.11(b). Therefore, a comprehensive parametric study should be conducted to select the additional parameters used for the nonlocal analysis. Due to the complexity involved with the over-nonlocal parameter, results from GandS method will be used for further comparison between local and nonlocal NS models. Further, this method is computationally faster than other two methods since the strain at the considered stress point has no influence on the nonlocal strains calculated in the current calculation step.

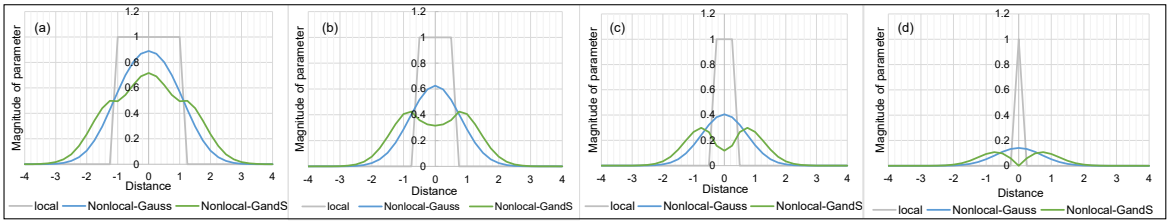

Fig. 4.13 Influence of weight functions for varying mesh size to characteristic length ratios: (a) 1 , (b) 0.5, (c) 0.25 and (d) 0.00001

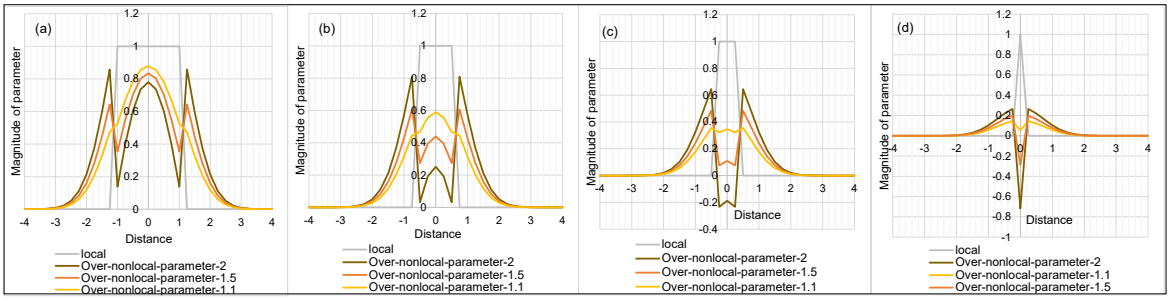

Fig. 4.14 Influence of over-nonlocal parameter for varying mesh size to characteristic length ratios: (a) 1 , (b) 0.5, (c) 0.25 and (d) 0.00001

4.8.3 Shear strain contours

Accumulated deviatoric strain contours at a softening stage and the critical state can be compared in Figures 4.15 and 4.16 for the local and nonlocal analysis respectively. The concentrated plastic deformation can distinguish the shear band from unloading areas. Figure 4.15 exhibits that shear zone width predicted by local NS model is sensitive to the mesh size at both stages. On the contrary, contour plots of accumulated deviatoric strain from GandS

nonlocal method in Figure 4.16 portray almost similar shear band widths irrespective of the mesh size during both softening and in the critical state.

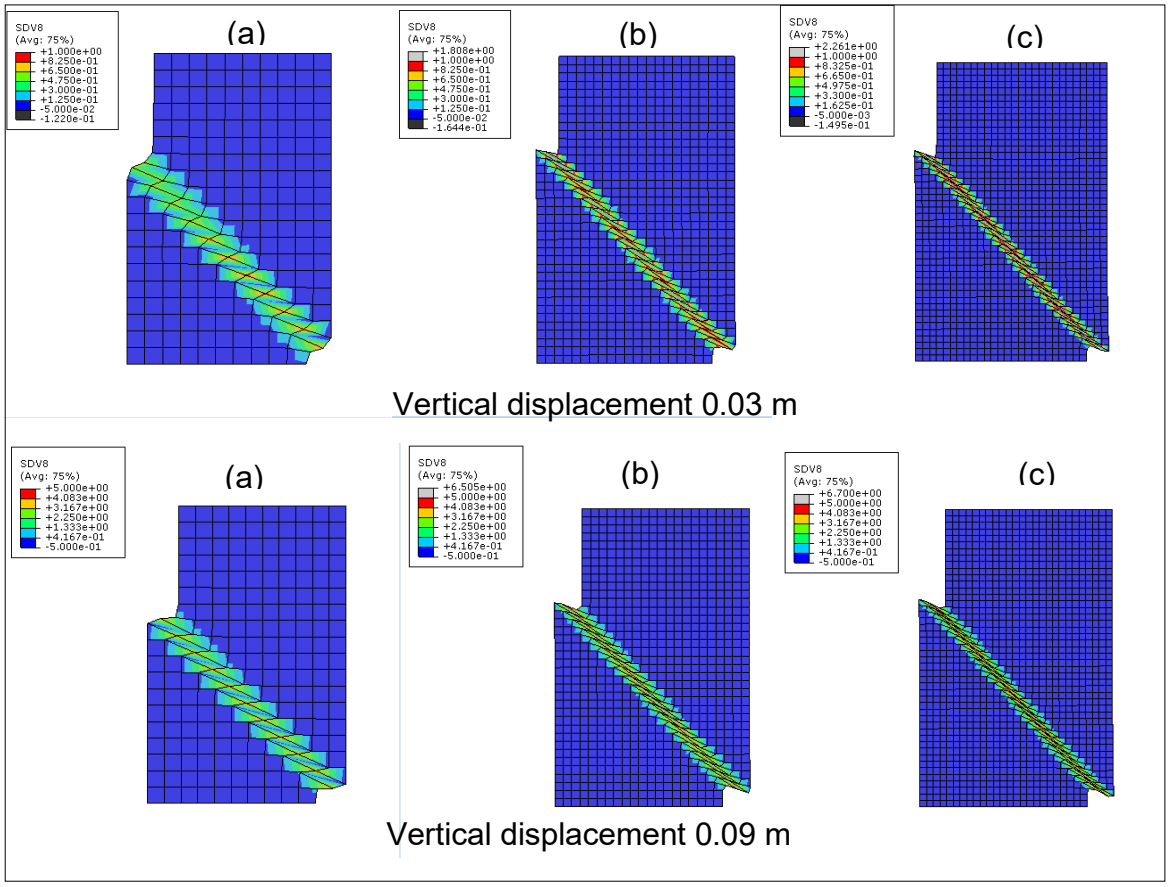

Fig. 4.15 Contours of accumulated deviatoric plastic strain from local NS model at two stages of deformation: (a) large,(b) medium (c) small meshes

4.8.4 Thickness of shear band

The width of the shear band can be found based on either change in displacement gradient or change in strain fields. Vermeer and Marcher (2000) and Galavi and Schweiger (2010) respectively used velocity and displacement profiles to estimate the shear zone. In Figures 4.18, 4.19 and 4.20, the evolution of the shear band thickness is elaborated with cross-sectional profiles of displacement, deviatoric strain and state parameter across the shear zone. Profiles of both local and nonlocal methods are displayed across the cross-section 2. Four stages of deformation are portrayed to get an insight into the growth of the band. A clear distinction can be seen between pre-peak homogeneous deformation vs post-localised deformation. Although continuous, both displacement gradient and strain fields show abrupt changes within the shear zone after bifurcation. Tables 4.1 and 4.2 encapsulate average shear band widths of two cross-sections. It is noted that the band widths calculated based on deviatoric strain are larger than those based on displacement. Apparently, the shear zone

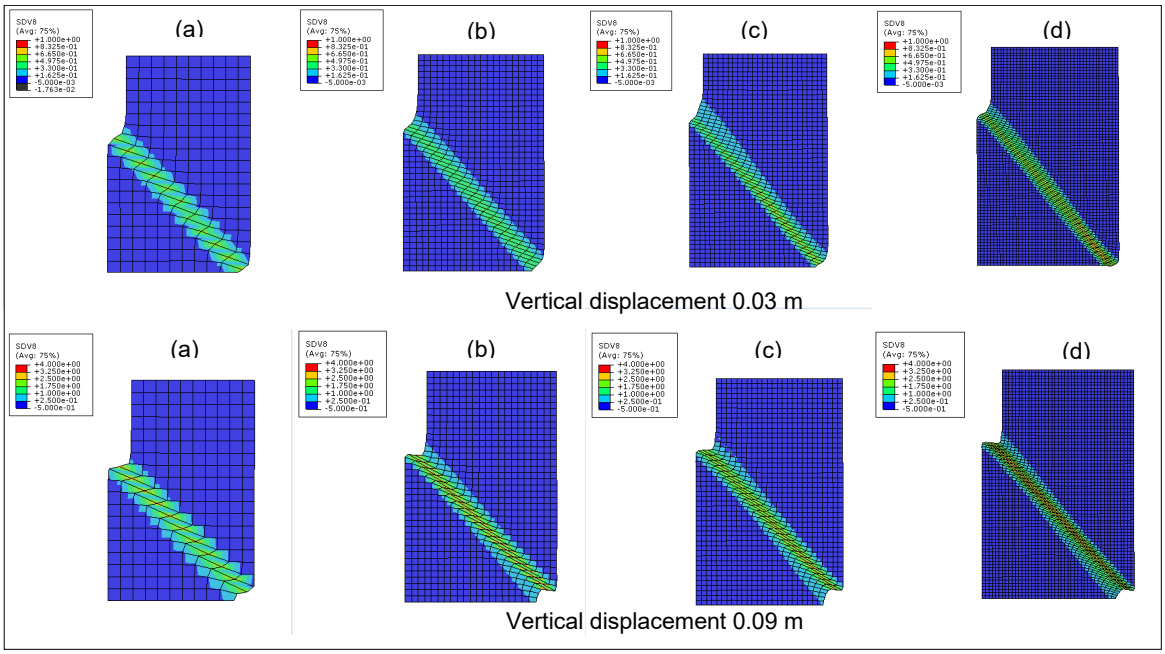

Fig. 4.16 Contours of accumulated deviatoric plastic strain from nonlocal NS model with GandS weight function at two stages of deformation: (a) large,(b) medium, (c) small and (d) extra-small meshes

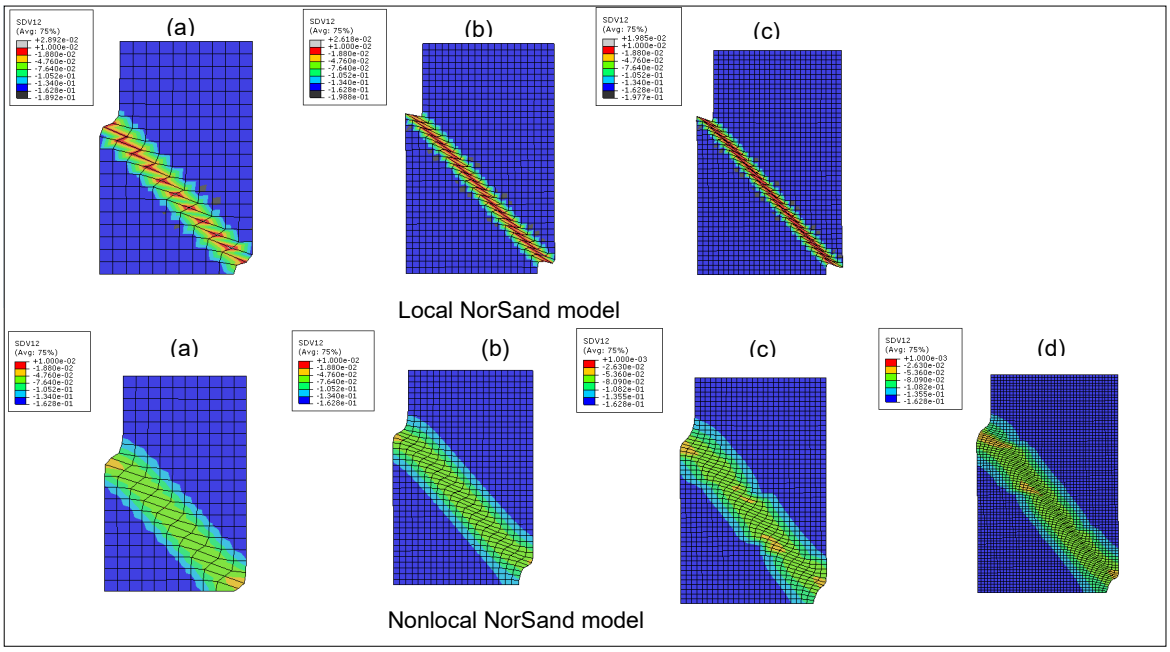

Fig. 4.17 Contours of state parameter from local and nonlocal NS models with GandS weight function: (a) large,(b) medium, (c) small and (d) extra-small meshes

enlarges with the deformation until it stabilises at the residual state. This is attributed to the expansion of dilating shear band. This observation is in line with shear band widths calculated from gradient flow theories (Chunhua and Drescher, 1993) and micro-polar models (Bardet and Proubet, 1992). The position and orientation of the shear band also vary slightly with the deformation.

In the local NS model, widths of the deviatoric strain concentration and changed displacement gradients are proportional to the mesh size during softening and the critical state. Moreover, the maximum deviatoric strain inside the shear band increases when the mesh is refined. In other words, finer discretisations inherit thinner shear bands with higher strain jumps. After nonlocal regularisation, the widths of the displacement gradient and shear strain concentration appear to be mesh independent. The displacement gradients in Figures 4.18 (e) to (h) are flatter than their local counterparts in Figures 4.18 (a) to (c). Even the maximum deviatoric strains inside the shear bands in Figures 4.19 (e) to (h) are almost similar irrespective of different mesh size. This suggests that the spatial discretisation does not dictate the deformation inside the shear band after the nonlocal regularisation.

Errors in calculating the numerical thickness

It is noted in Table 4.2 that, even after nonlocal regularisation, the thickness of the large mesh is slightly higher. Further, shear band thicknesses based on deviatoric strain are larger than those based on displacement. Several limitations of continuum methods may have caused these disagreements.

In FEM, displacement values are calculated at nodes, and deviatoric strains are calculated at integration points. Both contour plots and cross-sectional profiles are based on interpolated values between either nodes or integration points. This can be the reason for the difference between widths calculated from displacement gradients and strain values.

There can be an error in estimating the border of the shear band since the changes in displacement gradient and deviatoric strain occur gradually within the interface of the loading-unloading region. Undulations of loading and unloading observed in shear band boundary also may have contributed for the discrepancy.

Ortiz et al. (1987) pointed out that iso-parametric elements have inherent limitations in presenting localised deformation. During iso-parametric interpolation, elements try to conform to the deformation field by averaging deformation in both sides of the discontinuity as shown in Figure 4.21. So true discontinuous interface is smeared over several elements. Hence the minimum shear band thickness is larger than one element width. When the mesh is finer, element boundaries can follow shear band directions whereas large iso-parametric

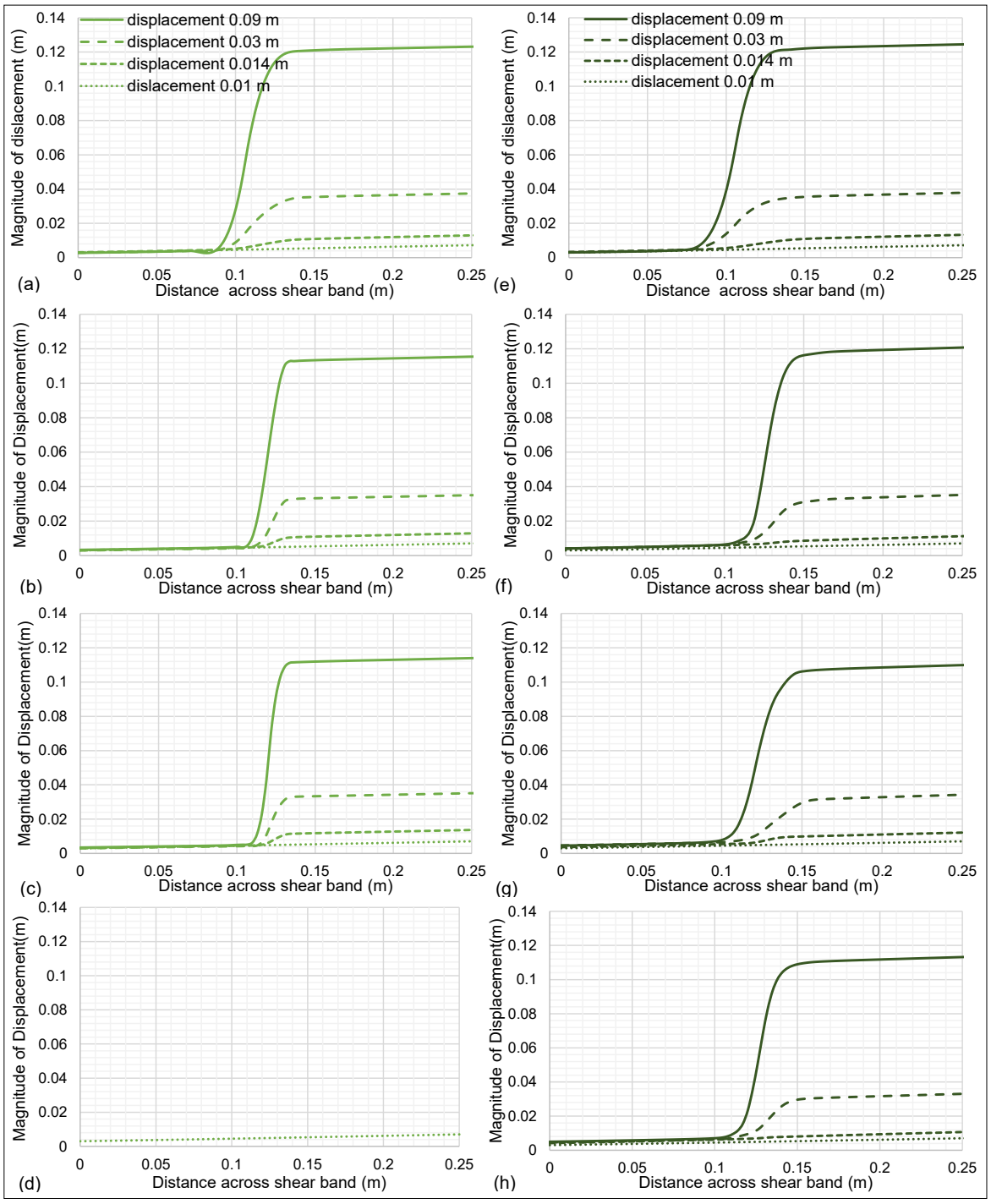

Fig. 4.18 Cross-sectional profiles of displacement of local (left) and nonlocal (right) analysis with NS model: (a),(e) large (b),(f) medium (c),(g) small and (d),(h) extra-small meshes

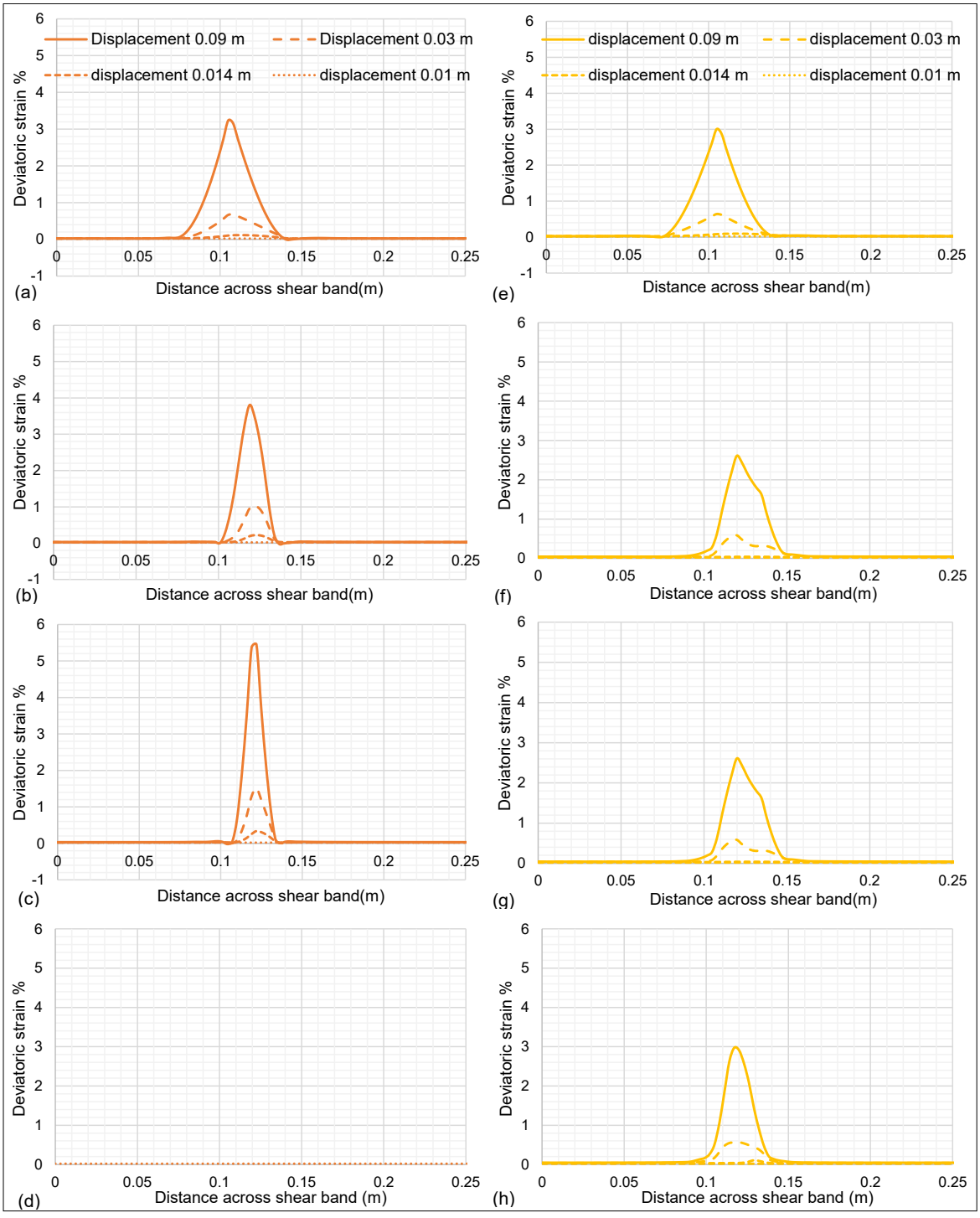

Fig. 4.19 Cross-sectional profiles of accumulated deviatoric strain of local (left) and nonlocal (right) analysis with NS model: (a),(e) large (b),(f) medium (c),(g) small and (d),(h) extra-small meshes

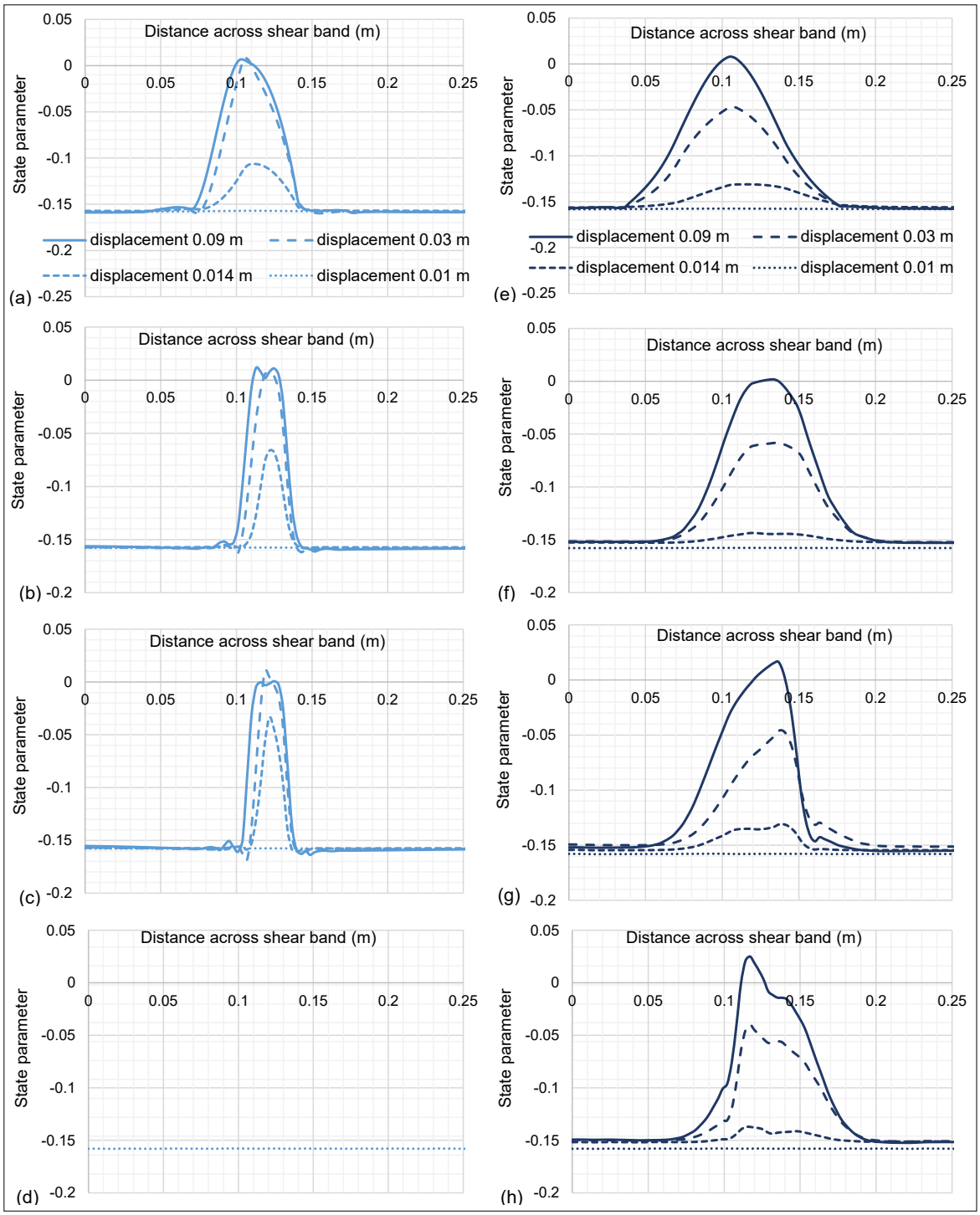

Fig. 4.20 Cross-sectional profiles of state parameter of local (left) and nonlocal (right) analysis with NS model: (a),(e) large (b),(f) medium (c),(g) small and (d),(h) extra-small meshes

elements cannot accurately resolve a shear band. In comparison, triangular elements are proved to be much better in representing localisations. In fact, the shear band boundaries are hard to be modelled by continuum methods, and particle methods are more suitable to capture this transition.

Table 4.1 Measured shear band thickness (from cross-sectional profiles) and shear band angles (from contour plots)- local NS analysis

	Stage of deformation (m)	Large	Medium	Small	Extra-small
Shear band angle		45°	47.7°	48.24°	
Shear band thickness based on displacement (m)	0.09	0.06	0.03	0.025	
	0.03	0.05	0.025	0.02	
Shear band thickness based on deviatoric strain (m)	0.09	0.075	0.04	0.03	
	0.03	0.07	0.03	0.025	
Width of state parameter (m)	0.09	0.07	0.04	0.04	
	0.03	0.06	0.04	0.03	

Table 4.2 Measured shear band thickness (from cross-sectional profiles) and shear band angles (from contour plots)- nonlocal NS analysis

	Stage of deformation (m)	Large	Medium	Small	Extra-small
Shear band angle		45°	47.7°	48.23°	50.77°
Shear band thickness based on displacement (m)	0.09	0.055	0.05	0.05	0.045
	0.03	0.05	0.04	0.04	0.04
Shear band thickness based on deviatoric strain (m)	0.09	0.065	0.06	0.06	0.06
	0.03	0.06	0.05	0.05	0.05
Width of state parameter (m)	0.09	0.13	0.13	0.12	0.12
	0.03	0.13	0.13	0.13	0.13

4.8.5 State parameter across the shear band

The width of the concentration of state parameter is of paramount importance when localisations are modelled with NS. It controls the degree of dilation hence the ability to soften within the band. This is slightly larger than the width of the shear band itself. As shown in

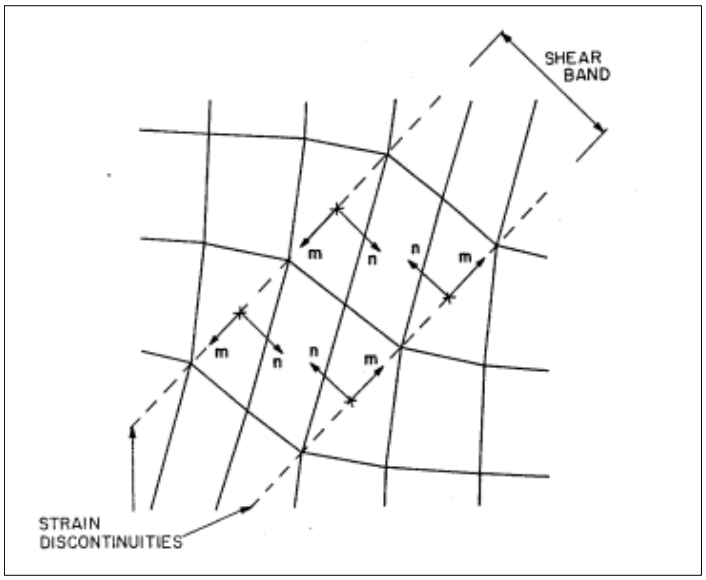

Fig. 4.21 Behaviour of iso-parametric elements in a strain discontinuity (Ortiz et al., 1987)

contour plots of Figure 4.17 (upper raw) and cross-sectional profiles in Figures 4.20 (a) to (d), the width of the concentration of state parameter varies with the mesh size in the local analysis. This mesh sensitivity is alleviated after nonlocal regularisation is applied for the state parameter. It is smeared over approximately 5 times the characteristic length in Figures 4.20 (e) to (h). Hence the time to approach the critical state or zero dilation is delayed.

Regularised state parameter profiles in small and extra-small meshes in Figures 4.20 (g) and (h) display irregular and skew distribution compared to those of large and medium meshes. Contours of state parameter in Figures 4.17 (c) and (d) also show areas of extreme deformations. Further, oscillations are observed in force-displacement curves of finer meshes. All these observations are due to the aforementioned drawback of GandS function when the characteristic length is more than twice the mesh size.

4.8.6 Shear band angle

According to Table 4.1, the orientations of shear bands from local NS model are slightly mesh dependent, displaying the largest angle for the finest mesh. Even after nonlocal regularisation, the angles are still mesh dependent as given by Table 4.2. The shear band angle is governed by mesh alignment, shape, type of the element and number of nodes etc. Relative locations of nodes decide both thickness and the direction of the shear band development. The size and type of weak elements also influence the decision. Although the same element type is used for all meshes, finer meshes have higher flexibility during the post-bifurcation deformation compared to larger meshes. Hence they show greater inclination angles due to mobilised dilation. With further mesh refinement, the band angle calculated from bifurcation theory

in Table 3.2 can be obtained. Contrary, when the mesh is coarse, the band angle is mostly dictated by square weak element.

The nonlocal theory is unable to regularise the shear band orientation properly because the method adopted here is partly nonlocal. Only the softening parameter (scalar) is regularised within the constitutive level. The direction of nodal degrees of freedom is hardly affected. If fully nonlocal method is used by averaging the strain vector, the shear band angle is likely to be mesh insensitive.

4.8.7 Correlations for numerical shear band thickness

The numerical shear band thickness in the local analysis is a function of the mesh size. Figure 4.22(a) displays simple correlations between mesh size vs average numerical shear band thickness for the local NS analysis. Regression lines show that the numerical band thickness is twice the mesh size during the softening and 2.1 times at the critical state. Figure 4.22(b) encapsulates shear band thickness of nonlocal NS analysis for three characteristic lengths. The numerical shear band thickness during softening can be approximately correlated as twice the characteristic length whereas it is 2.2 times at the critical state. It should be emphasised that these correlations are only valid for the type of mesh selected for this study. Galavi and Schweiger (2010) reported that the numerical shear band thickness is the same as the characteristic length. They used triangular elements which have more flexibility in deforming along localisations than rectangular elements. It can be concluded that the correlation between the numerical shear band thickness and the characteristic length depends on the weight function, mesh shape, size and number of nodes etc.

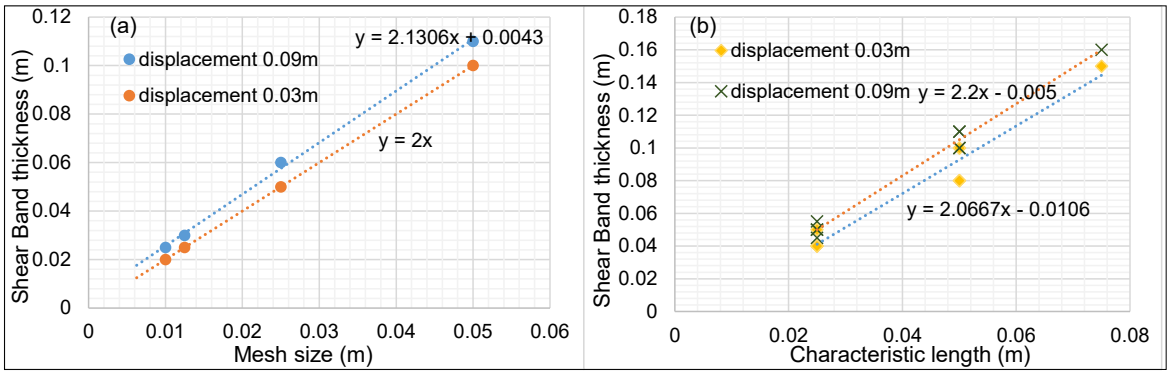

Fig. 4.22 Correlations of numerical shear band thickness with (a) mesh size in local analysis and (b) characteristic length in nonlocal analysis

4.8.8 Results from softening scaling

The nonlocal method grants the user the power of selecting the softening stiffness with an appropriate characteristic length such that well-posedness of boundary value problem is preserved. However, Table 4.2 suggests that the nonlocal method produces unrealistically

large numerical shear band thickness reducing the softening rate. Therefore, the resulted load-displacement curves do not represent realistic soil behaviour. This is because the used characteristic length does not represent the physical length of sand. If the actual length scale of sand is used here, the mesh size has to be lower than that for the nonlocal method to be effective. Nonetheless, it is practically impossible to refine the mesh to comply with the real shear band thickness. Hence, the softening scaling discussed in section 4.5 is introduced here to scale the load-displacement response to match with the real soil. However since the softening modulus is not constant in the NS model, the application of Equation 4.13 is not straight forward. The softening stiffness in the NS model is governed by the state parameter and hence the volumetric strain. Hence, it is decided to adjust the nonlocal void ratio in Equation 4.14 to scale the softening rate. This is justifiable since the rate of volume change controls the shear band thickness.

In this study, the physical shear band thickness of sand is assumed to be 10 D_{50} with $D_{50} = 1$mm. The numerical shear band thickness is approximated as 2 l_c during softening (from Figure 4.22(b)). From Equation 4.13, the scaling factor of softening stiffness is calculated to be 5 for the characteristic length of 0.025m. Scaling is introduced to the NS model by modifying the nonlocal Equation 4.14 as

$$e = e + (1+e)\, d\varepsilon_{v,avg}\, \frac{t^{sb,num}}{t^{sb,sand}} \tag{4.16}$$

It is evident that the scaling has increased the peak in nonlocal NS simulations in Figure 4.23 (a). This is because the scaling is applied automatically to the hardening function of the NS model which augments the hardening stiffness. Vermeer and Marcher (2000) reported the same observation when scaling was introduced to their nonlocal HS model. This drawback can be remedied by applying the scaling only after the localisation is signalled. The zero acoustic tensor criterion calculated according to Chapter 3 can be used as an indication of the initial bifurcation. For associative models, this coincides with the peak. Hence it is important for hardening and softening models, that only the softening part of the function is scaled. Even nonlocal regularisation should be applied only to the softening part of the NS model, but as long as there is no heterogeneity in the hardening part, the results of the nonlocal method are identical to those of the local model. Figure 4.23 (b) depicts nonlocal simulations of NS model with only post-peak scaling. It can be witnessed that both peak and critical state strengths are close to those of Figure 4.10 (c). Only the softening rate is increased to match with the realistic soil behaviour.

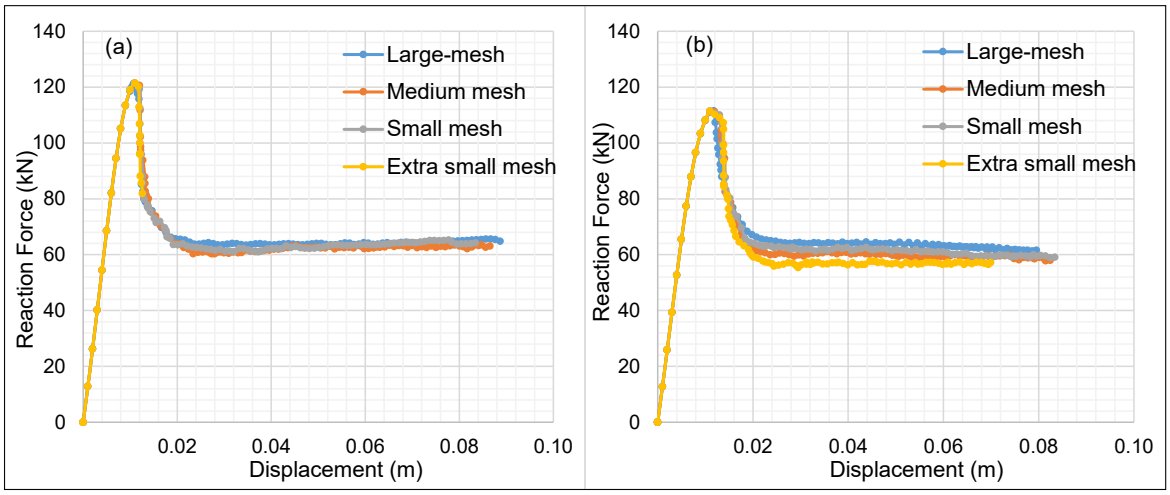

Fig. 4.23 Force-displacement curves of nonlocal NS model with scaling applied (a) in general and (b) only after bifurcation (width of specimen 0.25m)

It should be mentioned here that scaling is a mathematical artefact which is not inherent to the nonlocal method. It can be applied with any other regularisation method or even without a regularisation. Moreover, this method will not provide a realistic shear band thickness.

4.9 Limitations of Nonlocal Theory

Even though the nonlocal theory is proved to be a successful regularisation technique, its practical applicability for large scale geotechnical problems relies on the scaling. Therefore, it is worthwhile to probe in detail the error introduced by this scaling. A comprehensive parametric study is conducted as detailed in Table 4.3. Five mesh sizes and three characteristic length to mesh size ratios are explored.

Extra-small mesh (purple line) serves here as the benchmark case with scaling factor 1. It has numerical shear band thickness of 12.5mm. Other simulations are scaled to match with the band thickness of the extra-small mesh. Resulted force-displacement curves are illustrated in Figure 4.24. Maximum deviations from the benchmark case at selected stages of deformation are mentioned in Figure 4.24. It is observed that the influence of characteristic length (for GandS function) is marginal if it is within the limit $h \leq l_c \leq 2h$.

When the mesh is 8 times larger, the error of predicting the residual strength is 18%. The error of peak prediction is within 2.6% and during the softening stage (at 20% strain) it is 13% . It is noticed that the error becomes larger at the residual stage. This is because the volumetric regularisation is not much effective at the critical state. Nevertheless, compared to the local analysis with the extra-large mesh, the mesh sensitivity is reduced 22% at the residual stage. It is reduced 38% at 20% strain. It is also emphasised that these results are

Table 4.3 Details of parametric study on mesh size and characteristic length

	h (m)	l_c (m)	$\frac{l_c}{h}$	Scaling factor $\frac{2l_c}{12.5mm}$
Extra-large	0.05	0.05	1	8
Extra-large	0.05	0.075	1.5	12
Large	0.025	0.025	1	4
Large	0.025	0.0375	1.5	6
Large	0.025	0.05	2	8
Medium	0.0125	0.0125	1	2
Medium	0.0125	0.01875	1.5	3
Medium	0.0125	0.025	2	4
Small	0.01	0.01	1	1.6
Small	0.01	0.015	1.5	2.4
Extra-small	0.00625	0.00625	1	1

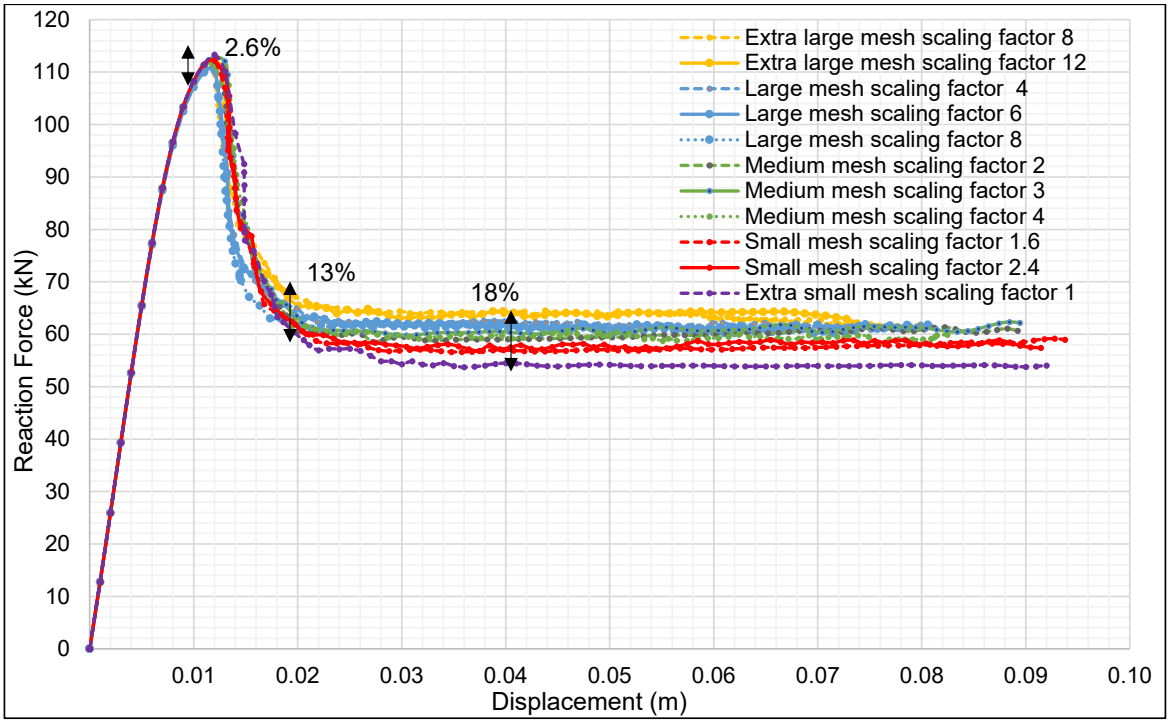

Fig. 4.24 Force-displacement curves of nonlocal NS model with different mesh sizes and characteristic lengths, scaled down for 12.5mm shear band thickness (width of specimen 0.25m)

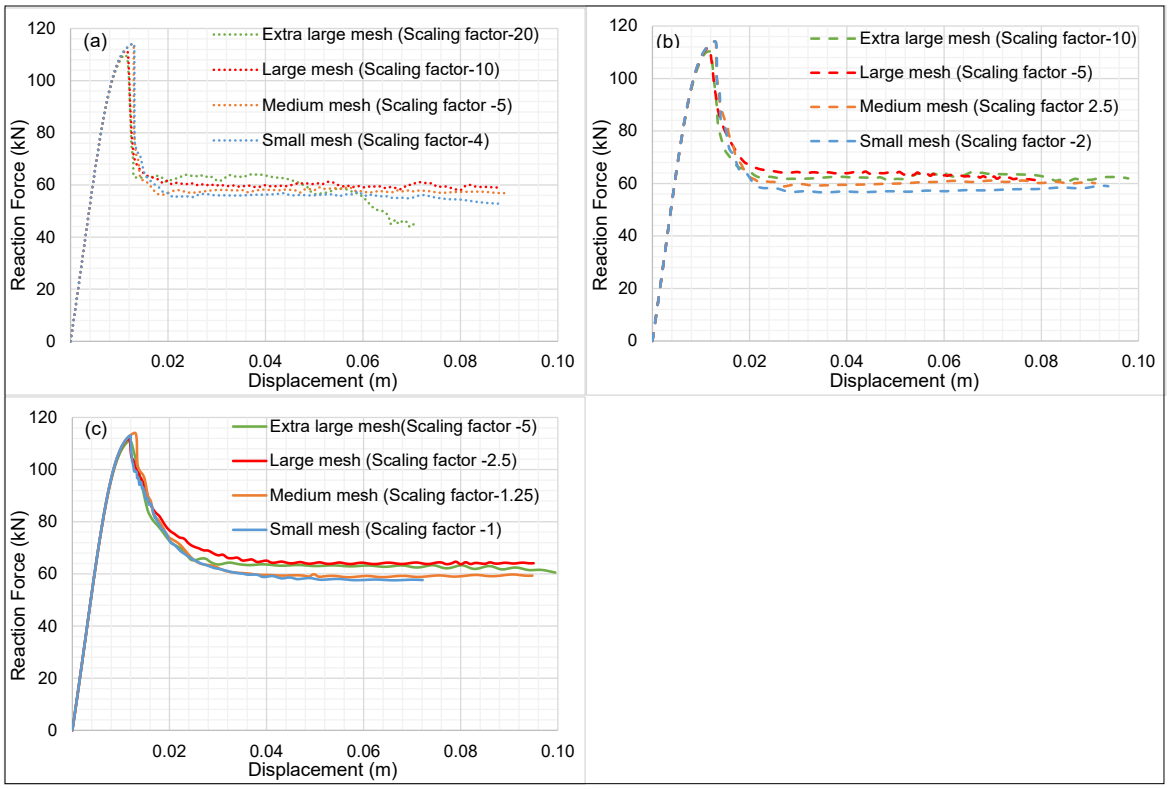

Fig. 4.25 Force-displacement curves scaled for shear band thickness of (a) 5mm,(b) 10mm and (c) 20mm (width of specimen 0.25m)

subjective to the dimensions of the sample. A further increase of mesh size or characteristic length beyond those given in Table 4.3, suppressed the localisation. Hence it is difficult to recommend a maximum mesh size for which this method is valid.

In Figure 4.10 the smallest mesh size to provide converged results is 10mm. This means conventional FEM can not simulate band thickness lower than 20mm. When nonlocal regularisation is applied, the minimum element size which can be fully converged reduced to 6.25mm. Hence the minimum shear band thickness simulated with the nonlocal method without scaling is 12.5mm. However, in granular material with fine particles, shear band thickness can be smaller than this. Hence, it is worthwhile to investigate the minimum shear band thickness nonlocal regularisation can handle along with scaling.

Figure 4.25 portrays the response of three shear band thickness modelled by four element sizes. The characteristic length is taken as equal to the mesh size. It is evident from Figure 4.25(a) that softening curves are almost vertical when the shear band thickness reduces to 5mm, irrespective of the mesh size. Beyond this, numerical convergence issues with spurious oscillations are witnessed even with nonlocal regularisation. It can be deduced that, for the considered specimen size, the shear band can be modelled as a weak discontinuity

only up to this thickness. The scaling is not accurate after that. In essence, the nonlocal method can handle thinner shear bands than conventional FEM, but its ability is also limited. Agreeing with Borja and Regueiro (2001), it is concluded that even shear bands in frictional materials should be modelled as strong discontinuities or displacement jumps beyond a certain threshold length scale.

4.10 Conclusions

The nonlocal theory is first time implemented in the critical state based NS model. Nonlocal averaging with GandS function successfully produces mesh independent force-displacement curves and shear band thickness. Softening scaling is utilised along with nonlocal regularisation to obtain physically realistic mechanical response without extreme mesh refinement. It makes this method more versatile. The numerical shear band thickness is calculated as twice the mesh size in local analysis and twice the characteristic length in the nonlocal analysis. However, limitations inherent to conventional FEM apply to this method as well. Therefore, results are sensitive to the type of elements, the number of nodes etc. Mesh alignment cannot be regularised by this method. For a considered specimen dimension, there is a minimum band thickness which can be accurately represented by nonlocal method and scaling.

4.10.1 Contributions

The main contributions of this chapter are

- Integration of nonlocal theory to critical state soil model

  In previous literature, the nonlocal theory has been implemented in DP, MC type models with cohesion and/or friction softening with constant dilation. Those models adopt constant softening moduli. Therefore, post-peak softening is linear, and the residual strength is independent of the mesh size. Hence, the implementation of the nonlocal theory is straightforward. In critical state plasticity, the dilation evolves with deformation, and the critical state strength is also mesh dependent. In this study, the critical state NS model is enriched with nonlocal theory. Nonlocal averaging of void ratio leads to the regularisation of the state parameter. Mesh independent load-displacement curves of dense sand are obtained during both softening and the critical state. Hence it is capable of adequately regularising the post-peak dilation.

  For the considered characteristic length and mesh sizes, GandS weight function provides the most reliable results than Gauss and over-nonlocal methods. Nevertheless, GandS method bestows irregular homogenisation when the characteristic length is larger than twice the mesh size. Scaling can be used with nonlocal regularisation to

produce a physically realistic mechanical response without extreme mesh refinement. Unlike purely softening models, in the NS model, scaling should be applied only after the bifurcation point. Otherwise, pre-peak hardening is affected by the scaling.

- Recognising limitations of the nonlocal NS model

  The nonlocal method is capable of circumventing the sensitivity of mesh size, not mesh alignment. After regularisation shear band angles are still mesh dependent. Moreover, volumetric regularisation becomes less active when the critical state is reached. Therefore, when mesh size is 8 times larger, the error of predicting the residual strength by the nonlocal method is 18%. The regularisation is more effective during softening. However, the greater the mesh size to physical band thickness ratio, the error from scaling becomes larger.

  The nonlocal theory is applicable only for granular material with a finite band thickness. For a considered specimen size, there is a minimum band thickness simulated by the nonlocal method and scaling. Below that, the shear band cannot be modelled as a weak discontinuity.

Chapter 5

Rate Effect and Local Drainage during Shear Localisation in Saturated Dense Sand

5.1 Preface

The introduction of an internal length to rate-independent plasticity is sufficient to diminish the mesh dependence of single-phase material. When it comes to localisation in the fluid-saturated soil, the transient behaviour of hydro-mechanical coupling introduces a rate dependence although underlying effective material is rate independent (Garagash and Rudnicki, 2002). Hence finite element results are dependent on both space and time. The characteristic internal length is dictated not only by material behaviour but also by solid-fluid interaction. The degree of coupling between a solid skeleton and pore fluid is governed by drainage length, permeability, compressibility and loading rate. Since the drainage length is numerically affiliated with element size, the pore fluid diffusion is mesh sensitive.

There are two main objectives of this chapter. The first is to critically assess the numerical factors which influence the internal fluid exchange between shear band and outer material in saturated dense sand. The second is to examine whether the regularisation of rate-independent plasticity is sufficient to circumvent its mesh sensitivity .

Section 5.2 outlines factors affecting the pore fluid movements. Experimental and numerical findings on diffusion rate effect are summarised in sections 5.3 and 5.4 respectively. Mesh sensitivity during finite element analysis of multi-phase material and regularisation techniques are included in section 5.5. Simulations of biaxial compression tests are conducted

to identify numerical factors which affect internal water movements between the shear band and outer materials. The numerical programme is outlined in section 5.6. Results of the parametric study are detailed in sections 5.7 to 5.9. The potency of nonlocal regularisation to circumvent the mesh dependence in saturated sand is evaluated in section 5.10.

5.2 Factors Affecting the Pore Fluid Flow

The pore fluid flow can be deterred by low permeability of the soil, fast loading rate or impervious boundaries of the domain. Low permeable soil such as of clay or silty sand can lead to locally undrained conditions whereas impervious surfaces may result in globally undrained conditions. These two scenarios impose kinematic constraints locally (constant pore volume) and globally (constant volume of the domain) respectively. When the granular skeleton is constrained to isochoric deformation either locally or globally, its tendency to dilate or contract can induce excess pore pressure. Loose sand generates positive excess pore pressure which results in a reduction of effective stress whereas dilative sand develops negative excess pore pressure and increases in strength.

The rate of loading, length of drainage and consolidation properties of soil are main factors which dictate the fluid flow within the porous media. For saturated sand, the interplay between the rate of shearing and the rate of dissipation of excess pore pressure governs the drainage behaviour. The magnitude of generated excess pore pressure of a material point depends on its volume constraint, fluid compressibility, soil dilatancy and shear rate. Its dissipation depends on soil diffusivity (permeability, compressibility), drainage length and time. Depending on the relative magnitude of these parameters, the amount of local drainage can vary. Finnie (1993) introduced a dimensionless velocity V_n to aggregate the influence of the loading velocity V, drainage length L and coefficient of soil diffusivity c_v.

$$V_n = \frac{V\,L}{c_v} \tag{5.1}$$

$$c_v = \frac{\bar{k}}{m_v\,\gamma_w} \tag{5.2}$$

where γ_w is the unit weight of water, $\bar{k}$ is permeability and m_v is one dimensional compressibility of soil. Drainage length is bounded by the shear band thickness and the specimen dimensions. A change to any parameter of this normalised velocity can result in a change in drainage. In this chapter, the term "rate effect" implies to the change in the normalised velocity.

5.3 Experimental Evidence on Rate Effect and Local Drainage in Soil

The material behaviour of sand is not inherently rate dependent as clay. However, the interaction between the soil skeleton and pore fluid introduces a rate dependence. The strength of saturated dense sand has been observed to increase with the loading rate. There is a controversy interpreting the reason behind this strength enhancement. Based on the results of triaxial compression tests, Watanabe and Kusakabe (2013) commented that, if global boundaries are drained, the effect of loading rate is due to the combined effect of consolidation and viscosity of the pore fluid. The rate effect is solely due to the viscous effect if shearing is carried with undrained boundaries. This theoretical reasoning is demonstrated in Figure 5.1. On the other hand, Palmer (1999) and Kutter (2006) attributed the rate dependent plough resistance in the seabed to counteracting mechanisms of generation and dissipation of excess pore pressure. This thesis hypothesises that irrespective of the drainage conditions at remote boundaries, dilation induced pore pressure generation and its dissipation co-occur in shear zones. This phenomenon which happens within soil microstructure governs the relative strength of soil at different rates.

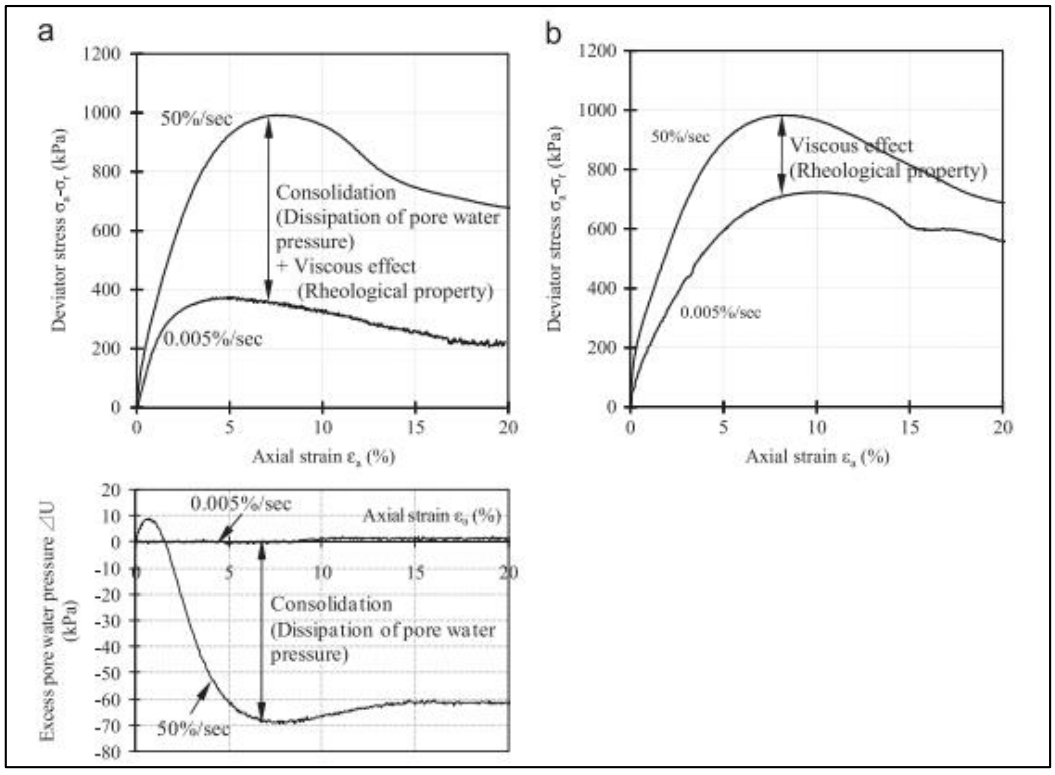

Fig. 5.1 Loading rate effects in triaxial compression tests with (a) drained and (b) undrained boundaries (Watanabe and Kusakabe, 2013)

There is very limited experimental data available on the local drainage during shear localisation of soil. Most of the available literature is focused on the internal fluid flow in localised clay (Gylland, 2012; Thakur, 2007). Atkinson and Richardson (1987) explored the local drainage effect of over-consolidated clays and dense sand in globally undrained triaxial tests. They claimed that in undrained tests relatively large hydraulic gradients can occur near shear zones. This may lead to local drainage and local volume changes such that the tests are not strictly undrained even during rapid loading conditions. They estimated the degree of local drainage from the geometry of shear zones based on the hypothesis that only locally undrained shear zones intersect orthogonally. Otherwise, shear bands intersect at angles larger than 45° (to the minor principal axis) depending on the degree of local volume changes. Viggiani et al. (1994) revealed that there is a pore pressure difference between in and out of the shear band in an undrained biaxial compression test of stiff clay. At the onset of localisation, the pore pressure gradient boosts suddenly due to concentrated shearing as shown in Figure 5.2 but equalises rapidly afterwards.

"There is a significant difference between a globally drained and a locally drained response. The same concept applies to globally undrained response, where local drainage and volume changes can occur close to the localised zone" (Viggiani et al., 1994)

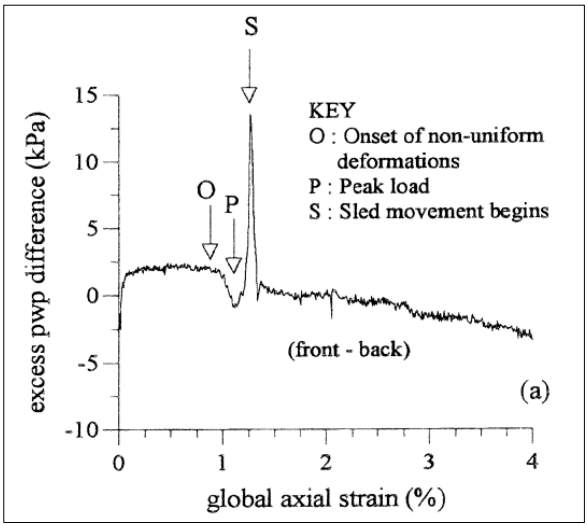

Fig. 5.2 Pore pressure difference between in and out of shear band (Viggiani et al., 1994)

Thakur (2007) and Gylland (2012) experimentally investigated the strain softening accompanied by shear localisation of globally undrained clay. The influence of rate effect on the generation and dissipation of pore fluid flow was studied. They noticed a pore pressure difference between in and out of the shear band. They claimed that faster tests are more prone to diffuse type failure since they do not have enough time to equalise the pore pressure gradient. Dominating single shear bands occurred in slower tests since they have enough

time to dissipate the pore pressure gradient. These observations substantiate the concept of the local drainage under the globally undrained conditions. However, due to the high permeability, the internal fluid flow is rarely observed in laboratory experiments of undrained sand.

Han and Vardoulakis (1991) provided experimental evidence on the local drainage in the saturated dense sand during globally undrained biaxial compression. Tests were conducted under sufficient back pressure to avoid cavitation. The failure occurred after the Coulomb state of the background drained behaviour. X-ray radiographs showed conjugate periodic shear band arrays corresponding to alternative dilatant and contracting behaviour. They appear to be linked together by the internal fluid flow which accounts for the locally drained condition. However, Han and Vardoulakis (1991) did not observe a pore pressure difference between in and outside the shear band. They deduced this is because the internal flow occurs in a time scale smaller than the response time of pore pressure transducers. Therefore, it was not possible to capture the transient exchange of fluid between the shear band and surrounding.

To the author's knowledge, Han and Vardoulakis (1991)'s observation on locally drained shear bands was not verified by any other experiments conducted later. Mooney et al. (1997),Roger et al. (1997) and Desrues and Mokni (1998) reported that they could not find any evidence of local drainage in their undrained biaxial tests of saturated sand. Instead they observed cavitation induced localisations.They ascribed it to possible time and scale effects. For the strain rate imposed on the specimen, the viscosity of the pore fluid can be too high to flow into the shear band. Moreover, the size of the specimen compared to the grain size may be too small to allow the balance between dilative and contracting zones.

5.4 Finite Element Studies on Diffusion Rate Effects and Local Drainage in Saturated Dense Sand

Charlier et al. (1997) numerically showed the possibility of locally drained shear bands in biaxial compression tests of saturated dense sand under globally undrained conditions. They showed that, if the permeability is small compared to the loading velocity, there is not enough time for water to move. The specimen is then both locally and globally undrained. Hence no localisation appears if the back pressure is high enough. If the specimen is sheared until the cavitation pressure is reached, a drained localisation appears releasing the isochoric constraint both locally and globally. However, if the permeability is large enough compared to the loading velocity, internal water movements can occur allowing strain localisation even

when the average volumetric changes over the whole sample are null. Hence the undrained condition is only global. This phenomenon may precede the cavitation (Charlier et al., 1997).

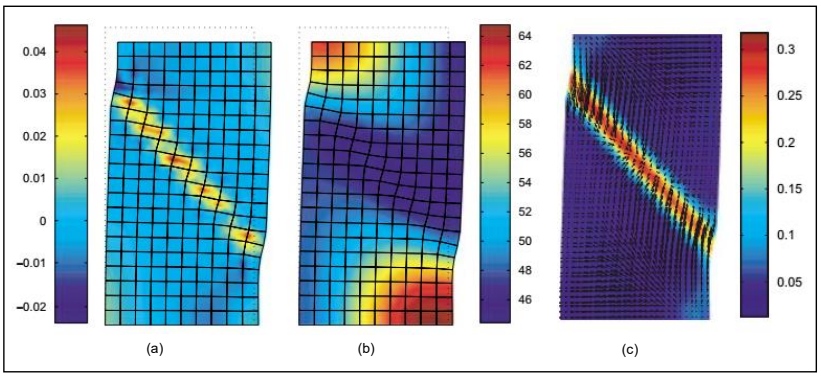

Fig. 5.3 Contours of (a) volumetric strain, (b) fluid pressure and (c) deviatoric strain with relative flow vectors at 5% axial strain in a globally undrained biaxial test (Andrade and Borja, 2007)

Desrues and Viggiani (2004) simulated biaxial compression tests of dense sand with impermeable and permeable horizontal global boundaries. They noted loading rate effect for the partially drained case, but similar responses were recorded for both fast and slow cases in globally undrained tests. They only recognised fully drained and undrained conditions, not local drainage. Liu et al. (2005) reported that low permeability delays the localisation and widens the shear band thickness based on undrained triaxial tests of dense sand.

Andrade and Borja (2007) noticed the local drainage in the vicinity of shear bands in the saturated dense sand with globally undrained boundary conditions. Even under quasi-static loading rates, they observed a hydraulic gradient as shown in Figure 5.3(b). The local volume change is depicted in Figure 5.3(a), and fluid flow is directed towards the shear band in Figure 5.3(c). Apparently, the dilative shear band is sucking the pore fluid. They did not explore the influence of permeability or loading rate on the degree of local drainage.

Using a mesh independent second gradient DP model, Sieffert et al. (2014) encapsulated the influence of permeability, loading velocity and dilatancy on the formation of shear bands under globally isochoric constraint. The initial pore pressure was equivalent to the atmospheric pressure. For dilative sand, they defined two types of shear bands namely stable (the band does not change orientation or location after the onset) and unstable (the band evolves in position and thickness, and ultimately the whole specimen becomes plastically loaded). They observed that high values of permeability and slower loading rates bestow stable shear bands since local pore pressure gradients equalise gradually as shown in Figures 5.4 (a),(b),(c). In these, the cavitation occurred only after the localisation. Contrary, dense sand with higher loading rates and lower permeability were prone to show unstable shear

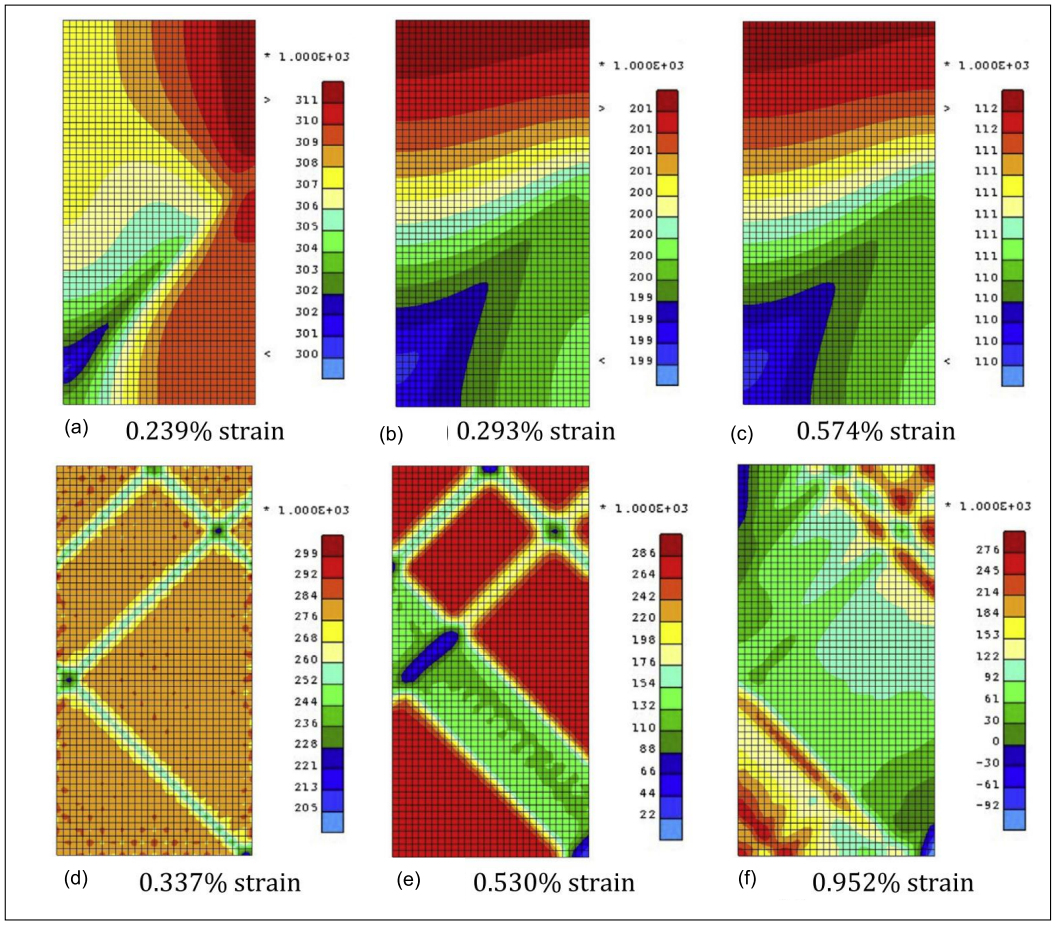

Fig. 5.4 Contours of pore water pressure numerically observed for undrained biaxial tests with permeability ((a),(b),(c)) 10^{-7}m/s and ((d),(e),(f)) 10^{-12}m/s (Sieffert et al., 2014)

band during undrained shearing. For these cases, the continuous increase in effective stress was terminated by the cavitation which released the globally undrained condition and induced localisation. Pore pressure shocks with steeper pressure gradients were observed as shown in Figure 5.4 (d),(e) and (f). This is further illustrated in the cross-sectional pore pressure profiles in Figure 5.5.

Although Sieffert et al. (2014) did not explicitly used the word "local drainage", it is fair to think that stable and unstable shear bands refer to locally drained and locally undrained conditions respectively. Therefore, a clear separation between stable and unstable shear bands is questionable as there are certain combinations of loading rates and permeabilities for which the shear band is neither fully drained nor undrained. It depends on the time required for the pore pressure gradient to dissipate. Further, they assumed a cavitation pressure of -100kPa. Hence the behaviour of unstable shear bands under greater initial back pressure was not discussed.

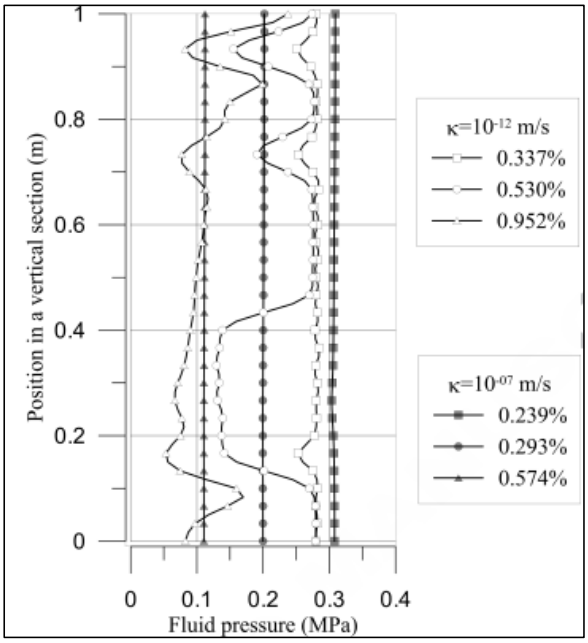

Fig. 5.5 Cross-sectional profiles of pore water pressure (Sieffert et al., 2014)

5.5 Mesh Sensitivity during Shear Localisation in a Multi-phase Porous Medium

Aforementioned numerical studies scrutinise the pore fluid diffusion rate effect associated with localisations in saturated dense sand, but mesh sensitivity during hydro-mechanical coupling is not probed in detail. There are contentious notions regarding the inherent regularisation in a multi-phase medium.

Schrefler et al. (1995, 1996), Larsson and Larsson (2000a), Liu et al. (2005) mentioned that mesh dependence of fluid-saturated solids is not dramatic as single phase materials. This is because of the presence of the gradient term in Darcy's equation which introduces a natural regularisation in governing equations. It is analogous to viscous regularisation in single phase material (Ehlers et al., 2001; Ehlers and Volk, 1998). An internal length scale is represented by the permeability. It dominates the degree of coupling between soil skeleton and pore fluid during the localisation.

Zhang et al. (1999), Zhang and Schrefler (2001, 2004) further elucidated the role of inherent characteristic length in a multi-phase porous medium during dynamic localisation. They defined a wave number domain within which an internal length scale exists. Within this region, multi-phase porous materials encounter loss of stability (the solid skeleton is softening) but do not loose hyperbolicity of dynamic governing equations. However, Zhang and Schrefler (2004) claimed that the quasi-static loading condition does not inherit the

natural internal length scale provided by the permeability and an external regularisation is required. Andrade and Borja (2007) also reported that fluid saturated solids display "mild" mesh dependence during quasi-static loading of globally undrained biaxial tests. Both the width of the shear band and force-displacement curves are shown to be mesh dependent. Vardoulakis (1996a,b) also reported that boundary value problems become ill-posed even with two-phase formulations.

In summary, there is no consensus about the degree of regularisation provided by the fluid component. The aforementioned observations depend on the loading rate, permeability, dilative characteristics of the soil, sample dimensions and boundary conditions as well. Hence it is concluded that the viscous term introduced by the permeability is not sufficient to fully eliminate the mesh sensitivity in the fluid-saturated soil, especially for static and quasi-static loading conditions. A regularisation of effective stress equations is necessary for true mesh independence.

5.5.1 Regularisation methods for multi-phase materials

Similar methods used to regularise single-phase materials have been utilised with multi-phase materials. Most techniques involve regularising the mechanical behaviour of the underlying drained solid. In this case, the complexity lies in the interplay between the external characteristic length introduced by regularisation techniques and the natural regularisation bestowed by the permeability.

Visco-plastic models (Loret and Prevost, 1991; Oka et al., 1995), Cosserat continuum models (Ehlers et al., 2001; Ehlers and Volk, 1998), higher gradient models, (Collin et al., 2006, 2010; Sieffert et al., 2014; Zhang and Schrefler, 2004) and nonlocal models (Summersgill et al., 2017a) introduce explicit characteristic length to overcome the mesh dependence of fluid-saturated medium. Further, extended finite element method (Thakur, 2007) and embedded localisation method (Larsson and Larsson, 1999; Larsson et al., 1996) employ strong discontinuity approach.

Nonlocal regularisation in multi-phase materials

Summersgill et al. (2017a) conducted a slope stability analysis with coupled consolidation formulations with nonlocal averaging. Non-associative MC model was utilised. They reported that the nonlocal regularisation reduced but not fully circumvented the mesh dependency. They attributed it to different patterns of slip surfaces formed, which are sensitive to pore pressure distribution during consolidation. However, they did not discuss the local drainage or the viscous regularisation provided by permeability.

Lazari et al. (2015a,b) studied the mesh dependence of globally undrained dense sand using a visco-plastic model augmented with nonlocal regularisation. They replaced the local viscous nucleus by its average over a representative volume. They used three phase hydro-mechanical formulations under quasi-static conditions. The non-associative DP model was utilised. They assumed that strain localisation coincides with cavitation. Lazari et al. (2015a,b) claimed that both visco-plasticity and nonlocal theory introduce length scales implicitly and explicitly to prevent the mesh dependency. For high values of viscosity, the visco-plasticity, in conjunction with nonlocal theory, governs the regularisation. For low viscosity values and small loading rates, the nonlocal method overrides the influence of viscoplastic internal length. Lazari et al. (2015a) stated that, if real physical values of viscosity and permeability are used, the regularisation provided by these might be lost for certain material properties and loading rates. Hence, Lazari et al. (2015a) recommended the use of nonlocal method over visco-plasticity.

In summary, the potency of nonlocal regularisation for coupled problems is not critically evaluated, especially using rate-independent plasticity. Apparently, there is a range of loading velocities and permeabilities, for which the regularisation of effective material behaviour is sufficient to eradicate the mesh dependence.

5.6 Biaxial Compression Analysis of Saturated Sand

To investigate both rate and mesh effects, a series of displacement controlled biaxial compression analysis of saturated dense sand is conducted. The dimensions, boundary and initial conditions are similar to section 4.7. A transient consolidation analysis is adopted here such that hydro-mechanical coupled formulations are solved. Plane-strain quadratic isoparametric elements with reduced integration and additional pore pressure degrees of freedom (CPE8RP) are selected.

In all simulations, the initial back pressure is 5 kPa, and soil is assumed to remain fully saturated throughout the deformation. The initial confining pressure is 95 kPa. For the calculation of normalised velocity, the compressibility is assumed to be $0.00002\,\mathrm{m^2/kN}$. The initial void ratio is 0.55. The material properties of the original NS model are same as given in Table 2.1.

5.6.1 Numerical programme to investigate the rate effects in saturated sand

A comprehensive numerical scheme is conducted to explore the influence of loading velocity, permeability and specimen size on the local drainage of the shear band. Equations 5.1 and 5.2 are combined and rearranged to scrutinise the influence of different parameters.

$$V_n = \frac{V\ L\ m_v\ \gamma_w}{\bar{k}} = \frac{\Delta u}{\Delta t}\ \frac{L}{\bar{k}}\ m_v\ \gamma_w \tag{5.3}$$

where Δu and Δt are applied displacement and its duration respectively. The drainage length L is assumed as the height of the specimen H. The programme consists of two segments. The simulation series $1,2$ and 3 explore globally undrained remote boundaries whereas the simulation series 4 studies the open drainage boundary conditions. In series $1,2$ and 3, four edges of the biaxial specimen are assumed impermeable whereas in series 4 top and bottom boundaries are presumed to be permeable. Details of the four simulation series are summarised in Table 5.1. All specimens are displaced to reach the same final strain (20 %). Series 1 and 4 are re-analysed to reach 40 % axial strain. It should be mentioned that static consolidation analysis is conducted here even for extreme loading rates without considering acceleration. Accuracy of these simulations will be discussed, pointing out the minimum loading rate to shift for a dynamic simulation.

Table 5.1 Details of simulation series 1, 2, 3 and 4

Number of simulation series	Specimen height - H (m)	Specimen width - W (m)	Permeability - $\bar{k}$ (m/s)	Applied displacement - Δu (m)	Boundary condition	Durations of loading - Δt (s)
Series 1	0.5	0.25	0.001	$0.1, 0.2$	undrained	1000, 100, 10, 1 , 0.1, 0.01, 0.001, 0.0001, 0.00001
Series 2	0.5	0.25	0.00001	0.1	undrained	100, 1 , 0.01
Series 3.1	0.25	0.125	0.001	0.05	undrained	1000, 100, 10, 1 , 0.1, 0.01, 0.001, 0.0001, 0.00001
Series 3.2	1	0.5	0.001	0.2	undrained	1000, 100, 10, 1 , 0.1, 0.01, 0.001, 0.0001, 0.00001
Series 4	0.5	0.25	0.001	$0.1, 0.2$	top and bottom fully drained	1000, 100, 10, 1 , 0.1, 0.01, 0.001, 0.0001, 0.00001

The mesh sensitivity at different rates is investigated for all series. The analysis comprises of comparing four different element sizes (h). They are extra-large (0.05 m), large (0.025 m), medium (0.0125 m) and extra-small (0.006 25 m). An additional element size (0.005 m) is studied for series 1. All cross-sectional profiles are taken perpendicular to the shear band starting from the coordinates 0.0 m,0.015 m.

Series 1 and 4 are re-analysed with nonlocal regularisation and scaling. The characteristic length is equal to the largest mesh size, unless otherwise specified. Based on the findings of Chapter 4 only GandS weight function is used for the nonlocal analysis.

The results of the above parametric study are organised as shown in Figure 5.6 to serve several purposes. The first is to identify factors affecting the normalised velocity under different remote boundary conditions. The second is to characterise the localisations based on the degree of drainage. The third is to elucidate the mesh sensitivity under different degrees of drainage. The fourth is to distinguish the global vs local pore fluid diffusion. Finally, the range of normalised velocity for which nonlocal regularisation can successfully eliminate the mesh dependence is recognised.

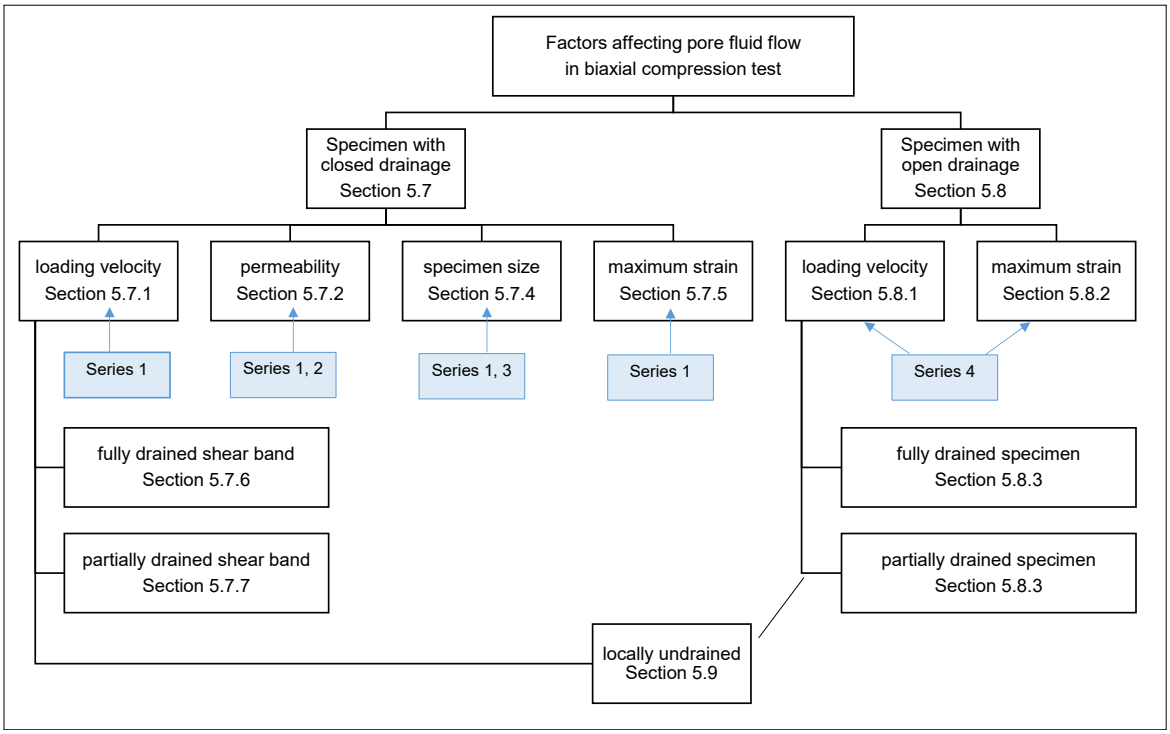

Fig. 5.6 Overview of the results from the parametric study in Table 5.1

5.7 Results of Globally Undrained Biaxial Compression Tests

This section explores the influence of loading rate, permeability and specimen dimension on the behaviour inside the shear band when remote boundaries are undrained. The mesh dependence of saturated dense sand is explored for the each case.

5.7.1 Effect of loading velocity

Figure 5.7 illustrates the influence of loading duration on the load-displacement response of globally undrained saturated dense sand. For the sake of brevity, only results of extra-large and extra-small mesh are shown. It is observed that globally undrained deformation of dense sand does not show any sign of softening or a peak force for any rate or mesh size. Even after the formation of a shear band caused by the local drainage, the reaction force continues to progress. This is consistent with the numerical results of Sieffert et al. (2014). They attributed this observation to elastic reloading of elements outside the band and post-peak dilation of elements inside the band.

For both meshes, when loading velocity is increased, the ultimate load at the end of shearing is increased. As more clearly seen for extra-small mesh in Figure 5.7(b), the onset of inhomogeneous deformation, as marked by the change in stiffness, is delayed as the loading rate is increased. As mentioned in Chapter 3, the continuous dilative hardening of undrained deformation is interrupted by the formation of a shear band. Its initiation is decided by the relative generation and dissipation of excess pore pressure. When the rate of shearing increases the hydro-mechanical coupling enhances. A higher proportion of load increment is taken by fluid slowing the transfer of load to the soil skeleton. Thus the migration of fluid caused by local volume changes is delayed when the loading rate is increased.

Another distinct feature of both Figures is that the range of load-displacement curves is bounded by two extreme cases. The lower boundary is associated with the fully locally drained shear band. For the considered diffusive properties of the material and specimen dimensions, this condition occurs when the time of loading exceeds 1 s for both meshes. This means 1 s is sufficient for the pore pressure built up inside the band to dissipate across the specimen (within the same time increment). Therefore, even when the duration exceeds 1 s, soil-fluid interaction is the same and hence there is no difference in the mechanical response.

The upper boundary marks the fully homogeneous deformation. The material is both locally and globally undrained. There is hardly any water movements in this case leading to a continuous generation of negative excess pore pressure. The loading rate required to achieve the locally undrained deformation is not the same for two mesh sizes. The force-displacement curves in between these two extremes display an intermediate response.

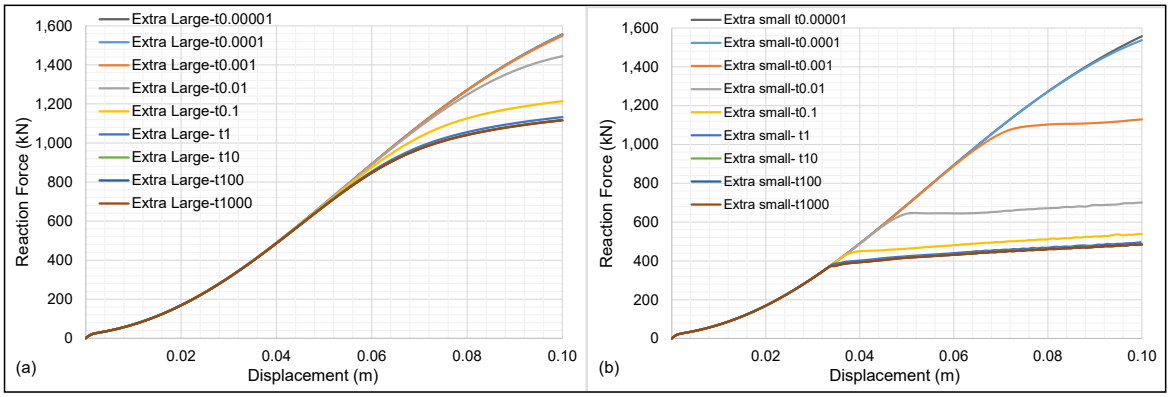

Fig. 5.7 Load-displacement relationships of undrained analysis with different durations of loading in (a) extra-large and (b) extra-small mesh : $p'_0 = 95$kPa, $W = 0.25$m

When Figures 5.7(a) and (b) are compared, the mesh dependence for different velocities of loading can be observed. The appearance of localisation in the extra-large mesh is much delayed compared with the smaller mesh. Figure 5.8 further illustrates the mesh sensitivity for individual loading rates. It is observed at first glance that Figures 5.8(f) to (h) are closely identical. This suggests that 1 s is sufficient to equalise the pore pressure across the specimen. As the earliest localisations are observed for these cases, the mesh dependence appears in advance compared to higher rates. When shear band material is fully drained, the hydro-mechanical coupling is lower. Hence the mesh sensitivity inherent to the effective material is much pronounced here. However, it should be noted that this response is not similar to fully drained behaviour in Chapter 4 where all material points are drained. This is because of the isochoric constraint imposed by impermeable global boundary conditions. Due to this kinematic constraint the unloading regions re-harden almost under a constant volume when the shear band material is softening.

Figure 5.8(a) and (b) show a mesh independent response when the loading rate is very large. In these two cases, a shear band does not appear for any mesh size at least until 0.1 m of displacement. This is because there is insufficient time for local water movements. Hence a mesh independent homogeneous response is observed.

Figures 5.8(c),(d) and (e) portray a clear mesh dependence after the localisation. The onsets of shear bands are delayed relative to the fully drained shear band cases. This time lag is because of the stabilising effect and dilative hardening due to hindered water movement. When the loading rate is greater, the transfer of load from fluid to soil skeleton is slow. An important observation in Figures 5.8(c) and (d) is that, when the element size is larger, the onset of localisation is delayed. In Figure 5.8(c), extra-large and large meshes do not localise

(until 0.1 m displacement) whereas medium and extra-small meshes portray the formation of shear bands.

Table 5.2 and 5.3 summarise the onset of two bifurcation criteria for different loading rates and mesh sizes. As discussed in Chapter 3, in associative NS model the determinant of acoustic tensor becomes zero at the peak deviatoric stress. Undrained dilative hardening materials do not achieve this state if the deformation is homogeneous. However, as predicted analytically by Guo (2013) and Vardoulakis (1996b) local volume changes are likely to happen after the maximum effective stress ratio. Hence partially drained shear bands can occur during the softening of the mobilised effective friction angle. Therefore, the Coulomb state marks the start of potential local volume changes whereas the singularity of the drained acoustic tensor signals the onset of drained localisation.

As observed in Table 5.3, the Coulomb state is subjective of both mesh size and loading duration. Therefore, the onset of the local drainage is mesh and time dependent. Table 5.2 confirms that, when the mesh size is larger, the localisation is delayed in saturated sand. This is in contrast to fully drained (dry) sand in which different element sizes inherent the same peak and start to localise at the same point. For fully drained sand only post-localised deformation is mesh sensitive whereas in saturated sand both onset and propagation of shear bands are mesh dependent. Moreover, when the loading rate is increased, the homogeneous deformation continues further delaying the onset of locally drained shear bands.

Table 5.2 Displacements at the first occurrence of zero determinant of drained acoustic tensor for different loading rates and mesh sizes

Duration of loading- Δt (s)	Displacement at first singularity of acoustic tensor (m)			
	Extra-large mesh	Large mesh	Medium mesh	Extra-small mesh
1000	0.0485	0.039	0.036	0.033
100	0.0485	0.039	0.036	0.034
10	0.0485	0.039	0.036	0.034
1	0.049	0.041	0.036	0.034
0.1	0.054	0.045	0.039	0.036
0.01	0.065	0.058	0.047	0.04
0.001	0.082	0.08	0.065	0.052
0.0001			0.088	0.071

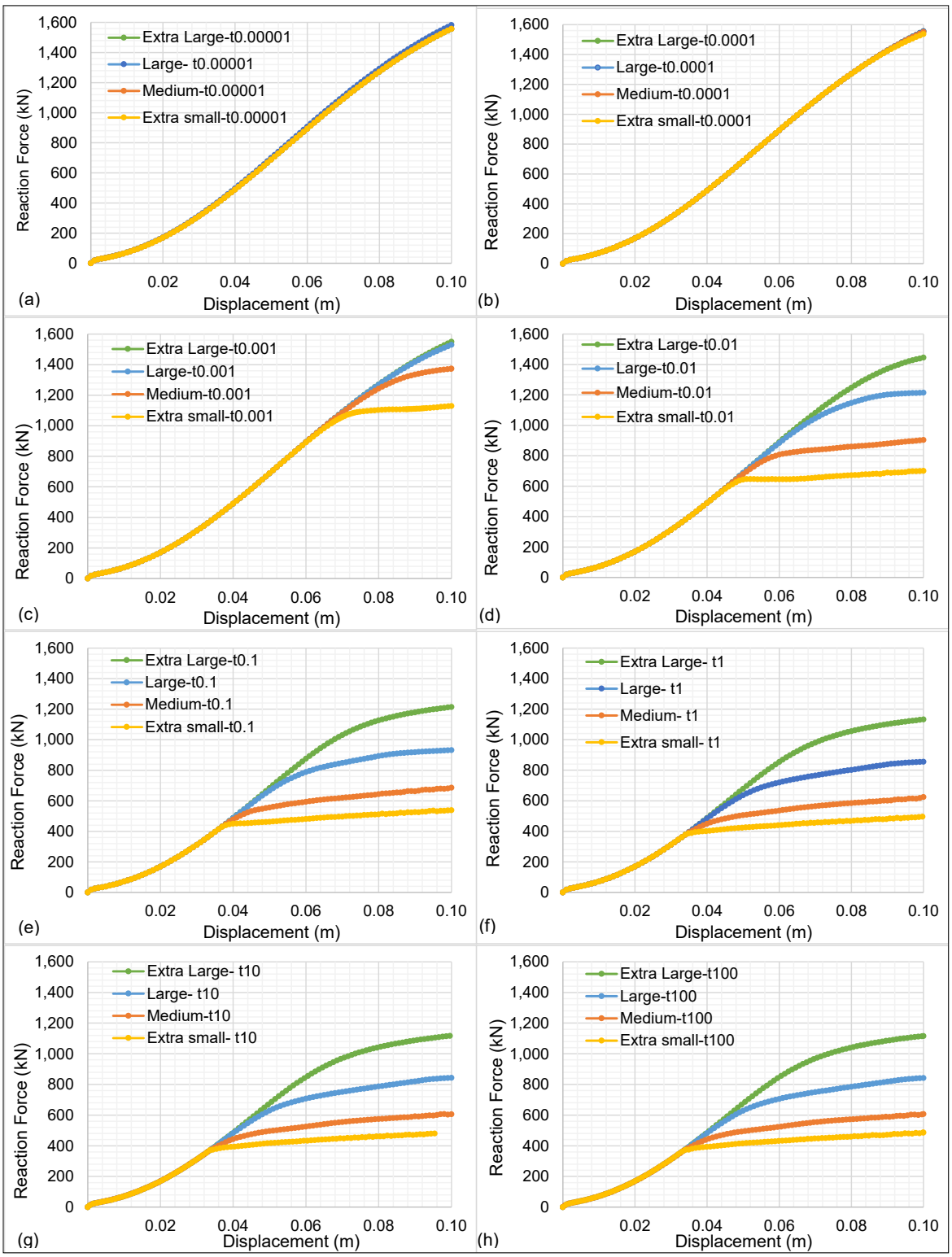

Fig. 5.8 The influence of element size on load-displacement relationships with different durations of loading: (a) 0.00001 s, (b) 0.0001 s, (c) 0.001 s, (d) 0.01 s,(e) 0.1 s, (f) 1 s, (g) 10 s and (h) 100 s : $p'_0 = 95\text{kPa}, W = 0.25\text{m}$

Table 5.3 Displacements at the first occurrence of Coulomb state for different loading rates and mesh sizes

Duration of loading- Δt (s)	Displacement at the first occurrence of Coulomb state (m)			
	Extra-large mesh	Large mesh	Medium mesh	Extra-small mesh
1000	0.017	0.016	0.016	0.0148
100	0.017	0.016	0.016	0.015
10	0.017	0.0164	0.016	0.015
1	0.017	0.017	0.016	0.015
0.1	0.018	0.018	0.017	0.016
0.01	0.02	0.02	0.019	0.019
0.001	0.023	0.023	0.022	0.022
0.0001	0.023	0.023	0.023	0.023

5.7.2 Effect of permeability

The previous section explored the effect of loading velocity keeping the permeability constant. Simulation series 2 investigates the role of permeability on the rate of diffusion and internal water movements. According to Equation 5.4 permeability has the counter effect of loading velocity. Thus decreasing permeability has similar consequences as the increasing loading rates. This is demonstrated in Figure 5.9 in which two permeabilities create the same response for different loading rates. In practical circumstances, the loading rate may not be large as considered in simulation series 1, but the permeability of sand can be reduced due to the mixing of silt and clay particles. The combined effect may lead to greater normalised velocity.

5.7.3 Classification of shear bands based on the local degree of drainage when remote boundaries are undrained

This section encloses the combined effect of both the loading rate and permeability. The maximum forces of the load-displacement curves in Figures 5.8 are plotted in Figure 5.10 against the normalised velocity. Since it is not possible to define peak loads, the maximum forces at 20 % strain are plotted for different mesh sizes. Based on Figure 5.10, the local drainage inside the specimen (when remote boundaries are undrained) can be divided into three regions: fully drained, partially drained and undrained homogeneous deformation.

A localisation appears when the characteristic pore fluid diffusion length ($l_k = \sqrt{\frac{c_v}{\dot{\gamma}}}$) is larger than the microstructural length (shear band thickness- t^{sb}) which is related to grain size

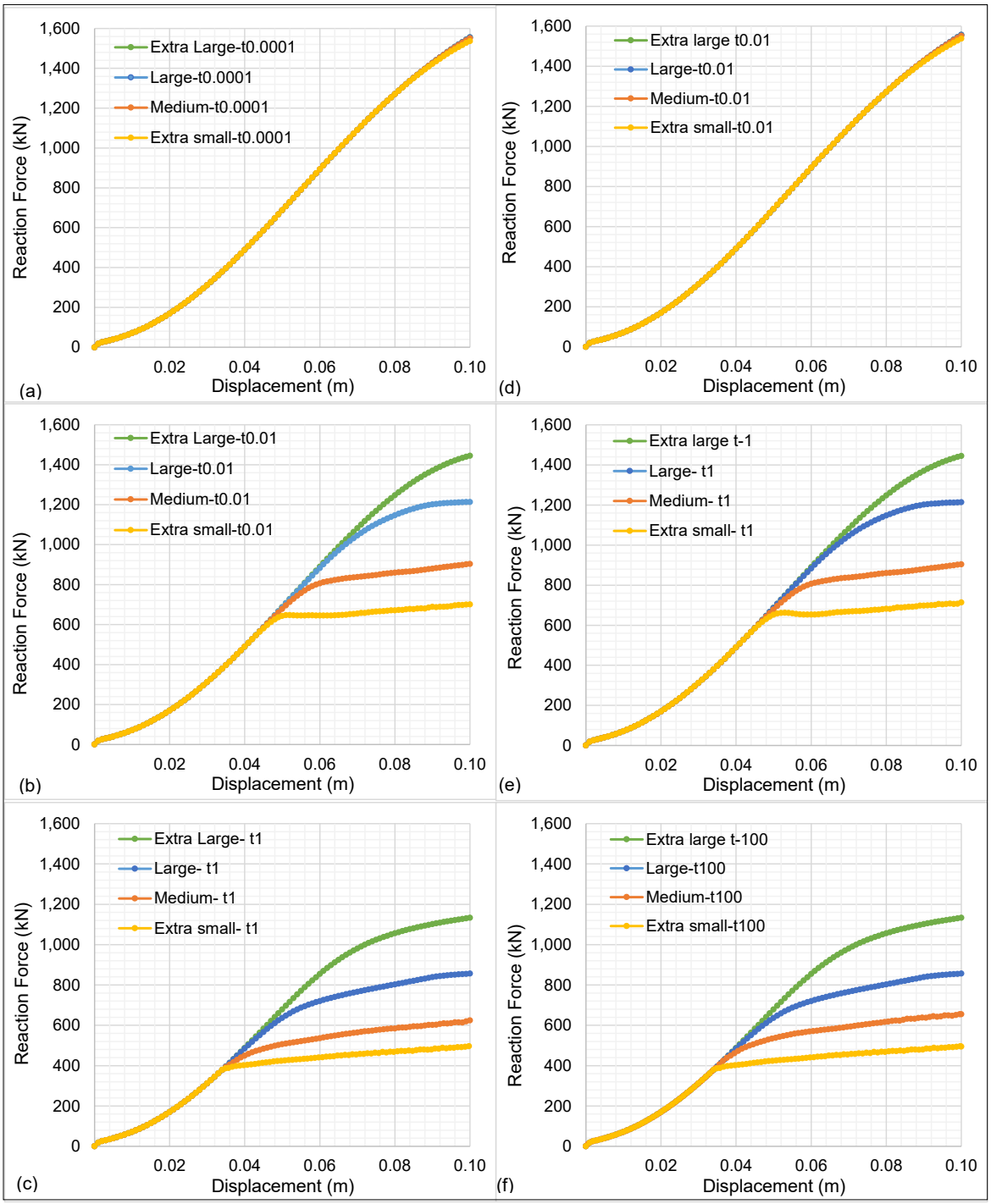

Fig. 5.9 The influence of permeability on load-displacement relationships under different rates of loading: (a),(b),(c) permeability 0.001 m/s and (d),(e),(f) permeability 0.00001 m/s:$p'_0 =$ 95kPa,$W = 0.25$m

experimentally or element size numerically. If the characteristic pore fluid diffusion length becomes larger than the specimen dimension, the shear band is fully drained. If it is smaller than the specimen dimension, the shear band is partially drained. If the characteristic pore fluid diffusion length is even smaller than the element size, then the instability appears in a diffused manner. This is what happens when the loading velocity becomes larger. Hence the perturbation wavelength is bounded by the element size and the specimen size.

The upper boundary for the fully (locally) drained shear band is at normalised velocity 0.01. Apparently, it is independent of the mesh size. On the contrary, the lower boundary for undrained homogeneous deformation depends on the mesh size. For the smallest mesh considered in this study, the locally undrained deformation is achieved at the normalised velocity 100. It is observed in Figure 5.10 that larger the mesh, the undrained condition is reached earlier. For the extra-large mesh, the undrained boundary is at a normalised velocity around 1. This means, when the mesh size is increased 10 times, the error in detecting the internal drainage is about normalised velocity 97. This clearly elucidates the deficiency of large meshes to capture the local fluid diffusion properly.

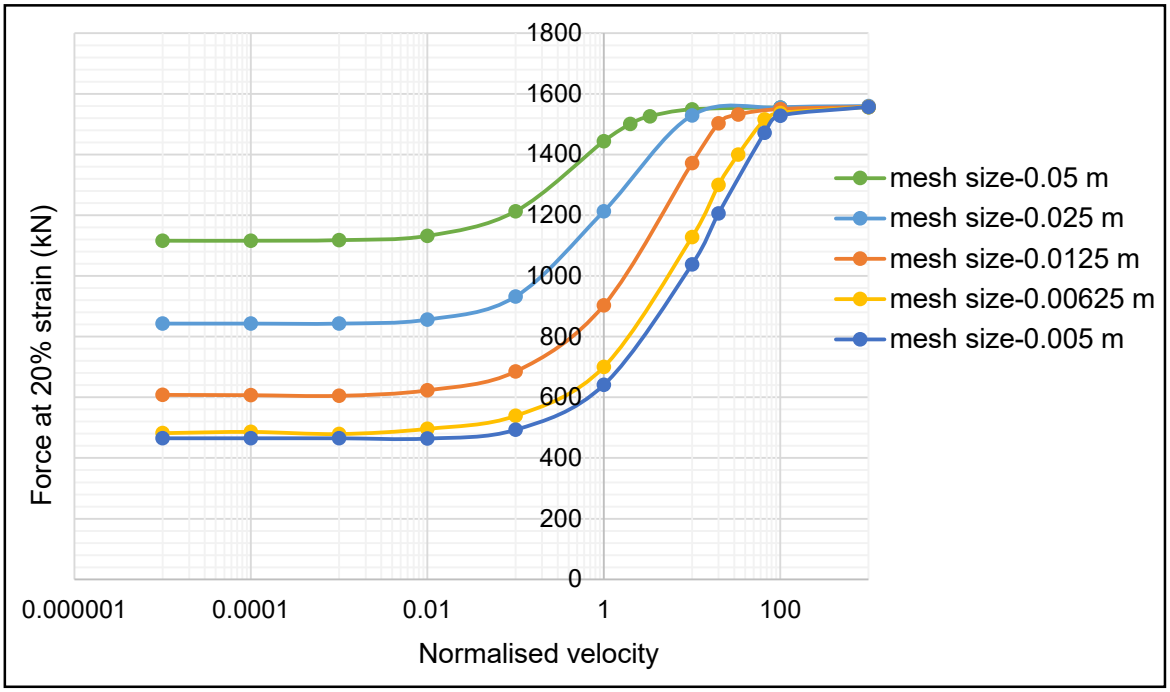

Fig. 5.10 Forces at 20 % of strain for different loading velocities and mesh sizes : $p'_0 = 95$ kPa,$W = 0.25$m

5.7.4 Effect of specimen size

Similar to velocity and permeability, the drainage distance also significantly influences the migration of pore fluid in saturated soil. A pore pressure gradient is generated within the

shear band thickness due to concentrated undrained shearing. Its drainage length depends on the proximity of the shear band to the remote boundaries. When boundaries are impermeable, pore water does not have the freedom to flow in or out. The drainage path can be assumed infinite if specimen dimension is large enough compared to the thickness of the band. Moreover, for the occurrence of a locally drained shear band, the dilative expansion inside the band should be accommodated by the contraction of outside material. Therefore, the element size as well as the specimen dimension, play crucial roles in the initiation of localisation.

The results of simulation series 1 and 3 are displayed in Figure 5.11. The forces at 20 % strain for a unit width of the specimen are plotted against the normalised velocity. Figures 5.11(a),(b) and (c) display the results of specimens with heights 0.5 m, 1 m and 0.25 m respectively. It is observed that the upper boundary of the fully drained region depends on the specimen size, not on the mesh size. This observation complies with Vardoulakis (1996b)'s theoretical derivation. He derived a global volume balance equation to be satisfied for the initiation of a locally drained shear band. It is independent of shear band thickness and depends on the specimen size, dilation and displacement rate.

Figure 5.11(d) aggregates the results of (a),(b) and (c). It illuminates that an equivalent response is shown when the ratio of specimen height to mesh size is the same. The lower boundary for the uniform deformation is sensitive to the ratio of specimen height to the mesh size. When the ratio is smaller, the undrained uniform deformation is achieved quicker. This means the instability caused by local drainage is suppressed when the specimen dimension to element size is small. This observation is consistent with the theoretical prediction of Vardoulakis (1996b). He predicted that zero fluid flux across specimen boundaries renders a stabilising effect prohibiting the internal fluid flow. This effect is dominant in the sand, for which specimen dimension to grain size ratio is small. Locally drained shear bands are more visible in clay for which this ratio is large.

Moreover, the locally undrained homogeneous strength is the same for all specimen and element sizes whereas the strength of fully (locally) drained shear band is sensitive to the specimen dimension to element size ratio. In essence, Figure 5.11(d) encapsulates both scale and time effects of locally drained shear bands when remote boundaries are undrained. To the author's knowledge, this is the first time this type of comprehensive numerical analysis is conducted to probe the scale and time effects behind the internal drainage in the saturated dilative sand. Irrespective of the numerous theoretical insights, this area has not been thoroughly investigated. Most of the experimental and numerical investigations on the localisation of saturated dense sand have emphasised on the phenomenon of cavitation and overseen the possibility of locally drained shear bands.

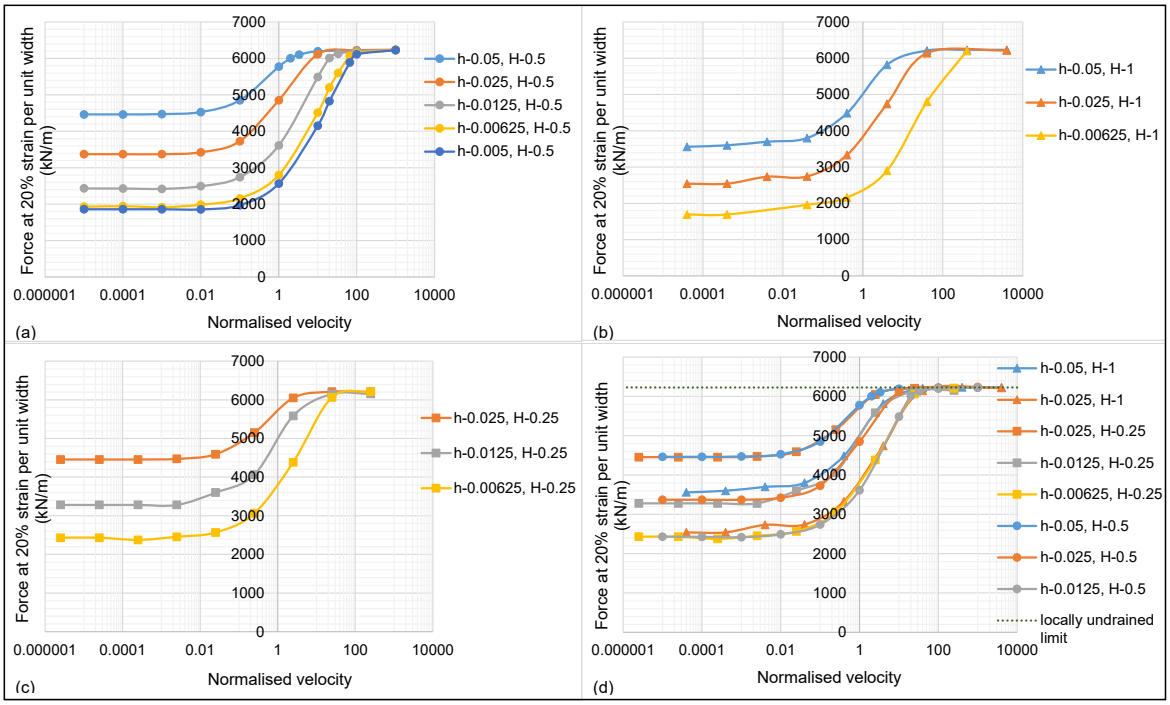

Fig. 5.11 Forces (at 20 % strain) per unit width of specimen for different loading velocities and mesh sizes for $p'_0 = 95$kPa: specimen heights (a) 0.5 m, (b) 1 m, (c) 0.25 m and (d) all

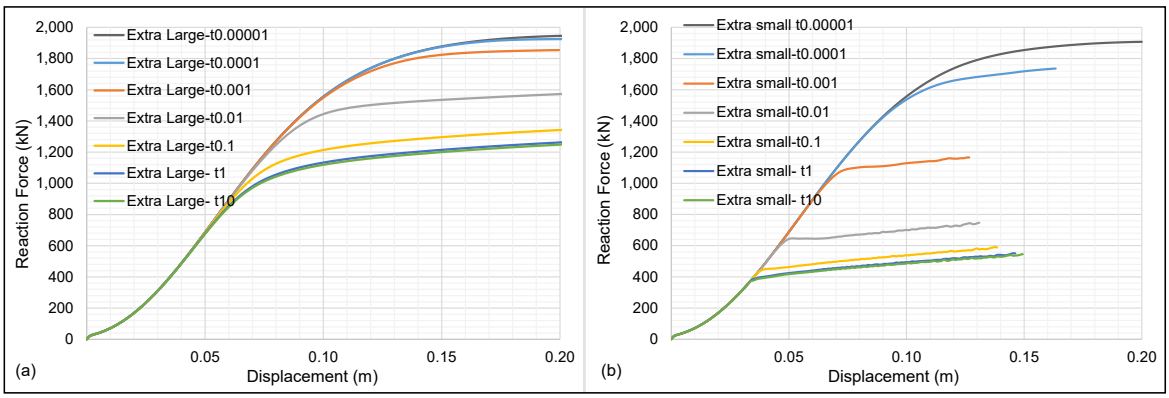

Fig. 5.12 Load-displacement relationships with different durations of loading in (a) extra-large and (b) extra-small mesh until 40 % strain : $p'_0 = 95$kPa,$W = 0.25$m

5.7.5 Effect of maximum strain

The maximum undrained force is dependent on the strain at which it is measured. If the undrained specimen is compressed up to the critical state maintaining the same velocity, the maximum force will be increased. Simulation series 1 is re-analysed displacing the samples up to 40 % strain. The results are shown in Figure 5.12. It is observed that reaction forces of all loading rates and mesh sizes increase with strain. Tests with higher loading rates reach the critical state uniformly and terminate further increase of load. The reaction forces of lower loading rates keep on increasing continuously due to the progressive development of shear

bands. Different material points reach the critical state at different stages, and the shear band thickness keeps on increasing attaching more material points to the band. Therefore, these reaction forces never achieve constant plateaus irrespective of the mesh size.

5.7.6 Features of fully drained shear bands when remote boundaries are undrained

It is observed in Figure 5.8 that when the loading duration exceeds 1s, the mechanical response of the undrained biaxial test is no longer rate dependent. The main characteristic in this region is the non-existence of a pore pressure gradient. As shown in Figure 5.13 the excess pore pressures in all meshes are uniform across the specimen from the beginning.

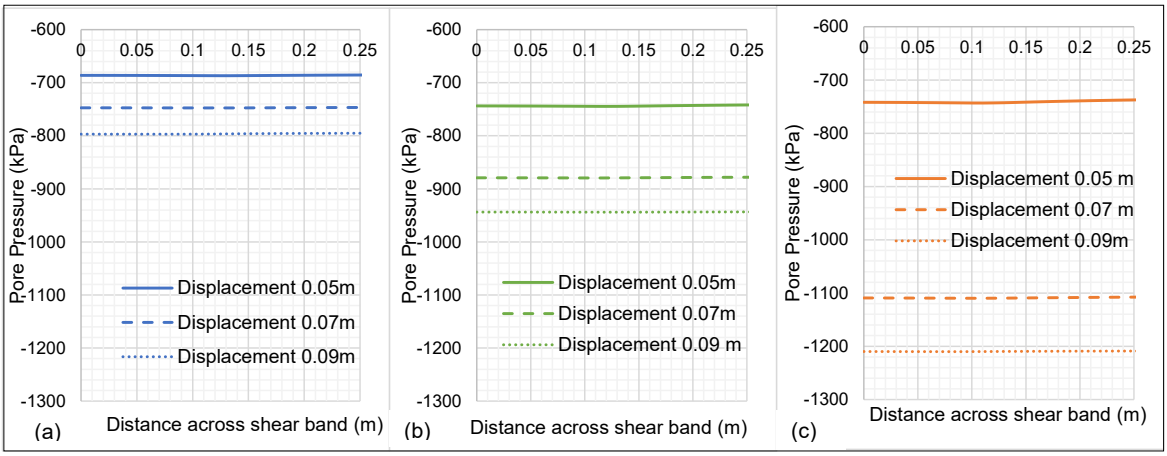

Fig. 5.13 Cross-sectional profiles of pore water pressure for loading duration 1s: (a) extra-small (b) medium and (c) large meshes

Material response in and out of the fully drained shear band

First, it is noticed in Figure 5.14(a) that the deviatoric strain inside the band escalates drastically compared to that outside, after the onset of localisation. It appears that all shear strain is concentrated inside the band while strain outside is almost constant throughout. Secondly, it is observed in Figure 5.14(b) that the constant volume constraint is broken locally by shear band material after the bifurcation. Localised material points inside the shear band expand considerably resembling almost a drained behaviour whereas those outside contract slightly. Figure 5.14(f) reflects that the state parameter inside the band has reached the critical state very early due to enhanced shear and volumetric strain. On the contrary, the state parameter outside hardly changes. This is further delineated in Figure 5.14(g). The outside material maintains almost a constant volume constraint and tries to reach the critical state by increasing the mean pressure. Shear band material breaks the volume constraint and reaches the critical state easily while decreasing the mean pressure. Complying with the local boundary conditions the deviatoric stress inside the shear band displays a drained

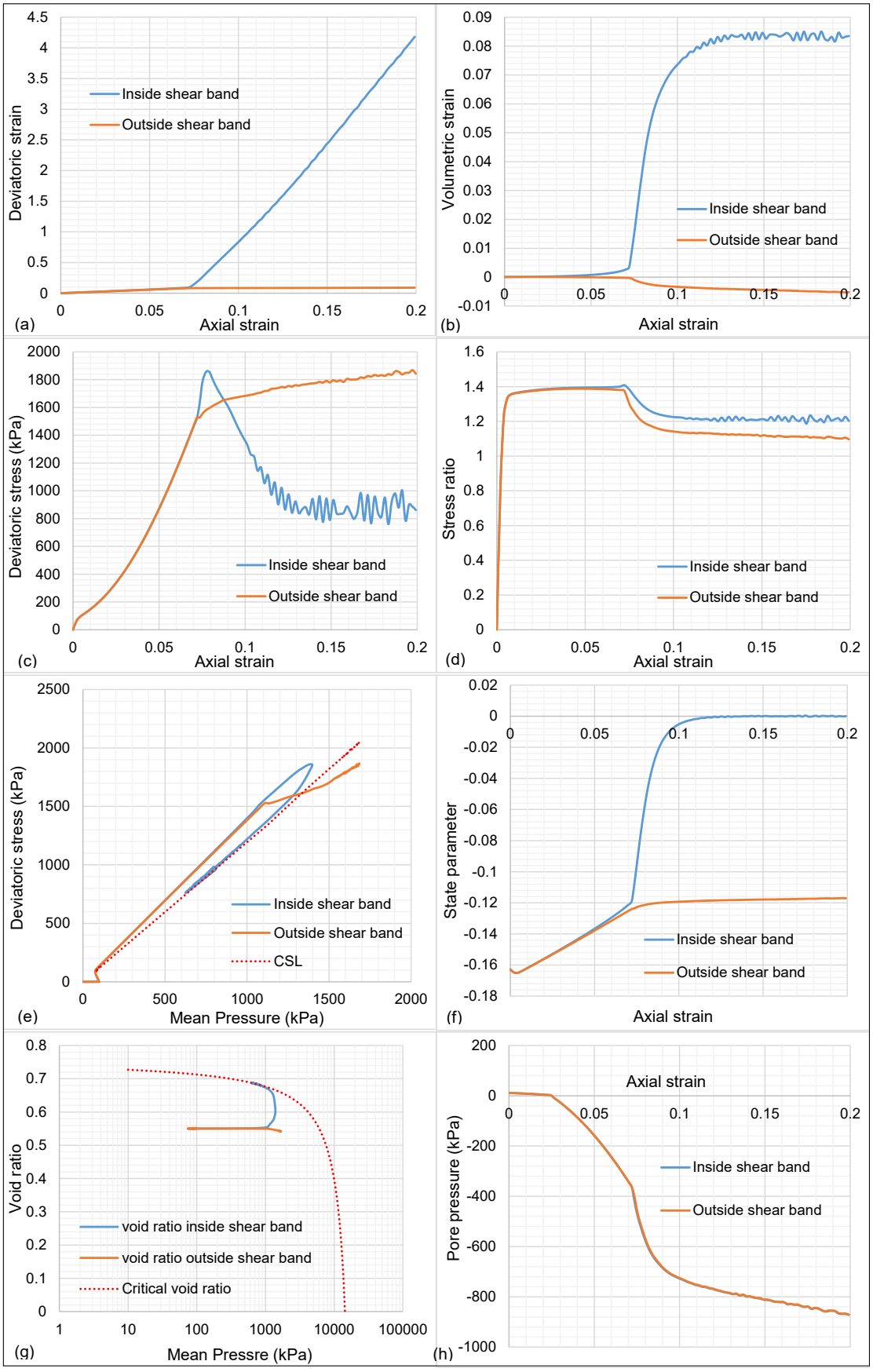

Fig. 5.14 Behaviour of selected material points in and out of the shear band in extra-small mesh for loading duration 1s: (a) shear strain (b) volumetric strain (c) deviatoric stress (d) stress ratio (e) stress path (f) state parameter (g) volumetric path and (h) excess pore water pressure

behaviour with softening as shown in Figure 5.14(c). Instead of elastic unloading, intact material outside the band hardens plastically.

Figure 5.14(e) further demonstrates that the stress path inside the shear band reverses after the peak while that of outside continues to increase although with a reduced gradient. Moreover, Figures 5.14(d) and (e) depict that the shear band has reached the critical stress ratio. Another important observation is that the material outside the shear band contributes more to the global response. In Figure 5.14(h) the nodal pore pressures in and out of the shear band are the same. This indicates a fully drained shear band without a pore pressure jump. In other words, there is sufficient time to dissipate the shear generated excess pore pressure across the specimen. In fact, the shear band sucks the outside fluid to prevent a pore pressure gradient. Still, the negative pore pressure keeps on increasing globally with the deformation.

5.7.7 Features of partially drained shear bands when remote boundaries are undrained

The upper boundary for fully drained bands and the lower boundary for the undrained homogeneous deformation set the limits of partially drained shear bands. Hence the lower boundary of partially drained shear bands is sensitive to the permeability and loading rate but independent of element size. Its upper boundary is sensitive to both rate and mesh size. This section investigates the characteristics of partially drained shear bands compared to fully (locally) drained shear band in the previous section. Results of simulation series 1, in which loading durations are smaller than 1s are probed in details here.

Local excess pore pressure gradient

Figures 5.15 displays cross-sectional pore pressure profiles across the shear bands of extra-small and extra-large mesh for loading durations of 0.01 s, 0.001 s and 0.0001 s. It is well observed in Figures 5.15(a) and (b) that pore pressure gradients are generated in the extra-small mesh. Although less pronounced, extra-large mesh also displays slight pore pressure gradients in Figures 5.15(d) and (e). This is in contrast to homogeneous pore pressure profiles in Figure 5.13 for fully drained shear bands. When the loading time is 1 s and permeability is 0.001 m/s, the excess pore pressure generated inside the band has sufficient time to dissipate. Hence the shear band is fully (locally) drained. On the contrary, when the loading duration is smaller, the pore pressure gradient can sustain longer. This is further demonstrated by the contours of pore pressure in Figure 5.16. When loading duration is 0.01 s, Figure 5.16 (a) shows an excess pore pressure gradient over the whole length of the shear band at displacement 0.05 m. It has sufficiently equalised by the displacement of

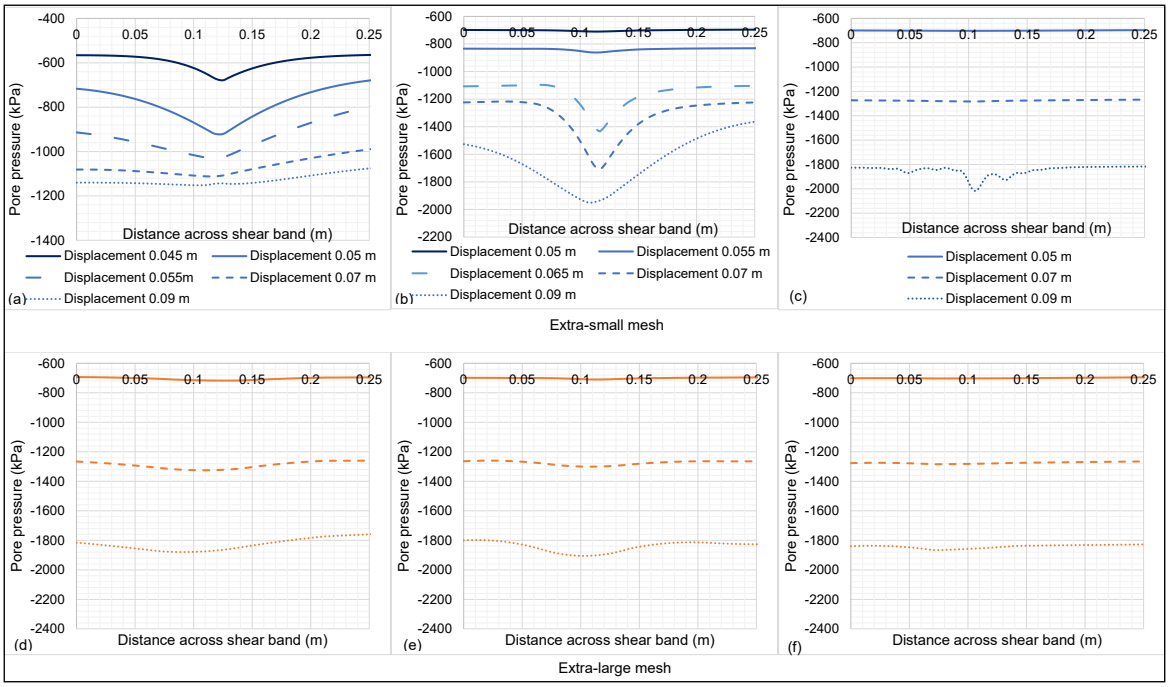

Fig. 5.15 Cross-sectional profiles of excess pore pressure for loading rates (a),(d) 0.01 s, (b),(e) 0.001 s and (c),(f) 0.0001 s : (a),(b),(c) extra-small mesh and (d),(e),(f) extra-large mesh

0.09 m. However, when the loading duration is 0.001 s, a pressure gradient persists at the displacement of 0.09 m.

Counter mechanisms of generation and dissipation of excess pore pressure in the vicinity of a saturated shear band can be explained assuming a constant shear rate, permeability and compressibility. When a shear band initiates, the difference between excess pore pressure inside and outside the band is relatively small. Hence the rate of dissipation is slower. On top of that, the rate of generation is greater as the dilation is larger during the initiation of a shear band. As a joint effect, the accumulated excess pore pressure gradient increases. However, with continuous shearing, the increased pressure difference causes the rate of dissipation to accelerate. Further, when the shear band reaches near the critical state, the dilation is diminished which in turn reduces the generation rate. As a consequence, the accumulated excess pore pressure gradient starts to reduce until it is fully equalised.

Comparing Figure 5.15 (a) and (b) it can be observed that, when the loading duration is shorter, the pressure gradient is sustained longer. However, under a sufficient deformation, the pore pressure gradient should subside and reach a steady state. In this state, the pore water volume flowing into the dilative shear band should be accommodated by the contraction

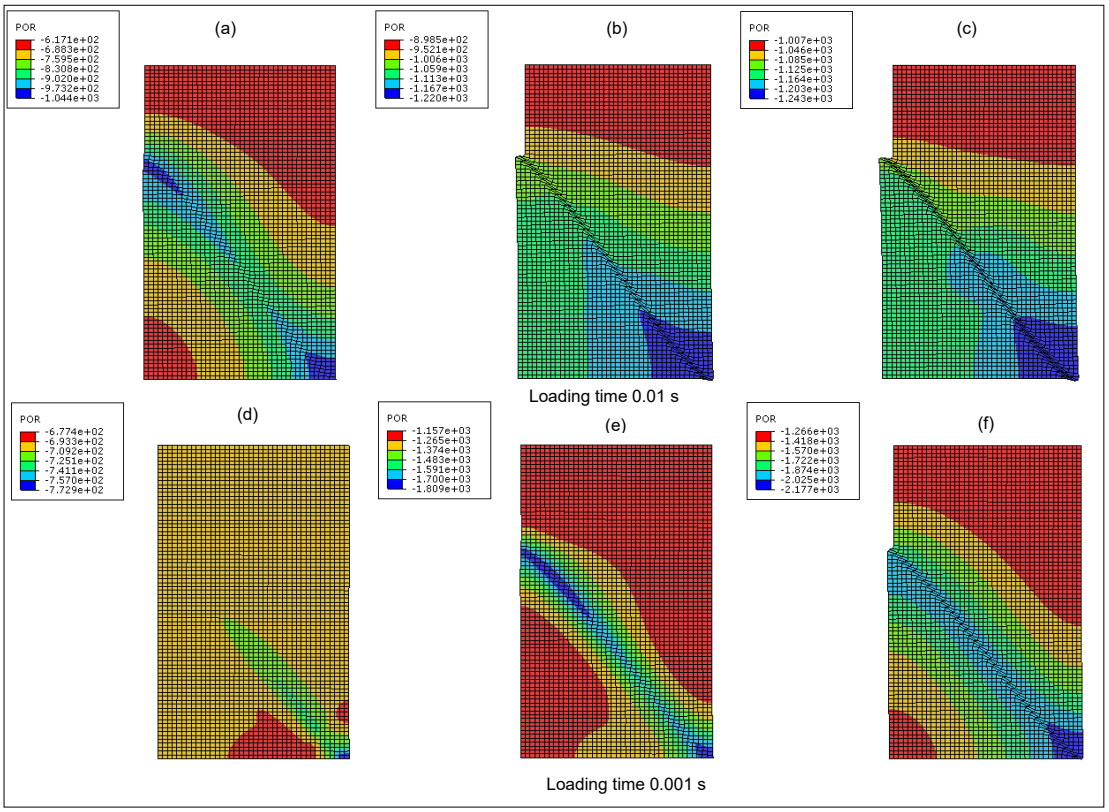

Fig. 5.16 Contours of excess pore pressure at displacements (a),(d) 0.05 m, (b),(e) 0.07 m and (c),(f) 0.09 m in extra-small mesh : for loading durations (a),(b),(c) 0.01s and (d),(e),(f) 0.001s

outside. It can be assumed that when the loading duration is larger than 1s, the pore pressure gradient have developed and dissipated during a single time step.

Local volume changes

The dissipation of excess pore water pressure mentioned above is associated with the flowing of fluid into the shear band. For this, the void space between particles inside the shear band should be increased. Hence the aforementioned local drainage is associated with a local volume change. This is shown in Figure 5.17 for different loading rates. It is first observed that the ability to capture the internal volume change is dependent on the mesh size. Smaller meshes are more competent in capturing local volume and shear deformations than larger meshes. This is a common observation even for localisation in dry sand, but the impotence of the large mesh is pronounced here due to the global isochoric constraint.

Moreover, Figures 5.17 (b),(c) and (f) show that, when the loading rate is increased, the local volume changes are inhibited and the locally isochoric constraint is achieved. This is further illustrated in cross-sectional profiles of the state parameter in Figure 5.18. When the loading rate is lower, the material inside the shear band in extra-small mesh reaches the

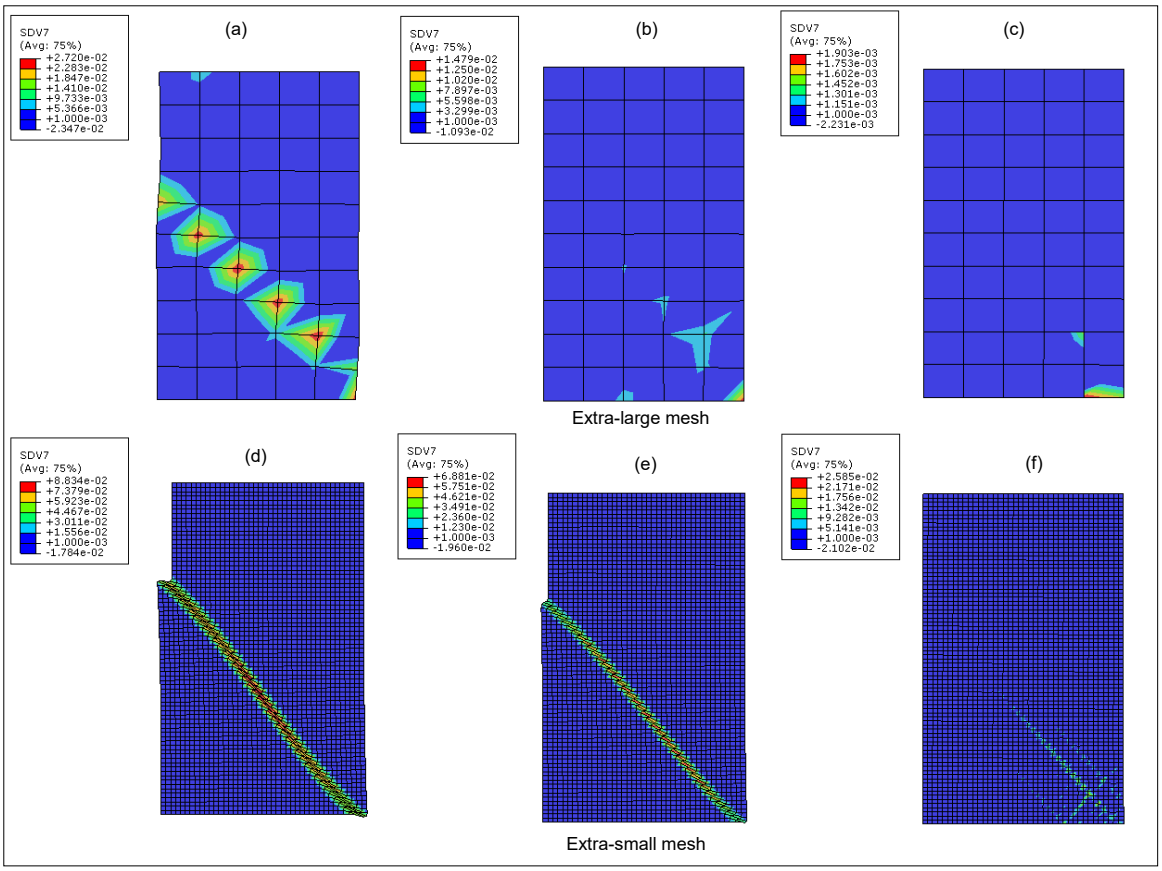

Fig. 5.17 Contours of volumetric strain for loading durations: (a),(d) 0.01 s, (b),(e) 0.001 s and (c),(f) 0.0001 s : (a),(b),(c) extra-large mesh and (d),(e),(f) extra-small mesh

critical state (due to local volume and mean pressure changes) whereas those outside stays at a constant volume and mean pressure. For higher loading rates, the state parameter increases homogeneously due to the increase of effective mean pressure albeit the local volume is constant. In the extra-large mesh, an almost homogeneous increase of state parameter is always observed due to mean pressure increase.

Material response in and out of the partially drained shear band

In this section, the shear band response for the loading duration 0.001 s is investigated. Compared to Figure 5.14, delayed onset of bifurcation is observed in Figure 5.19. Also, shear and volumetric deformations inside the band are much lower than Figure 5.14. Contraction of outside material cannot be seen in Figure 5.19(b) as in Figure 5.14(b). Since the bifurcation is delayed the deviatoric stress is much higher here compared to the fully drained case. The deviatoric stress inside the band in Figure 5.19(c) shows a softening. However, the material outside the band continues to harden plastically at a reduced rate even after the bifurcation. Only the stress path inside the shear band reaches the critical state. Also, the effective mean stress inside the band decreases along the critical state line as shown in Figures 5.19(e) and

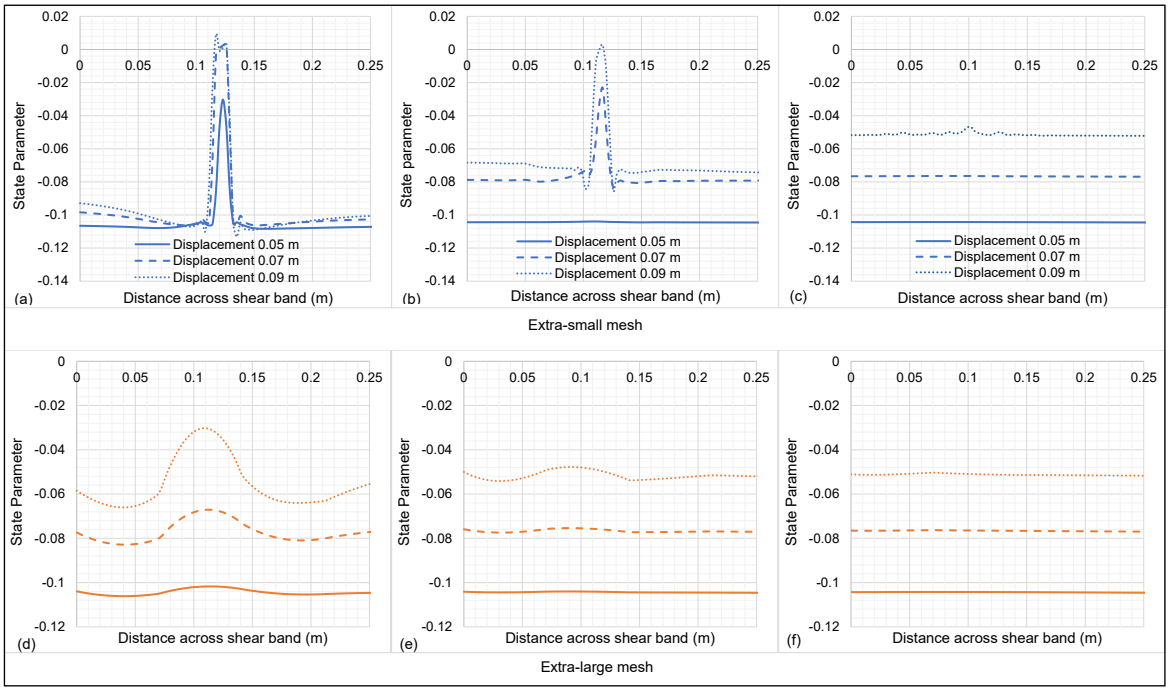

Fig. 5.18 Cross-sectional profiles of state parameter for loading durations: (a),(d) 0.01 s, (b),(e) 0.001 s and (c),(f) 0.0001 s : (a),(b),(c) extra-small mesh and (d),(e),(f) extra-large mesh

(g). The negative excess pore pressure inside the band is greater than outside as displayed in Figure 5.19(h). This demonstrates the partially drained behaviour in contrast to the fully drained behaviour in Figure 5.14(h).

5.7.8 Influence of normalised velocity on angle and thickness of shear bands

Table 5.4 displays shear band angles for different loading rates and mesh sizes from the results of simulation series 1. Angles are measured at 20 % strain. It is observed that in large elements shear bands are inclined at 45° representing a locally undrained behaviour irrespective of the duration of loading. Smaller meshes show larger inclinations close to the Coulomb angle. At the deformation of 20 % strain, shear band angles seem to be independent of loading rates and dependent only on the mesh size.

The evolution of shear band thickness in the extra-small mesh is given in Table 5.5 and Figure 5.20. Due to the inaccuracy in detecting the shear band thickness for larger meshes only results of the extra-small mesh is shown here. Saturated shear band thickness also increases with deformation due to accumulated dilation. It is observed that shear band thickness is hardly affected by the loading rate. In Figure 5.20, only the position of the band seems to be changed as the loading rate is increased.

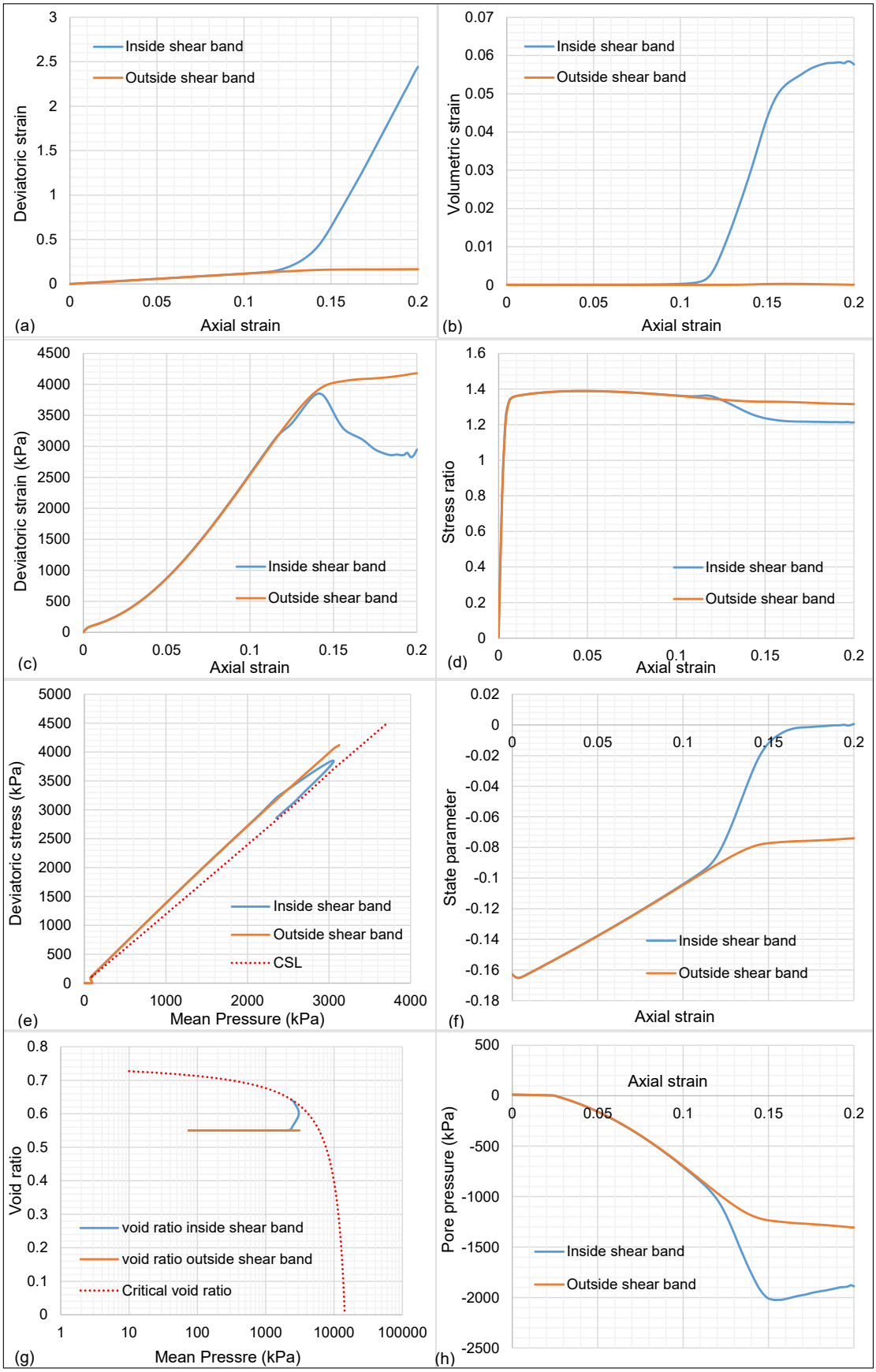

Fig. 5.19 Behaviour of selected material points in and out of the shear band in extra-fine mesh with loading duration 0.001 s: (a) shear strain (b) volumetric strain (c) deviatoric stress (d) stress ratio (e) stress path (f) state parameter (g) volumetric path and (h) excess pore water pressure

Table 5.4 Inclination of shear bands for different loading rates and mesh sizes

Duration of loading- Δt (s)	Shear band angles			
	Extra-large	Large	Medium	Extra-small
1000	45°	45°	49°	52.43°
1	45°	45°	49°	52.43°
0.1	45°	45°	49°	52.9°
0.01		45°	49°	52.9°
0.001			50.2°	52.3°

Table 5.5 Shear band thickness of extra-small mesh for different loading rates

Duration of loading- Δt (s)	Stage of deformation (m)	Shear band thickness (m)
1000	0.05	0.013
	0.07	0.015
	0.09	0.02
1	0.05	0.013
	0.08	0.015
0.1	0.05	0.015
	0.07	0.018
	0.09	0.018
0.01	0.05	0.015
	0.07	0.018
	0.09	0.02
0.001	0.05	
	0.07	0.015
	0.09	0.018

Both Thakur (2007) and Gylland (2012) reported from experimental observations that both shear band thickness and angle decrease with the loading rate in saturated soft clay. For contractive material, localisation is caused by the positive pore pressure gradient. It is dissipated when the shearing is slow enough, and as a result, the shear band is expanded. For faster rates, shear bands become thinner and inclined at 45°. For dilative shear bands both dilation and pore pressure dissipation cause the expansion of band. Hence it is difficult to identify the individual role played by the pore pressure gradient during formation of a shear band. Besides, the generation and dissipation of pore pressure is a simultaneous process. Therefore, the widths of excess pore pressure gradient in Figure 5.15 are much larger than the shear band widths in Figure 5.20.

This investigation is not comprehensive enough to draw a solid conclusion since it considers only a single cross-section. However, based on the presented results it can be concluded that the influence of permeability and loading rate dominates the onset of localisation in the saturated dilative sand. The post-bifurcation properties such as shear band thickness and angle are not much affected by the diffusion rate. According to Liu et al. (2005), if the permeability is greater, the shear bands are thinner in dense sand. It should be mentioned that it is not fair to compare shear band thickness at the same vertical displacement if permeability or loading rates are different; because shear bands are at various stages of their development since the onsets are dissimilar. Hence the percentage of load transfer from the fluid to the soil skeleton varies.

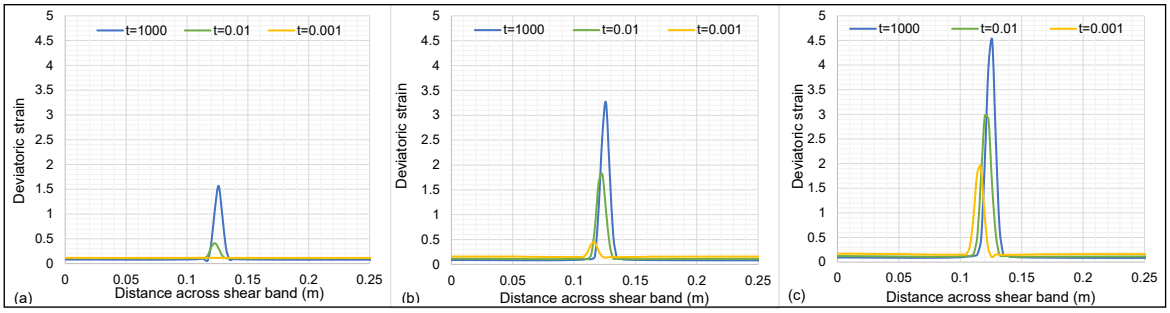

Fig. 5.20 Cross-sectional profiles of accumulated deviatoric strain at displacements: (a) 0.05 m, (b) 0.07 m and (c) 0.09 m in extra-small mesh with different loading rates

5.8 Results of Biaxial Compression Tests with Open Drainage Boundaries

In all the above analysis, global boundaries were considered as impermeable. This section investigates biaxial compression analysis with open drainage at top and bottom surfaces. Hence, water is allowed to flow in and out during shearing of dilative dense sand.

5.8.1 Effect of loading velocity

The results of the simulation series 4 are displayed in Figure 5.21. It illustrates the mesh sensitivity of biaxial compression tests with open drainage. It can be observed in Figure 5.21(a) and (b) that, when the loading durations are 0.00001 s and 0.0001 s, reaction forces are objective of the mesh size. At least up to 20 % strain, the biaxial specimens of all mesh sizes deform almost uniformly without any sign of shear bands. This is similar to Figures 5.8(a) and (b), but undrained reaction forces in Figures 5.21(a) and (b) are comparatively lower.

Similar load-displacement curves are observed when loading durations are 10 s and 100 s. Their peaks are mesh independent, but post-peak deformations are mesh sensitive. These

results are analogous with reaction forces of dry sand in Figure 4.10(a). It indicates the fully drained behaviour of all material points. They are different from Figures 5.8(g) and (h) where only shear band material points are fully drained.

When loading durations are in between 0.0001 s and 10 s, both peak and post-peak behaviours are mesh dependent as shown in Figures 5.21(c) to (f). Solid-fluid coupling is more active in these cases, and hence the onsets of localisations are mesh sensitive as well. A clear difference between Figure 5.8 and Figure 5.21 is the post-peak softening observed in these cases. In the former case, the internal drainage and volume changes occurred only inside the shear band. The global isochoric constraint dominated outside material points. On the contrary, when the top and bottom boundaries are permeable, external water is free to flow in. Hence outside material points can be partially drained as well.

5.8.2 Effect of maximum strain

Figure 5.22 displays the force-displacement curves of extra-large and extra-small meshes up to 40 % strain. In most cases, the post-peak deformations are reluctant to converge. When the loading duration is large enough to fully drain all the material points, further deformation does not change the residual strength. On the other extreme, when the loading duration is too fast, further deformation increases the strength. This is because all material points dilatively harden until the critical state is reached. Therefore, when the loading velocity is high, there is hardly any influence from the drainage conditions at remote boundaries.

5.8.3 Classification of shear bands based on the degree of drainage when horizontal boundaries are permeable

Figure 5.23 shows the maximum forces within 20 % strain. These are equivalent to peak forces if the peak is achieved within 20 % strain. Otherwise, they are reaction forces at 20 % strain. Figure 5.23 also displays three regions: fully drained, partially drained and undrained uniform deformation. It should be emphasised that in this case, the degree of drainage is applicable for all material points whereas in section 5.7.3 it is valid only for shear band points. The normalised velocity at the upper boundary of the fully drained region is almost the same as Figure 5.10. The lower boundary of uniform undrained deformation is achieved at a greater velocity than in Figure 5.10. The other difference is the mesh independent peak loads in the drained region.

When the water is allowed to flow in through the top and bottom boundaries, shear band patterns are different between drained and partially drained regions. Figure 5.24 illustrates contours of shear strain and excess pore water pressure for loading durations of 0.001 s and 10 s at displacement 0.07 m. Cross-shaped shear bands appear when the material points are

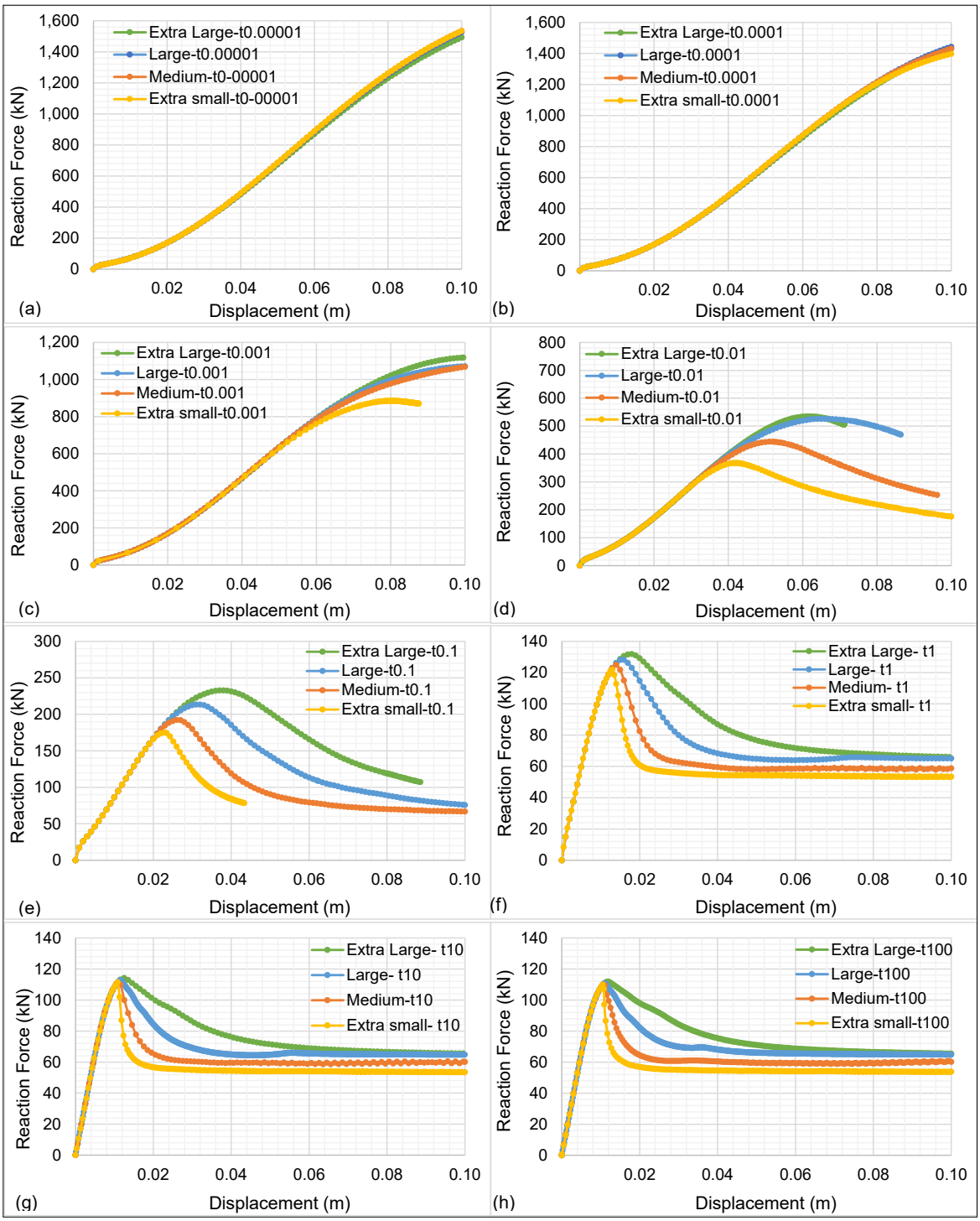

Fig. 5.21 The influence of element size on load-displacement relationships under open drainage boundaries with different durations of loading: (a) 0.00001 s, (b) 0.0001 s, (c) 0.001 s, (d) 0.01 s,(e) 0.1 s, (f) 1 s, (g) 10 s and (h) 100 s : $p_0' = 95\text{kPa}, W = 0.25\text{m}$

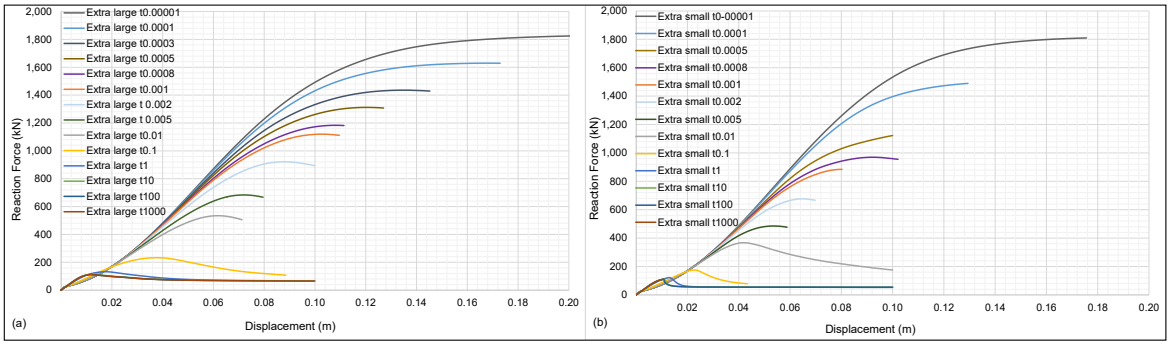

Fig. 5.22 Force-displacement relationships under open drainage boundaries with different durations of loading for (a) extra-large and (b) extra-small mesh till 40 % strain : $p'_0 = 95$kPa, $W = 0.25$m

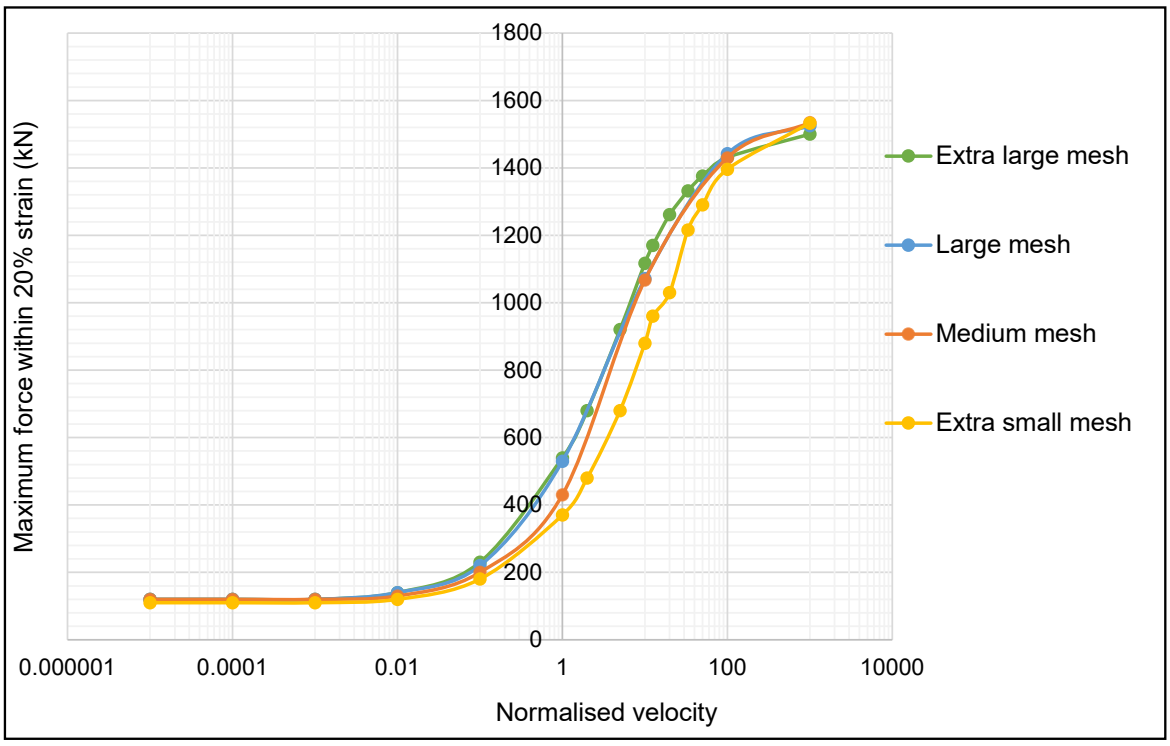

Fig. 5.23 Maximum forces within 20 % strain for different velocities and mesh sizes under open drainage boundaries : $p'_0 = 95$ kPa, $W = 0.25$m

partially drained whereas single diagonal shear bands emerge when they are fully drained. As seen in Figure 5.24(b), a pore pressure sink is created in the middle when there is not enough time to fully drain the specimen.

In conclusion, the ability of fluid movement at remote boundaries has a considerable impact on the overall behaviour of biaxial tests of saturated dense sand. However, its influence diminishes when the velocity is very fast or the permeability is low.

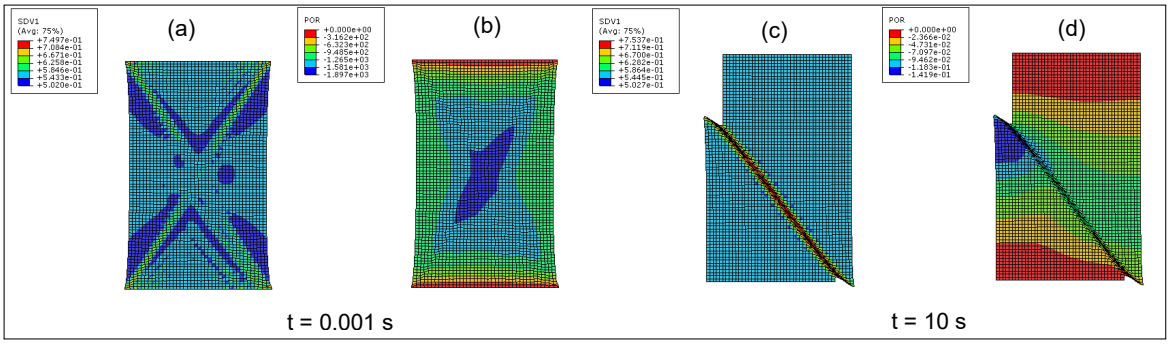

Fig. 5.24 (a),(c) Shear strain contours and (b),(d) pore pressure contours for loading durations: (a),(b) 0.001 s and (c),(d) 10 s at displacement 0.07m

5.8.4 Effect of drainage boundary conditions

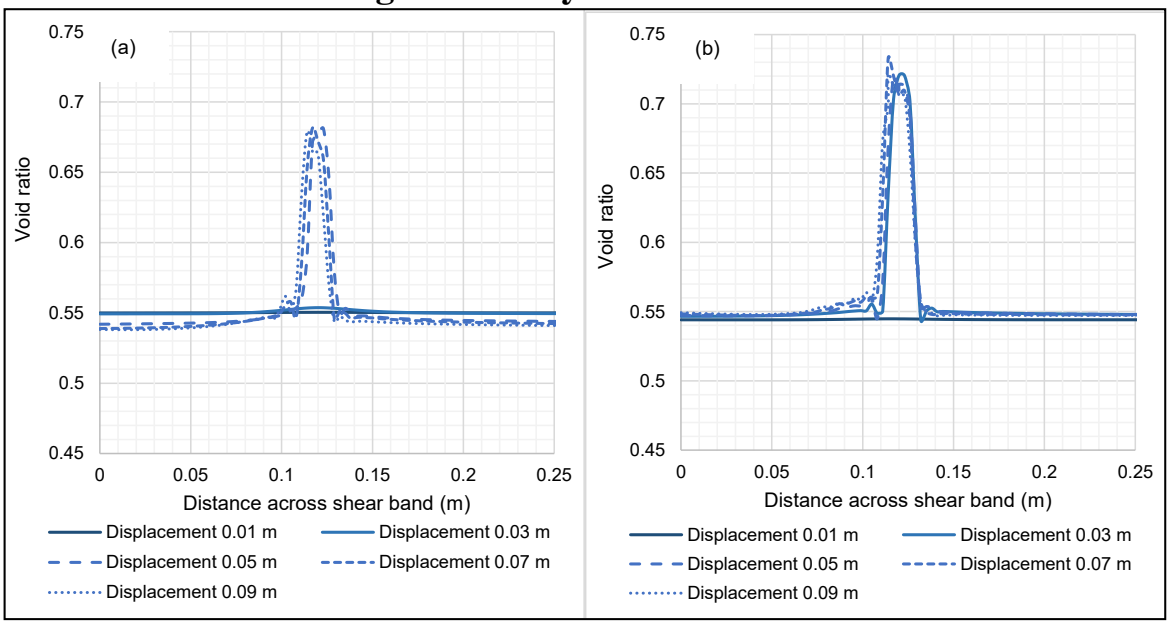

Fig. 5.25 Cross-sectional profiles of void ratio across the shear band when horizontal boundaries are (a) impermeable and (b) permeable: loading duration 10 s

The mechanism of pore fluid movement during localisation is sensitive to drainage condition at the top and bottom surfaces of the biaxial specimen. Figures 5.25 and 5.26 respectively demonstrate profiles of void ratio and excess pore pressure when drainage boundaries are closed vs open. Only the loading duration of 10 s is shown in Figures.

Under open drainage boundaries, volume changes can occur in all material points of the specimen. As shown in Figure 5.25 (b), until onset of the shear band, the whole specimen contracts initially followed by dilation. Pore fluid can move out of the specimen during contraction, and external fluid can flow into the specimen during dilation. After localisation, plastic volume changes are concentrated inside the shear band. Volume changes due to elastic

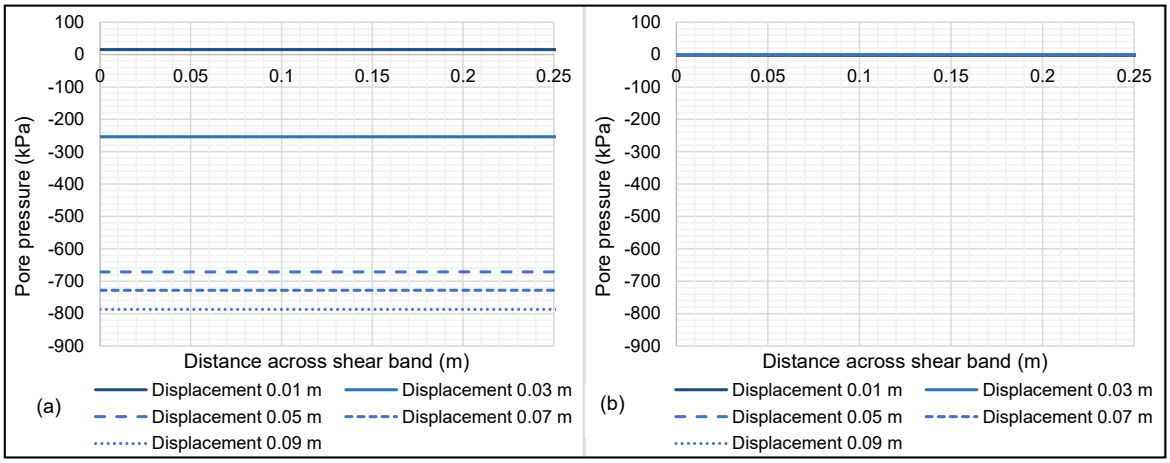

Fig. 5.26 Cross-sectional profiles of pore pressure across the shear band when horizontal boundaries are (a) impermeable and (b) permeable: loading duration 10 s

unloading of intact material are comparatively small. Figure 5.26 (b) displays that excess pore pressure is not generated throughout the deformation. This infers that when the loading duration is 10 s, the specimen is fully drained. The volume expansion inside the shear band is filled by water flowing in through top and bottom boundaries.

When drainage boundaries are closed, the local volume is constant until localisation. The tendency of dense sand to contract (initially) and then dilate produces positive and negative excess pore pressures successively, as shown in Figure 5.26 (a). After localisation, a considerable dilation takes place inside the shear band, creating a negative hydraulic gradient. As the fluid is not allowed to flow through the boundaries, the intact material contract, as shown by Figure 5.25 (a). Pore fluid inside the intact material flows into the shear band, satisfying the pressure gradient. The expansion of the shear band is equal to the contraction outside. Hence the global volume is constant in an average sense. According to Vardoulakis (1996b) this global volume conservation is dependent on dilatation of soil, specimen dimension, rate of loading and bulk modulus of water.

As previously explained by Figure 5.13, an accumulated hydraulic gradient can not be observed for loading duration of 10 s. Because a single time step of this duration is enough to dissipate the pore pressure gradient fully. If the loading duration is smaller the generation and dissipation of pore pressure gradient can be witnessed as in Figure 5.15.

5.9 Locally Undrained Deformation

For the sake of completeness, the observations made on fully undrained deformation are mentioned here. According to Figure 5.17(c), when the loading duration is 0.0001, the deformation appears to be homogeneous for the extra-large mesh. Each material point

behaves uniformly undrained. However, arrays of dilative and contractive bands are observed in the extra-small mesh in Figure 5.17(f). These are pore pressure shocks inclined at 45°. Vardoulakis (1996a) dismissed the possibility of locally undrained shear bands in experimental situations.

When the adopted time step for the consolidation analysis is below the minimum unstable time step provided by Vermeer and Verruijt (1981) spurious non-physical oscillations appear in pressure-sensitive plasticity. This critical time step depends on mesh size (Equation 5.4). Therefore, the results of FE simulations within this region is doubtful.

$$\text{time step} \geq \frac{\gamma_w h^2}{12(1+\nu)G^e \bar{k}} \tag{5.4}$$

Theoretically, locally undrained behaviour is unique irrespective of the drainage conditions of remote boundaries if the loading rate is fast enough. In these cases, the maximum reaction force is reached when all material points have uniformly approached the critical state. However, the normalised velocity required to achieve this condition is smaller if global boundaries are impermeable.

Further investigation on the locally undrained shear bands is beyond the scope of this thesis. Instead of transient consolidation simulation, a dynamic stability analysis considering the inertia terms similar to Vardoulakis (1986) is more accurate to study these kind of problems.

5.10 Application of Nonlocal Regularisation for Different Loading Rates

In Chapter 4 the nonlocal method was proved to be a successful localisation limiter for dry sand. When it comes to saturated sand, it is doubtful whether the regularisation of effective stress equations is sufficient to prevent mesh sensitivity. Because the generation and dissipation of excess pore pressure also contribute. The viscous effect of pore fluid governed by permeability and loading rates also play a role.

To evaluate the applicability of nonlocal theory on coupled problems, the extra-large mesh of numerical series 1 and 4 are re-analysed with regularisation. The method is the same as Chapter 4. The characteristic length is taken to be equivalent to the mesh size. The local analysis of extra-small mesh is considered as the benchmark case. Hence the scaling factor is 8. The regularised and scaled load-displacement curves of the extra-large mesh are compared with local analysis of extra-small mesh for different rates of loading. Figure 5.27 shows the globally undrained case whereas Figure 5.28 indicates results with permeable horizontal

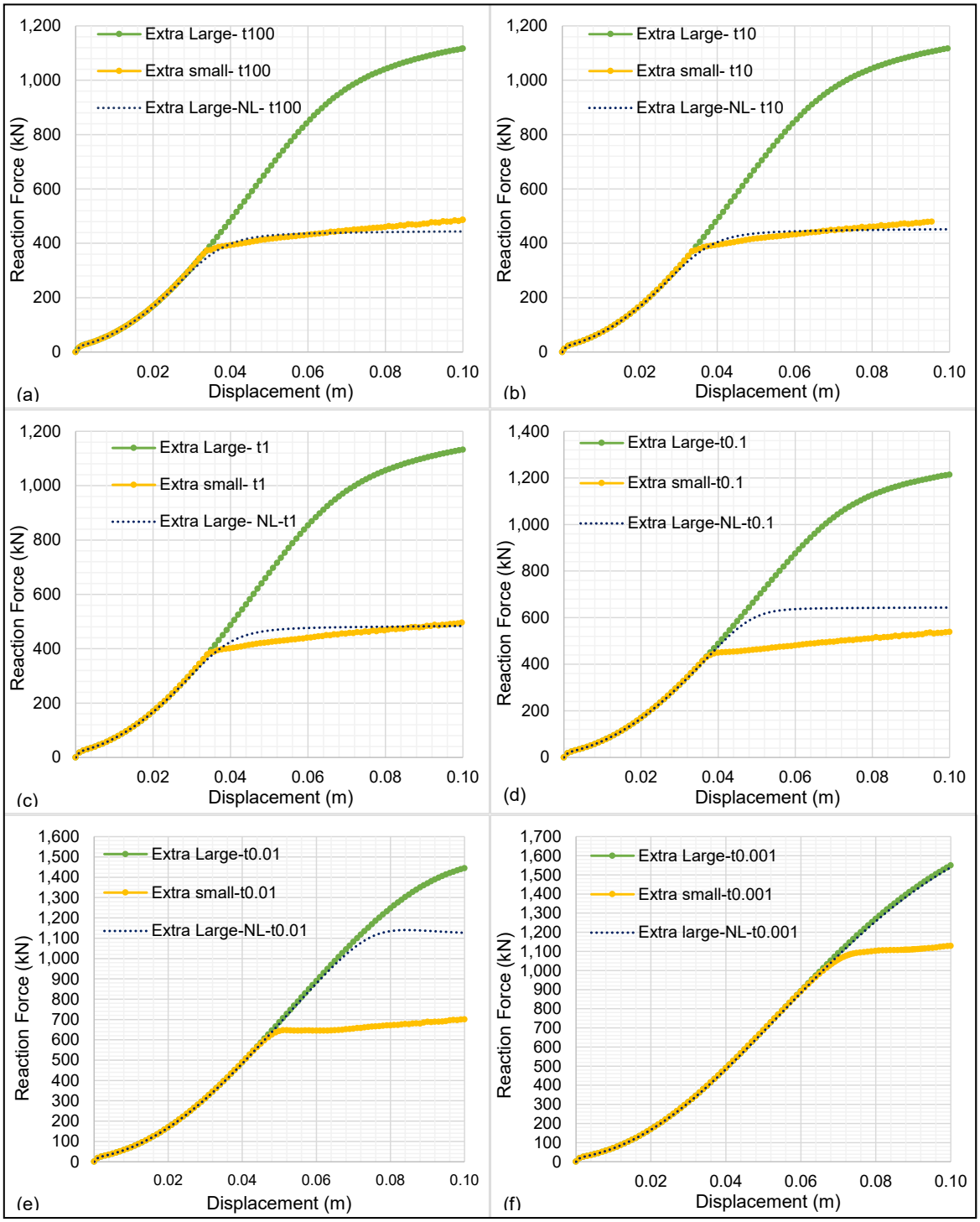

Fig. 5.27 Nonlocal regularisation and scaling applied to extra-large mesh with closed drainage boundaries under different durations of loading: (a) 100 s, (b) 10 s, (c) 1 s, (d) 0.1 s,(e) 0.01 s, (f) 0.001 s : $p'_0 = 95\text{kPa}$, $W = 0.25\text{m}$

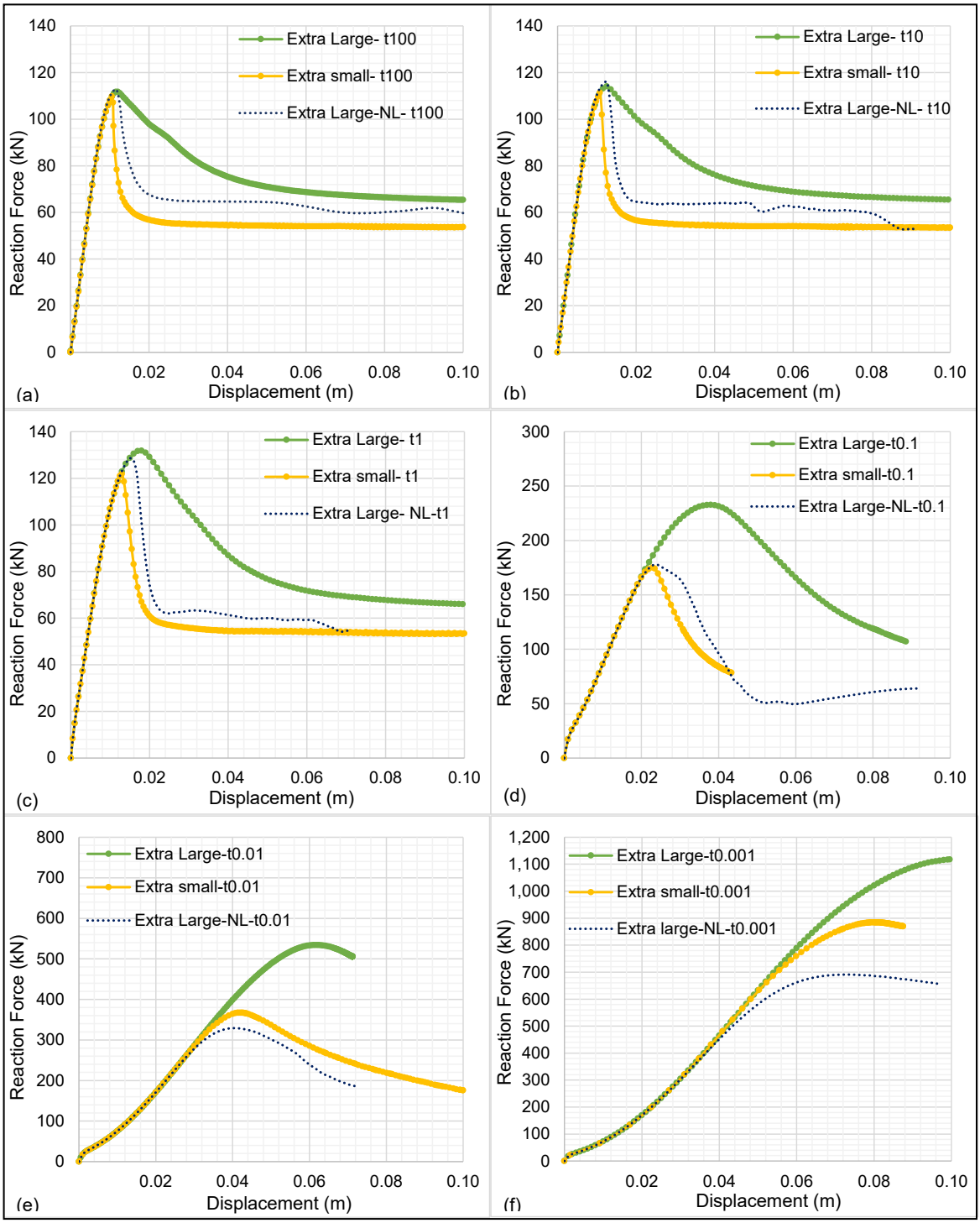

Fig. 5.28 Nonlocal regularisation and scaling applied to extra-large mesh with open drainage boundaries under different durations of loading: (a) 100 s, (b) 10 s, (c) 1 s, (d) 0.1 s,(e) 0.01 s, (f) 0.001 s : $p_0' = 95\text{kPa}$, $W = 0.25\text{m}$

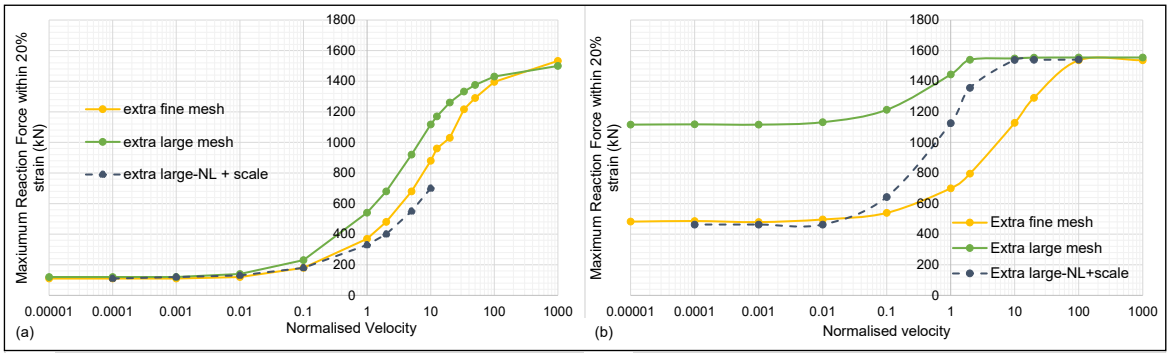

Fig. 5.29 Maximum forces plotted against normalised velocity for 0.5 m × 0.25 m biaxial compression tests with (a) permeable horizontal boundaries and (b) all impermeable boundaries

boundaries. It is noted when the hydro-mechanical coupling is involved, the minimum mesh size to produce converged results by conventional FEM decreased to 0.00625m while it was 0.01m for the dry analysis in Chapter 4. It must be due to the stabilisation provided by the viscous effect.

The extra-large mesh with regularisation and scaling produces closely matching responses to extra-small mesh only in Figures 5.27 and 5.28(a),(b) and (c). This means the nonlocal theory and scaling is effective only when there is sufficient time for the pore pressure to dissipate across the specimen. In Figures 5.28(a),(b) and (c) all material points are fully drained whereas in Figures 5.27(a),(b) and (c) the shear band is fully drained.

Table 5.6 Error of peak prediction using extra-large elements

	open drainage boundaries		closed drainage boundaries	
Normalised velocity	local NS	nonlocal NS	local NS	nonlocal NS
0.0001	1%	1%	130%	4%
0.001	3%	3%	130%	4%
0.01	6%	3%	132%	0%
0.1	31%	1%	130%	20%
1	46%	10%	107%	60%
10	23%	20%	40%	40%

Figure 5.29 encapsulates the maximum forces within 20 % strain for both mesh sizes against normalised velocity. Table 5.6 presents the mesh sensitivity error of extra-large mesh with local and nonlocal analysis. In the open drainage case, error on the peak prediction by the nonlocal method is within 10% when the normalised velocity is lower than 1. In fully undrained or closed drainage case, the local analysis with extra-large mesh shows 130% error when the normalised velocity is lower than 0.1. This can be reduced 4% to 20% with the

nonlocal averaging technique. Nevertheless, as shown in Figure 5.29 the error from nonlocal method gets higher when the normalised velocity is greater than 0.1.

The nonlocal NS model used here is based on nonlocal averaging of volumetric strain. Hence it works only when there are sufficient volume changes either locally or globally. When the loading rate increases, the pore pressure gradient is sustained longer diminishing the local volume changes inside the shear band. Hence the nonlocal NS model is hardly useful for the regularisation of the partially drained cases. For example, in Figure 5.27(f) the extra-large mesh does not bifurcate at all when the extra-small mesh shows a localisation. Moreover, scaling is applicable only for post-bifurcation deformation when shear band material points are softening. The nonlocal method cannot detect the onset of localisation decided by the hydro-mechanical coupling. The verdict might be the rate-independence of the constitutive model.

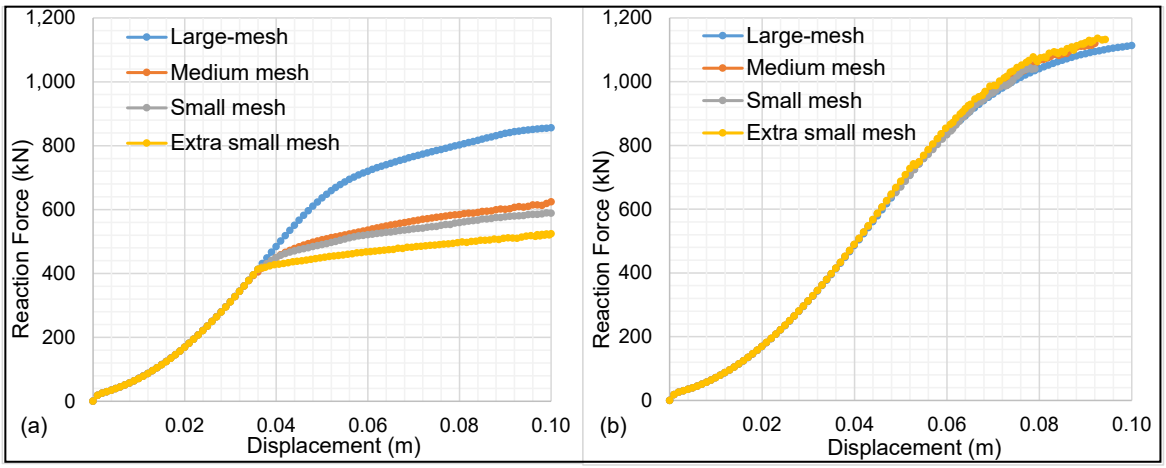

Fig. 5.30 Force-displacement relationships of undrained analysis: (a) local NS model and (b) nonlocal NS model with GandS weight function : $p'_0 = 95$kPa, $W = 0.25$m

5.10.1 Nonlocal regularisation of locally drained shear band

This section details the mechanism of nonlocal regularisation of fully drained (locally) shear band when global boundaries are impermeable. A mesh sensitivity analysis similar to Chapter 4 is conducted with large, medium, small and extra-small meshes under globally undrained condition. The loading duration is maintained as 1s such that the band is fully drained and pore pressure is uniform across the specimens. Hence, the time lag of the onsets of localisations between largest and smallest meshes is minimum. Both local and nonlocal force-displacement relationships are depicted in Figure 5.30. It is observed that the inclusion of an external characteristic length delays the onset of localisation and results are mesh independent after the bifurcation.

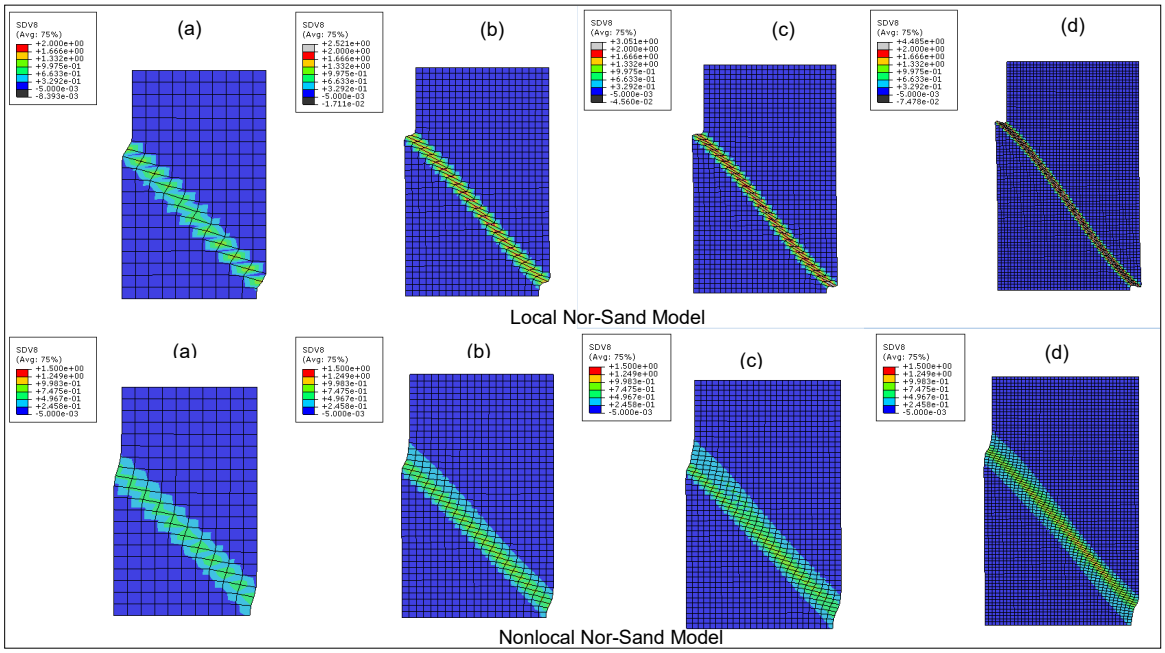

Fig. 5.31 Contours of accumulated plastic deviatoric strain from local NS model (upper row) and nonlocal NS model (lower row) at displacement 0.08m: (a) large,(b) medium, (c) small and (d) extra-small meshes

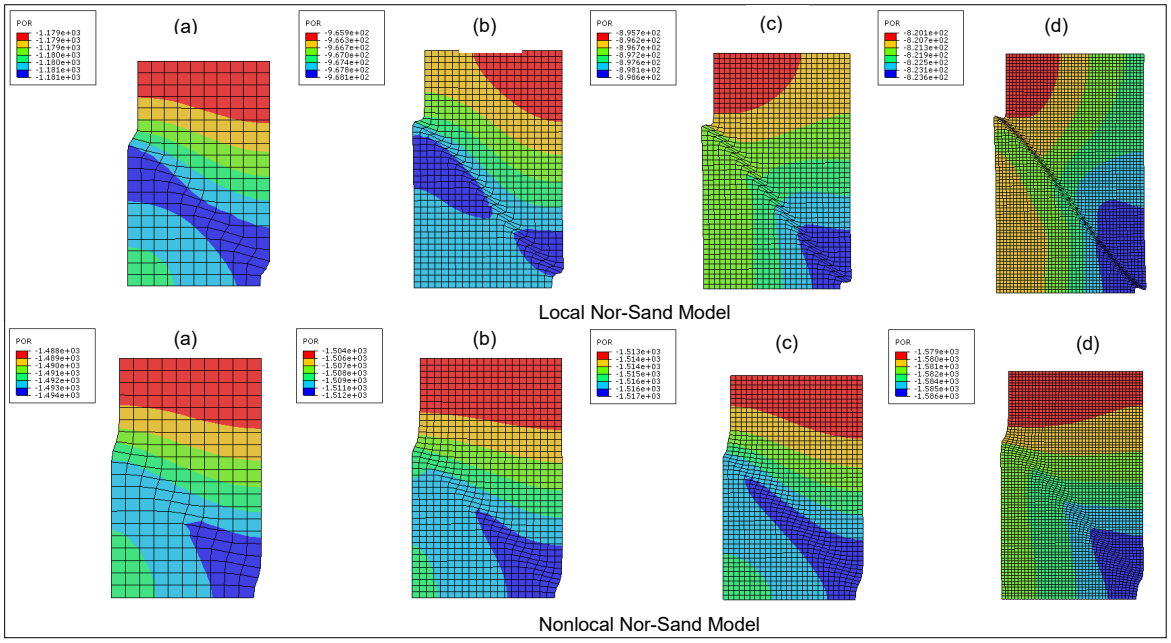

Fig. 5.32 Contours of pore pressure from local NS model (upper row) and nonlocal NS model (lower row) at displacement 0.08m: (a) large,(b) medium, (c) small and (d) extra-small meshes

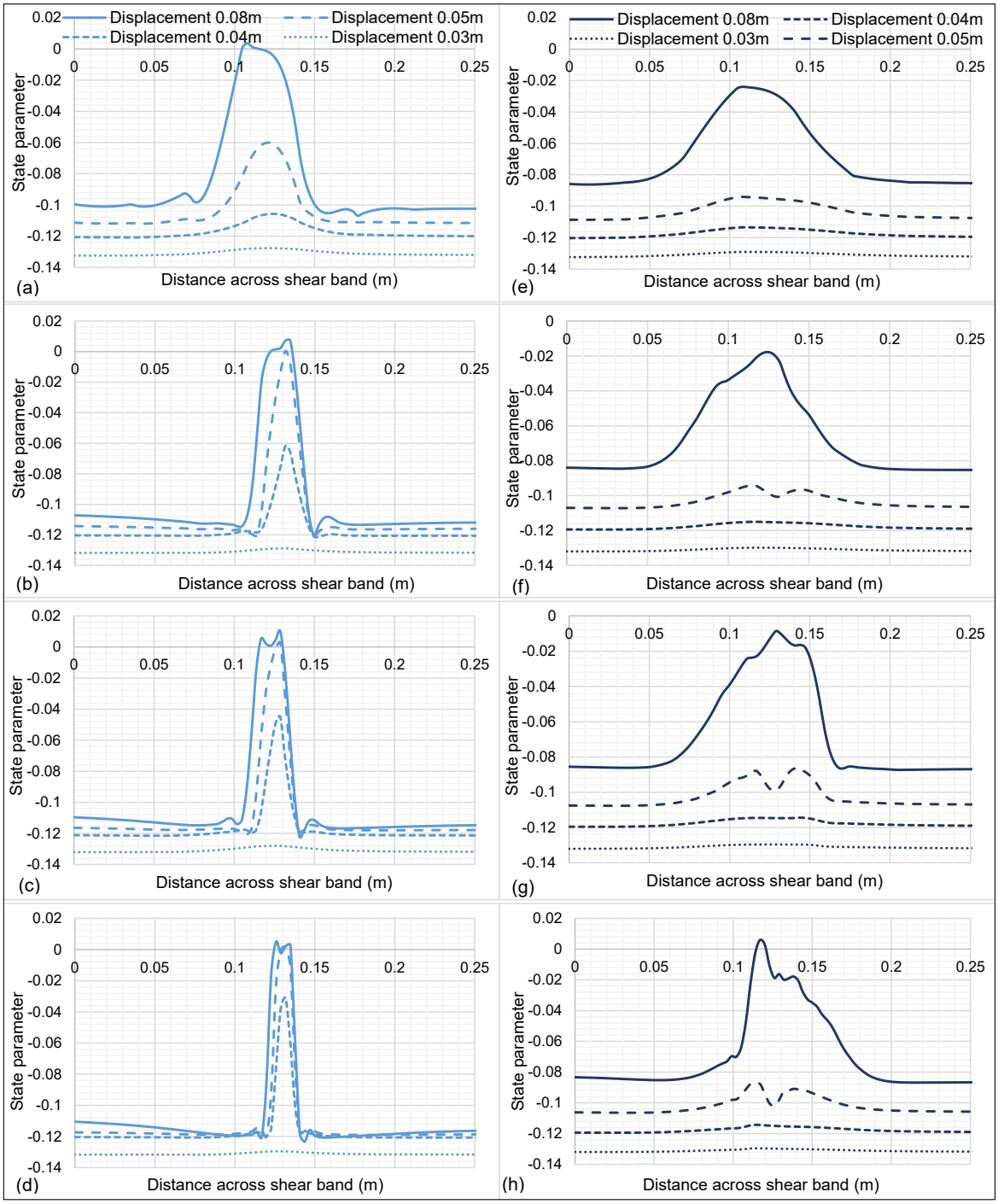

Fig. 5.33 Cross-sectional profiles of state parameter from local (left) and nonlocal (right) analysis of (a),(e) large (b),(f) medium (c),(g) small and (d),(h) extra-small meshes

Shear strain contours of local and nonlocal NS simulations at the vertical displacement of 0.08m are illustrated in Figure 5.31 upper and lower rows respectively. The nonlocal regularisation with GandS weight function alleviates the mesh sensitivity resulting in a similar shear band thickness.

The cross-sectional profiles of the state parameter at various states of deformations are shown in Figure 5.33. Before the localisation, the whole specimen tries to dilate homogeneously under a constant volume, which results in an increased mean pressure, hence a reduction of the critical void ratio. As a result, the state parameter can rise even without a volume change. Compared to the drained case in Figure 4.20 where the state parameter outside the shear band remains in its initial value, in the undrained case the state parameter increases outside as well. This is more obvious for the large mesh sizes. This is because, in the drained case, most material points outside elastically unload whereas in this case, the unloading is followed by the re-hardening. The effective mean pressure outside increases receiving the negative pore water pressure dissipated from the band, which causes re-hardening. Nonlocal regularisation has smeared the state parameter as shown in Figure 5.31 (right). Hence the dilation is spread over a larger area, albeit reduced. This results in more negative pore pressure outside the band leading to enhanced overall reaction forces. Figure 5.32 depicts that after regularisation the magnitude of pore pressure is mesh independent.

5.11 Conclusions

This chapter explores the time and space parameters which influence the pore fluid diffusion in saturated dense sand. Both permeable and impermeable remote boundaries are scrutinised. A rate-independent critical state elasto-plastic model is utilised for the numerical parametric study. The generation and dissipation of excess pore pressure gradients across localised bands are governed by the permeability, compressibility, loading velocity, mesh and specimen size as well as the remote boundary conditions. These factors decide whether localised zones are fully or partially drained. On the other extreme, the deformation can be uniformly undrained. Both the onset of the shear band and the post-bifurcation strength are sensitive to the above parameters. Internal water movements are always associated with local volume changes. Hence local boundary conditions are different from global ones. The onset of this local drainage is mesh sensitive.

The nonlocal regularisation with scaling is not effective when the hydro-mechanical coupling is more active. It can be applied for saturated sand only when there is no pore pressure difference between the shear band and outside.

5.11.1 Contributions

The main contributions of this chapter are

- A parametric study on the local drainage in saturated dense sand with undrained remote boundaries

  Additional to the loading velocity and permeability, the internal drainage (and volume changes) in globally undrained dense sand are sensitive to the mesh size and specimen dimensions. Both onset and propagation of localised deformation triggered by local drainage are governed jointly by both time and space parameters. Depending on the degree of local drainage, the globally undrained deformation can be characterised into three regimes: full or partial drainage inside the shear band and undrained homogeneous deformation. A localisation appears only when the characteristic pore fluid diffusion length is larger than the element size. If it is larger than the specimen dimension, the shear band is fully drained and partially drained otherwise. The normalised velocity at the upper boundary of (locally) fully drained shear bands is independent of the mesh size. On the contrary, the normalised velocity at the lower boundary of the locally undrained homogeneous deformation is governed by the mesh size. Hence, larger meshes overlook the pore fluid diffusion which occurs at a smaller scale.

- Investigation of characteristics of fully drained shear bands in saturated dense sand when remote boundaries are undrained.

  When the normalised velocity is lower than a certain limiting value, the amount of generated excess pore pressure dissipates within the same time step. Hence, there is no pressure difference between the shear band and outside. Within this region, the behaviour is rate independent but mesh dependent. The material points inside the band show fully drained behaviour with local volume changes whereas those outside display slight contractions. A global balance condition is achieved such that expansion inside the band is accommodated by contraction outside. The pore fluid is sucked into the band preserving the global isochoric constraint.

- Examining the characteristics of partially drained shear bands during globally undrained deformation of dense sand.

  There exists a range of normalised velocities within which localised bands are not fully drained. A pore pressure gradient can be sustained across these bands when there is no sufficient time to fully equalise the pore pressure across the specimen. The interplay between the rate of generation and dissipation of excess pore pressure inside the band decides the degree of local drainage. The local volume changes are affiliated with

local fluid movements irrespective of remote boundary conditions. This phenomenon which is hard to observe experimentally plays an important role in the development of strength. The generation and diffusion of the pore pressure gradient are mesh and rate sensitive. Except the onset of localisation, the inclination and thickness of partially drained bands are not sensitive to the normalised velocity. They are only dependent on the mesh size.

- Exploring the influence of global boundary conditions on the local drainage

  When global boundaries are impermeable, fluid is not allowed to flow in or out of the specimen. Hence the drainage is allowed only inside the specimen, irrespective of the normalised velocity. However, full drainage and volume changes are only permitted inside the shear band, because global volume should be constant in an average sense. The expansion inside the band should be compensated by contraction outside. Therefore, the strength of deformation with locally drained (fully or partially) shear bands is mesh sensitive. This strength increases even after the localisation, due to progressive dilation and reloading outside.

  On the contrary, when the water is allowed to flow across the remote boundaries, all material points can be fully or partially drained depending on the normalised velocity. Still, the drainage and volume changes inside the band are greater than the outside. If all material points are fully drained the peak strengths are not mesh-dependent; but if they are partially drained peak strengths are mesh-dependent.

  The locally undrained strength is independent of boundary conditions. However, the normalised velocity required to reach the locally undrained uniform deformation is sensitive to drainage condition at remote boundaries.

- Investigating the effectiveness of nonlocal averaging on circumventing the mesh sensitivity of saturated dense sand under different loading rates

  Nonlocal regularisation with scaling is effective only when either all material points or shear band material points are fully drained. Since the nonlocal NS model is built upon the volume averaging, it functions only when there are sufficient volume changes. This method is, in fact, suitable for the regularisation during the softening of the soil skeleton. Hence its accuracy is not good enough when the hydro-mechanical coupling is active. The mesh sensitivity error of 8 times larger mesh with nonlocal averaging is less than 20% when the normalised velocity is smaller than 0.1 and 1 for impermeable and permeable horizontal boundaries respectively. However, these remarks are only valid for the considered specimen size.

Chapter 6

A Constitutive Model for Undrained Dense Sand with Internal Drainage

6.1 Preface

Chapter 4 and 5 revealed that nonlocal averaging of the volumetric strain of the soil skeleton successfully alleviates the mesh sensitivity of fully drained (dry) sand and undrained sand with fully drained shear bands. Irrespective of global boundary conditions both cases are time independent. The duration of external loading is sufficient to fully drain the material points inside the shear band. Hence there is no pore pressure gradient across the shear band in both cases. The only discontinuity arises from the displacement gradient in effective stress equations. Thus, regularisation of underlying drained soil skeleton is proved to be successful.

Chapter 5 pointed out that there is a pore pressure discontinuity across partially drained shear bands. In these cases, the hydro-mechanical coupling is more active, and the problem is both time and space dependent. Therefore, explicit regularisation provided by the nonlocal method is not sufficient as there are two discontinuity fields. Notably, the accuracy of scaling during solid-fluid interaction is also doubtful. However, this may not be the case if a rate dependent constitutive model is used. According to Lazari et al. (2015a), the explicit internal length provided by nonlocal approach overrides the implicit length of visco-plasticity for slower loading rates. For high values of viscosity or greater loading rates, the visco-plasticity dominates the regularisation. In this case, the internal length provided by the viscous term is greater.

A similar argument can be applied here considering the rate effect of pore fluid flow. When the loading rate is high, or permeability is low, the effectiveness of nonlocal regularisation

diminishes. Nevertheless, the viscous regularisation bestowed by the hydro-mechanical coupling cannot be relied upon as the sole regularisation mechanism in these cases. Instead of including an artificial viscous term in the material behaviour to include rate effects, the focus here is to simulate the internal drainage at the material point level. The generation and dissipation of pore pressure for an assumed shear band thickness can be calculated at each gauss point which in turn adjusts the effective material behaviour.

This chapter introduces a novel phenomenological material model to apprehend internal water movements at the shear band scale, independent of the element size. Both time and space dependence of pore fluid diffusion in saturated dense sand is captured. Section 6.2 summarises several constitutive models which have the same school of thought and previous theoretical studies on pore fluid diffusion. Section 6.3 outlines the hypothesis of the proposed approach. The numerical formulations are given in section 6.4. The proposed model is calibrated with undrained extra-small mesh in section 6.5. Then its validity for large scale boundary problems is assessed in section 6.6. Chapter 6 concludes by discussing the limitations of the method in section 6.7.

6.2 Previous Studies on Modelling Internal Drainage

Fluid migration happens within pore volume which has a much smaller scale than the element size. To allow internal drainage within the elements Larsson et al. (1996), Larsson and Larsson (1999, 2000a,b) developed an embedded shear band approach. The regularised strong discontinuities of pore pressure and displacement are implemented in mixed variational formulations from "enhanced strain" method. Two additional degrees of freedom: enhanced strain and enhanced pore pressure are included to regularise discontinuities. The embedded shear band is activated in elements which satisfy the lowest of drained or undrained localisation criteria. Equilibrium equations are solved both at the element and global levels. Numerical results indicated that embedded localisation captured both the onset and post-localised regime minimising the mesh sensitivity.

The aforementioned approach needs tedious changes of equilibrium equations and involves extra degrees of freedom. Instead, Pietruszczak (1995, 1999) opted to augment the constitutive relations governing the macroscopic undrained response in the presence of a fully drained or undrained shear band. This method captured the exchange of fluid inside the element (between the shear band and intact material) under globally undrained constraint. The macroscopic response is formulated by homogenisation based on volume averaging of both constituents. As the thickness of the shear band is included in constitutive relations, this method is inherently mesh independent. First, he explored the behaviour when both

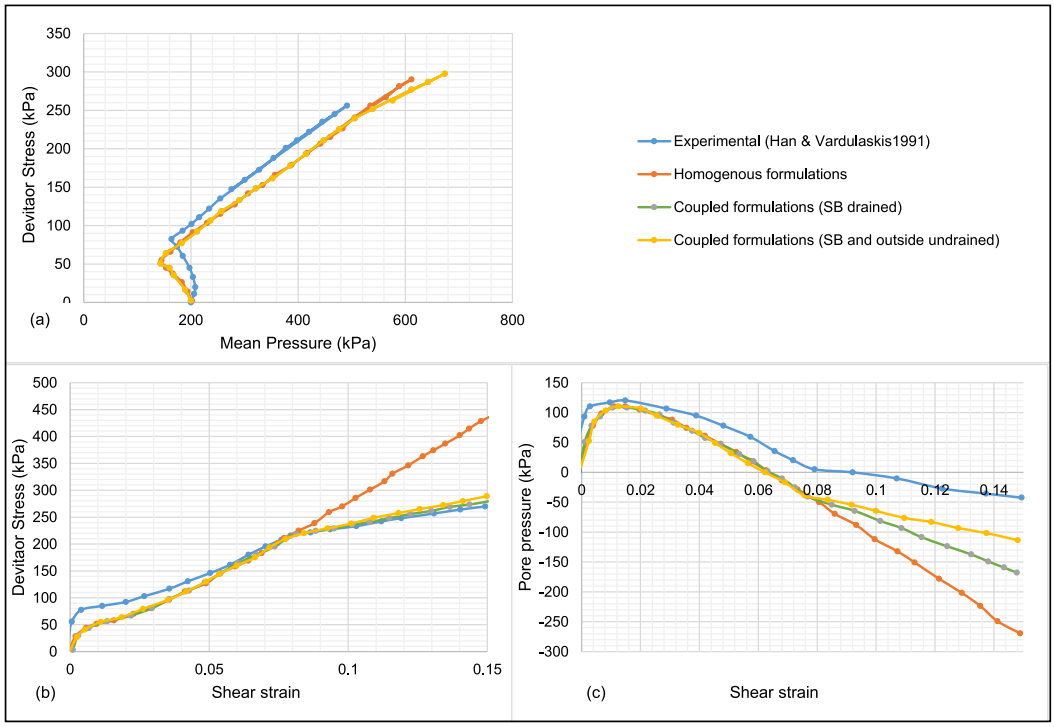

Fig. 6.1 Undrained response of dense sand: (a) effective stress path, (b) deviatoric stress-strain relationship and (c) excess pore pressure (Pietruszczak, 1995)

constituents are undrained, and there is no transient flow of water either externally or internally. This phenomenon occurs during raid loading when there is insufficient time for the excess pore pressure to dissipate. Then, he studied the internal drainage at a steady state under globally undrained deformation.

To determine the point of transition from homogenised to localised deformation under undrained constraint, Pietruszczak (1995) decided to use a physically based criterion rather than the conventional bifurcation analysis. So he selected the onset of the shear band based on experimental data. As illustrated in Figure 6.1(a) and (b) the force of the homogeneous deformation mode continuously advances while the inhomogeneous mode shows a decrease of stiffness after the incept of localisation. However, the deviatoric stress-strain curve is still stable irrespective of strain softening inside the shear band material. Hence the impact of localisation caused by internal drainage is less severe than the full drained case.

When both constituents are undrained, they undergo plastic loading whereas in coupled formulations the intact material is unloading. Hence the rate of pore pressure generation decreases abruptly at localisation as depicted in Figure 6.1(c). Fully undrained formulations predict different pore pressures in and out of the shear band. In the coupled drained formulations, both shear band and outer material share the same pore pressure, and it is

lower than the undrained pore pressure. These numerical predictions qualitatively agree with experimental observations even though there is no solid data to validate.

In the author's point of view, this method is quite simple and promising. The drawback of this approach is that it cannot take account of the rate effect involved with pore pressure diffusion. Hence it can only model fully drained or undrained shear bands. It is interesting to see the behaviour of a partially drained shear band in this context.

6.2.1 Analytical Solutions for Fluid Diffusion

Rate effects of pore pressure diffusion during localised deformations were theoretically investigated by Rudnicki (1983),Palmer (1999) and Vardoulakis (1996b). These studies lay the foundation of the intended constitutive model. Based on the simple consolidation theory, Thakur (2007), Puzrin and Randolph (2015) derived analytical expressions for the variation of pore pressure inside a shear band during undrained shearing. In Equation 6.1, shear-induced dilation is the additional source of volume expansion inside the band.

$$\frac{\partial U}{\partial t} = c_v \frac{\partial^2 U}{\partial^2 z} + \frac{tan(\psi)\dot{\gamma}}{m_v} \tag{6.1}$$

where $\dot{\gamma}$ is the shear strain rate and ψ is the dilation angle. Outside the shear band experiences elastic unloading with minimum volumetric changes. Hence the simple diffusion equation without the last term represents outside.

6.3 Motivation and Objective

In the conventional multi-phase finite element method, pore pressure values are calculated at nodes similar to displacement. Hence the generation of pore pressure gradient and its dissipation depend on the relative positions of nodes. The diffusion cannot occur in a length scale smaller than the element size. This makes internal water movements in and out of the shear band mesh dependent. The implication of pore fluid interaction with soil affects the onset, inclination and thickness of the shear band. The development of localised zones dramatically increases the internal drainage which ultimately decides the mechanical response of soil. Since the mesh refinement is extremely expensive for large scale problems bridging the micro and macro response is necessary.

The objective of this study is to develop a phenomenological constitutive relationship for the undrained dense sand, which is embedded with a fully or partially drained shear band. It should be able to capture the internal fluid movements and volume changes between the shear band and intact material taking both the rates of loading and the size of the band into consideration. Therefore, both time and space effect can be captured in the constitutive

level. The macroscopic strength is decided by the excess pore pressure generation and diffusion within the shear band. Thus, the influence of underlying micro-kinematics can be apprehended with sufficient accuracy without changing equilibrium equations.

The proposed concept captures the inhomogeneous deformation of a fine mesh by a single material point. The school of thought is similar to Pietruszczak (1995), but different in implementation. The hypothesis of this development is illustrated in Figure 6.2. Figure 6.2(a) shows a globally undrained biaxial compression specimen with an extra-small mesh. A locally drained shear band is propagated in it due to the weak material points. Figure 6.2(b) shows a single element (or material point) with the same dimensions and boundary conditions. Impermeable boundaries are presumed in both tests to maintain the globally undrained and constant volume condition. The aim is to replicate the mechanical response of the extra-small mesh by a phenomenological constitutive relationship of a single point.

The hypothesis here is that the finite element analysis with an extra-fine mesh can reproduce the actual local drainage in dense sand. This is the most plausible alternative due to the lack of experimental evidence. Another important assumption here is that global isochoric constraint is not broken at the localisation. This means desaturation or phase change does not occur. This assumption is valid for deep sea condition where the hydrostatic pressure is large enough to delay the cavitation.

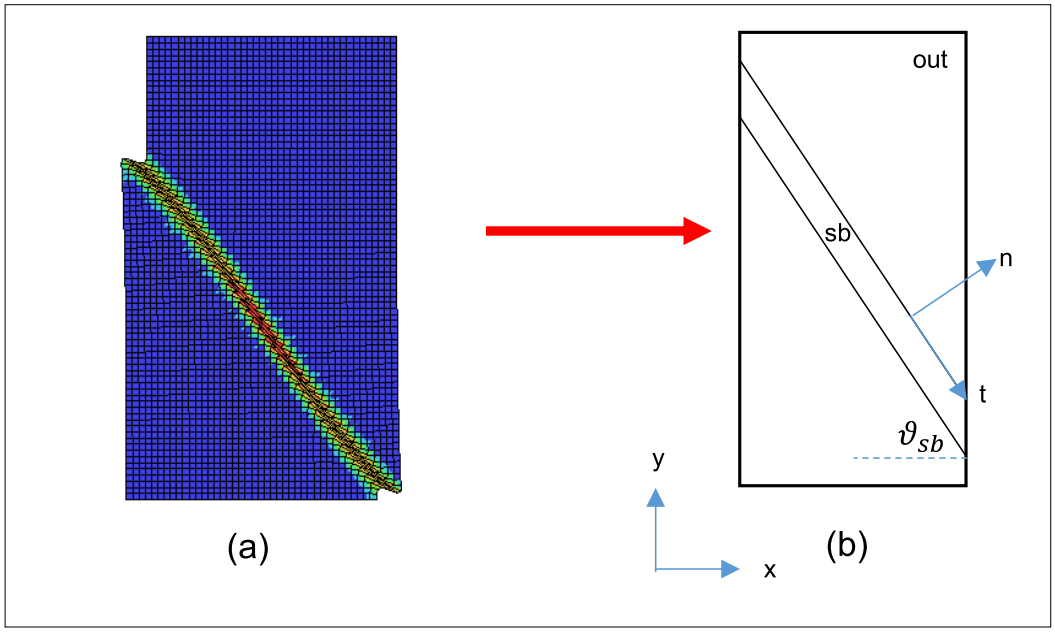

Fig. 6.2 Globally undrained biaxial compression of (a) an extra-small mesh represented by (b) a single material point

6.4 Numerical Procedure for the Embedded Shear Band

The details of mathematical formulations derived for the embedded shear band approach is described in this section. The hierarchical formulations of the overall process are encapsulated in the flow diagram in Figure 6.3. Ordinary constitutive formulations are carried out until the bifurcation criterion is met. A single shear band with a finite thickness t^{sb} is assumed to occur in material points which have reached the bifurcation deviatoric strain ε_q^{sb}. A detailed discussion about the onset of localisation and its inclination angle in the saturated sand was given in Chapter 3. It was emphasised that the onset of local drainage cannot be captured from the uniformly undrained constitutive behaviour of dense sand. Hence the bifurcation is decided upon the first time the determinant of drained acoustic tensor becomes zero in any material point in the extra-small mesh. Therefore, ε_q^{sb}, θ^{sb} and t^{sb} are input parameters which should be calibrated for the selected extra-fine mesh.

After the bifurcation point, the material response cannot be accurately described by a continuum constitutive model. The homogeneity might be valid separately in each region (inside and outside the band) but not as a whole. The modes of deformation inside and outside the shear band take different forms regardless of the boundary conditions of the overall element. Therefore, to accurately capture the post-bifurcation response, two separate stress-strain relationships are required to describe the behaviour inside and outside the localised zone (Nguyen et al., 2016, 2012). The average macroscopic response is calculated based on volume averaging procedure following works of Pietruszczak and Niu (1993), Pietruszczak (1999), Nguyen et al. (2016, 2012). Finally, the averaged macroscopic stress is utilised to solve the equilibrium equations according to global boundary conditions. The evolution of underlying micro-deformation dictates the macro response. Main formulations of this approach are summarised below.

6.4.1 Transformation of stress and strain to the local coordinate system

Similar to works of Pietruszczak and Mroz (1981) and Nguyen et al. (2012), a gauss point is assumed to be intercepted by a distinct shear band with inclination angle θ^{sb} to the horizontal as displayed in Figure 6.2(b). Hence a single material point is assumed to consist of two sub-elements made out of the shear band and intact materials. Both share the same material properties but different modes of deformation. This approach integrates both the size and orientation of the shear band into constitutive relationships beyond the localisation. However, thickness and orientation of the shear band are assumed to be constant regardless of ample experimental and numerical evidence on the evolution of both throughout the deformation.

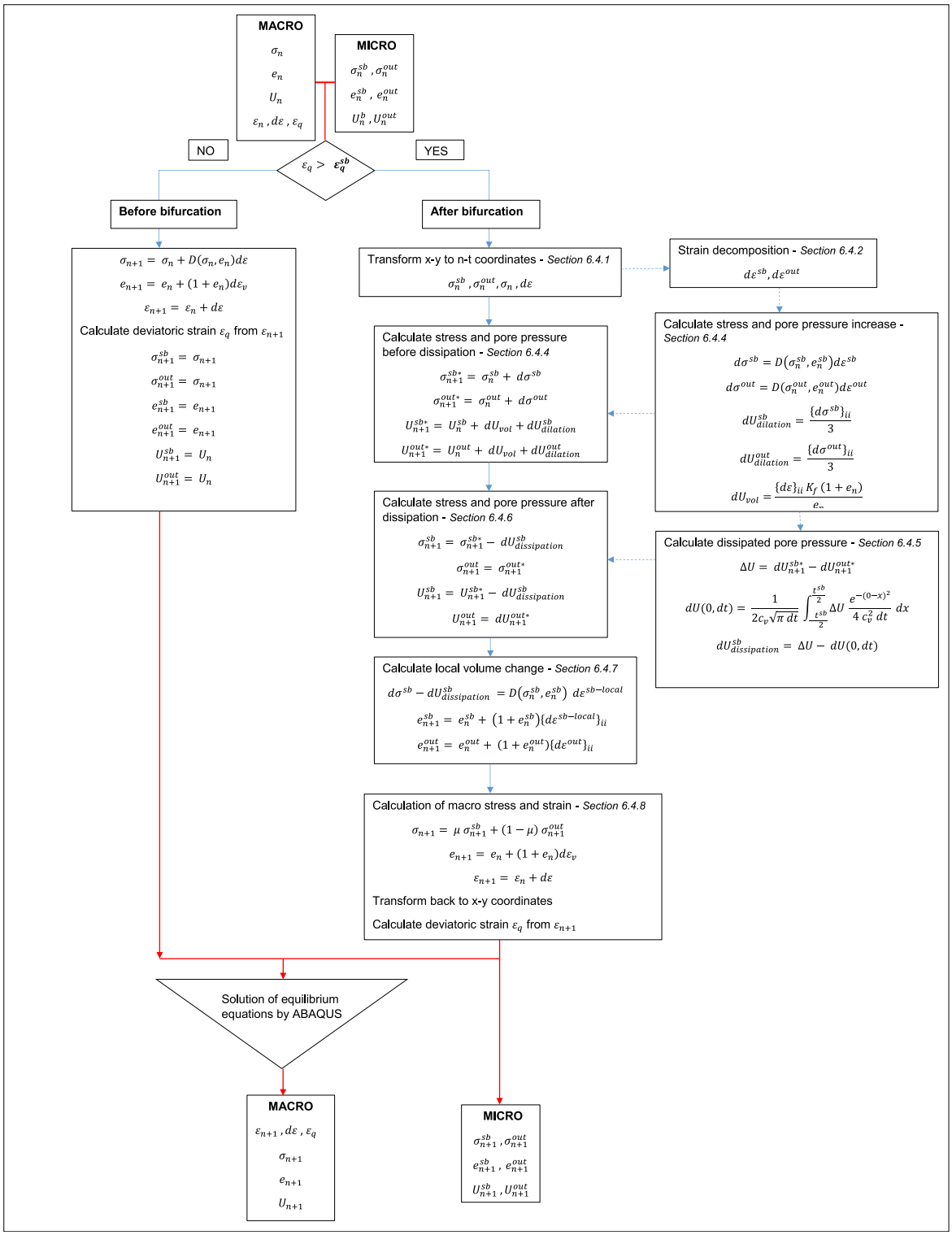

Fig. 6.3 Numerical flow chart for the diffusion SB method

All constitutive relations are developed assuming a plane-strain condition. The homogeneous deformation before bifurcation is described with reference to the global coordinate system $(x-y)$ according to equations in Chapter 2. For clarity, the post-bifurcation analysis is attached to a local coordinates system $(n-t)$ which is aligned with the shear band. The directions parallel and perpendicular to the shear band are denoted as t and n respectively.

When the criterion for the bifurcation is met, homogeneous effective stress vector- σ'_{ij} and strain increment vector- $d\varepsilon_{ij}$ are transformed from global coordinates $(x-y)$ to local coordinates $(n-t)$ as shown in Equations 6.2 and 6.3.

$$\begin{bmatrix} \sigma'_{nn} \\ \sigma'_{tt} \\ \sigma'_{zz} \\ \sigma'_{nt} \end{bmatrix} = \begin{bmatrix} T \end{bmatrix} \begin{bmatrix} \sigma'_{xx} \\ \sigma'_{yy} \\ \sigma'_{zz} \\ \sigma'_{xy} \end{bmatrix} \tag{6.2a}$$

$$\begin{bmatrix} d\varepsilon_{nn} \\ d\varepsilon_{tt} \\ d\varepsilon_{zz} \\ d\varepsilon_{nt} \end{bmatrix} = \begin{bmatrix} T \end{bmatrix} \begin{bmatrix} d\varepsilon_{xx} \\ d\varepsilon_{yy} \\ d\varepsilon_{zz} \\ d\varepsilon_{xy} \end{bmatrix} \tag{6.2b}$$

The transformation matrix is defined as

$$\begin{bmatrix} T \end{bmatrix} = \begin{bmatrix} \cos^2\theta^{sb} & \sin^2\theta^{sb} & 0 & 2\sin\theta^{sb}\cos\theta^{sb} \\ \sin^2\theta^{sb} & \cos^2\theta^{sb} & 0 & -2\sin\theta^{sb}\cos\theta^{sb} \\ 0 & 0 & 1 & 0 \\ -\sin\theta^{sb}\cos\theta^{sb} & \sin\theta^{sb}\cos\theta^{sb} & 0 & \cos^2\theta^{sb}-\sin^2\theta^{sb} \end{bmatrix} \tag{6.3}$$

Hereafter all calculations are conducted in local coordinates until they are transformed back to global coordinates. Two constitutes involved: shear band and intact material are denoted by superscripts *sb* and *out* respectively.

6.4.2 Averaging of strains according to area ratio

Area factor- μ is defined as the ratio of shear band area- A^{sb} to the total area of the element or material point- $A^{element}$. For reduced integration elements (4 gauss points), the length of a material point is half the element size. If the element has a single gauss point, the length of the material point is the same as that of the element.

$$\mu = \frac{A^{sb}}{A^{element}} \approx \frac{t^{sb}}{a} \tag{6.4}$$

where a is the element or material point length and t^{sb} is the shear band thickness. As shown in Figure 6.4, the weak discontinuity approach or Hill-Mandel condition assumes a velocity

jump or a change in the gradients of displacement across the boundaries of the shear band. Hence a linear scaling of the strain rate is valid according to Equation 6.5.

$$d\varepsilon_{ij} = \mu \; d\varepsilon_{ij}^{sb} + (1-\mu) \; d\varepsilon_{ij}^{out} \tag{6.5}$$

This can be rearranged with last term denoting the jump in strain rate.

$$d\varepsilon_{ij}^{sb} = d\varepsilon_{ij}^{out} + \frac{d\varepsilon_{ij} - d\varepsilon_{ij}^{out}}{\mu} \tag{6.6}$$

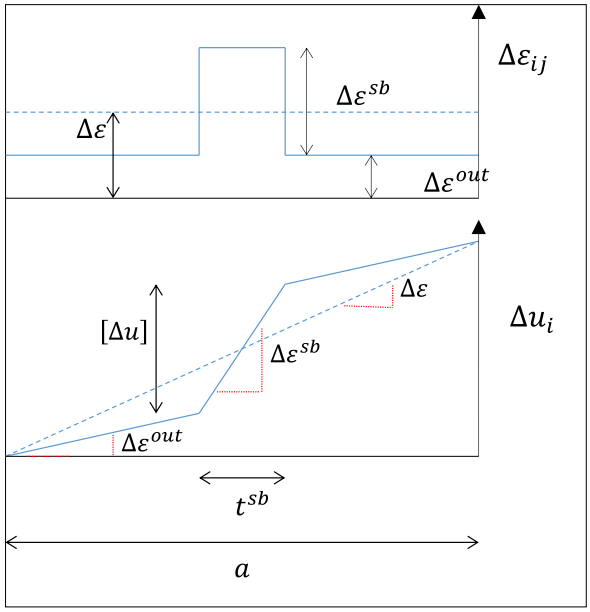

Fig. 6.4 Strain and displacement increment profiles across a shear band, reproduced from Nguyen et al. (2016)

According to the principle of virtual work equation, the work produced by macroscopic stress and strain rate should equilibrate the volume average of work due to stress and strain rates inside and outside the shear band (Nguyen et al., 2016).

$$\sigma'_{ij} \; d\varepsilon_{ij} = \mu \; \sigma'^{sb}_{ij} \; d\varepsilon^{sb}_{ij} + (1-\mu) \; \sigma'^{out}_{ij} \; d\varepsilon^{out}_{ij} \tag{6.7}$$

Nguyen et al. (2016) derived that the average virtual work Equation 6.7 can be satisfied if the volume averaging of stress (Equation 6.8) is assumed along with the traction continuity in Equation 3.5. Hence the composite behaviour can be described by the volume averaging of both stress and strain (Nguyen et al., 2016). This approach which is commonly used in layered composites was first introduced to the shear band analysis by Pietruszczak and Niu (1993).

$$\sigma'_{ij} = \mu \; \sigma'^{sb}_{ij} + (1-\mu) \; \sigma'^{out}_{ij} \tag{6.8}$$

It is evident from the above equations that, if strain rates of each sub-element are known, their stresses can be updated, and average stress can be calculated.

Decomposition of strain rates

Previous researchers used the smeared shear band approach to predict the post-localisation response of drained geo-materials. At a very early stage, Pietruszczak and Mroz (1981) assumed purely elastic strain outside and plastic strain inside the band. Later on Pietruszczak and Stolle (1985, 1987),Nguyen (2014) conducted more accurate and rigorous calculations on the strain rate inside the shear band using the traction continuity. Thus the internal equilibrium at shear band boundary is maintained.

In this study, the smeared shear band method is used to explore post-localisation of undrained geo-materials. Without comprehensive calculations using traction continuity, simple assumptions are made on strain rates inside and outside the shear band considering two scenarios. They are derived from the undrained simple shear deformation shown in Figure 6.5.

- Case 1

  A unique feature of undrained deformation is negligible volumetric strains. Therefore, without comprehensive calculations, it is hypothesised that the shear strain is concentrated inside the shear band while volumetric strain is shared by both shear band and intact material. Thus Equation 6.6 can be rewritten as

$$d\varepsilon_{ij}^{out} = \frac{d\varepsilon_{ii}}{3} \tag{6.9a}$$

$$d\varepsilon_{ij}^{sb} = \frac{d\varepsilon_{ii}}{3} + \frac{de_{ij}}{\mu} \tag{6.9b}$$

  where $de_{ij} = d\varepsilon_{ij} - \dfrac{d\varepsilon_{ii}}{3}$

- Case 2

  Similar to the Case 1, the volumetric strain is assumed to be shared by both shear band and intact material equally. However, in this case, a small shear strain is allowed outside the shear band. Satisfying the virtual work equation (Equation 6.7) and linear averaging of strain (Equation 6.5), the Equation 6.6 can be modified as

$$d\varepsilon_{ij}^{out} = \frac{d\varepsilon_{ii}}{3} + (1-k)\frac{de_{ij}}{1-\mu} \tag{6.10a}$$

$$d\varepsilon_{ij}^{sb} = \frac{d\varepsilon_{ii}}{3} + k\frac{de_{ij}}{\mu} \tag{6.10b}$$

  where a shear factor k is introduced additionally.

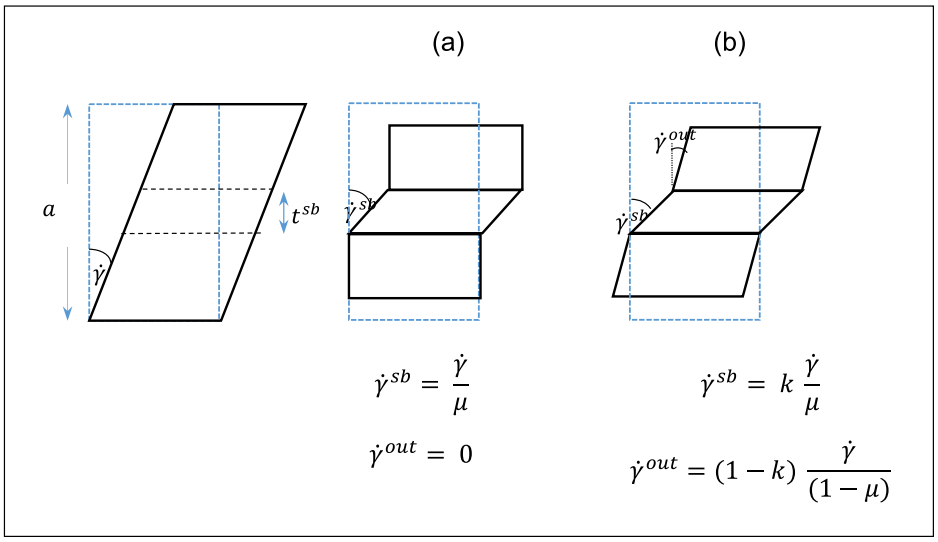

Fig. 6.5 Assumed strains inside and outside the shear band for (a) Case 1 and (b) Case 2

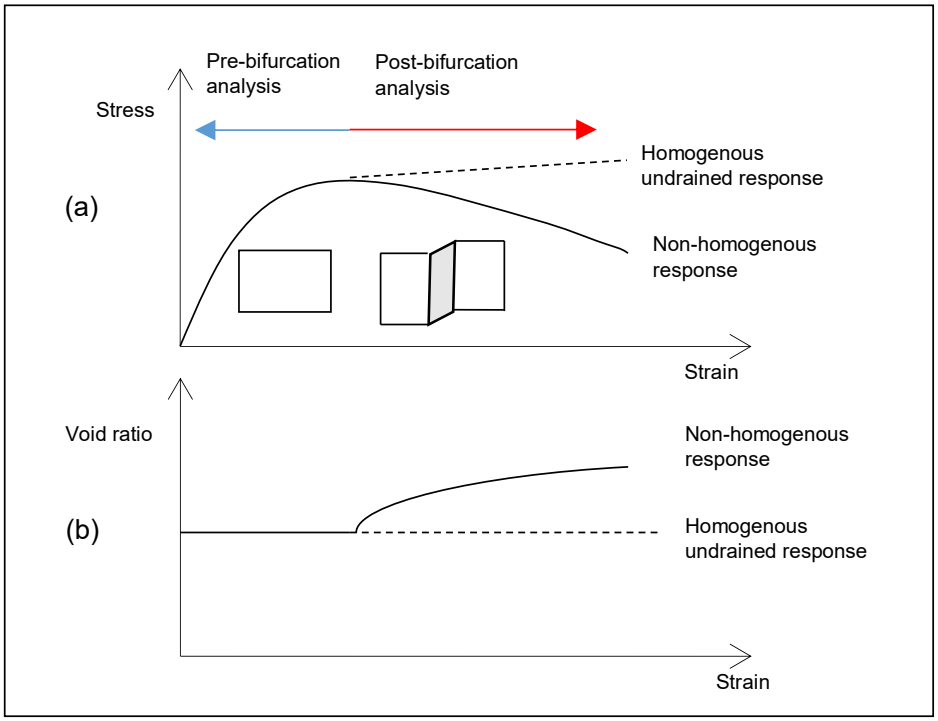

Fig. 6.6 Divergence from homogeneous response at the bifurcation point

6.4.3 Divergence from the bifurcation point

At the onset of bifurcation, the material responses inside and outside the shear band diverge from the same point in the stress and void ratio curves as shown in Figure 6.6. Therefore, effective stresses, void ratios and excess pore pressures inside and outside the shear band are equalised to homogeneous effective stress- σ'_{ij}, void ratio- e and negative pore pressure- U at the onset of bifurcation.

$$\sigma'^{sb}_{ij} = \sigma'^{out}_{ij} = \sigma'_{ij} \tag{6.11}$$

$$e^{sb} = e^{out} = e \tag{6.12}$$

$$U^{sb} = U^{out} = U \tag{6.13}$$

To simplify the calculation the generation and dissipation of excess pore pressure are decoupled as shown in Figure 6.7(a) and (b) though both occur simultaneously. Stress and pore pressure values after generation but before the dissipation of excess pore pressure are denoted by a superscript star.

6.4.4 Calculation of stresses and pore pressures before dissipation

During the post-bifurcation analysis, effective stresses and void ratios inside and outside the shear band are updated from time step n to $n+1$. This is done in two steps. The update of variables after the generation of pore pressure is given in this section.

$$\left[\sigma'^{sb*}_{ij}\right]_{n+1} = \left[\sigma'^{sb}_{ij}\right]_n + d\sigma'^{sb}_{ij} \tag{6.14}$$

$$\left[\sigma'^{out*}_{ij}\right]_{n+1} = \left[\sigma'^{out}_{ij}\right]_n + d\sigma'^{out}_{ij} \tag{6.15}$$

Since the material behaviours inside and outside are locally homogeneous, their stress-strain relationships take the form:

$$d\sigma'^{sb}_{ij} = D^{sb}_{ijkl}\, d\varepsilon^{sb}_{kl} \tag{6.16}$$

$$d\sigma'^{out}_{ij} = D^{out}_{ijkl}\, d\varepsilon^{out}_{kl} \tag{6.17}$$

The stiffness matrices are calculated from stress values remembered from the end of previous time step. The stiffness matrix of the shear band- D^{sb}_{ijkl} is calculated from the shear band stress - $\left[\sigma'^{sb}_{ij}\right]_n$ and void ratio- $\left[e^{sb}\right]_n$ whereas the stiffness matrix of intact material- D^{out}_{ijkl} is calculated from outside stress- $\left[\sigma'^{out}_{ij}\right]_n$ and void ratio- $\left[e^{out}\right]_n$.

During post-localisation analysis, excess pore pressures become non-homogeneous as shown in Figure 6.7(a). In shear band material, the pore pressure change is caused by both

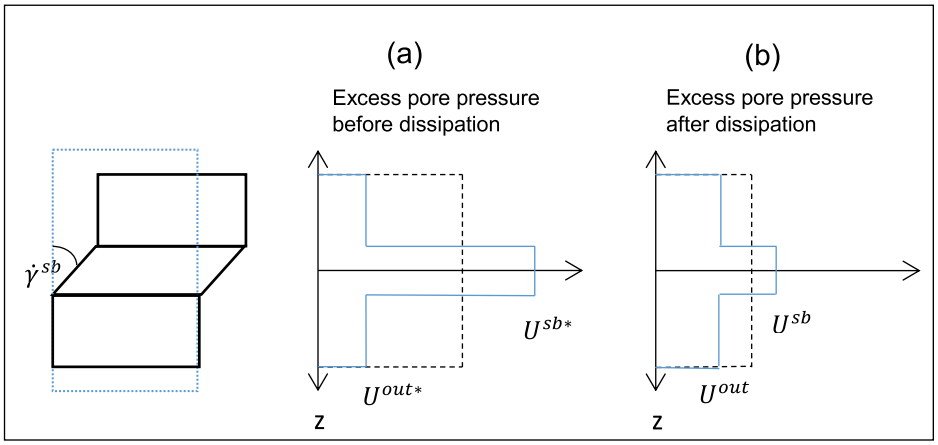

Fig. 6.7 Non-homogeneous negative excess pore pressure (a) before and (b) after dissipation

volumetric change and the shear-induced dilation. It exceeds the homogeneous pressure calculated at nodes from global equilibrium equations (shown in black dash line). Outside the shear band, the only reason for the pore pressure generation is the volumetric change for the Case 1. However, for the Case 2, a small amount of dilation induced pore pressure occurs in outside material as well. Hence the Equation 6.18(b) should be modified accordingly.

$$\left[U^{sb*}\right]_{n+1} = \left[U^{sb}\right]_n + dU_{vol} + dU^{sb}_{dilation} \tag{6.18a}$$

$$\left[U^{out*}\right]_{n+1} = \left[U^{out}\right]_n + dU_{vol} + dU^{out}_{dilation} \tag{6.18b}$$

Shear-induced pore pressure rise is calculated as the increase in mean effective stress in particular materials.

$$dU^{sb}_{dilation} = \frac{d\sigma^{tsb}_{ii}}{3} \tag{6.19a}$$

$$dU^{out}_{dilation} = \frac{d\sigma^{tout}_{ii}}{3} \tag{6.19b}$$

Generated pore pressure due to volumetric change during undrained condition can be assumed as

$$dU_{vol} = \frac{d\varepsilon_{ii}\, K_f}{e}(1+e) \tag{6.20}$$

6.4.5 Calculation of dissipated pore pressure

Due to the difference in dilation induced pore pressures inside and outside the shear band, an excess pore pressure gradient- ΔU is created as shown in Figure 6.7(a).

$$\Delta U = \left[U^{sb*}\right]_{n+1} - \left[U^{out*}\right]_{n+1} \tag{6.21}$$

Depending on the duration of loading and diffusive properties of the material, the pore pressure gradient can be accumulated from previous steps. The main hypothesis of this analysis is that a certain percentage of this gradient should be dissipated within the same time step ($t_{n+1} - t_n = dt$). The dissipated amount- $dU^{sb}_{dissipation}$ is governed by the pressure gradient- ΔU, diffusivity coefficient- c_v and the time step- dt of the analysis.

The magnitude of pore pressure remaining after dissipation can be calculated simply from the $1D$ diffusion from Equation 6.23. For $2D$ applications, this is an approximation assuming that diffusion mainly occurs perpendicular to the band. $dU(z,dt)$ is the pore pressure profile at the end of the time step. The initial pore pressure profile $dU(z,0)$ is assumed to be a step function with a magnitude of ΔU inside the band and zero outside. Figure 6.8 displays $\frac{dU(z,dt)}{\Delta U}$ for different loading durations. The initial profile is shown in red.

$$dU(z,0) = \Delta U \qquad -\frac{t^{sb}}{2} < z < \frac{t^{sb}}{2} \tag{6.22a}$$

$$= 0 \qquad \text{otherwise} \tag{6.22b}$$

$$dU(z,dt) = \frac{1}{2\,c_v\sqrt{\pi dt}} \int_{-\frac{t^{sb}}{2}}^{\frac{t^{sb}}{2}} dU(z,0)\, e^{\frac{-(z-x)^2}{4c_v^2\,dt}}\, dx \tag{6.23}$$

The dissipated amount of pore pressure in the middle of shear band ($z = 0$) is calculated as

$$dU^{sb}_{dissipation} = \Delta U - dU(0,dt) \tag{6.24}$$

$dU(z,dt)$ depends on the duration of external loading. Hence this includes the time dependent behaviour in the context of time independent plasticity. Generally, it is assumed that the fully undrained response of saturated soil is time independent. The hypothesis here is that although the global behaviour is independent of time, the local drainage depends on the time, hence should be taken into account.

6.4.6 Correction of stresses and pore pressures after dissipation

The enhanced shear strain inside the shear band produces dilation induced pore pressure inside. However, during the loading of saturated soil, dissipation of excess pore pressure also occurs simultaneously with generation. If the loading is slow enough, excess pore pressure inside can be dissipated making the shear band fully or partially drained. After dissipation, the excess pore pressure inside the band reduces, and the pressure outside the band increases as shown in Figure 6.7(b). Therefore, the pore pressures are corrected as

$$\left[U^{sb}\right]_{n+1} = \left[U^{sb}\right]_n + dU_{vol} + dU^{sb}_{dilation} - dU^{sb}_{dissipation} \tag{6.25a}$$

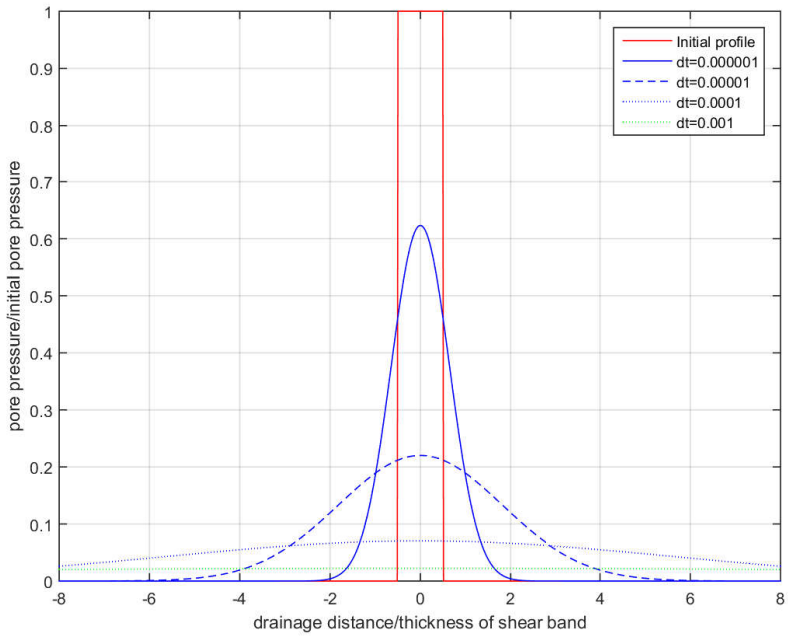

Fig. 6.8 Diagram of excess pore pressure distribution across a shear band for different loading durations

$$[U^{out}]_{n+1} = [U^{out}]_n + dU_{vol} + dU^{out}_{dilation} + dU^{out}_{recieved} \tag{6.25b}$$

The remaining excess pore pressure after dissipation contributes to the final effective stress in and out of the shear band. Hence, effective stress inside the shear band should be corrected as

$$\left[\sigma'^{sb}_{ij}\right]_{n+1} = \left[\sigma'^{sb*}_{ij}\right]_{n+1} - dU^{sb}_{dissipation} \text{ when } \quad i = j \tag{6.26}$$

$dU^{out}_{recived}$ depends on drainage distance as shown in Figure 6.8. If the shear band thickness is at least 8 times smaller compared to the length of material point, $dU^{out}_{recived}$ is negligible. Hence, the outside effective stress is assumed not to be changed by the dissipation.

$$\left[\sigma'^{out}_{ij}\right]_{n+1} = \left[\sigma'^{out*}_{ij}\right]_{n+1} \tag{6.27}$$

It should be mentioned that, although effective stress states are different, total stress inside and outside the shear band should be essentially similar to homogeneous total stress to maintain equilibrium. Therefore at any time step:

$$\begin{aligned}
\sigma_{ij} &= \sigma' ij + U && \text{homogenous stress} \\
&= \sigma'^{out*}_{ij} + U^{out*} && \text{stress outside shear band before dissipation} \\
&= \sigma'^{sb*}_{ij} + U^{sb*} && \text{stress inside shear band before dissipation} \\
&= \sigma'^{out}_{ij} + U^{out} && \text{stress outside shear band after dissipation} \\
&= \sigma'^{sb}_{ij} + U^{sb} && \text{stress inside shear band after dissipation}
\end{aligned}$$

Figure 6.9 illustrates stress increments between two consecutive time steps. Red vertical lines denote the total stress whereas yellow lines indicate effective stresses.

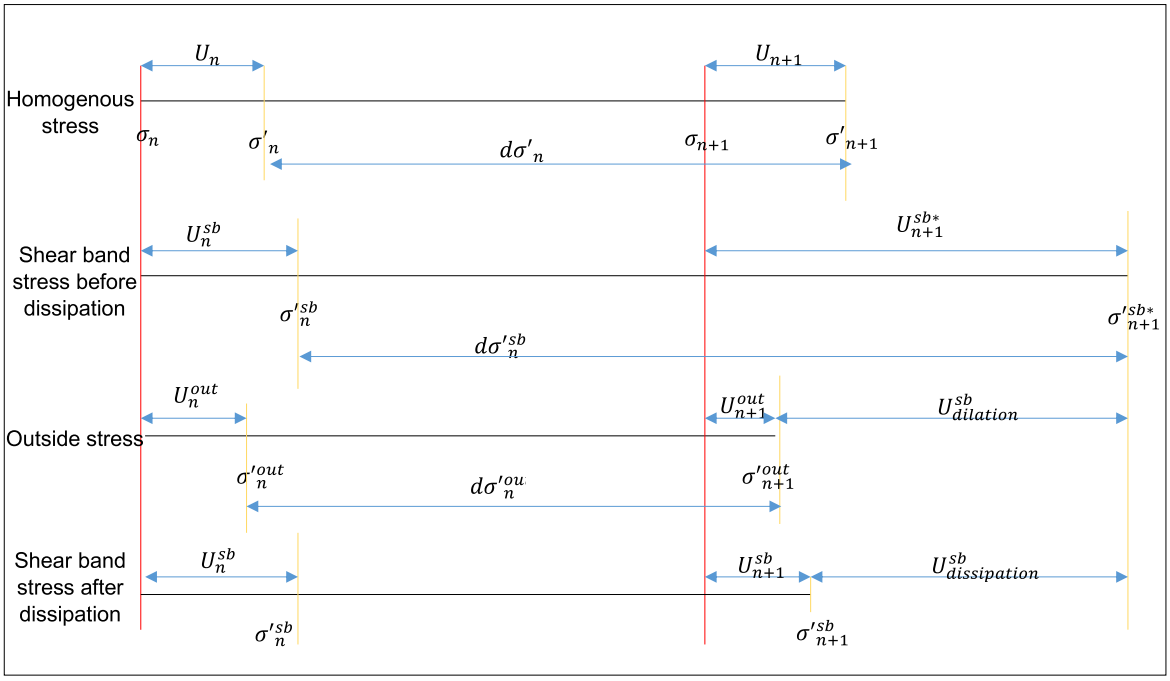

Fig. 6.9 Total and effective stress states between time steps t_n and t_{n+1}

6.4.7 Calculation of local volume changes inside the shear band

Due to undrained global boundary conditions, the volumetric strain at a material point is negligible. However, the above section delineates that a portion of excess pore pressure generated due to undrained mean pressure increase inside the band is reduced due to the dissipation. This changes the boundary conditions of shear band material from undrained to partially drained. In other words, there is a net volumetric strain increment inside the shear band due to the dissipated pore pressure. The corrected strain increments inside the shear band $d\varepsilon_{ij}^{sb-local}$ can be recalculated from the corrected stress increments. Since intact material acts as almost undrained, $d\varepsilon_v^{out}$ is negligible.

$$d\sigma'^{sb}_{ij} - dU^{sb}_{dissipation} = D^{sb}_{ijkl}\, d\varepsilon^{sb-local}_{kl} \quad \text{when} \quad i = j \tag{6.28}$$

$$d\varepsilon_v^{sb-local} = d\varepsilon_{ii}^{sb-local} \tag{6.29}$$

The void ratio inside and outside should be updated according to the respective volumetric strains.

$$\left[e^{sb}\right]_{n+1} = \left[e^{sb}\right]_n + (1 + \left[e^{sb}\right]_n)\, d\varepsilon_v^{sb-local} \tag{6.30}$$

$$[e^{out}]_{n+1} = [e^{out}]_n + (1 + [e^{out}]_n)\, d\varepsilon_v^{out} \tag{6.31}$$

6.4.8 Calculation of macroscopic stress

The macroscopic stress of the material point is established by averaging corrected shear band stress and outside stress.

$$\left[\sigma'_{ij}\right]_{n+1} = \mu\ \left[\sigma'^{sb}_{ij}\right]_{n+1} + (1-\mu)\ \left[\sigma'^{out}_{ij}\right]_{n+1} \tag{6.32}$$

Finally, the homogenised effective stress at the end of the time step is transformed back to global coordinates. It is utilised by ABAQUS to solve equilibrium equations at nodes. Corrected stresses, void ratios and excess pore pressures of respective material are carried forward for the next time step. The aforementioned method is termed as diffusion SB model hereafter.

6.5 Results of Diffusion Shear Band Model

The objective of the new diffusion SB model is to macroscopically capture undrained deformation appreciating underlying internal fluid movements in shear zones. First, the diffusion SB model is calibrated to recreate the undrained macroscopic response bestowed by the extra-small mesh. Secondly, the microscopic behaviours inside and outside shear band predicted by the diffusion SB model are compared with individual material point behaviours inside and outside the shear band in the extra-small mesh. Then, the calibrated diffusion SB model is exploited to simulate up-scaled versions of the biaxial compression tests with general boundary conditions.

6.5.1 Calibration of diffusion SB model with undrained extra-small mesh

In the lack of experimental evidence on the post-localised behaviour of globally undrained deformation (without cavitation), numerical simulations of undrained biaxial tests with an extra-small mesh are utilised for the calibration. A single element biaxial compression test with undrained boundaries is simulated with the diffusion SB model for various loading durations. The dimensions of the single element are $0.25\,\text{m} \times 0.5\,\text{m}$. The diagram in Figure

6.10 illustrates the two models in comparison. The validity of both assumptions mentioned in section 6.4.2 is examined.

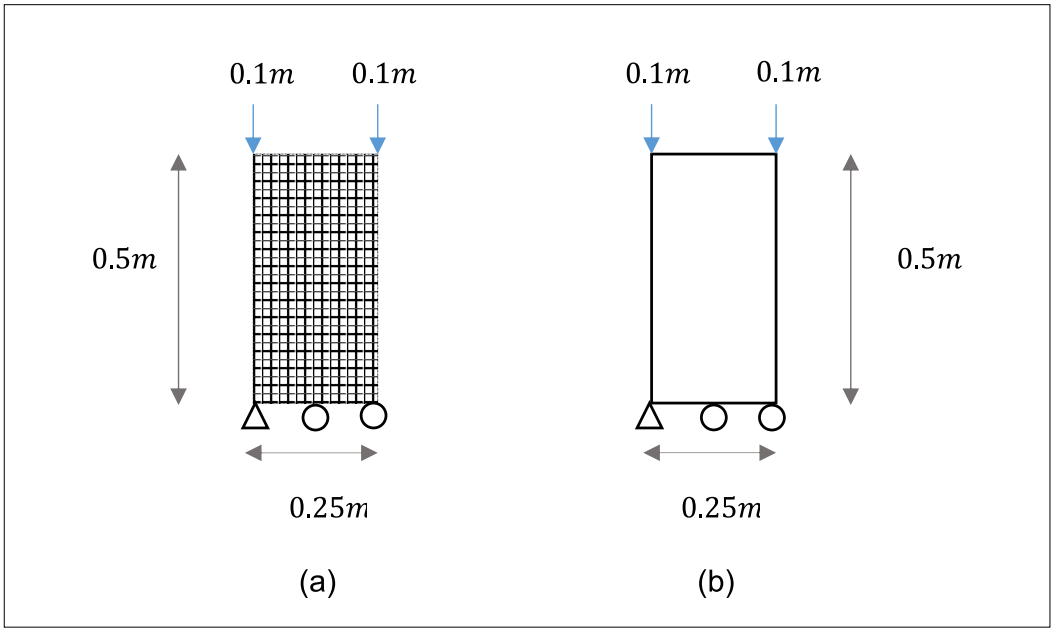

Fig. 6.10 Biaxial compression tests with (a) extra-small mesh simulated with original NS model and (b) single element simulated with diffusion SB model

Material properties of the NS model are the same as specified in Table 2.1. The thickness of the shear band is evaluated from the extra-small mesh. The area factor is calculated as the ratio of this shear band thickness to the average length of a gauss point in the single element. The inclination of the band is assumed to be 53° similar to the extra-small mesh. The onset of localisation in the single element occurs when the acoustic tensor at any material point of extra-small mesh first becomes zero. The shear factor is calibrated to match with the global response of the extra-small mesh. The calibrated input parameters of the diffusion SB model are given in Table 6.1. Information from Tables 5.2, 5.4 and 5.5 are incorporated for the calibration. Figure 6.11 displays the total reaction forces of extra-small mesh along with single element simulations of the diffusion SB model for both Cases 1 and 2.

It is observed that the reaction forces of the diffusion SB model (Case 1) reach constant plateaus after shear bands are formed for the loading durations 1 s, 0.1 s and 0.01 s. In Case 1, the outside shear strain is zero; thus the mean pressure increases only inside the shear band. When the loading time step is large enough to fully dissipate the dilation induced pore pressure inside the band effective mean pressure becomes a constant. Hence there is no longer an increase in shear strength. However, when the loading duration is 0.001 s, initially a pore pressure gradient accumulates inside the shear band which leads to a slight increase of

Table 6.1 Calibrated input parameters for diffusion shear band model

Loading duration (s)	Area factor - μ	shear factor - k	Diffusive coefficient - c_v (m^2/s)	Deviatoric strain at onset of shear band- ε_q^{sb}
1	0.084	0.93	5	0.08
0.1	0.1	0.92	5	0.085
0.05	0.11	0.91	5	0.09
0.01	0.11	0.91	5	0.115
0.005	0.11	0.91	5	0.14
0.001	0.11	0.91	5	0.16

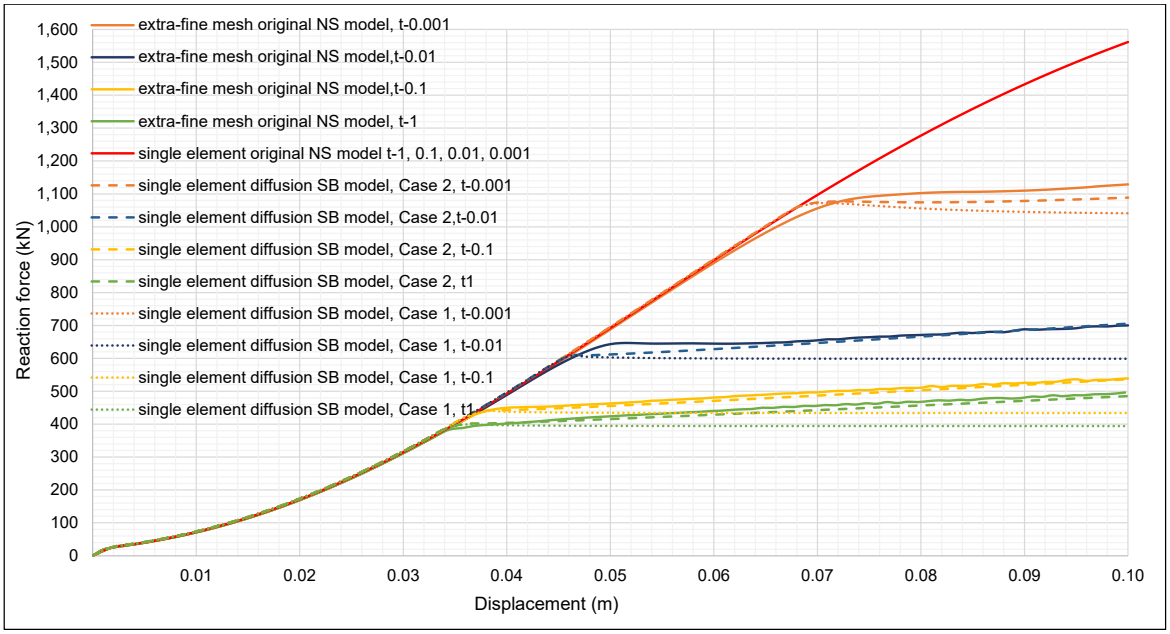

Fig. 6.11 Comparison of the global reaction forces of extra-small mesh by original NS model with single element forces of diffusion SB model : $p_0' = 95$kPa, $W = 0.25$m

stiffness as shown in Figure 6.11 (orange dotted line). Nevertheless, a large pressure gradient, in turn, accelerates the dissipation and reduces the shear strength soon.

In Case 2 material outside the shear band is allowed to shear a little. Hence a certain amount of dilation induced negative pore pressure occurs outside the band as well. Therefore, a close resemblance to extra-small mesh can be witnessed. In reality, strength in material outside the shear band also increases due to two reasons. First, it also undergoes a slight dilation and produces negative pore pressure. Second, it receives dissipated negative pore pressure from the shear band. The diffusion SB model does not consider this since the

amount of received pressure subsides if the band thickness is minimal compared to material point size.

The red line in Figure 6.11 displays the single element undrained response of the original NS model, and it is independent of loading durations. It is observed that results of the diffusion SB model are closer to those of extra-small mesh than the uniform undrained deformation predicted by the original NS model.

Several factors should be taken into the account when the global reaction forces of the extra-small mesh are compared with constitutive response of the diffusion SB model. The localisation in a continuum mesh is progressive in nature. Different material points reach bifurcation criteria at various stages of deformation. Generally, weak material points initiate the shear band. Therefore, the change of stiffness in the global response of extra-small mesh appears when acoustic tensors of weak points start to become null. Thus the drained localisation of the extra-small mesh is used as an input value for the diffusion SB model. It happens after the Coulomb state of the homogeneous deformation. This is experimentally justifiable since Vardoulakis (1996b) mentioned that the onset of shear band occurred after the Coulomb state. Guo (2013) also theoretically proved that local volume change in undrained deformation is most likely after the maximum stress ratio.

Moreover, when the shear band is fully drained (when the loading duration is greater), the reaction forces in extra-small mesh continue to increase. This observation is not dramatic for the partially drained cases. This is because material points reach the critical state at different stages. The shear band develops progressively widening its thickness. Further, outside elements unload at the start of localisation and reload again. These features cannot be apprehended by constitutive relations in the diffusion SB model. Hence a small amount of shear should be included in outside material to match with the results of extra-small mesh.

6.5.2 Material response inside and outside the shear band

As the global response is close enough, it is worthwhile to investigate the constitutive behaviour inside and outside the shear band predicted by the diffusion SB model. Figures 6.12 to 6.14 illustrate the stress, strain as well as volumetric relationships inside and outside the shear band for different loading durations.

Results of the diffusion SB model- Case 1, when the loading duration is 1 s are depicted in Figure 6.12. These can be qualitatively compared with Figure 5.14 which shows the behaviour of selected material points in and out of the shear band in the extra-small mesh. It is observed in Figures 6.12(a), that after bifurcation, the deviatoric strain is concentrated inside the band similar to Figure 5.14(a). Figure 6.12(b) shows a local volume change

only inside the band in line with Figure 5.14(b). Nevertheless, in the diffusion SB model, the volume outside the band is almost constant whereas in the extra-small mesh (in Figure 5.14(b)) there is a little compaction outside.

Figure 6.12(c) shows that the deviatoric stress inside the band reaches a peak after bifurcation and softens until the critical state. This is in agreement with Figure 5.14(c), although the residual stress is much higher in the diffusion SB model. The deviatoric stress outside the band becomes a constant in Figure 6.12(c) in contrast to increasing stress in Figure 5.14(c). This due to the assumption of Case 1 which dictates a zero shear strain outside the shear band. Due to the same reason, the stress ratio outside the band in Figure 6.12(d) remains constant after bifurcation. The stress ratio inside the band slightly increases at the bifurcation point and then reaches the critical stress ratio similar to Figure 5.14(d).

According to Figure 6.12(e), the diffusion SB model predicts that the stress path outside the band terminates without reaching the critical state line whereas the path inside approaches the critical state line maintaining a constant effective mean stress. This is mainly because the duration of loading is large enough to dissipate the whole amount of dilation induced excess pore pressure generated inside the band within each time step. As there is no dilation induced pore pressure outside the band, the excess pore pressure also becomes a constant as shown in Figure 6.12(h). Both effective mean pressures and excess pore pressures are similar both inside and outside the band indicating full local drainage. This is because the diffusion SB model assumes that the dilation induced pore pressure is equal to the effective mean pressure increase. When it is fully dissipated, the effective mean pressure becomes constant. This is a contrast to extra-small mesh results in Figure 5.14(e) and (h). Although there is no difference in pore pressures in and outside the band, Figure 5.14(h) shows that the negative excess pore pressure keeps on increasing.

Further, Figures 5.14(e) and (g) show that the effective mean pressure inside the band is decreasing along the critical state line after the peak. Although this appears as a contradicting observation, the increase of suction is a result of global strength enhancement. In the extra-small mesh, the mean pressure is calculated at gauss points whereas the pore pressure is calculated at nodes based on the global equilibrium. The macroscopic response is closer to the outside behaviour. Figures 6.12(f) and (g) display that state parameter and void ratio inside the shear band have reached the critical state whereas those parameters do not change outside. This observation closely resembles the results of extra-small mesh in Figures 5.14(f) and (g).

In the extra-small mesh, the expansion inside the band is compensated by the contraction outside, when the band is fully drained. The simplified SB model does not consider this

global volume conservation. Moreover, in extra-small mesh, there is a slight drop in the global response at the onset of bifurcation due to material softening and elastic unloading outside. The diffusion SB model cannot replicate this.

Figure 6.13 illustrates results of the diffusion SB model- Case 2 when the loading duration is 1 s. Deviatoric, volumetric strains as well as state parameter inside and outside the band are similar to Figure 6.12. However, both deviatoric stress and effective mean pressure inside and outside the band are increasing in this case. This is because dilation is allowed outside material as well. Due to the same reason, both negative excess pore pressures in and out of the band accumulate, albeit without a pressure gradient in between. This is similar to Figure 5.14(h); thus the assumption Case 2 closely matches the global response of the extra-fine mesh. Compared to Figure 6.12(e), stress paths in and out of shear band keep on rising in Figure 6.13(e). This is because dilative hardening takes place in both components even though material inside the shear band has reached the critical state. Unlike in Case 1, now only a portion of pore pressure inside the band dissipates.

The results of diffusion SB model- Case 2 when the loading duration is 0.001 s are shown in Figure 6.14. Much difference is not observed between Cases 1 and 2. This Figure can be compared with the material behaviour inside and outside the shear band of extra-small mesh for a similar loading duration (Figure 5.19). The first observation is the delayed onset of bifurcation compared to Figure 6.12. Therefore, the shear band is not progressed much. Concentrated shear strain in Figure 6.14(a) and local volume change in Figure 6.14(b) are similar to those in Figure 5.19. Significant compaction outside the band is not observed in this case, because the global volume stability which happens in fully drained shear bands is not reached yet. Figure 6.14(c) shows that the deviatoric stress inside the band reaches a peak and softens afterwards, but the deviatoric stress outside is continuously increasing. This observation agrees with Figure 5.19(c). Both Figures 5.19(d) and 6.14(d) display that the stress ratio inside the band is decreasing up to the critical stress ratio while the ratio outside the band remains constant. The state parameter in Figure 6.14(f) has not reached the critical state yet.

In Figures 6.14(e) and (g), the stress paths reverse and approach the critical state line similar to Figures 5.19(e) and (g). This is the main difference compared to fully drained shear bands in Figures 6.12 and 6.13. The accumulated pore pressures in and out of the shear band show qualitatively similar behaviours in Figures 6.14(h) and 5.19(h). Since the loading duration is too fast to dissipate the dilation induced excess pore pressure inside the band, it accumulates initially. This is because the rate of generation is greater than the rate of dissipation. However, enhanced pore pressure gradient, in turn, accelerates the excess

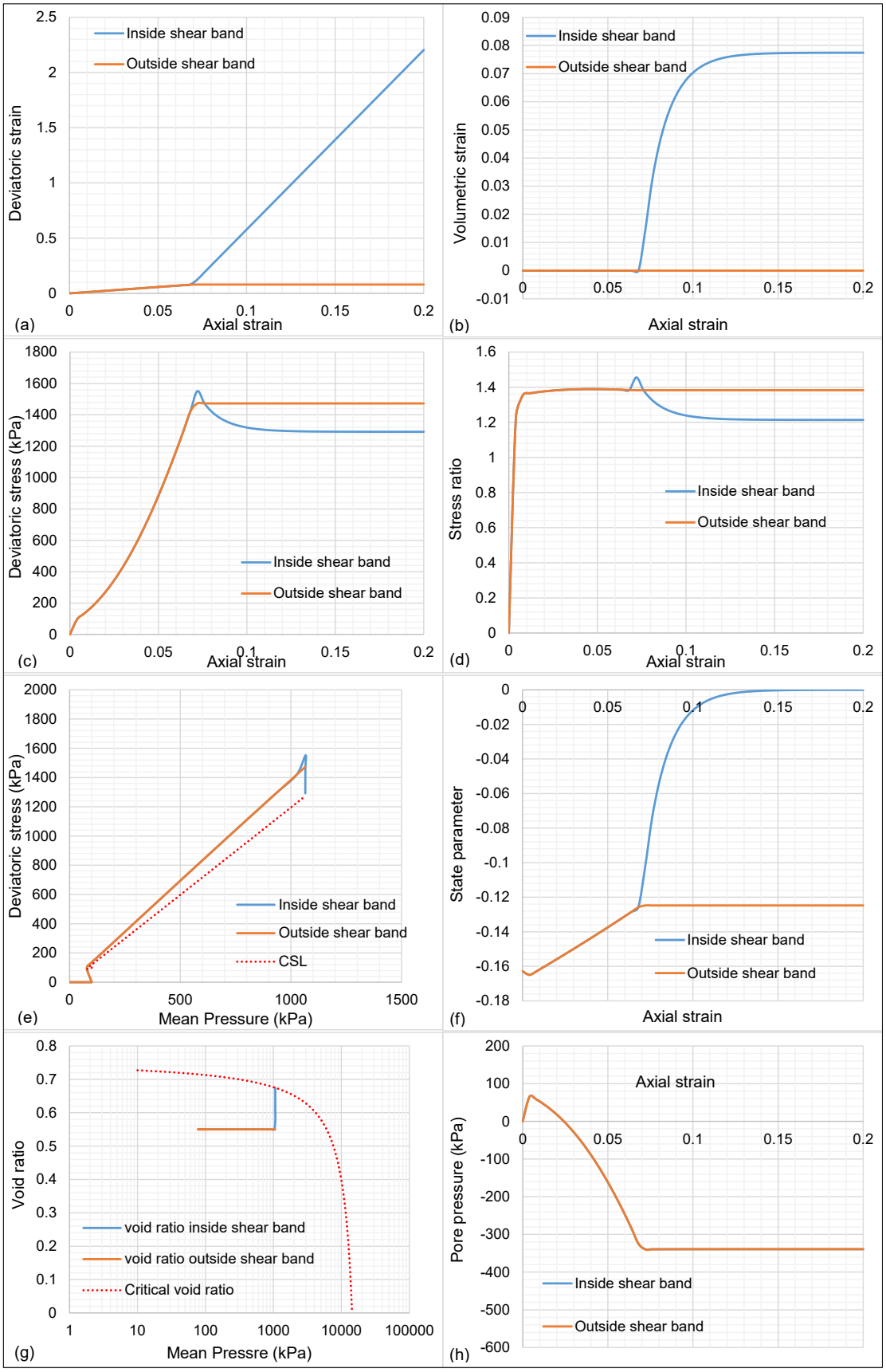

Fig. 6.12 Material response in and out of the shear band for loading duration 1 s predicted by diffusion SB model- Case 1 (a) shear strain (b) volumetric strain (c) deviatoric stress (d) stress ratio (e) stress path (f) state parameter (g) volumetric path and (h) excess pore water pressure

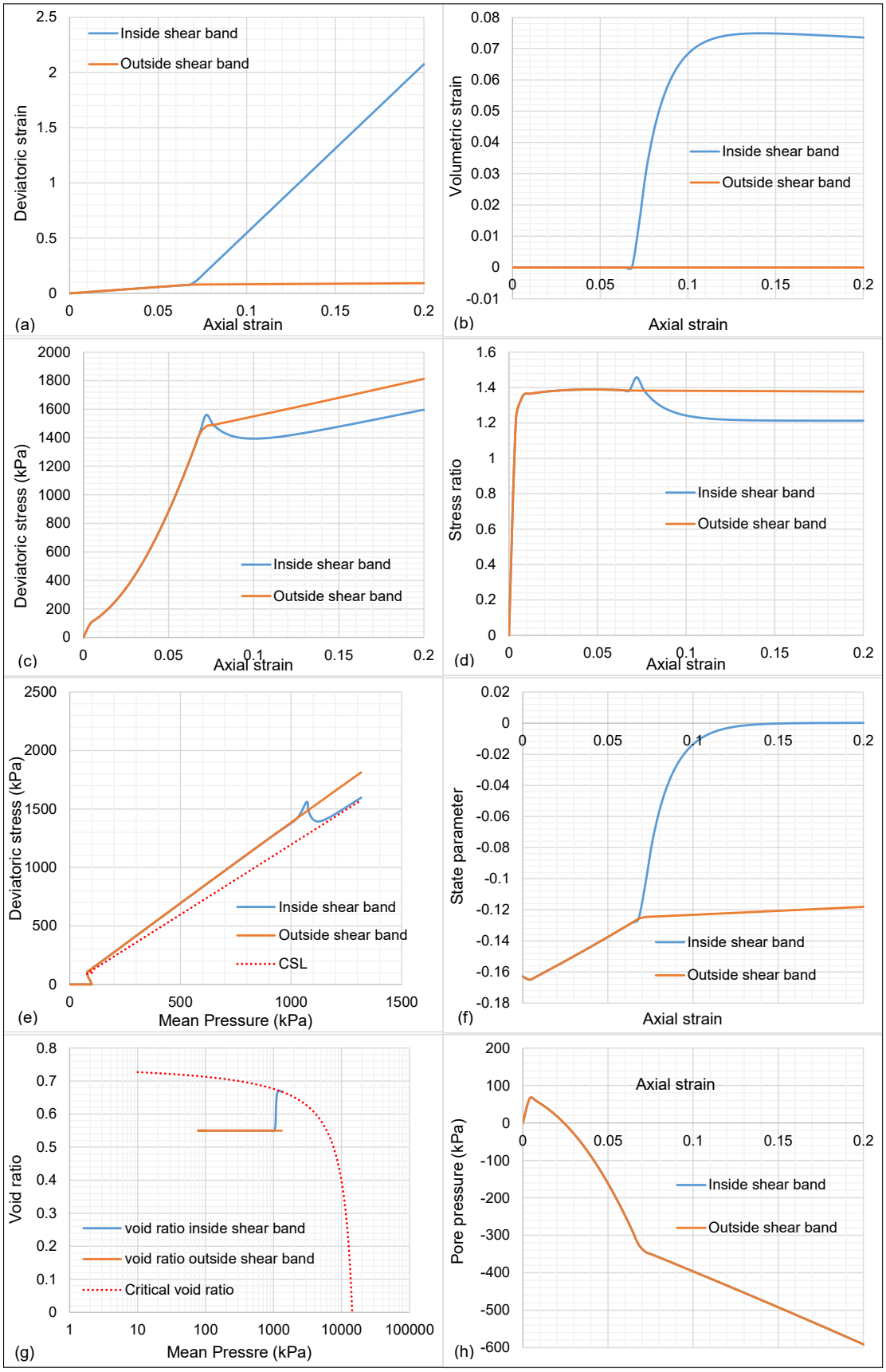

Fig. 6.13 Material response in and out of the shear band for loading duration 1 s predicted by diffusion SB model- Case 2 (a) shear strain (b) volumetric strain (c) deviatoric stress (d) stress ratio (e) stress path (f) state parameter (g) volumetric path and (h) excess pore water pressure

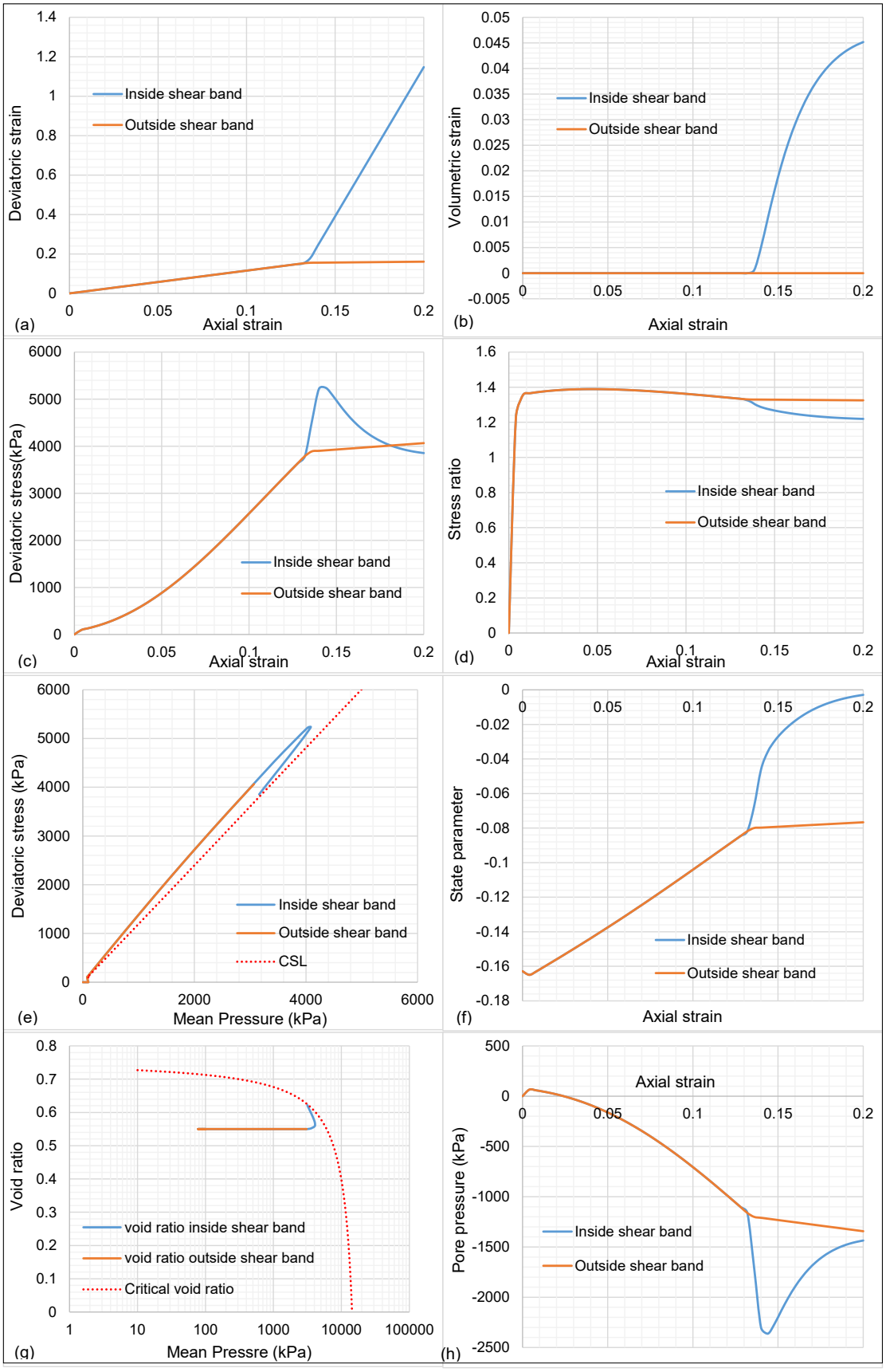

Fig. 6.14 Material response in and out of the shear band for loading duration 0.001s predicted by diffusion SB model- Case 2 (a) shear strain (b) volumetric strain (c) deviatoric stress (d) stress ratio (e) stress path (f) state parameter (g) volumetric path and (h) excess pore water pressure

pore pressure dissipation. Therefore, both accumulated pore pressure and mean effective pressure start to decrease. This is illustrated by Figures 6.14(e),(g) and (h). Until the 20 % strain, there is a net pore pressure gradient which clearly demonstrates the partially drained behaviour of the shear band. All in all, Figure 6.14 is qualitatively in good agreement with Figure 5.19. It confirms that the diffusion SB model sufficiently captures the response of partially drained shear band.

The main achievement of this diffusion SB approach is that constitutive relations alone capture both macroscopic and microscopic (inside and outside the shear band) behaviour of the extra-small mesh. Furthermore, this constitutive response is sensitive to both time and scale effects observed in the extra-small mesh.

Validity of the assumption of homogeneous material behaviour inside and outside the shear band

Figure 6.2(b) displays the conceptual single element diffusion SB model which replicates the behaviour of undrained biaxial compression of extra-small mesh in Figure 6.2(a). Here it is assumed that the material behaviours inside and outside the shear band are homogeneous. However, neither in real soil nor in numerically modelled biaxial tests, the material behaviour inside the shear band is uniform throughout. The stress state outside the band is fairly uniform, but the stress states inside the shear band differ in longitudinal and transverse directions.

The shear band behaviour near boundaries and corners are significantly different from the interior shear band. FE simulations of plane-strain compression tests exhibit kinks where the shear band connects boundaries as shown in Figure 6.2(a). In these regions, the material behaviour continuously oscillates from loading to unloading. Therefore, only a material sample inside the biaxial compression test should be considered as a representative of the diffusion SB model. The idealised body should be unbounded and traversed by a shear band with a constant thickness and a constant angle.

In the transverse direction, the behaviours of middle and boundary shear band elements are different. It is mainly due to the pathological drawback of iso-parametric quadrilateral elements. These elements cause the shear band to extend over more than a single element. It is clearly observed in Figure 6.15 that apart from the distinct response of shear band and outside elements, boundary elements (780,783) show an intermediate response. This is because the discontinuity is smeared over boundary elements rather than a sharp transition from the localisation zone to the surrounding area. It is observed that the state parameter has reached the critical state only in the middle shear band elements (781,782). This observation is valid for both dry and saturated simulations. However, it is more complex in the saturated case

since it contains two discontinuous fields. The response of boundary elements is disregarded in the diffusion SB model.

On top of that, the mechanism of failure during plane-strain compression is a complex phenomenon. The apparent softening in sand observed in experiments or numerical models is a joint result of many factors. There are structural and geometrical instabilities in plane-strain tests which cannot be explained by the constitutive behaviour itself. Especially, kinks at the boundaries significantly contribute to the load drop followed by the localisation (Needleman and Ortiz, 1991). This complex structural response cannot be fully captured as a constitutive feature.

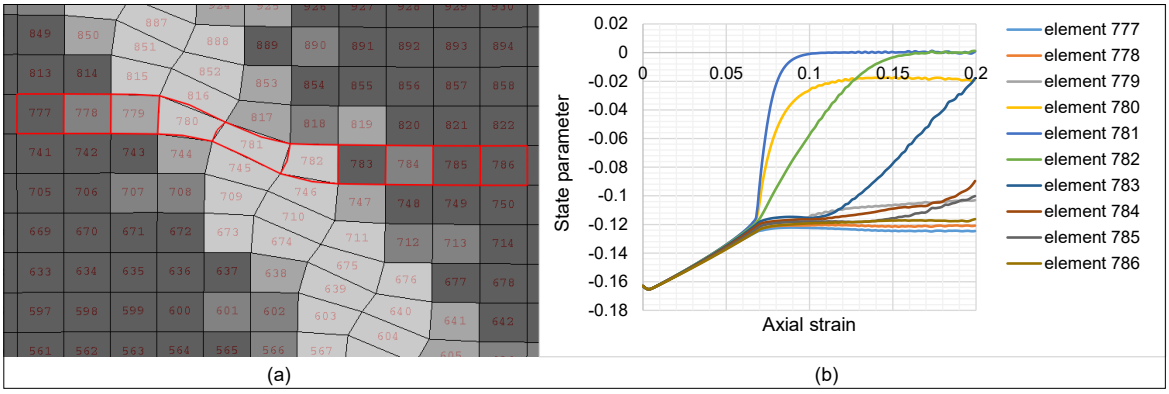

Fig. 6.15 (a) An enlarged view of localised elements and (b) state parameters at the centre of each element

6.6 Application of Diffusion Shear Band Model

The ability of the diffusion shear band model to replicate both macroscopic and microscopic response of undrained extra-small mesh was elucidated before. The ultimate goal is to use this model for large-scale field problems where the element size is several orders larger than the actual shear band thickness. As an initial step to demonstrate the applicability of diffusion SB model for macro-scale problems, an up-scaled biaxial compression test is conducted. The specimen dimensions are 1 m $\times$ 2 m. Quadratic elements with reduced integration are utilised throughout. Element dimensions are 0.5 m $\times$ 0.25 m similar to the calibrated element in section 6.5.1. This model is referred hereafter as the extra-large mesh which is different from the extra-large mesh in previous chapters. For comparison, the up-scaled biaxial test is also simulated with an extra-small mesh (0.00625m) which will be used as the benchmark case. Hence compared mesh size ratio is around 56.

Displacement of 0.4 m is applied at the top nodes to maintain the same strain rate as section 6.5.1. Different loading durations are considered. A permeable top boundary is

assumed in section 6.6.1, and fully impermeable boundaries are considered in section 6.6.2. No weak element is included in the top drained case. The element 16 is prescribed with weak material parameters in the fully undrained case. The diffusion SB model (Case 2), calibrated in section 6.5.1, is utilised for the up-scaled analysis. The mechanical responses of extra-large mesh with both the original NS model and the diffusion SB model are compared with those of extra-small mesh with the original NS model.

As graphically illustrated in Figure 6.16 a single bifurcated material point in Figure 6.16(a) can be represented by an undrained extra-small mesh with a shear band (Figure 6.16(b)). Non-bifurcated gauss points should follow the original NS model. The validity of this assumption will be discussed in section 6.7. Figure 6.16 elucidates three scales: the shear band is in micro scale, the element size is in meso scale and dimensions of the up-scaled biaxial test are in macro scale. Although this up-scaled biaxial test does not represent the actual field conditions, it can simply demonstrate the validity of the proposed approach for different remote boundary conditions.

6.6.1 Results of up-scaled biaxial compression test with open drainage at the top boundary

Global response

Figure 6.17 illustrates the global reaction forces of 1 m $\times$ 2 m biaxial compression tests with permeable top boundary. The disparity between the extra-small (yellow) and extra-large (green) meshes simulated with the original NS model is well evident. Predictions of diffusion SB model using the extra-large mesh are plotted in red dash line. The deviatoric strain contours of selected loading rates are displayed in Figure 6.18. A coloured cross indicates the number of bifurcated material points in each element.

Due to numerical singularities, simulations of the extra-small mesh are terminated prematurely. The termination occurred when two shear bands intersect leading to extreme mesh distortions at the intersection as displayed in Figures 6.18(a),(d) and (i). Shear strain contours in Figure 6.18 show localisations only in the extra-small mesh. Deformations in the extra-large mesh are more or less homogeneous except for elements near the top surface. The diffusion SB model is activated only for gauss points which have reached the bifurcation strains mentioned in Table 6.1. It is observed that the concentrated deformation is encouraged by the diffusion SB model although it does not fully capture the localised shear strains similar to the extra-small mesh.

In Figure 6.17, the mechanical responses of the extra-large mesh modelled with the diffusion SB model closely replicate the behaviours of the extra-small mesh when the loading

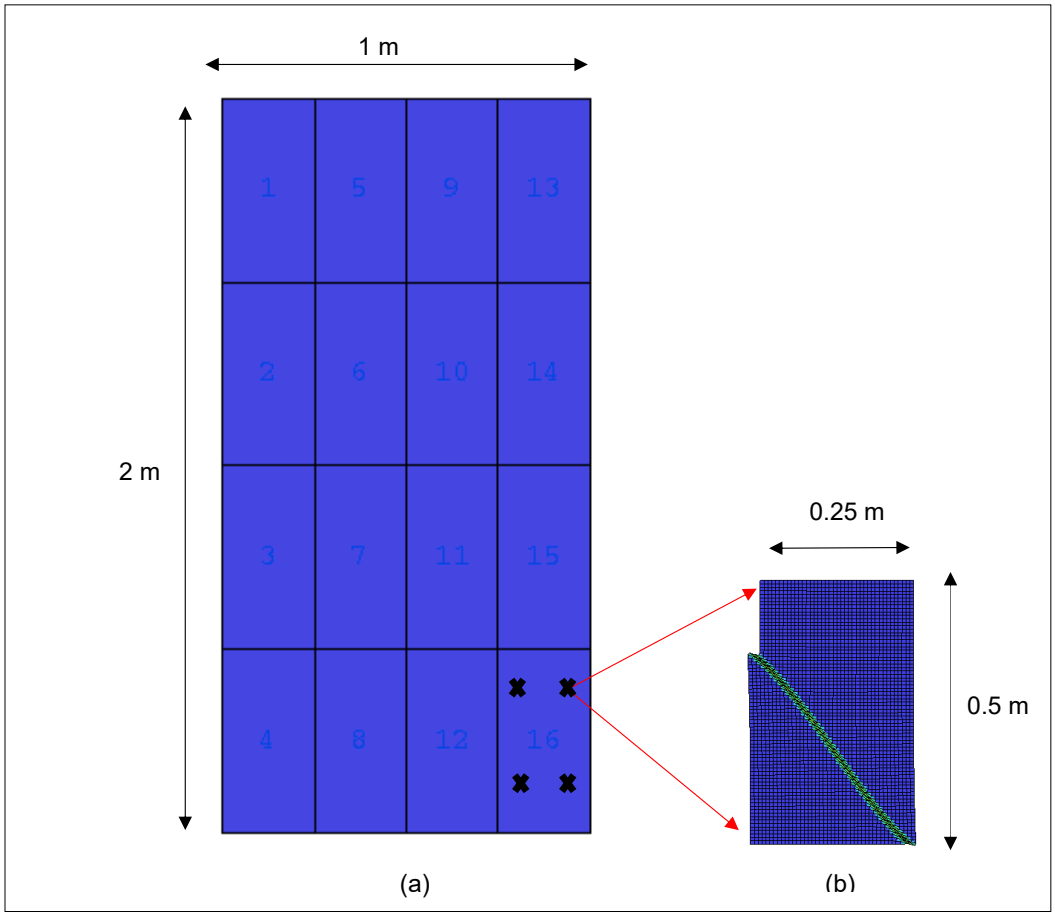

Fig. 6.16 (a) Up-scaled biaxial compression specimen with diffusion SB elements and (b) undrained material point discretised with 0.006 25 m mesh

durations are 0.005 s and 0.01 s. The deviatoric strain contours of the extra-small mesh corresponding to those loading rates show a single set of cross-shaped shear bands (Figure 6.18(d)).

When the loading durations are smaller (or faster loading rates), results of these static simulations are doubtful. The deviatoric strain contours of extra-small mesh in Figure 6.18(a) display pore pressure shocks (alternative dilative and contractive shear bands). Therefore, a dynamic simulation with inertia terms will be more appropriate for these rates. According to Abaqus 6.11 (2011), Darcy's law is only accurate for smaller flow velocities. High flow velocities have the effect of reducing the effective permeability and "choking" of pore fluid flow. In this region the minimum time step is smaller than the critical time step in Equation 5.4.

On the other hand, when the loading duration becomes slower, there is enough time for the fluid movement at internal nodes. In these cases, local volume changes may occur at

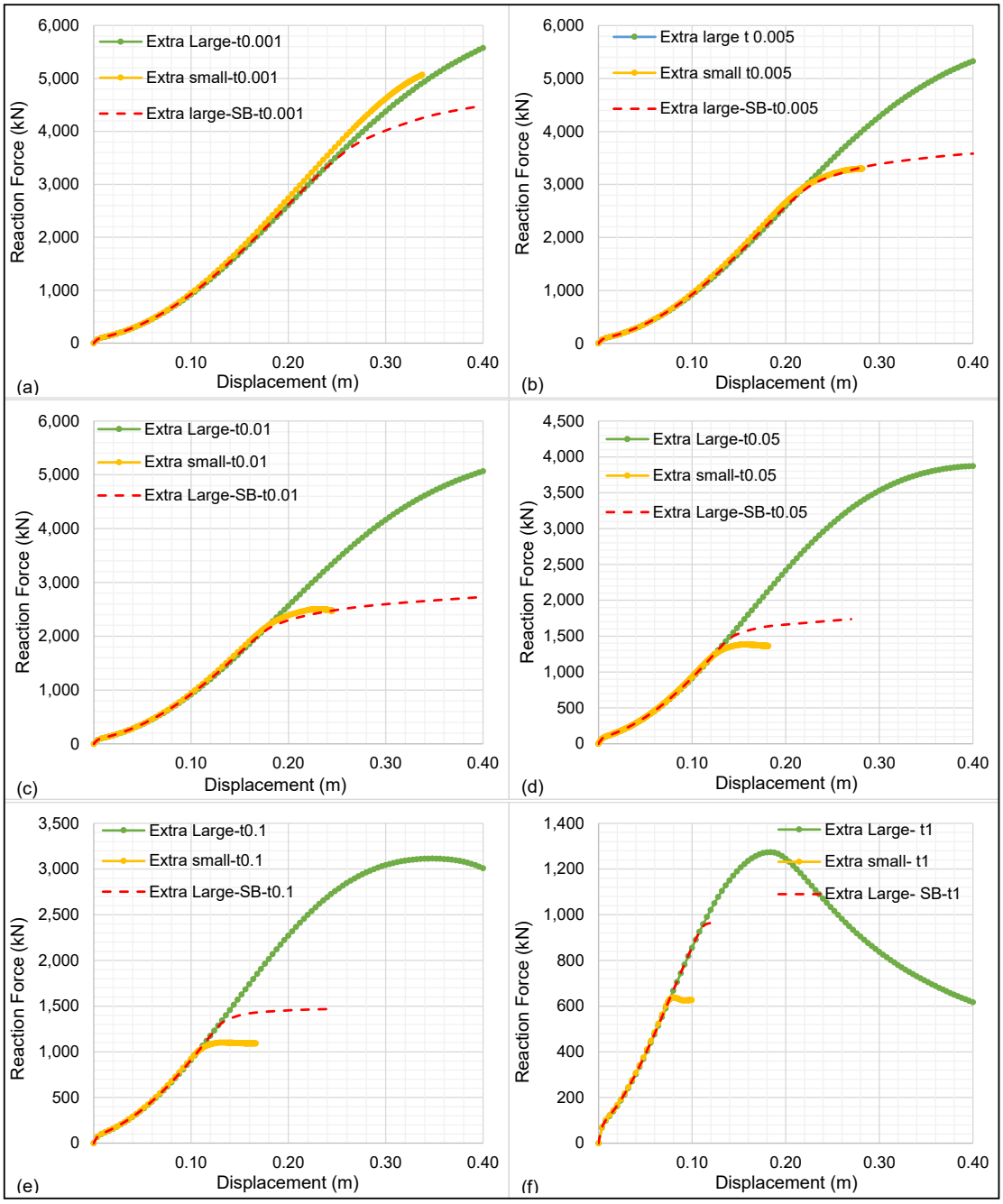

Fig. 6.17 Global reaction forces of top drained 1 m × 2 m biaxial compression tests for loading durations: (a) 0.001 s, (b) 0.005 s, (c) 0.01 s, (d) 0.05 s,(e) 0.1 s, (f) 1 s

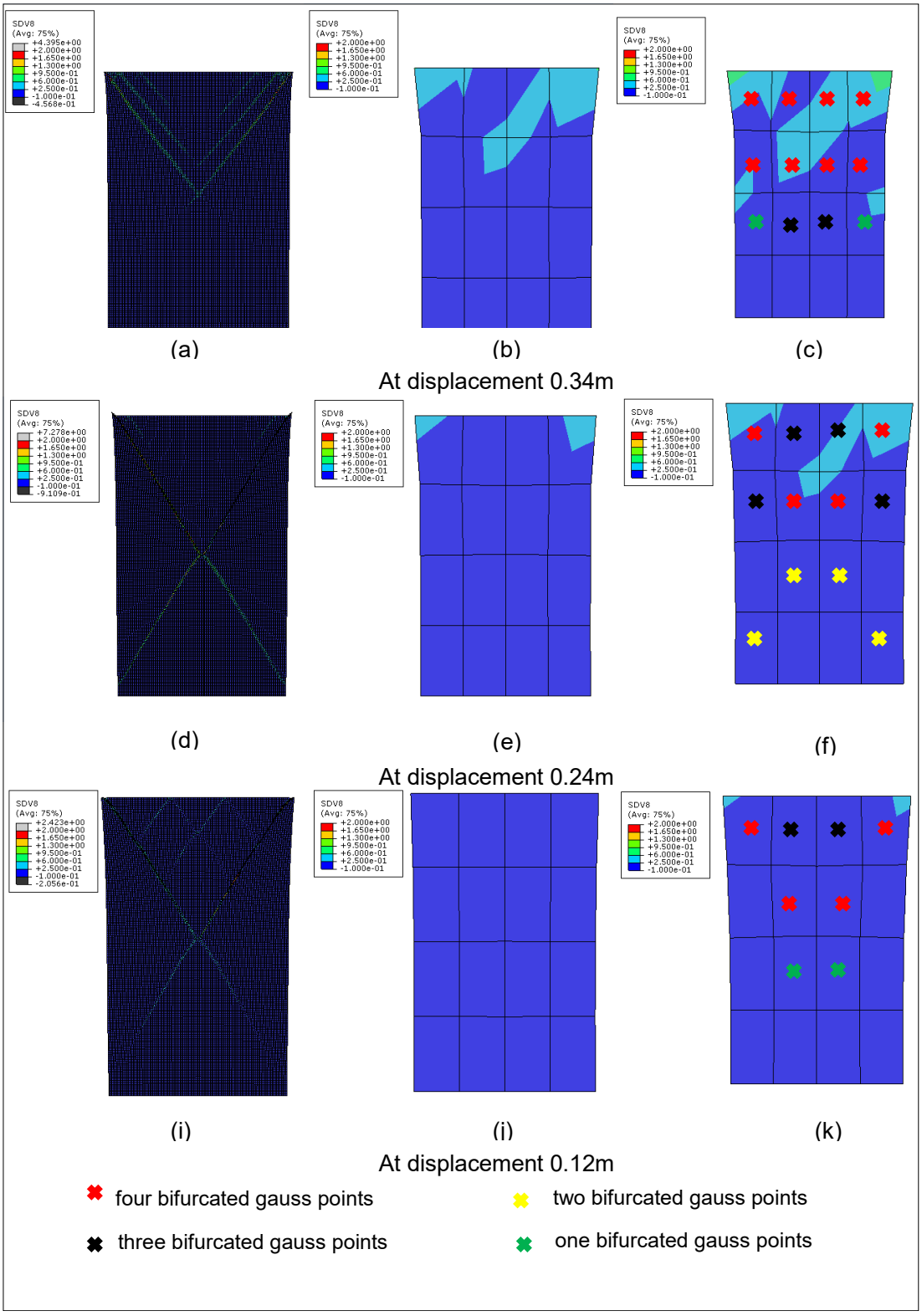

Fig. 6.18 Shear strain contours of top drained 1 m × 2 m biaxial compression tests for loading durations: (a)(b)(c) 0.001 s, (d)(e)(f) 0.01 s, (i)(j)(k) 1 s (left: extra-small mesh with original NS, middle: extra-large mesh with original NS, right: extra-large mesh with diffusion SB model)

interior nodes of the extra-large mesh contradicting the hypothesis of the undrained diffusion SB model. The global force-displacement relationships of loading durations 0.05 s, 0.1 s and 1 s ascertain that local drainage takes place internally. The green lines in Figure 6.17(d) to (f) tend to show peaks which signals the singularity of the drained acoustic tensor. It means internal drainage have started before that. Moreover, when the loading duration is 1s, deviatoric strain contour of extra-small mesh shows arrays of tributary localised bands as displayed in Figure 6.18(i). These tributary shear bands facilitate more drainage at the top boundary. Therefore, for these loading rates, the onset of bifurcation predicted by the SB model (which is calibrated for an undrained element) is much delayed than predictions of the extra-small mesh. In other words, as shown in Figure 6.17(d),(e),(f), the diffusion SB model overestimates the peaks of extra-small mesh for slower loading rates.

It is evident that the applicability of the diffusion SB model depends on the loading rate, permeability, drainage length as well as the remote boundary conditions. Nevertheless, as compared to simulations of extra-large mesh with the original NS model, the error from the proposed method is marginal.

Average elemental response

Apart from the material behaviour, the global response of the biaxial compression test is also dominated by remote boundary constraints. Hence global behaviour itself is not adequate to conclude about the validity of the proposed method. Therefore, it is worthwhile to compare the average constitutive behaviour of each element (four gauss points) in extra-large mesh with the average response of a respective subset of elements in the extra-small mesh. The purpose is to check whether the proposed constitutive model captures the average mechanical response of the extra-small mesh locally.

Only results of loading duration 0.01 s are considered for the discussion below. The extra-small mesh is partitioned such that each partition is equivalent to a respective element in the extra-large mesh as shown in Figure 6.19. The average mechanical responses of partitions in the extra-small mesh are compared with those of equivalent elements in the extra-large mesh. Because of the symmetrical loading, only average stress-strain relationships of element number 9 to 16 are compared in Figure 6.20.

The progressive development of two crossed shear bands in the extra-small mesh (Figure 6.18(d)) can be described using Figure 6.21(a) which encloses the stress-strain responses of each partition. In the extra-small mesh, there are only eight partitions which contain shear bands (1, 4, 6, 7, 13, 10, 11 and 16). Out of them, partitions 1 and 13 have drained top boundaries, and hence localisation initiates in them. Therefore, these two partitions inherit the highest deformation as shown in Figure 6.21(a). Also, their ultimate strengths are

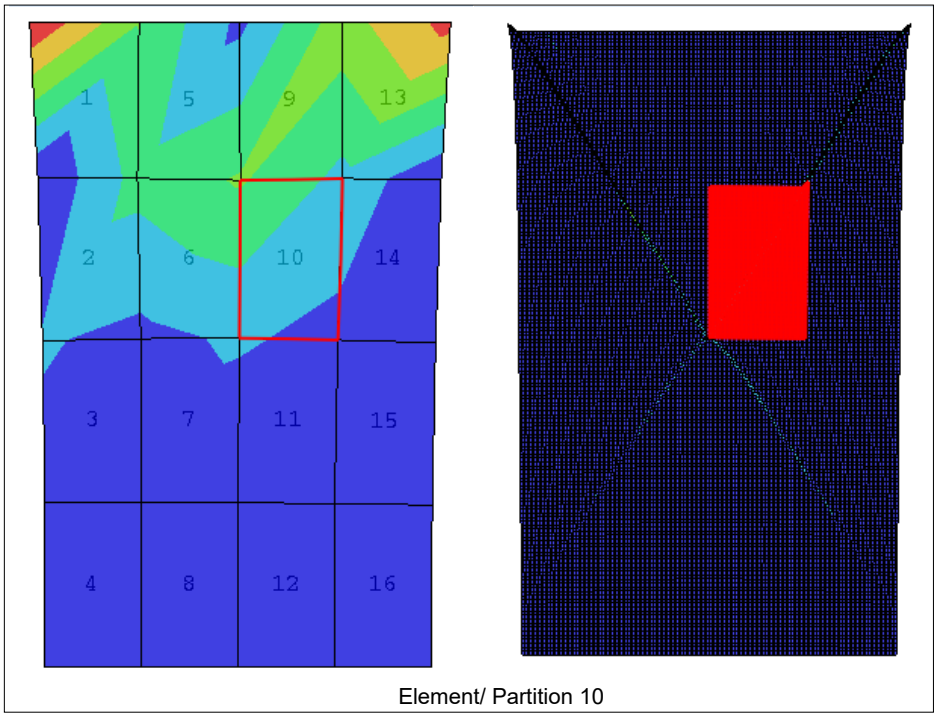

Fig. 6.19 Partition 10 in extra-small mesh corresponding to element 10 in extra-large mesh

smaller since there is no volume constraint. These shear bands then progress to partitions 6 and 10, thus they have second highest deformation. With further axial displacement on the top, these shear bands approach to partitions 7 / 11 and then 4/16 successively. The partitions without shear bands (9, 5, 3, 15, 12, 8, 14 and 2) display slight unloading after the bifurcation. Nevertheless, a continued post-localised deformation could not be observed for the extra-small mesh. Extreme mesh distortions at the intersection of two shear bands cause convergence difficulties resulting in termination around 65 % of applied displacement. From the overview of the average behaviour of partitions in the extra-small mesh, it is observed that partitions with shear bands show enhanced deformation compared to others.

On the contrary, the extra-large mesh can hardly capture this progressive failure. No visible shear band is seen in Figure 6.18(e), and all elements except those in the first two rows show a continuous dilative hardening. Also, as the distance between two nodes is comparatively high in the extra-large mesh, the boundary movement has more influence on other elements. Therefore, they tend to show larger deformation than their respective extra-small partitions.

When the diffusion SB model is applied to the extra-large mesh, a considerable improvement in capturing the post-localised deformation can be seen. Figures 6.20(b),(c),(e) and (h) illustrate the average stress-strain relationships of partitions with shear bands (10, 11, 13 and

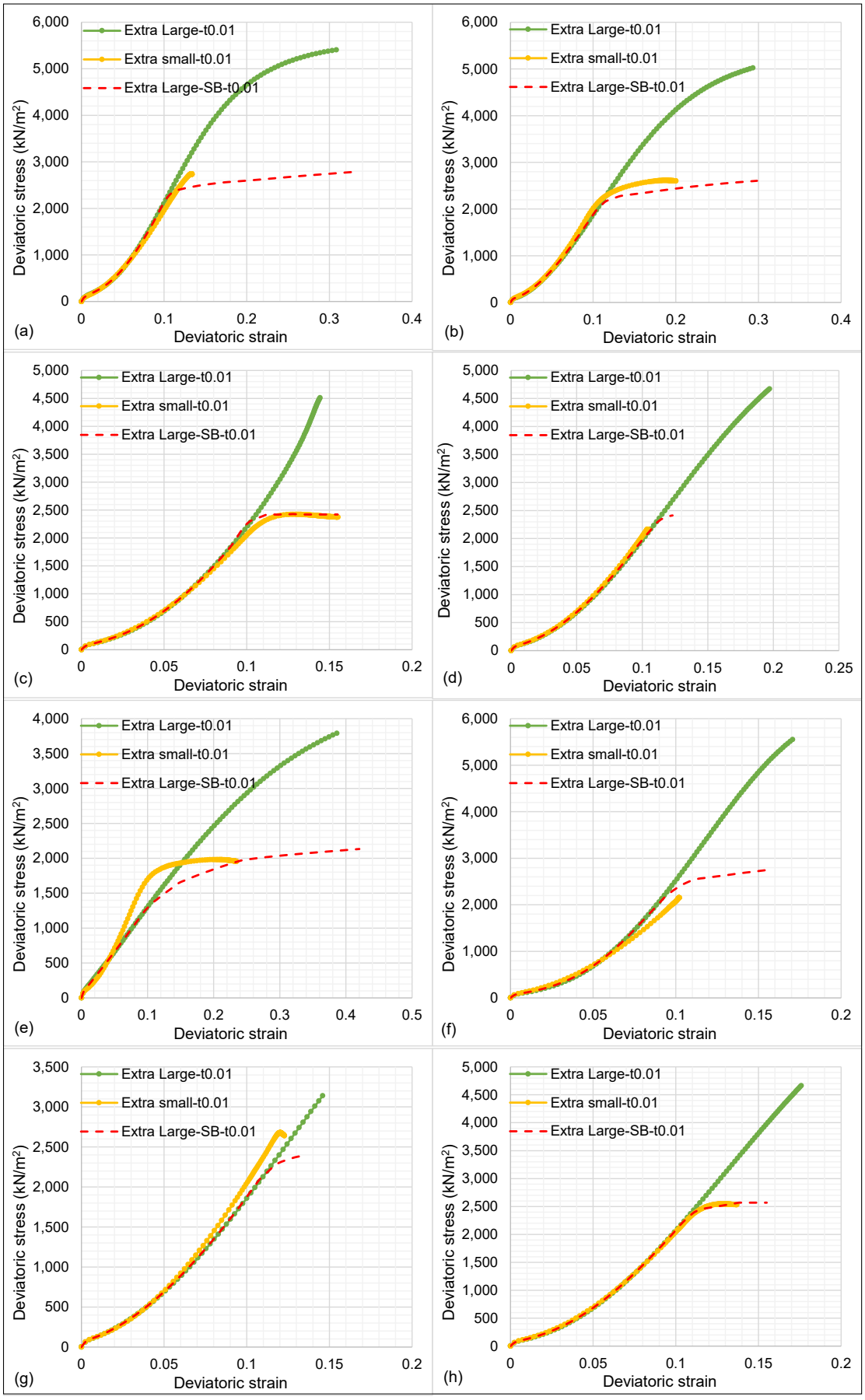

Fig. 6.20 Average stress-strain relationships of partitions in extra-small mesh compared with respective elements in extra-large mesh for loading duration 0.01 s: Element/partition number (a) 9, (b) 10,(c) 11, (d) 12, (e) 13, (f) 14,(g) 15, (h) 16

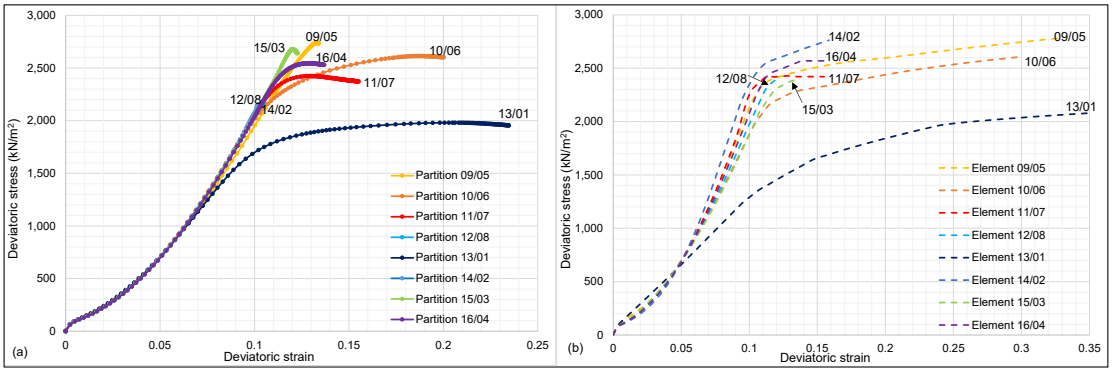

Fig. 6.21 Average stress-strain relationships of (a) partitions in extra-small mesh predicted by original NS model and (b) elements in extra-large mesh predicted by diffusion SB model for loading duration 0.01 s

16) in the extra-small mesh. They are closely replicated by the diffusion SB model except for the partition 13. This is because the SB model is intended only for undrained elements and element 13 has a permeable surface.

In Figures 6.20(a),(d),(f) and (g), the deformations of partitions 9, 12, 14 and 15 in extra-small mesh, abruptly terminate after the bifurcation. It is because all elements in those partitions are unloading and their average response shows a slight snap-back. If the extra-small mesh had converged fully, further reloading and unloading could be expected depending on the development of secondary shear bands. Although the diffusion SB model captures this diminished deformation for elements 12 and 15, it inaccurately predicts a continuous shear deformation for elements 9 and 14. In fact, the element 14 in the extra-large mesh is subjected to greater deformation than the partition 14 in the extra-small mesh. This is because the impact of moving boundaries are more critical when the distance between two nodes is greater. As the onset of the shear band is detected based on deviatoric strain, the diffusion SB model cannot distinguish the difference between concentrated and uniform deformation. Hence the SB model wrongly assumes that an internal shear band has occurred in the element 14. The same observation applies for the element 9 as well. Due to the permeable surface, it deforms considerably even without a shear band. As the proposed method is intended for elements with zero volumetric strain, it can not be recommended for elements close to moving or permeable boundaries.

In conclusion, the diffusion SB model is competent in reducing the stiffness caused by local drainage and correcting the stress increment when the strain increment is given, for bifurcated elements. However, the method used to detect the onset of the shear band is ambiguous for arbitrary loading conditions.

Apart from element size, the dimension of the specimen, number of nodes, integration points and boundary conditions influence the deformation. Probably the up-scaled model with 16 elements is not appropriate to assess the validity of the proposed approach. One reason is that there is a considerable impact from moving boundaries. Also due to incompressible material behaviour at higher loading rates, larger elements do not perform very well.

6.6.2 Results of up-scaled biaxial compression test with fully impermeable boundaries

To alleviate the influence of drained top boundary, an up-scaled biaxial compression test with fully impermeable boundaries is conducted. The global force-displacement curves for different loading rates are displayed in Figure 6.22. The deviatoric strain contours of selected loading rates are also illustrated in Figure 6.23.

Global response

Due to the weak element included at the lower right corner, a single shear band is triggered as illustrated in Figure 6.23. When loading durations are smaller than 1 s, extra-large mesh displays identical load-displacement curves in Figures 6.22(a) to (e). They indicate almost uniform dilative hardening throughout the specimen. In contrast, the load-displacement responses of extra-small mesh show distinct peaks followed by softening except Figure 6.22(a). It should be mentioned here that post-bifurcation softening was not observed for undrained global boundaries when the specimen size was smaller. When the ratio of sample height to the element size is greater, more material points outside the band are unloading. This causes the post-peak softening. Another observation is that the onset of the peak is delayed for greater loading rates.

Except for loading duration 0.001 s, the diffusion SB model closely captures the onset of bifurcation and post-localised deformation globally. However, it cannot apprehend the post-peak softening caused by elastic unloading. The force keeps on increasing after the localisation albeit with reduced stiffness. This is because a small portion of shear-induced dilation is prescribed to the outside material as well (Case 2). Shear strain contours of diffusion SB model in Figures 6.23(c),(f),(k) tend to display more localised patterns compared to contours of the original NS model in Figures 6.23(b),(e),(j).

Average elemental response

The average mechanical responses of partitions in the extra-small mesh are compared with those of equivalent elements in the extra-large mesh for loading duration 0.01 s. Only partition/element numbers 9 to 16 are shown in Figure 6.24. The extra-small mesh terminates the analysis around 85 % of applied displacement.

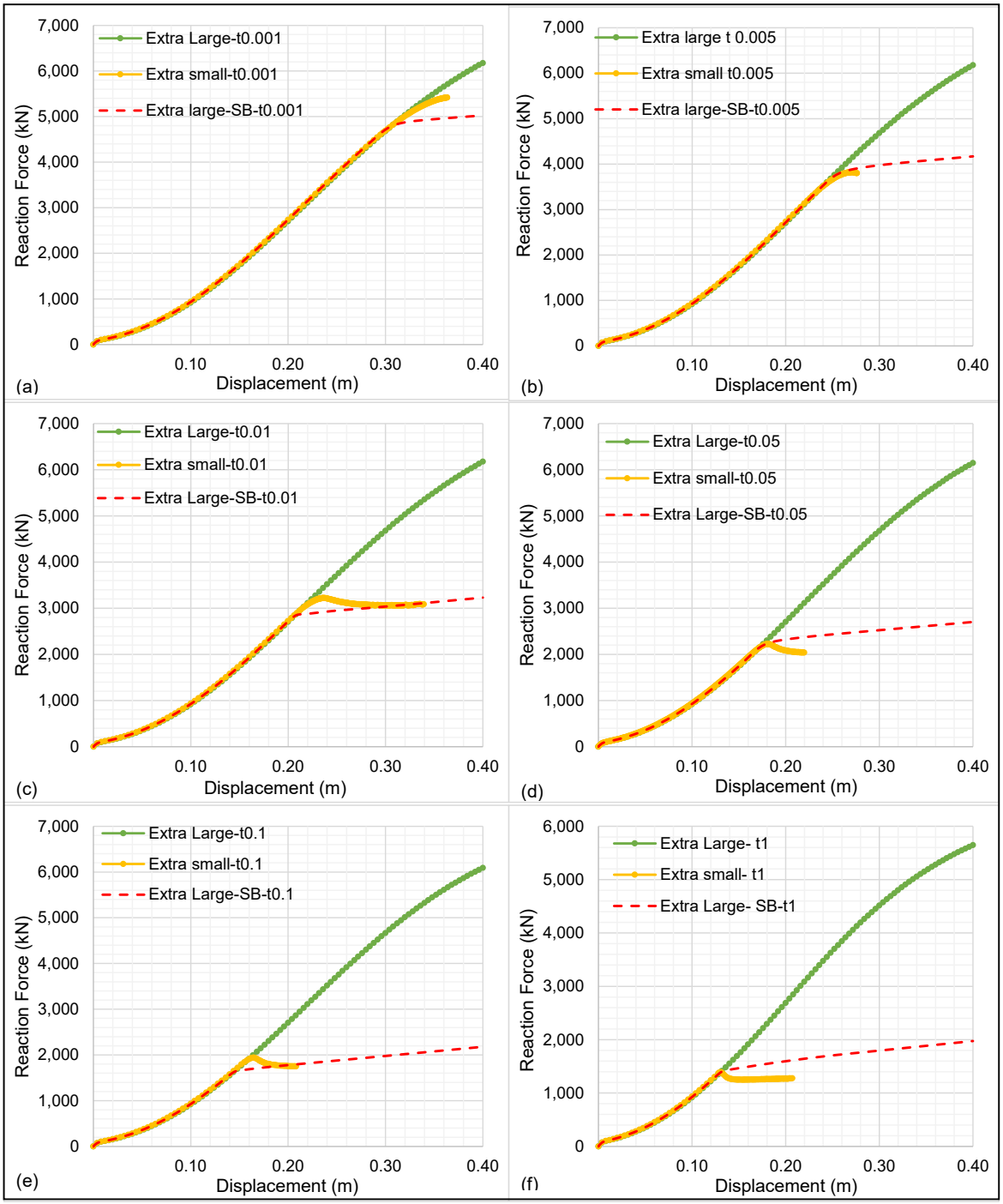

Fig. 6.22 Global reaction forces of fully impermeable 1 m $\times$ 2 m biaxial compression tests for loading durations: (a) 0.001 s, (b) 0.005 s, (c) 0.01 s, (d) 0.05 s,(e) 0.1 s, (f) 1 s

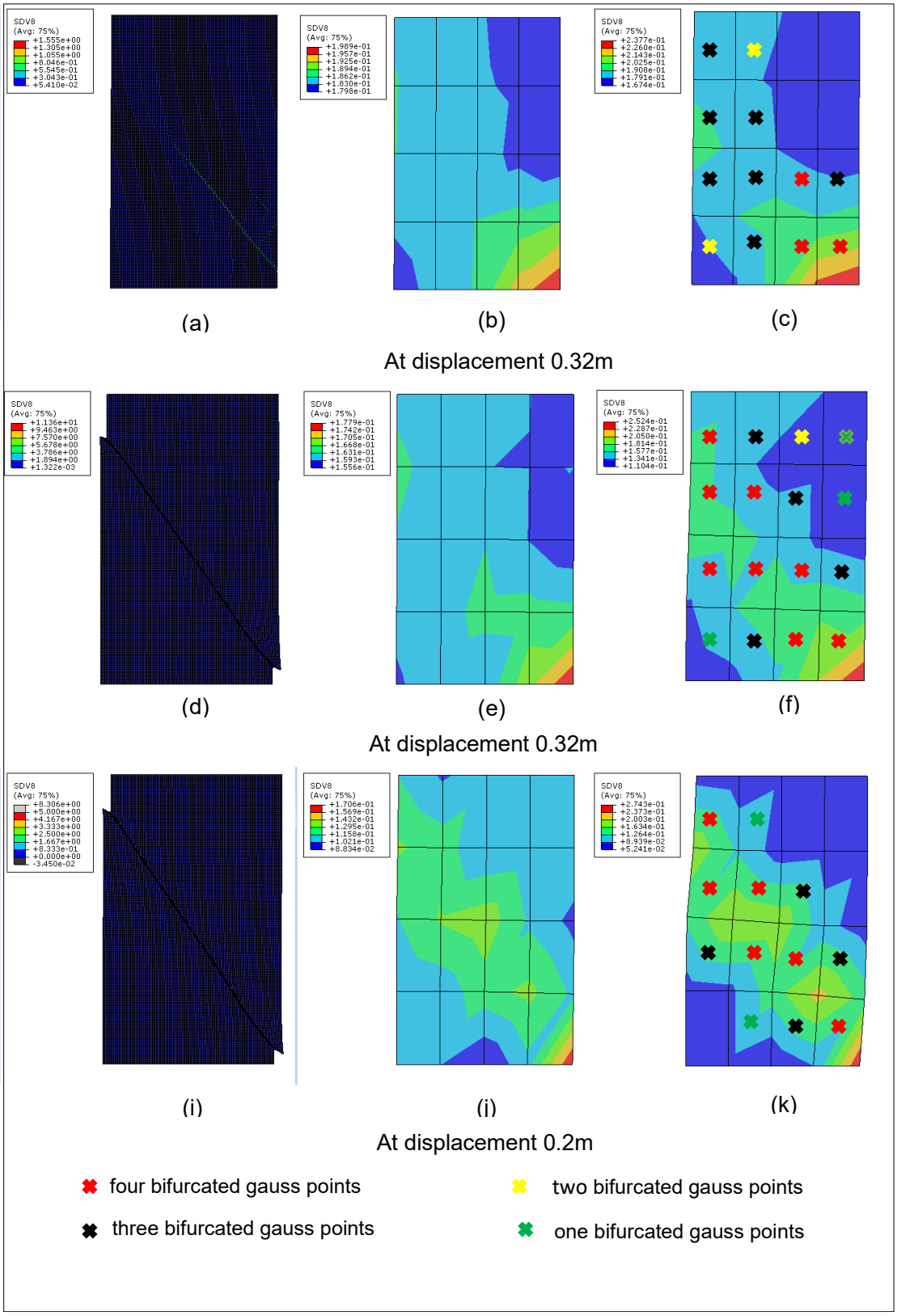

Fig. 6.23 Shear strain contours of fully impermeable 1 m × 2 m biaxial compression tests for loading durations: (a),(b),(c) 0.001 s, (d)(e)(f) 0.01 s, (i)(j)(k) 1 s (left: extra-small mesh with original NS, middle: extra-large mesh with original NS, right: extra-large mesh with diffusion SB model)

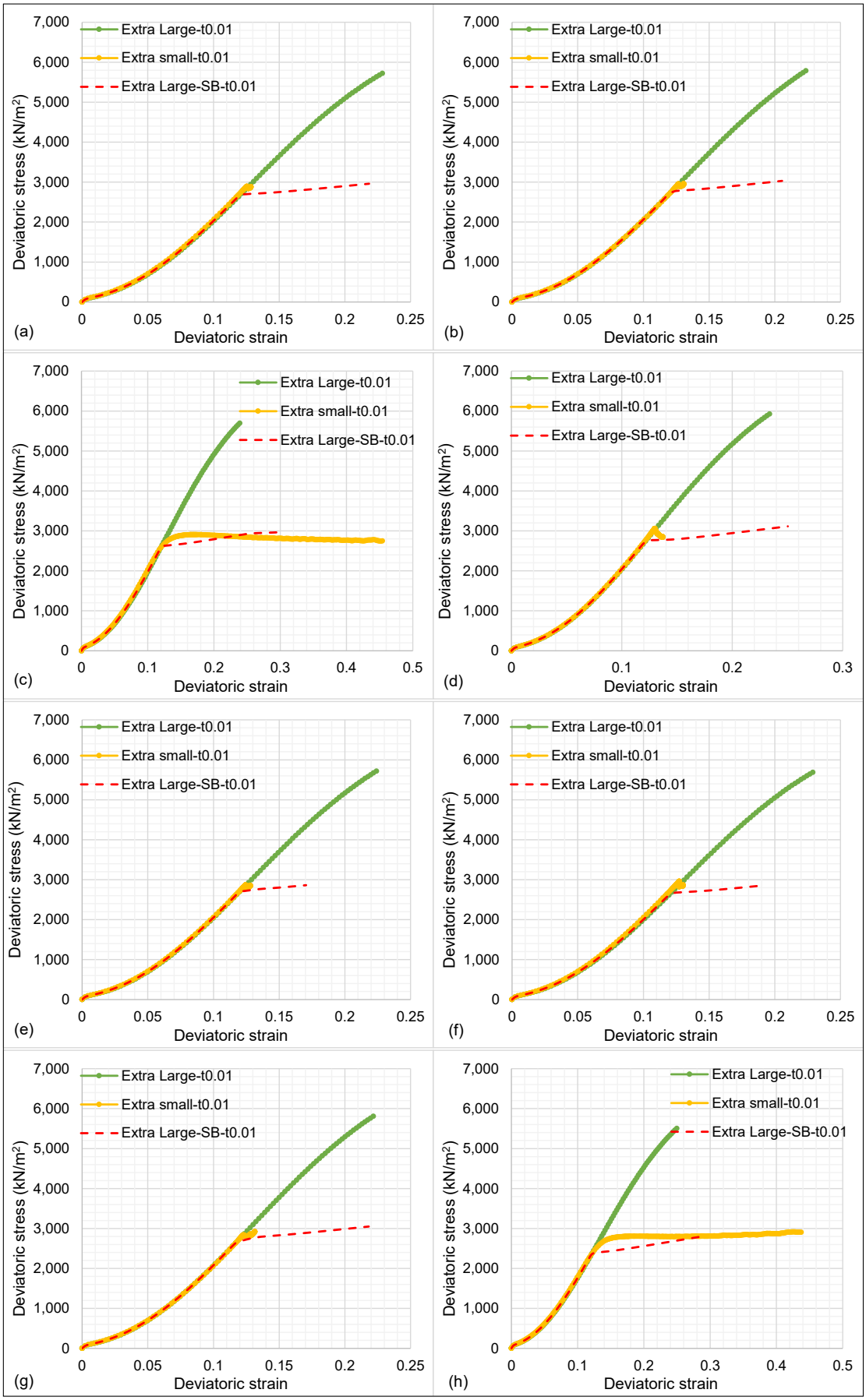

Fig. 6.24 Average stress-strain relationships of partitions in extra-small mesh compared with respective elements in extra-large mesh for the loading duration 0.01 s: Element/partition number (a) 9, (b) 10,(c) 11, (d) 12, (e) 13, (f) 14,(g) 15, (h) 16

It is evident from the deviatoric strain contours in Figure 6.23(d), that only partitions 1, 6, 11 and 16 include shear bands. The original NS model predicts greater average strain for those partitions, whereas deformation of other partitions terminates soon after the localisation is triggered. On the contrary, all elements in extra-large mesh indicate almost uniform deformation. This is because, for the considered specimen dimensions, the element size is too large to capture the strain concentration. As previously discussed, larger iso-parametric elements smear the discontinuous deformation over several elements. When the diffusion SB model is applied to the extra-large mesh, a comparatively better match with the extra-small mesh can be seen for partitions with shear bands as shown in Figures 6.24(c) and (h). However, for those without bands, the extra-large elements with the diffusion SB model overestimate the shear deformation.

When the numerical shear band is very thin (for extra-small mesh), the strain discontinuity is greater. Thus, shear strain inside the band is much higher than outside. For a larger mesh, the discontinuity is smeared over neighbour elements. Hence it shows an almost homogeneous deformation. The diffusion SB model slightly overcomes this issue by redistributing more strain in elements 11 and 16 and less in others, such that the global response matches. Nevertheless, it still inaccurately predicts prolonged post-localised deformations for elements 9, 10, 12, 13, 14 and 15. Furthermore, 16 element model is not capable of replicating the elastic unloading which happens in the extra-small mesh.

6.6.3 Range of applicability

It is evident that the applicability of diffusion SB model is governed by the degree of internal drainage which depends on boundary constraints, drainage length, loading rate and permeability. Figure 6.25 plots the maximum reaction forces achieved within 20 % strain by extra-large and extra-small meshes. The normalised velocity is calculated based on diffusive properties stated in Chapter 5. The drainage length is assumed as the height of the specimen. Hypothesising that the extra-small mesh predicts the ground truth, Table 6.2 presents the error of predicting maximum forces by the extra-large mesh with and without diffusion SB model. The loading duration 0.001 s is ignored here since it closely represents the locally undrained case. It is observed that when mesh size is increased nearly 56 times, the error of predicting peak by the original NS model is between 61% to 195% for the top drained case and between 89% to 389% for the fully undrained case. When the diffusion SB model is used with extra-large mesh, this error is between 8% to 52% for the top drained case and 0.6% to 36% for the fully undrained case.

The accuracy of the diffusion SB model is within 20% when the normalised velocity is between 10 to 40 for the top drained case. For the globally undrained case, 20% accuracy is

achieved when the normalised velocity is between 1 to 40. In these regions, mesh sensitivity of conventional FEM is reduced more than 50%. However, it should be mentioned that these values are dependent on the specimen to mesh size ratio as well.

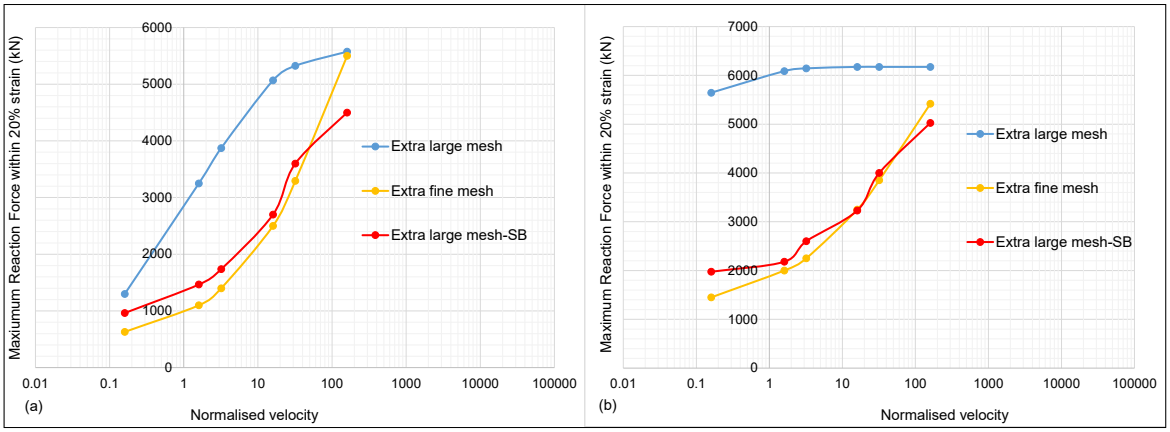

Fig. 6.25 Maximum reaction forces plotted against normalised velocity for 1 m $\times$ 2 m biaxial compression tests with (a) permeable top boundary and (b) all impermeable boundaries

Table 6.2 Error of using extra-large elements

	top drained		fully undrained	
Loading duration (s)	original NS	diffusion SB	original NS	diffusion SB
1	106%	52%	389%	36%
0.1	195%	33%	204%	9%
0.05	176%	24%	273%	15%
0.01	102%	8%	89%	0.6%
0.005	61%	9%	160%	4%

6.7 Limitations of the Diffusion SB Model

The proposed approach is a heavily simplified mathematical model which takes account of internal fluid movements within the constitutive level without changing equilibrium equations. It has several restrictions which are discussed below.

Validity of the ground truth

The proposed model is calibrated with respect to another FE model with an extra-small mesh. Hence the validity of the ground truth itself is questionable. By default, it has all the drawbacks of FEM. Moreover, due to numerical singularities, there is a minimum shear band thickness (smallest mesh size) this model can be calibrated with. So it is not appropriate for soil with very fine particles.

Scale effects

There are scale effects which influence the range of normalised velocity within which this model is applicable. It is shown that the diffusion SB model is mostly valid in the partially drained region. The boundaries of this region depend on the element size, specimen size, loading rate and permeability. Therefore, disparities can occur when the diffusion SB model is calibrated in meso scale and applied in macro scale. In Figure 6.16, the up-scaling ratio is 4. If this ratio is high, there can be a disparity between the calibrated onset of localisation and the actual one. As shown in Figure 6.26, the calibration of the model is done for a single element with certain boundary conditions and a deformation mode (isochoric biaxial compression). In this case, the deviatoric strain is a function of axial deformation. On the contrary, in the macro scale model, the elements can be subjected to complex combinations of deformations. Apart from arbitrary translations at four nodes as displayed in Figure 6.26, shear deformation can cause principal axis rotations as well. Therefore, the calibrated deviatoric strain at the onset of localisation based on biaxial compression may not fit for an arbitrary deformation. For example, the model is not suitable for elements near permeable boundaries.

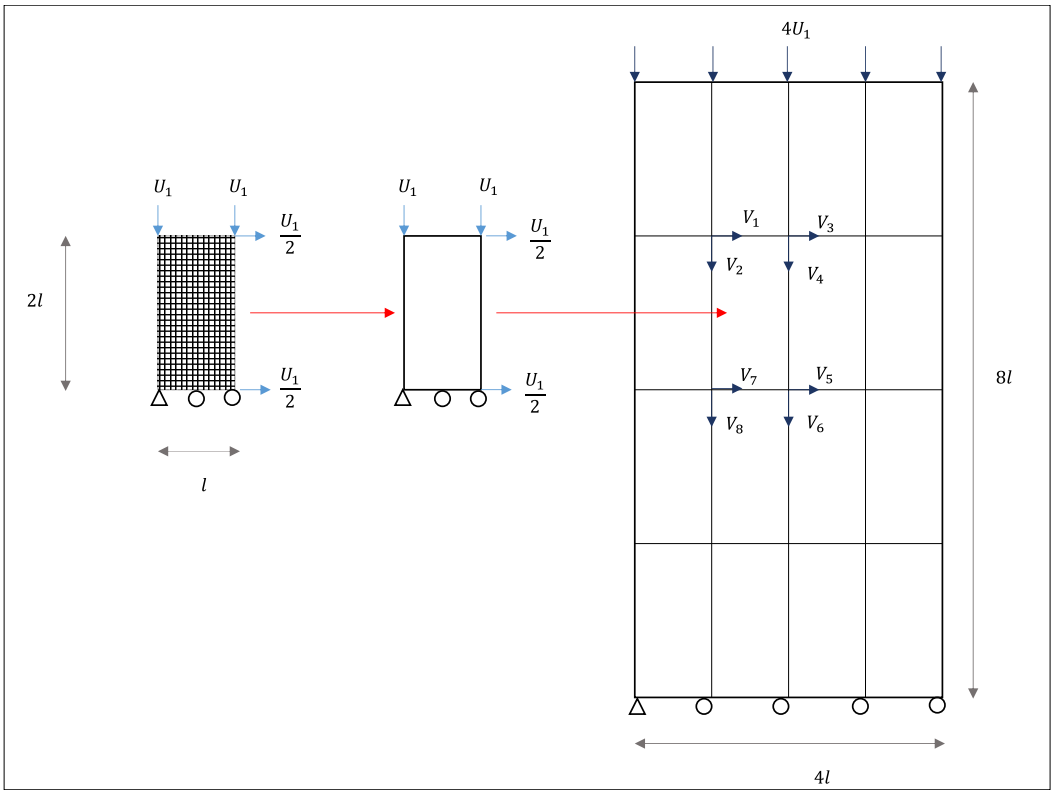

Fig. 6.26 Concept of up-scaling

Minimum element size

The 1D diffusion equation is based on the assumption that water can dissipate an infinite distance. Also, it is assumed that the pore pressure outside the shear band is not decreased due to this dissipation. These assumptions are valid only when the thickness of the shear band is very small compared to element dimensions. According to Figure 6.8, the length of integration point should be at least 8 times the shear band thickness to assume that material outside does not receive pore pressure (for the considered range of time increments).

Allowance for local volume changes

It is observed in Figure 6.25 that this model is not accurate for any arbitrary loading rate. It is only valid in a region of normalised velocity within which large elements display almost undrained behaviour, but a fine mesh can capture the local drainage. When the loading duration is high, pore fluid starts to flow at nodes of large elements. This is accompanied by local volume changes. In this region, the applicability of the diffusion SB model is doubtful. Figure 6.25 shows that model predictions drift from reality when the loading time is greater.

Accuracy of predicting the onset of shear band

The diffusion SB model is activated in material points which have reached the calibrated deviatoric strain at bifurcation. However, in the up-scaled model, the larger mesh smears the deviatoric strain over several elements. Therefore, the diffusion SB model is activated in the surrounding elements as well. This is also the case for elements near the moving boundaries.

Inability to reproduce complex shear band patterns

The diffusion SB model is calibrated for a simple diagonal shear band only. The extra-small mesh is capable of producing very complex shear band patterns which cannot be replicated by the diffusion SB model.

6.8 Conclusions

Chapter 6 presents a phenomenological constitutive model for the undrained deformation of saturated dilative sand in the presence of a locally drained shear band. Rate and space dependence of hydro-mechanical coupling is captured through the diffusion equation. Separate constitutive relationships are generated for the band and intact material which are averaged to calculate the macroscopic response. Single element results are first calibrated with the global response of the extra-small mesh with impermeable boundaries. Then it is applied for up-scaled boundary value problems. Although the proposed method is successful in reproducing both global and local behaviours of extra-small mesh, it has certain limitations when applied to large-scale problems.

6.8.1 Contributions

The main contributions of this chapter are

- Development of a novel conceptual constitutive model to describe the deformation of undrained dilative hardening materials

  A theoretical model is presented to apprehend local pore fluid movements at the shear band scale. The model can be used at the constitutive level without changing equilibrium equations. The proposed method can predict the macroscopic mechanical response of saturated dense sand appreciating the underlying micro-kinematics. It integrates the material behaviour at two scales: the thickness of the shear band and the size of the material point. Hence it is inherently independent of the spatial discretisation. The influence of time and space parameters on the competing mechanisms of pore pressure generation and dissipation is taken into account. Therefore the model can be used for large-scale boundary value problems without extreme mesh refinement.

  The diffusion SB model can replicate the macroscopic reaction during the globally undrained deformation of a biaxial compression test with extremely fine mesh. It is pointed out that undrained dilative hardening predicted by a homogeneous material model is perceptibly reduced due to the local drainage associated with shear localisation. The model is validated for different loading rates. Two hypotheses are made during the formulation: total shear strain is concentrated inside the band, or the outside material shares a portion of shear strain. It is shown that the global strength based on the latter can more accurately represent the progressive development of a locally drained shear band.

  The distinct material behaviours inside and outside the band predicted by the diffusion SB model are qualitatively in good agreement with those of extra-small mesh. It is illustrated that depending on the loading rate and the shear band thickness adopted, the behaviour inside the band can be fully or partially drained. This degree of drainage, in fact, governs the strength. The pore fluid diffusion is associated with local volume changes irrespective of boundary conditions of the material point.

  After Pietruszczak (1995), this is the first time a constitutive model is developed specifically for undrained dilative material. Compared to his implementation, this model is more advanced in capturing the rate-dependence of pore fluid diffusion. A further step forward, the partial or full drained response inside the shear band is qualitatively validated here with a fine mesh. In contrast to the strong discontinuity approach by Larsson and Larsson (2000a,b), this simplified method is easy to implement. Moreover,

compared to all previous attempts, this model takes advantage of critical state concepts for the simulation of partial volume change and its relation to strength development.

- Application of the developed model to large-scale boundary value problems

  Based on up-scaled biaxial compression results, it is observed that applicability of the diffusion SB model depends on the loading rate, permeability, drainage length as well as the remote boundary conditions. With the original NS model, the error of predicting the maximum force by 56 times larger mesh is between 61% to 195% for the top drained case and between 89% to 389% for the fully undrained case. When the diffusion SB model is used, this error is between 8% to 52% for the top drained case and 0.6% to 36% for the fully undrained case. For both boundary conditions, the diffusion SB model reduces the mesh sensitivity more than 50% when the normalised velocity is between 1 and 40. These values are however dependent on tested mesh and specimen sizes.

  In essence, the model is designed for locally undrained (isochoric) material points. Hence it is not valid for gauss points near permeable boundaries or when the loading rate is slow enough to induce local volume changes. It also cannot replicate complex localisation patterns. However, even with these limitations, the prediction error of the SB model is much less than that of the conventional material model.

Chapter 7

Conclusions and Recommendations

7.1 Summary and Conclusions

This thesis numerically investigates the behaviour of dilative granular material. The purpose is to improve the accuracy of modelling saturated dense sand under varying degrees of drainage conditions. The difference between global and local fluid movements and its association with localisation are identified. The rate and mesh dependence on the initiation of the shear band and post-localised deformation is investigated. This study upgrades the constitutive modelling of saturated dense sand mimicking the underlying micro-kinematics within the limitations of the continuum based finite element method.

Associative NS model can successfully capture the soil in the dry side of the critical state, due to its state parameter and limiting hardness concepts. It is capable of modelling undrained dilative hardening and cease of dilation at the critical state. The non-coaxial rule is active only during principal axis rotations, and its effect subsides near the critical state. The impact of the non-associative rule is noticeable after the peak. Both flow rules reduce the model's tendency to dilate. However, the original NS model with associative and coaxial flow rule is sufficient to apprehend the basic characteristics of dense granular material under both drained and undrained conditions.

The onset of localisation depends on the adopted flow rule in the constitutive model. For drained tests, the associative NS model predicts instability at the peak, whereas modified rules detect localisation in the hardening regime. For undrained tests, bifurcation criterion is not satisfied by original or modified NS models. The local drainage caused by a heterogeneity is the triggering mechanism for localisation in globally undrained dense sand. This can not be captured by the constitutive behaviour.

The nonlocal regularisation introduces a characteristic length into constitutive equations. For dry sand, it produces mesh objective mechanical responses and a unique shear band thickness after the peak. Along with scaling the nonlocal theory can be used to obtain physically realistic load-displacement curves without extreme mesh refinement. For 8 times larger elements, mesh objectivity is achieved by the nonlocal method and scaling within 20% accuracy limit. The volumetric regularisation is more effective during softening than at the critical state. The nonlocal method and scaling decrease the smallest band thickness simulated by FEM (without losing ellipticity of governing equations) from 0.02m to 0.005m.

The hydro-mechanical coupling governs the onset of localisation in saturated granular material. Depending on the degree of local drainage, shear zones can be fully or partially drained, or locally undrained. It is numerically decided by the permeability, compressibility, loading rate, mesh and specimen size. The drainage condition at remote boundaries also influences the initiation of shear bands. The maximum loading rate that can be simulated by static consolidation analysis without losing accuracy is sensitive to the element size. In reality, heterogeneities caused by non-uniform particle size and distribution also act as triggering factors of shear bands.

The nonlocal regularisation of soil skeleton is effective in saturated sand only when either shear band or all material points are fully drained. It is not successful in partially drained regions. Hence a mesh independent constitutive relationship is developed with an embedded localisation for partially drained region. It bridges the micro and macro response by capturing pore fluid diffusion at the grain scale. It is validated with globally undrained extremely fine mesh and applied for up-scaled boundary value problems. It is observed that dilative hardening during undrained deformation is diminished due to fluid movements which occur at a smaller scale than element size.

Table 7.1 and Figure 7.1 summarise the range of normalised velocities during which the mesh objectivity is achieved within 20% accuracy limit from both nonlocal NS and diffusion SB methods. The comparison is done with 0.00625m benchmark meshes (shown right in Figure 7.1). Table 7.1 provides recommendations on normalised velocities and element to grain size ratios, for which these two methods are applicable. These values are subjective of tested specimen size and boundary conditions.

The nonlocal method is applicable for the softening of soil skeleton. Hence it is recommended when the normalised velocity is in the fully drained region. Since scaling always introduces an error, there is a maximum element size for which this method can be used. The diffusion SB model is intended for hydro-mechanical coupled problems, and it is suitable when the normalised velocity is in the partially drained region. Only a minimum element

size can be recommended for this, and the maximum size depends on the dimension of the problem.

Table 7.1 Range of applicability of nonlocal and diffusion NS models in saturated dense sand

Model	Tested specimen	Average mesh size	mesh ratio compared to benchmark	20% accuracy in specimen with open drainage	20% accuracy in specimen with closed drainage	mesh size recommen-dation
nonlocal NS	$0.5m \times 0.25m$	0.05m	8	$V_n \leq 1$	$V_n \leq 0.1$	$\leq 10\, t^{sb}$
diffusion SB	$2m \times 1m$	0.35m	56	$10 \leq V_n \leq 40$	$1 \leq V_n \leq 40$	$\geq 16\, t^{sb}$

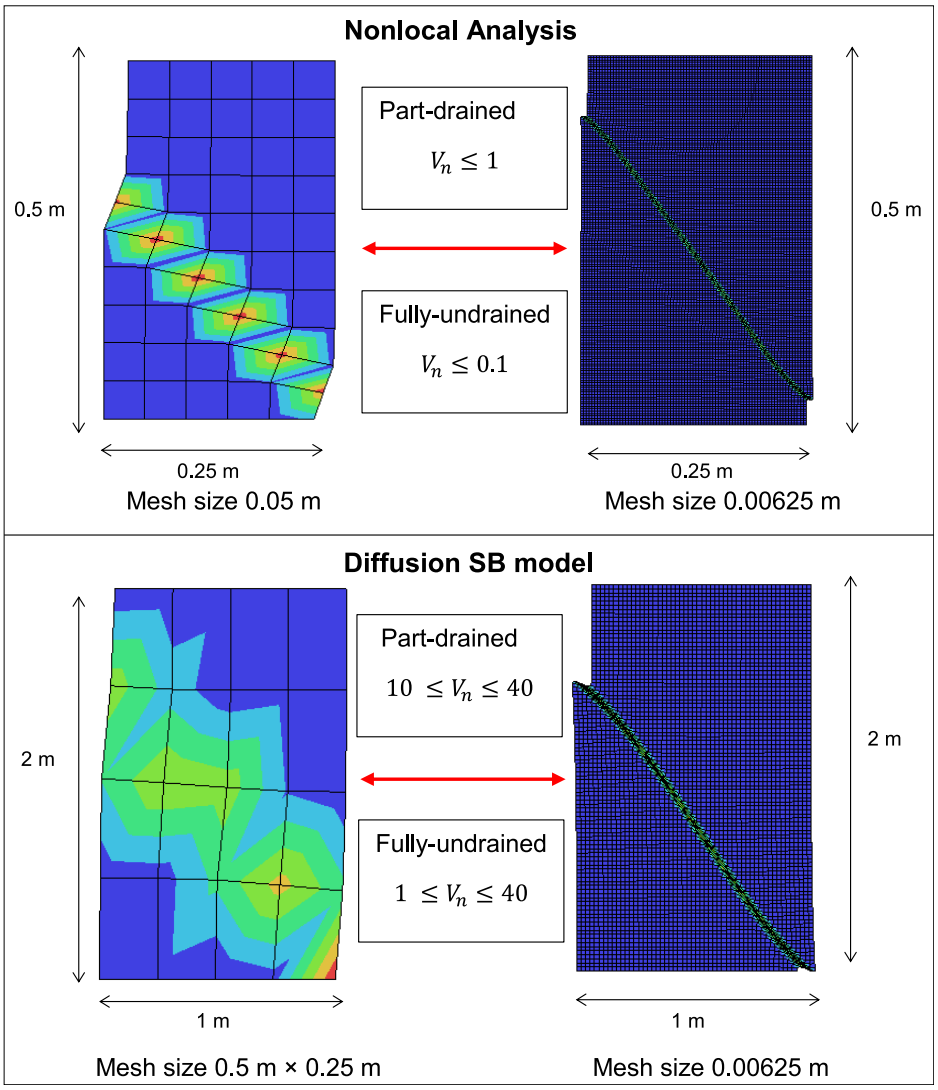

Fig. 7.1 Applicability of two methods: top- nonlocal analysis, bottom- diffusion SB model

7.2 Recommended Future Works

Possible extensions of this research can be proposed in three directions: laboratory testing, constitutive modelling and numerical simulations of field problems.

- Laboratory testing

  One of the limitations of the method proposed in Chapter 6 is that it is calibrated with another finite element model. Hence it inherits all the drawbacks of continuum-based methods. The best option is to calibrate the model with experimental data of undrained biaxial compression tests (with sufficient back pressure to avoid cavitation). Laboratory testing under different loading rates could be conducted for low permeable silty sand. Stress, void ratio and pore pressure could be measured inside and outside the shear band during post-localised deformation. It would provide insight into the rate effect on the initiation and propagation of the shear band. Expectations are in the developing research areas of x-ray tomography in which micro CT scanning may provide insights into local volume changes and pore fluid diffusion (Andò et al., 2013; Manahiloh and Meehan, 2017; Périard et al., 2016; Taylor, 2016). Possible size and time effects responsible for the suppression of locally drained shear bands (ratio of specimen size to grain size, permeability, viscosity and loading velocity) could be probed in detail. The impact of a small imperfection for the initiation of local drainage and localisation could be examined. However, X-ray computed micro-tomography (X-ray μCT) imaging of fluid saturated medium is still an emerging field. According to personal communications with Andò (2019), there are practical challenges to be conquered when imaging techniques are used to probe micro-mechanics of globally undrained sand.

- Improvements on constitutive modelling

  Several enhancements can be suggested to improve the constitutive description of the diffusion SB model. The non-coaxial NS model can be used to describe the constitutive behaviour inside the shear band while the original NS model is used for the outside. Since the deviatoric strain cannot detect whether the deformation is uniform or localised, a different parameter should be explored to check the onset of localisation. Representative biaxial strain can be calculated from the arbitrary strain field at any material point. It can be used to detect the onset of localisation in material points of the up-scaled model. The viable alternative to lack of experimental evidence is to calibrate the SB model with a discontinuum method such as a discrete element method. It can

simulate micro-kinematics at the grain scale comparatively with more accuracy level than FEM.

- Numerical simulations of field problems

  Both nonlocal regularisation and diffusion SB method can be utilised for large-scale $2D$ field problems under saturated condition. Possible applications are buckling of buried pipelines, dragging of anchors, ploughs, pull-out of suction caissons and other offshore foundations etc. These applications involve large deformations with shear localisations. Hence, conventional FE simulations are pathologically mesh dependent. The influence of different loading rates and permeabilities create various drainage conditions. The current practice is to conduct mesh refinement analysis until a convergent solution is reached. Nevertheless, it is computationally expensive for field problems with dimensions in the range of meters to kilometers. Furthermore, with continuous mesh refinement, the shear band thickness can be infinitely small, losing the ellipticity of governing equilibrium equations. Therefore, a regularisation tool is desirable such that an affordable mesh size can be used without loss of accuracy. The nonlocal regularisation with scaling can be utilised when localisations take place under fully drained conditions. The diffusion SB model can be used for partially drained conditions in deep-sea problems (when cavitation is delayed due to hydrostatic pressure).

  However, several improvements are necessary to when the diffusion SB model is applied for field problems. First, some scale effect on calibrated parameters of the model is foreseeable when it will be used in up-scaled applications. The influence of three scales: grain size (or real shear band thickness), element size and the dimension of the boundary value problem should be scrutinised to evaluate the range of applicability of the proposed method. Second, the model should be enhanced to take account of intricate localised patterns such as curved and tributary shear bands. Also, the evolution of shear band thickness and inclination should be considered. Third, fluid movements at soil-structure interface should be further studied. Finally, the diffusion SB model is currently only valid for $2D$ applications.

  Similar complications can arise when nonlocal regularisation and scaling is used for field problems. The applicability of this method near boundaries and soil-structure interface is questionable. Values for suitable characteristic length and scaling factor are doubtful when primary and secondary shear bands are formed with different inclination angles.

References

Abaqus 6.11 (2011). *Theory manual*. Dassault Systèmes Simulia Corp, Providence, RI, USA.

Ai, J., Langston, P. A., and Yu, H. S. (2014). Discrete element modelling of material non-coaxiality in simple shear flow. *International Journal for Numerical and Analytical Methods in Geomechanics*, 38(6):615–635.

Aifantis, E. (1984). Microscopic processes and macroscopic response. In Desai, C. S. and Gallagher, R. H., editors, *Mechanics of engineering materials*, pages 1–22. Wiley, New York.

Alshibli, K. A., Batiste, S. N., and Sture, S. (2003). Strain localization in sand: Plane strain versus triaxial compression. *Journal of Geotechnical and Geoenvironmental Engineering*, 129(6):483–494.

Andò, E. (2019). Personal communication.

Andò, E., Viggiani, G., Hall, S. A., and Desrues, J. (2013). Experimental micro-mechanics of granular media studied by x-ray tomography: recent results and challenges. *Géotechnique Letters*, 3(3):142–146.

Andrade, J. E. and Borja, R. I. (2007). Modeling deformation banding in dense and loose fluid-saturated sands. *Finite Elements in Analysis and Design*, 43(5):361–383.

Arthur, J., Chua, K., Dunstan, T., and Rodoriguez, J. (1980). Principal stress rotation: a missing parameter. *Journal of the Geotechnical Engineering Division*, 106(4):419–433.

Atkinson, J. H. and Richardson, D. (1987). The effect of local drainage in shear zones on the undrained strength of overconsolidated clay. *Géotechnique*, 37(3):393–403.

Bardet, J. P. and Proubet, J. (1992). Shear band analysis in idealized granular material. *Journal of Engineering Mechanics*, 118(2):397–415.

Bazant, Z. P. and Chang, T. (1984). Instability of nonlocal continuum and strain averaging. *Journal of Engineering Mechanics*, 110(10):1441–1450.

Bazant, Z. P. and Jirasek, M. (2002). Nonlocal integral formulations of plasticity and damage: Survey of progress. *Journal of Engineering Mechanics*, 128(11):1119–1149.

Bazant, Z. P. and Lin, F. (1988). Nonlocal yield-limit degradation. *International Journal of Numerical Methods in Engineering*, 26(8):1805–1823.

Bazant, Z. P. and Pijaudier, C. (1988). Nonlocal continuum damage, localization instability and convergence. *Journal of Applied Mechanics*, 55(2):287.

Been, K. and Jefferies, M. G. (1985). A state parameter for sands. *Géotechnique*, 35(2):99–112.

Been, K., Jefferies, M. G., and Hachey, J. (1991). The critical state of sands. *Géotechnique*, 41(3):365–381.

Benallal, A. and Comi, C. (1999). Some remarks on the elasto-plastic saturated porous media. In Muhlhaus, H., Dyskin, V., and Pasternak, E., editors, *Proceedings of 5th International Workshop on Bifurcation and Localisation Theory in Geomechanics*, pages 3–11, Perth. Balkema.

Benallal, A. and Comi, C. (2003). Perturbation growth and localization in fluid-saturated inelastic porous media under quasi-static loadings. *Journal of the Mechanics and Physics of Solids*, 51(5):851–899.

Bolton, M. (1986). The strength and dilatancy of sands. *Geotechnique*, 36(1):65–78.

Borja, R. I. and Regueiro, R. (2001). Strain localization in frictional materials exhibiting displacement jumps. *Computer Methods in Applied Mechanics and Engineering*, 190(20-21):2555–2580.

Bransby, M. F. and Ireland, J. (2009). Rate effects during pipeline upheaval buckling in sand. *Proceedings of the ICE - Geotechnical Engineering*, 162(5):247–256.

Brinkgreve, R. (1994). *Geomaterial Models and Numerical Analysis of Softening*. PhD thesis, University of Delft, Delft.

Cai, Y. (2010). *An Experimental Study of Non- coaxial Soil Behaviour using Hollow Cylinder Testing*. PhD thesis, University of Nottingham, Nottingham.

Chambon, R., Caillerie, D., and Matsushima, T. (2001). Plastic continuum with microstructure, local second gradient theories for geomaterials: Localization studies. *International Journal of Solids and Structures*, 38(46-47):8503–8527.

Charlier, R., Radu, J., and Barnichon, J. (1997). Water movement effect on the strain localisation during a biaxial compression. In Pietruszczak, S. and Pande, editors, *Numerical Models in Geomechanics*, pages 219–224, Balkema: Rotterdam.

Cheong, T. (2006). *Numerical Modelling of Soil -Pipeline Interaction*. PhD thesis, University of Cambridge, Cambridge.

Chow, L. C., Mao, J., and Shen, J. (2011). Nonlocal damage gradient model for fracture characterziation of aluminum alloy. *International Journal of Damage Mechanics*, 20(7):1073–1093.

Chunhua, H. and Drescher, A. (1993). Shear bands in biaxial tests on dry coarse sand. *Soils and Foundations*, 33(1):118–132.

Cole, E. (1968). *The Behaviour of Soil in Simple Shear Apparatus*. PhD thesis, University of Cambridge, Cambridge.

Collin, F., Chambon, R., and Charlier, R. (2006). A finite element method for poro mechanical modelling of geotechnical problems using local second gradient models. *International Journal for Numerical Methods in Engineering*, 65(11):1749–1772.

Collin, F., Sieffert, Y., and Chambon, R. (2010). Strain localization modeling in coupled transient phenomena. In Laloui, L., editor, *Mechanics of Unsaturated Geomaterials*, chapter 9, pages 209–231. John Wiley & Sons.

Cornforth, D. H. (1961). *Plane Strain Failure Characteristics of Saturated Sand*. PhD thesis, University of London, London.

de Borst, R., Sluys, L., Muhlhaus, H., and Pamin, J. (1993). Fundamental issues in finite element analysis of localization of deformation. *Engineering Computations*, 10(2):99–121.

Desrues, J. and Mokni, M. (1998). Strain localisation measurements in undrained plane-strain biaxial tests on Hostun RF sand. *Mechanics of Cohesive-Frictional Materials*, 4(4):419–441.

Desrues, J. and Viggiani, G. (2004). Strain localization in sand: An overview of the experimental results obtained in Grenoble using stereophotogrammetry. *International Journal for Numerical and Analytical Methods in Geomechanics*, 28(4):279–321.

Drucker, D., Robert, E. G., and Henkel, D. J. (1957). Soil mechanics and work hardening theories of plasticity. *Transactions of the American Society of Civil Engineers*, 122(1):338–346.

Duddu, R. and Waisman, H. (2013). A nonlocal continuum damage mechanics approach to simulation of creep fracture in ice sheets. *Computational Mechanics*, 51(6):961–974.

Ehlers, W., Ellsiepen, P., and Ammann, M. (2001). Time and space adaptive methods applied to localization phenomena in empty and saturated micropolar and standard porous materials. *International Journal for Numerical Methods in Engineering*, 52(5-6):503–526.

Ehlers, W. and Volk, W. (1998). On theoretical and numerical methods in the theory of porous media based on polar and non-polar elasto-plastic solid materials. *International Journal of Solids and Structures*, 35(34-35):4597–4617.

Eringen, A. (1966). A unified theory of thermo mechanical materials. *International Journal of Engineering Science*, 4(2):179–202.

Eringen, A. and Edelen, D. (1972). On nonlocal elasticity. *International Journal of Engineering Science*, 10(3):233–248.

Eringen, A. C. (1981). On nonlocal plasticity. *International Journal of Engineering Science*, 19(12):1461–1474.

Eringen, A. C. (1983). Theories of nonlocal plasticity. *International Journal of Engineering Science*, 21(7):741–751.

Eringen, A. C. and Kim, B. S. (1974). Stress concentration at the tip of a crack. *Mechanics Research Communications*, 1:233–237.

Fern, E. J. (2016). *Constitutive Modelling of Unsaturated Sand and its Application to Large Deformation Modelling*. PhD thesis, University of Cambridge, Cambridge.

Finnie, I. (1993). *Performance of Shallow Foundations in Calcerious Soil*. PhD thesis, University of Western Australia.

Galavi, V. and Schweiger, H. (2010). Nonlocal multilaminate model for strain softening analysis. *International Journal of Geomechanics*, 10(1):30–44.

Gao, Z. and Zhao, J. (2013). Strain localization and fabric evolution in sand. *International Journal of Solids and Structures*, 50(22-23):3634–3648.

Gao, Z. and Zhao, J. (2016). A non-coaxial critical-state model for sand accounting for fabric anisotropy and fabric evolution. *International Journal of Solids and Structures*, 106-107(February):1–13.

Garagash, D. and Rudnicki, J. (2002). Stability of undrained deformation of fluid saturated geo-materials. In Khan, A. and Lopez, P. O., editors, *Plasticity, Damage and Fracture at Macro, Micro and Nano Scales*, pages 492–494. NEAT Press.

Guo, P. (2013). Undrained shear band in water saturated granular media: A critical revisiting with numerical examples. *International Journal for Numerical and Analytical Methods in Geomechanics*, 37(4):353–373.

Guo, P. and Stolle, D. (2013). Coupled analysis of bifurcation and shear band in saturated soils. *Soils and Foundations*, 53(4):525–539.

Gutierrez, M. and Ishihara, K. (2000). Non-coaxility and energy dissipation in granular materials. *Soils and Foundations*, 40(2):49–59.

Gutierrez, M., Ishihara, K., and Ikuo, T. (1991). Flow theory for sand during rotation of principal stress direction. *Soils and Foundations*, 31(4):121–132.

Gutierrez, M., Ishihara, K., and Ikuo, T. (1993). Model for the deformation of sand during rotation of principal stress directions. *Soils and Foundations*, 33(3):105–117.

Gutierrez, M. and Vardoulakis, I. (2007). Energy dissipation and post-bifurcation behaviour of granular soils. *International Journal for Numerical and Analytical Methods in Geomechanics*, 31(3):435–455.

Gylland, A. S. (2012). *Material and Slope Failure in Sensitive Clays*. PhD thesis, Norwegian University of Science and Technology.

Han, C. and Vardoulakis, I. (1991). Plane strain compression experiments on water saturated fine grained sand. *Geotechnique*, 41(1):49–78.

Hashiguchi, K. (1991). Inexpedience of the non-associated flow rule. *International Journal for Numerical and Analytical Methods in Geomechanics*, 15(10):753–756.

Hashiguchi, K. (1993). Fundamental requirements and formulation of elastoplastic constitutive equations with tangential plasticity. *International Journal of Plasticity*, 9(5):525–549.

Hashiguchi, K. (1998). The tangential plasticity. *Metals and Materials International*, 4(4):652–656.

Hashiguchi, K. (2009). Elastoplasticity Theory. In Pfeiffer, F. and Wriggers, P., editors, *Lecture Notes in Applied and Computational Mechanics*, volume 42. Springer, Fukuoka.

Hashiguchi, K. and Tsutsumi, S. (2001). Elastoplastic constitutive equation with tangential stress rate effect. *International journal of plasticity*, 17(1):117–145.

Hashiguchi, K. and Tsutsumi, S. (2003). Shear band formation analysis in soils by the subloading surface model with tangential stress rate effect. *International Journal of Plasticity*, 19(10):1651–1677.

Hill, R. (1958). A general theory of uniqueness and stability in elastoplastic solids. *Journal of Mechanics and Physics of Solids*, 10(3):236–249.

Huang, M., Lu, X., and Qian, J. (2010). Non-coaxial elastoplasticity model and bifurcation prediction of shear banding in sands. *International Journal for Numerical and Analytical Methods in Geomechanics*, 34(9):906–919.

Huy, N. (2008). *Rapid Load Testing of Piles in Sand: Effects of Loading Rate and Excess Pore Pressure*. PhD thesis, University of Delft.

Ishihara, K. and Towhata, I. (1983). Sand response to cyclic rotation of principal stress directions as induced by wave loads. *Soils and Foundations*, 23(4):11–26.

Jefferies, M. and Been, K. (2006). *Soil liquefaction: A critical state approach*. Taylor and Francis Group.

Jefferies, M., Shuttle, D., and Been, K. (2015). Principal stress rotation as cause of cyclic mobility. *Geotechnical Research*, 2(2):66–94.

Jefferies, M. G. (1993). Nor-Sand: a simple critical state model for sand. *Géotechnique*, 43(1):91–103.

Jefferies, M. G. and Shuttle, D. A. (2002). Dilatancy in general Cambridge-type models. *Géotechnique*, 52(9):625–638.

Jiang, M. J., Liu, J. D., and Arroyo, M. (2016). Numerical evaluation of three non-coaxial kinematic models using the distinct element method for elliptical granular materials. *International Journal for Numerical and Analytical Methods in Geomechanics*, 40(18):2468–2488.

Jostad, H. P. and Grimstad, G. (2011). Comparison of distribution for nonlocal strain approach. In *2nd International Symposium on Computational Geomechanics*, pages 212–223, Cavtat-Dubrovnik, Croatia.

Kutter, B. (2006). Phenomena associated with undrained and partially drained dilatant soil. In Ng, C., Zhang, L., and Wang, Y., editors, *Proceedings of 6th international conference on Physical Modelling in Geotechnics*, pages 75–85, HongKong. Taylor and Francis Group.

Lade, P. and Bopp, P. (1993). Instability of dilating sand. *Mechanics of Material*, 16(3):249–264.

Larsson, J. and Larsson, R. (1999). Computational strategy for capturing localization in undrained soil. *Computational Mechanics*, 24(4):293–303.

Larsson, J. and Larsson, R. (2000a). Finite element analysis of localization of deformation and fluid pressure in an elastoplastic porous medium. *International Journal of Solids and Structures*, 37(48-50):7231–7257.

Larsson, J. and Larsson, R. (2000b). Localization analysis of a fluid-saturated elastoplastic porous medium using regularized discontinuities. *Mechanics of Cohesive-Frictional Materials*, 5(7):565–582.

Larsson, R., Runesson, K., and Sture, S. (1996). Embedded localization band in undrained soil based on regularized strong discontinuity- Theory and FE-analysis. *International Journal of Solids and Structures*, 33(20-22):3081–3101.

Lazari, M., Sanavia, L., and Schrefler, B. (2015a). Local and nonlocal elasto-viscoplasticity in strain localization analysis of multiphase geomaterials. *International Journal for Numerical and Analytical Methods in Geomechanics*, 39(14):1570–1592.

Lazari, M., Sanavia, L., and Schrefler, B. (2015b). Multiphase analysis of strain localization with regularized models. In Oñate, E., Bischoff, M., Owen, D., Wriggers, P., and Zohdi, T., editors, *IV International Conference on Particle based Methods - Fundamentals and Applications*, pages 149–160.

Li, X. (1997). Modelling of dilative shear failure. *Journal of Geotechnical and Geoenvironmental Engineering*, 123(7):609–616.

Li, X. S. (2002). A sand model with state-dependent dilatancy. *Géotechnique*, 52(3):173–186.

Liu, H. (2013). Unified sand modeling using associated or non-associated flow rule. *Mechanics Research Communications*, 50(June):63–70.

Liu, X., Scarpas, A., and Blaauwendraad, J. (2005). Numerical modelling of nonlinear response of soil. Part 2: Strain localization investigation on sand. *International Journal of Solids and Structures*, 42(7):1883–1907.

Loret, B. and Harireche, O. (1991). Accelaration waves, flutter instabilities and stationary discontinuities in inelastic porous media. *Journal of Mechanics and Physics of Solids*, 39(5):569–606.

Loret, B. and Prevost, J. (1991). Dynamic strain localization in fluid-saturated porous media. *Journal of Engineering Mechanics*, 117(4):907–922.

Lu, X., Huang, M., and Qian, J. (2014). Prediction of plane strain undrained diffuse instability and strain localization with non-coaxial plasticity. *Soils and Foundations*, 54(6):1070–1080.

Lu, X., Qian, J., and Huang, M. (2015). Study on the initiation of strain localization in soils by 3D non-coaxial plasticity. In Chau, K. and Zhao, J., editors, *Bifurcation and Degradation of Geomaterials in the New Millennium*, pages 253–258. Springer International Publishing Swizerland.

Mallikarachchi, H., Pelecanos, L., and Soga, K. (2018). Nonlinear finite element analysis of soil-pipe interaction for laterally loaded buried offshore pipelines. In Cardoso, A. S., Borges, J. L., Costa, P. A., Gomes, A. T., Marques, J. C., and Vieira, C. S., editors, *Proceedings of the 9th European Conference on Numerical Methods in Geotechnical Engineering*, volume 2, pages 1535–1540, Porto. CRC Press, Taylor & Francis.

Mallikarachchi, H. and Soga, K. (2018). The influence of non-coaxial plasticity in numerical modelling of soil-pipe interaction. In Cardoso, A. S., Borges, J. L., Costa, P. A., Gomes, A. T., Marques, J. C., and Vieira, C. S., editors, *Proceedings of the 9th European Conference on Numerical Methods in Geotechnical Engineering*, volume 1, pages 59–68, Porto. CRC Press, Taylor & Francis.

Mallikarachchi, H. E. (2015). Numerical Modelling of Large Deformations of Buried Offshore Pipelines- First year report. Technical report, University of Cambridge, Cambridge.

Manahiloh, K. N. and Meehan, C. L. (2017). Determining the Soil Water Characteristic Curve and Interfacial Contact Angle from Microstructural Analysis of X-Ray CT Images. *Journal of Geotechnical and Geoenvironmental Engineering*, 143(8):04017034–1–11.

Mangal, J. K. (1999). *Partially Drained Loading of Shallow Foundations*. PhD thesis, University of Oxford, Oxford.

Manzari, M. T. and Dafalias, Y. F. (1997). A critical state two-surface plasticity model for sands. *Geotechnique*, 47(2):255–272.

Matsuoka, H. and Nakai, T. (1974). Stress deformation and strength characteristics of soil under three different pricipal stresses. *Procceedings of JSCE*, (232):59–70.

Miura, K., Miura, S., and Toki, S. (1986). Deformation behavior of anisotropic dense sand under principal stress axes rotation. *Soils and Foundations*, 26(1):36–52.

Mokni, M. and Desrues, J. (1999). Strain localization measurements in undrained plane strain biaxial tests on Hostun RF sand. *Mechanics of Cohesive-Frictional Materials*, 4(4):419–441.

Mooney, M., Viggiani, G., and Finno, R. (1997). Undrained shear band deformation in granular media. *Journal of Engineering Mechanics*, 123(6):577–585.

Muhlhaus, H. and Vardoulakis, I. (1987). The thickness of shear bands in granular materials. *Geotechnique*, 37(3):271–283.

Needleman, A. and Ortiz, M. (1991). Effect of boundaries and interfaces on shear band localization. *International Journal of Solids and Structures*, 28(7):859–877.

Nguyen, G. (2014). An enriched constitutive modelling framework for localised failure of geomaterials. *Obras y proyectos*, 14:33–39.

Nguyen, G., Nguyen, C., Nguyen, V., Bui, H., and Shen, L. (2016). A size dependent constitutive modelling framework for localised failure analysis. *Computational Mechanics*, 58(2):257–280.

Nguyen, G. D., Einav, I., and Korsunsky, A. M. (2012). How to connect two scales of behaviour in constitutive modelling of geomaterials. *Géotechnique Letters*, 2(3):129–134.

Nova, R. (1982). A constitutive model for soil under monotonic and cyclic loading. In Pande, G. and Zienkiewicz, C., editors, *Soil mechanics - transient and cyclic loads*, pages 343–373. Wiley, Chichester.

Oda, M. and Konishi, J. (1974a). Microscopic deformation mechansim of granualr material in simple shear. *Soils and Foundations*, 14(4):25–38.

Oda, M. and Konishi, J. (1974b). Rotation of principal stresses in granular materials during simple shear. *Soils and Foundations*, 14(4):39–53.

Oka, F. (1985). Elasto/viscoplastic constitutive equations with memory and internal variables. *Computers and Geotechnics*, 1(1):59–69.

Oka, F., Adachi, T., and Yashima, A. (1995). A strain localization analysis using a viscoplastic softening model for clay. *International Journal of Plasticity*, 11(5):523–545.

Oka, F., Higo, Y., and Kimoto, S. (2002). Effect of dilatancy on the strain localization of water saturated elasto-viscoplastic soil. *International Journal of Solids and Structures*, 39(13):3625–3647.

Ortiz, M., Leroy, Y., and Needleman, A. (1987). A finite element method for localized failure analysis. *Computer Methods in Applied Mechanics and Engineering*, 61(2):189–214.

Palmer, A. C. (1999). Speed effects in cutting and ploughing. *Géotechnique*, 49(3):285–294.

Papamichos, E. and Vardoulakis, I. (1995). Shear band formation in sand according to non-coaxial plasticity model. *Geotechnique*, 45(4):649–661.

Périard, Y., Gumiere, S. J., Long, B., Rousseau, A. N., and Caron, J. (2016). Use of X-ray CT scan to characterize the evolution of the hydraulic properties of a soil under drainage conditions. *Geoderma*, 279:22–30.

Pestana, J. M. and Whittle, A. J. (1995). Compression model for cohesionless soils. *Geotechnique*, 45(4):611–631.

Pietruszczak, S. (1995). Undrained response of granular soil involving localized deformation. *Journal of Engineering Mechanics*, 121(12):1292–1297.

Pietruszczak, S. (1999). On homogenous and localised deformation in water infiltrated soils. *International Journal of Damage Mechanics*, 8(July):233–253.

Pietruszczak, S. and Mroz, Z. (1981). Finite element analysis of deformation of strain softening materials. *International Journal for Numerical Methods in Engineering*, 17(3):327–334.

Pietruszczak, S. and Niu, X. (1993). On the description of localized deformation. *International Journal for Numerical & Analytical Methods in Geomechanics*, 17(11):791–805.

Pietruszczak, S. and Stolle, D. F. E. (1985). Deformation of strain softeneing materials. Part 1: Objectivity of finite element solutions based on conventional strain softening formulations. *Computers and Geotechnics*, 1(2):99–115.

Pietruszczak, S. and Stolle, D. F. E. (1987). Deformation of strain softening materials. Part 2: Modelling of strain softening response. *Computers and Geotechnics*, 4(2):109–123.

Planas, J., Guinea, G. V., and Elices, M. (1996). Basic issues on nonlocal models: Uniaxial modeling. Technical report, Polytechnic University, Madrid, Spain.

Potts, D. and Zdravkovic, L. (1999). *Finite Element Analysis in Geotechnical Engineering*. Thomas Telford, London, 1st edition.

Puzrin, A. M. and Randolph, M. (2015). Effects of pore water pressure dissipation on rate dependency of shear strength in localised failure of soils. *International Journal for Numerical and Analytical Methods in Geomechanics*, 39(10):1045–1062.

Rechenmacher, A. L. (2006). Grain-scale processes governing shear band initiation and evolution in sands. *Journal of the Mechanics and Physics of Solids*, 54(1):22–45.

Rice, J. (1976). The localization of plastic deformation. In Koiter, W., editor, *14th International Congress on Theoretical and Applied Mechanics*, pages 207–220, Delft. North Holland Publishing Co.

Rice, J. and Rudnicki, J. (1980). A note on some features of the theory of localization of deformation. *International Journal of Solids and Structures*, 16(7):597–605.

Rice, J. R. (1975). On the stability of dilatant hardening for saturated rock masses. *Journal of Geophysical Research*, 80(11):1531–1536.

Robert, D. (2010). *Soil-pipeline Interaction in Unsaturated Soils*. PhD thesis, University of Cambridege, Cambridge.

Roger, V., Desrues, J., and Viggiani, G. (1997). Experiments on strain localisation in dense sand under isochoric conditions. In Toshihisa, A., Oka, F., and Yashima, A., editors, *Proceedings of Fourth International Workshop on Localization and Bifurcation Theory for soils and Rocks*, pages 239–248. Balkema.

Roscoe, K. (1970). The influence of strains in soil mechanics. *Geotechnique*, 20(2):129–170.

Roscoe, K., Schofield, A., and Thurairajah, A. (1963). Yielding of clays in states wetter than critical. *Geotechnique*, 13(3):211–240.

Rudnicki, J. (1983). A formulation for studying coupled deformation pore fluid diffusion effects on localization deformation. In Nemat, N., editor, *Proceedings of symposium on the mechanics of rocks and ice*, volume 57, pages 35–41, New York. American Society of Mechanical Engineers.

Rudnicki, J. (1985). Effect of pore fluid diffusion on deformation and failure of rock. In Bazant, Z. P., editor, *Mechanics of Geomaterials*, chapter 15, pages 315–347. John Wiley & Sons, Ltd.

Rudnicki, J. (2000). Diffusive Instabilities in Dilating and Compacting Geomaterials. In Rudnicki, J. and Chuang, T., editors, *Multiscale Deformation and Fracture in Materials and Structures*, pages 159–182. Kluwer Academic Publishers.

Rudnicki, J. and Rice, J. (1975). Conditions for the localization of deformation in pressure sensitive dilatant materials. *Journal of the Mechanics and Physics of Solids*, 23(6):371–394.

Rudnicki, J. W. (2009). Localization in undrained deformation. In *Proceedings of the 4th Biot Conference on Poromechanics*, New York.

Schrefler, B. A., Majorana, C. E., and Sanavia, L. (1995). Shear band localization in saturated porous media. *Archives of Mechanics*, 47(3):577–599.

Schrefler, B. A., Sanavia, L., and Majorana, C. E. (1996). Multiphase medium model for localisation and postlocalisation simulation in geomaterials. *Mechanics of Cohesive-Frictional Materials*, 1(1):95–114.

Sieffert, Y., Buzzi, O., and Collin, F. (2014). Numerical study of shear band instability and effect of cavitation on the response of a specimen under undrained biaxial loading. *International Journal of Solids and Structures*, 51(9):1686–1696.

Silva, M. and Bolton, M. (2005). Interpretation of centrifuge piezocone tests in dilatant, low plasticity soil. In Bilsel, H. and Nalbantoglu, Z., editors, *Procceedings of International Conference on Problemeatic Soils*, pages 25–27, Famagusta. Eastern Mediterranean University Press.

Soga, K., Pelecanos, L., Mallikarachchi, H., and Kumar, K. (2015). Finite element analysis of soil-pipe interaction for buried offshore pipelines. Technical report, University of Cambridge, Cambridge.

Soysa, A. (2015). *Monotonic and Cyclic Shear Loading Response of Natural Silts*. PhD thesis, University of British Columbia, Vancouver.

Stroud, M. A. (1971). *The Behaviour of Sand at Low Stress Levels in the Simple Shear Apparatus*. PhD thesis, University of Cambridge, Cambridge.

Summersgill, F., Kontoe, S., and Potts, D. (2017a). On the use of nonlocal regularisation in slope stability problems. *Computers and Geotechnics*, 82(February):187–200.

Summersgill, F. C., Kontoe, S., and Potts, D. (2014). A comparison of the mesh dependence of the nonlocal and local strain softening methods in a biaxial compression analysis. In Hicks, Brinkgreve, R., and Rohe, A., editors, *Numerical Methods in Geotechnical Engineering*, pages 289–294, London. Taylor and Francis Group.

Summersgill, F. C., Kontoe, S., and Potts, D. M. (2017b). Critical assessment of nonlocal strain-softening methods in biaxial compression. *International Journal of Geomechanics*, 17(7):1–14.

Taylor, D. (1948). *Fundamentals of Soil Mechanics*. Wiley, New York.

Taylor, H. (2016). *Assessing the potential for suffusion in sands using x-ray micro-CT images*. PhD thesis, Imperial College London, London.

Thakur, V. (2007). *Strain Localization in Sensitive Soft Clays*. PhD thesis, Norwegian University of Science and Technology.

Vardoulakis, I. (1985). Stability and bifurcation of undrained, plane rectilinear deformations on water-saturated granular soils. *International Journal for Numerical and Analytical Methods in Geomechanics*, 9(5):399–414.

Vardoulakis, I. (1986). Dynamic stability analysis of undrained simple shear on water saturated granualr soils. *International Journal for Numerical & Analytical Methods in Geomechanics*, 10(2):177–190.

Vardoulakis, I. (1989). Shear-banding and liquefaction in granular materials on the basis of a Cosserat continuum theory. *Ingenieur-Archiv*, 59(2):106–113.

Vardoulakis, I. (1996a). Deformation of water-saturated sand: I. uniform undrained deformation and shear banding. *Géotechnique*, 46(3):441–456.

Vardoulakis, I. (1996b). Deformation of water-saturated sand: II. effect of pore water flow and shear banding. *Géotechnique*, 46(3):457–472.

Vardoulakis, I. and Sulem, J. (1995). *Bifurcation Analysis in Geomechanics*. Blackie Academic & Professional, Glasgow, 1 edition.

Vermeer, P. and Marcher, T. (2000). Macromodelling of softening in non cohesive soils. In Vermeer, P., Diebels, S., Ehlers, W., Herrmann, H., Luding, S., and Ramm, E., editors, *Continous and Discontinous Modelling of Cohesive-Fricitional Material*, pages 89–108. Springer, Stuttgart.

Vermeer, P. and Verruijt, A. (1981). An accuracy condition for consolidation by finite elements. *International Journal for Numerical and Analytical Methods in Geomechanics*, 5(1).

Viggiani, G., Finno, R., and Harris, W. W. (1994). Experimental observations of strain localisation in plane strain compression of a stiff clay. In Chambon, R., Vardoulakis, I., and Desrues, J., editors, *Localisation and Bifurcation Theory for Soils and Rocks*, pages 189–198.

Wan, R., Pinheiro, M., Daouadji, A., Jrad, M., and Darve, F. (2013). Diffuse instabilities with transition to localization in loose granular materials. *International Journal for Numerical and Analytical Methods in Geomechanics*, 37(10):1292–1311.

Watanabe, K. and Kusakabe, O. (2013). Reappraisal of loading rate effects on sand behavior in view of seismic design for pile foundation. *Soils and Foundations*, 53(2):215–231.

Yang, Y. and Yu, H. S. (2006a). A non-coaxial critical state soil model and its application to simple shear simulations. *International Journal for Numerical and Analytical Methods in Geomechanics*, 30(13):1369–1390.

Yang, Y. and Yu, H. S. (2006b). Numerical simulations of simple shear with non-coaxial soil models. *International Journal for Numerical and Analytical Methods in Geomechanics*, 30(1):1–19.

Yang, Y. and Yu, H. S. (2010). Numerical aspects of non-coaxial model implementations. *Computers and Geotechnics*, 37(1-2):93–102.

Yang, Y., Yu, H. S., and Kong, L. (2011). Implicit and explicit procedures for the yield vertex non-coaxial theory. *Computers and Geotechnics*, 38(5):751–755.

Yang, Y. and Yu, S. (2006c). Application of a non-coaxial soil model in shallow foundation. *Geomechanics and Geoengineering: An International Journal*, 1(2):139–150.

Yatomi, C., Yashima, A., Iizuka, A., and Sano, I. (1989a). General theory of shear band formation by a non-coaxial Cam-Clay model. *Soils and Foundations*, 29(3):41–53.

Yatomi, C., Yashima, A., Iizuka, A., and Sano, I. (1989b). Shear band formation numerically simulated by a non-coaxial Cam-Clay model. *Soils and Foundations*, 29(4):1–13.

Yi, W. (1997). *Characterisation of Dilative Shear Failure in Sand*. PhD thesis, HongKong University of Science and Technology, Hong Kong.

Yu, H. S. (2006). *Plasticity and Geotechnics*. Springer, New York.

Yu, H. S. (2008). Non-coaxial theories of plasticity for granular materials. In *The 12th International Conference of International Association for Computer Methods and Advances in Geomechanics*, pages 361–378, Goa.

Zervos, A. and Papanastasiou, P. (2010). Computational post failure analysis with a second gradient theory: Gradient elastoplasticity. *European Journal of Environmental and Civil Engineering*, 14(1):1067–1079.

Zervos, A., Papanastasiou, P., and Vardoulakis, I. (2001). A finite element displacement formulation for gradient elastoplasticity. *International Journal for Numerical Methods in Engineering*, 50(6):1369–1388.

Zervos, a., Vardoulakis, I. G., and Papanastasiou, P. (2007). Influence of nonassociativity on localization and failure in geomechanics based on gradient elastoplasticity. *International Journal for Numerical and Analytical Methods in Geomechanics*, 7(1):63–74.

Zhang, H. W., Sanavia, L., and Schrefler, B. A. (1999). An internal length scale in dynamic strain localization of multiphase porous media. *Mechanics of Cohesive-Frictional Materials*, 4(5):443–460.

Zhang, H. W. and Schrefler, B. (2001). Uniqueness and localization analysis of elastic plastic saturated porous media. *International Journal for Numerical and Analytical Methods in Geomechanics*, 25(1):29–48.

Zhang, H. W. and Schrefler, B. A. (2004). Particular aspects of internal length scales in strain localization analysis of multiphase porous materials. *Computer Methods in Applied Mechanics and Engineering*, 193(27-29):2867–2884.